Nonequilibrium Steady-State Transport in Quantum Impurity Models

Frauke Schwarz

München 2017

Nonequilibrium Steady-State Transport in Quantum Impurity Models

Dissertation
an der Fakultät für Physik
der Ludwig-Maximilians-Universität
München

vorgelegt von
Frauke Magdalene Schwarz
aus Bad Mergentheim

München, den 10. Oktober 2017

Erstgutachter: Professor Dr. Jan von Delft
Zweitgutachter: Professor Dr. Ulrich Schollwöck
Tag der Abgabe: 10. Oktober 2017
Tag der mündichen Prüfung: 11. Dezember 2017

Zusammenfassung

Störstellenmodelle sind von großer Bedeutung für viele Bereiche der Festkörperphysik. Sie beschreiben Störstellen in Metallen, aber auch Nanostrukturen wie zum Beispiel Quantenpunkte. Außerdem finden sie Anwendung in der Charakterisierung starkkorrellierter Materialien. Im Falle magnetischer Störstellen kann sich bei tiefen Temperaturen der sogenannte Kondo-Effekt ausbilden, der auf komplexen Vielteilcheneffekten beruht. Er bewirkt in Quantenpunkten eine charakteristische Resonanz im Leitwert, die in vielen Experimenten gemessen wurde.

Ein geeignetes Instrument für die numerische Beschreibung von Vielteilchenzuständen sind die sogenannten Matrixproduktzustände. Zwei wichtige Methoden, die in einer solchen Beschreibung häufig Anwendung finden, sind die Numerische Renormierungsgruppe und die Dichtematrix-Renormierungsgruppe.

Mithilfe der Numerischen Renormierungsgruppe konnte ein sehr gutes Verständnis der Gleichgewichtseigenschaften des Kondo-Effekt erzielt werden. Die Beschreibung von stationären Zuständen im Falle von Nichtgleichgewicht, beispielsweise aufgrund einer angelegten Spannung, stellt jedoch nach wie vor eine große Herausforderung dar. Aufgrund des Teilchentransports entspricht der Aufbau einem offenen Quantensystem. Dies steht im Widerspruch zu einer Diskretisierung des Modells, wie sie für die Verwendung von Matrixproduktzuständen notwendig ist. Außerdem erfordert die Charakterisierung der Resonanz des Kondo-Effekts die Auflösung sehr kleiner Energieskalen.

Die vorliegende Arbeit diskutiert verschiedene Konzepte, die bei der Behandlung von Nichtgleichgewichtsprozessen in Störstellenmodellen eingesetzt werden können:

In einem ersten Teil wird die Möglichkeit diskutiert, trotz Diskretisierung des Modells ein offenes System zu beschreiben, indem man zusätzliche dissipative Terme im Sinne einer Lindbladgleichung einführt. Hierbei wird explizit aufgezeigt, wie diese dissipativen Terme zu wählen sind, um eine korrekte Darstellung der Physik zu gewährleisten. Außerdem wird erklärt, wie eine Formulierung erreicht werden kann, die eine numerische Behandlung mit Matrixproduktzuständen erleichtert.

In einem zweiten Teil wird dargelegt, wie Quench-Rechnungen dahingehend verbessert werden können, dass sie trotz der Beschränkung auf geschlossene Systeme zur Beschreibung von Kondo-Physik im Nichtgleichgewicht herangezogen werden können. Eine Kombination aus Numerischer Renormierungsgruppe und zeitabhängiger Dichtematrix-Renormierungsgruppe ermöglicht dabei die Behandlung kleiner Energieskalen, während die Verwendung der Thermofield-Methode eine günstige Darstellung der elektronischen Zuleitungen erlaubt. Dies ermöglicht eine Beschreibung der Kondo-Resonanz im Leitwert eines Quantenpunktes, inklusive ihrer Temperaturabhängigkeit und ihres Verhaltens in einem endlichen Magnetfeld.

Abstract

Quantum impurity models are of great interest in solid state physics as they describe impurities in metals as well as nanostructures such as quantum dots. Furthermore, they are relevant in the description of strongly correlated materials. An important many-body effect for magnetic impurities at low temperatures is the Kondo effect. In quantum dots it causes a zero-bias peak in the conductance, which has been measured in many experiments.

A useful tool in the numerical description of many-body physics is the concept of matrix product states. Two methods of great relevance in this context are the numerical renormalization group and the density-matrix renormalization group.

Regarding its equilibrium properties a deep understanding of the Kondo effect has been achieved based on the numerical renormalization group. However, the description of steady-state nonequilibrium, e.g. arising due to an applied voltage, remains a big challenge. Due to the transport of particles, in principle, one has to consider an open quantum system. This is in stark contrast to the discretization of the system that is necessary for a treatment using matrix product states. Moreover, the characterization of the Kondo resonance requires the resolution of small energy scales.

The present work presents different concepts which are useful in the description of nonequilibrium steady-state physics in quantum impurities.

In a first part it is pointed out how one can restore the continuous properties of a discretized impurity model using additional dissipative terms in the sense of a Lindblad equation. It is explicitly shown how the dissipative terms must be chosen to recover a correct representation of the physical model. Moreover, this Lindblad equation is brought into a form which is considered to be useful for a treatment based on matrix product states.

In a second part it is discussed how quench calculations can be improved in such a way that they can be used for the investigation of nonequilibrium Kondo physics in spite of the restriction to closed quantum systems. A combination of the numerical renormalization group and the time-dependent density-matrix renormalization group facilitates the investigation of nonequilibrium at small energy scales. In addition, the thermofield approach allows an efficient representation of the leads. This enables us to describe the zero-bias peak characterizing the Kondo effect in a quantum dot including, in particular, its dependence on temperature and magnetic field.

Contents

I Introduction

This work explains how to tackle a long-standing problem: the description of Kondo physics in nonequilibrium.

The Kondo effect is a fascinating many-body effect arising at low temperatures in the presence of magnetic impurities. Historically, it was first observed in metals with magnetic defects. Nowadays, its importance is also strongly linked to its appearance in quantum dots, where its primary characteristic is a striking zero-bias peak in the conductance when applying a source-drain voltage. The use of quantum dots has made it possible to study the Kondo effect systematically: During the last twenty years a series of experiments achieved a consistent and detailed picture of the transport properties of quantum dots in the Kondo regime. In particular, the behavior of the zero-bias peak with changing temperature and magnetic field is well established.

Theoretically, the equilibrium properties of the Kondo effect are well understood. The introduction of the numerical renormalization group by K. G. Wilson in 1975 was the crucial step to complete the theoretical picture. Despite considerable progress, getting reliable results on nonequilibrium steady-state properties of magnetic impurities in the Kondo regime, is still a big challenge. In particular, the situation of a finite source-drain voltage, which is standard in experiment, remains a major problem for theoretical calculations.

Many numerical descriptions of Kondo physics rely on the concepts of matrix product states, which have become a valuable tool to capture the many-body physics of quantum impurity models in a nonperturbative manner. Most importantly, two powerful many-body methods, the numerical renormalization group and the density-matrix renormalization group, are nowadays typically phrased in the language of matrix product states.

This work presents several concepts useful for the description of impurity models in nonequilibrium:

- The characterization of many-body physics based on matrix product states is typically accompanied by a discretization of the system into a finite number of modes, thereby rendering the system closed and restricting the calculations to finite time scales. This is in stark contrast to the description of a truly open quantum system and its steady-state limit. This work explains how a Lindblad driving can help to bridge this gap and to restore the continuous properties of discretized leads. It is derived how a Lindblad equation has to be set up to ensure a faithful representation of the leads, and a particularly simple form is presented that brings a solution of the Lindblad equation based on matrix product state within reach.

- The Kondo scale is an exponentially small energy scale. This work shows how the concept of renormalization used in the numerical renormalization group can be carried over to situations of steady-state nonequilibrium by combining it with methods such as the time-dependent density-matrix renormalization group. This allows studying arbitrary energy scales and in particular describing nonequilibrium physics on the Kondo scale.
- In standard quench calculations based on matrix product states one has to cope with limitations in the accessible time window due to finite-size effects and the growth in entanglement. However, by choosing the representation of the leads in an efficient way based on the thermofield approach, describing longer time scales becomes possible such that in many cases steady-state properties can be deduced.

A combination of the last two concepts allows the description of the zero-bias peak of a quantum dot in the Kondo regime, including its behavior with changing temperature and magnetic field, which is the greatest achievement of the above methodological developments.

This work includes the following two articles, presented in chapters V and VII:

[P1] F. Schwarz, M. Goldstein, A. Dorda, E. Arrigoni, A. Weichselbaum and J. von Delft, *Lindblad-driven discretized leads for nonequilibrium steady-state transport in quantum impurity models: Recovering the continuum limit*, Phys. Rev. B **94** (2016), 155142.

[P2] F. Schwarz, I. Weymann, J. von Delft and A. Weichselbaum, *Nonequilibrium Steady-State Transport in Quantum Impurity Models: A Thermofield and Quantum Quench Approach Using Matrix Product States*, Phys. Rev. Lett. **121** (2018), 137702.

Two further publications connected to this research are:

[P3] B. Bruognolo, N.-O. Linden, F. Schwarz, S.-S. B. Lee, K. Stadler, A. Weichselbaum, M. Vojta, F. B. Anders and J. von Delft, *Open Wilson chains for quantum impurity models: Keeping track of all bath modes*, Phys. Rev. B **95** (2017), 121115.

[P4] D. M. Fugger, A. Dorda, F. Schwarz, J. von Delft and E. Arrigoni, *Nonequilibrium Kondo effect in a magnetic field: auxiliary master equation approach*, New J. Phys. **20** (2018), 013030.

The main part is structured as follows: Chapter II gives a short introduction into quantum impurity models (II.1), the representation of leads (II.2), and the Kondo effect (II.3). Chapter III summarizes the main ideas of matrix product state methods (III.1), the time-dependent density-matrix renormalization group (III.2), the numerical renormalization group (III.3), and the concept of purification (III.4). Chapter IV is devoted to the idea of "Lindblad-driven discretized leads". As a first step, the quantum regression theorem in Lindbladian systems is extended to fermionic systems (IV.1). A first simple example illustrates the idea of Lindblad-driven leads (IV.2) before a formal derivation is given, which can be used to find a representation of Lindblad-driven leads which is local on the MPS chain (IV.3). A brief comment is given on the possibility to set up a local Lindblad driving directly in a chain representation based on the open Wilson chain approach (IV.4). In the last part of the chapter, some methods are discussed which can be used to solve Lindblad equations in the language of matrix product states (IV.5). Chapter V presents the publication [P1] on Lindblad-driven discretized leads. Chapter VI focuses on the description of nonequilibrium Kondo physics based on quantum quenches: After a short introduction to quench calculations (VI.1), the thermofield approach is presented as a valuable tool for the representation of thermal leads (VI.2), and a combination of numerical renormalization group and time-dependent density-matrix renormalization group is formulated to renormalize the impurity

also in situations of steady-state nonequilibrium (VI.3). These tools are then applied to the interacting resonant level model (VI.4) and the single-impurity Anderson model (VI.5) out of equilibrium. For the latter, results on the zero-bias peak at zero temperature, but also at finite temperature and finite magnetic field are shown. In a last part of the chapter, the quench method is compared to the auxiliary master equation approach (VI.6). Chapter VII presents the paper [P2] on the quench approach and the results for the zero-bias peak in the SIAM. Finally, Chapter VIII concludes with some closing remarks.

II Quantum Impurity Models and the Kondo Effect

For low temperatures the resistivity of most metals decreases strongly with decreasing temperature because the contributions of electron-phonon scattering as well as electron-electron scattering vanish in the limit of zero temperature. In this limit one expects the resistivity to saturate at a constant value stemming from the electrons scattering off the lattice defects. However, in 1934, W. J. de Haas et al. measured a striking minimum in the resistivity of gold wires at low temperature [5]. It took as much as thirty years until, in 1964, Jun Kondo was able to show based on perturbation theory that this increase in resistivity with decreasing temperature can be explained by scattering processes associated with magnetic impurities [6]. Named after him this remarkable feature goes under the name *"Kondo effect"* and the corresponding theoretical model used in his calculations is known as *"Kondo Model"*. While Kondo's calculations provided a physical explanation for the experimental results, it still contained unphysical divergences due to the limited scope of perturbation theory. A further step towards a better theoretical understanding was made by P. W. Anderson [7] with a calculation known as *"poor man's scaling"*. This renormalization group approach is also based on perturbation theory and could not fully solve the Kondo problem. Nevertheless, it gave further inside and in particular it already contained the idea of *scaling*. Finally, in 1975 Kenneth G. Wilson was able to solve the Kondo model using his famous *"numerical renormalization group"* (NRG) [8, 9]. With this nonperturbative method it is possible to determine approximate eigenstates of the Hamiltonian. Therefore, this technique is able to capture the full *many-body physics* of the Kondo effect. From all this theoretical work, the enhanced resistivity in metals is nowadays explained by scattering processes involving spin flips of a localized spin on the impurity. The local spin forms a singlet state with the conduction electrons.

While from this historical point of view the Kondo effect was of interest due to magnetic impurities in metals, it has experienced a revival in the context of *quantum dots* during the last twenty years. Quantum dots are also called "artificial atoms" because their properties resemble that of real atoms in many respects. Depending on the number of electrons on the quantum dot, these artificial atoms can be magnetic. Such a magnetic dot coupled to two electronic leads exhibits Kondo physics in analogy to magnetic impurities in metals. However, the geometry of the two systems is different: the electrons in the metal can "pass by" the magnetic impurities, while for the quantum dot setup all electrons have to go through the dot. As a consequence, the Kondo effect results in an increased resistivity in the former case and in a decrease in resistivity in the latter case. Due to their tunability, experiments in quantum dots allow a much more systematic characterization of Kondo

physics, see, e.g., references [10–12]. However, the wording in many cases still refers to the historic setup of magnetic impurities in metals such as the term *"quantum impurity models"*.

At the beginning of this chapter, different impurity models are introduced (section II.1). The second part focuses on the representation of the leads attached to the impurity (section II.2), and the last part gives an overview of the transport properties of quantum dots and in particular the characteristics of the Kondo effect in equilibrium and nonequilibrium (section II.3).

II.1 Quantum Impurity Models

The term *"quantum impurity models"* summarizes a class of models consisting of a *small* system (the "impurity") coupled to a *noninteracting* bosonic or fermionic bath. The Hamiltonian takes the form

$$H = H_{\text{imp}} + H_{\text{bath}} + H_{\text{hyb}}. \tag{1.1}$$

H_{imp} is the impurity Hamiltonian. This impurity Hamiltonian, in principle, is arbitrary. In particular, it can contain non-quadratic interaction terms which make it impossible to describe the impurity, and therefore the whole system, in terms of a single-particle picture.

The bath Hamiltonian H_{bath} is assumed to be noninteracting (quadratic). In the context of this work, only fermionic baths are considered. Typically, they represent the electronic leads and in the models considered here, the bath consists of two leads: the left and right leads, labeled by $\alpha \in \{L, R\}$. Representing the bath in energy, it takes the form

$$H_{\text{bath}} = \sum_{\alpha k(\sigma)} \varepsilon_k c^\dagger_{\alpha k(\sigma)} c_{\alpha k(\sigma)} = \sum_q \varepsilon_q c^\dagger_q c_q \,, \tag{1.2}$$

where α labels the different leads, k labels the different energies, and σ is a potential spin index. The index $q = \{\alpha, k, (\sigma)\}$ is a composite index referring to the different lead levels. In the original model the bath is continuous with infinitely many lead levels k. For numerical calculations, in practice, the bath is approximated by a finite number of such modes.

Finally, the Hamiltonian H_{hyb} describes the hybridization between bath and impurity. It is also assumed to be quadratic, but its exact shape depends on the impurity model.

In the following four important impurity models are introduced: the noninteracting resonant level model, the interacting resonant level model, the single-impurity Anderson model, and the Kondo model.

II.1.1 The Noninteracting Resonant Level Model

The noninteracting resonant level model (RLM) is the simplest impurity model: A spinless fermionic local level is coupled to fermionic leads,

$$H_{\text{imp}} = \varepsilon_d \, d^\dagger d, \tag{1.3a}$$

$$H_{\text{hyb}} = \sum_{\alpha k} v_{\alpha k} \, d^\dagger c_{\alpha k} + \text{h.c.} \tag{1.3b}$$

In principle, one can add a spin index. However, the different spin components do not interact. Therefore, the Hamiltonian would degenerate into two independent identical Hamiltonians.

Since the full Hamiltonian is noninteracting, the model can be described in a single-particle picture. It can therefore be solved exactly with analytic methods. For a structurless bath in equilibrium, the local density of states defined by $A(\omega) = -\frac{1}{\pi}\mathrm{Im}\left(G^R_{dd}(\omega)\right)$ with the retarded Green's function $G^R_{dd}(\omega) = -\mathrm{i}\int_0^\infty \mathrm{d}t\, \mathrm{e}^{\mathrm{i}\omega t}\,\langle\{d(t), d^\dagger\}\rangle$ is a simple Lorentzian peak with a width given by the total strength of the impurity-bath hybridization. For numerical methods, such analytic results provide a natural first point of comparison. However, one should bear in mind that due to the absence of interaction there is, e.g., no transfer of information between different energy scales in this model. For that reason it is only partially suitable as a benchmark model.

II.1.2 The Interacting Resonant Level Model

The interacting resonant level model (IRLM) is an extension of the RLM with two leads where in a physical picture an additional Coulomb repulsion U between resonant level and the leads is introduced as depicted in figure II.1(a). To bring such a model into the form of equation (1.1) the impurity is extended to three sites by including the linear combination of lead modes which directly couples to the local level into the impurity Hamiltonian: The central site d_C represents the local level, while the left site d_L and the right site d_R represent the lead modes of the left and right leads "closest" to the local impurity and thus affected by the Coulomb repulsion of the local level, see figure II.1(b). A more detailed explanation on the interpretation of d_L and d_R is given in section II.2.1. The Hamiltonian takes the form

$$H_{\mathrm{imp}} = \varepsilon_d\, n_C + U\,(n_L + n_R - 1)\, n_C + \left(t'\, d_C^\dagger d_L + t'\, d_C^\dagger d_R + \mathrm{h.c.}\right) \tag{1.4a}$$

$$H_{\mathrm{hyb}} = \sum_{\alpha k} v_{\alpha k} d_\alpha^\dagger c_{\alpha k} + \mathrm{h.c.}\,, \tag{1.4b}$$

where $n_i = d_i^\dagger d_i$, for $i \in \{L, R, C\}$. The additional term $-Un_C$ redefines the energy of the local level, such that the model is particle-hole symmetric at $\varepsilon_d = 0$. This model is an interesting

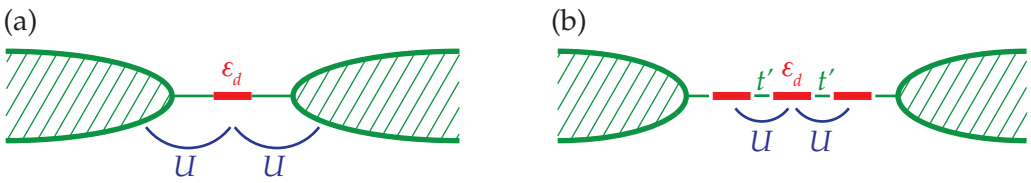

Figure II.1: (a) Physical idea of the IRLM: the local level feels a Coulomb repulsion from the lead electrons. (b) To make this Coulomb repulsion explicit, one uses a larger impurity by including two further sites. This additional sites represent the lead modes "closest" to the impurity.

toy model. Due to the interaction U it contains many-body aspects. But on the other hand, spin is not relevant in this model such that it is typically simpler to treat in numerics than, e.g., the single-impurity Anderson model.

II.1.3 The Single-Impurity Anderson Model

The single-impurity Anderson model (SIAM) was first written down by P. Anderson in 1961 to describe *"Localized Magnetic States in Metals"* [13]. Nowadays, it is also used to describe a local level in a quantum dot coupled to electronic leads. In this model the local level can be

occupied by the two different spin directions, see figure II.2(a). If the level is doubly occupied with a spin-up and a spin-down electron, the two electrons feel a Coulomb repulsion U,

$$H_{\text{imp}} = \sum_{\sigma=\{\uparrow,\downarrow\}} \varepsilon_d \, n_\sigma + U n_\uparrow n_\downarrow, \tag{1.5a}$$

$$H_{\text{hyb}} = \sum_{\alpha k \sigma} v_{\alpha k \sigma} d_\sigma^\dagger c_{\alpha k \sigma} + \text{h.c.} \tag{1.5b}$$

with $n_\sigma = d_\sigma^\dagger d_\sigma$.

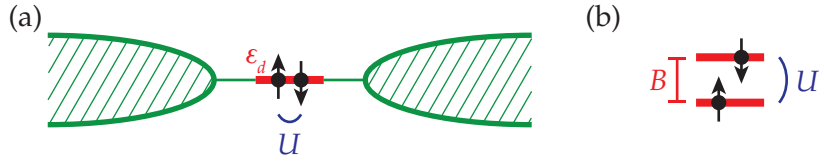

Figure II.2: Sketch of the SIAM: (a) The impurity consists of a single site. If it is occupied by two electrons with different spins, these electrons feel a Coulomb repulsion U. (b) A finite magnetic field B introduces a splitting between the two spin components.

A frequent extension of this model contains an additional local magnetic field, which introduces a Zeeman splitting between the two spins on the local level as sketched in figure II.2(b),

$$H_{\text{imp}} \to H_{\text{imp}} - \tfrac{B}{2}(n_\uparrow - n_\downarrow). \tag{1.6}$$

II.1.4 The Kondo Model

In specific parameter regimes, magnetic impurities can be described by a single localized spin with spin-spin interactions between impurity and the electrons of the leads. This is realized in the Kondo model with a Hamiltonian

$$H_{\text{hyb}} = -J \, \mathbf{S} \cdot \mathbf{s}, \tag{1.7a}$$

where $\mathbf{S}$ is the spin operator of the impurity and

$$\mathbf{s} = \sum_{\substack{\alpha,k,\sigma,\\ \alpha',k',\sigma'}} c^\dagger_{\alpha,k,\sigma} \boldsymbol{\sigma}_{\sigma,\sigma'} c_{\alpha',k',\sigma'}\,, \tag{1.7b}$$

where $\boldsymbol{\sigma}$ denotes the Pauli matrices. When lead electrons scatter off the localized spin, the Hamiltonian allows a spin flip of impurity spin and electron spin. For parameter regimes in which the single-impurity Anderson model shows a local moment behavior, its Hamiltonian is connected to the Kondo Hamiltonian by a Schrieffer-Wolff transformation [14]. In that sense the Kondo Hamiltonian can be seen as an effective Hamiltonian for the SIAM in the local moment regime.

II.2 Bath Properties

While the impurity consists of a small number of degrees of freedom, the fermionic bath, in principle, is a continuous system. For a numerical description based on matrix product

states it is necessary to find a suitable finite approximation of the bath. This bath representation should capture all relevant properties of the hybridization function introduced in sections II.2.1 and II.2.2, which is the only characteristic of the bath that enters the properties of the impurity. Furthermore, for a treatment based on matrix product states it is advantageous to bring the leads into a chain representation as described in section II.2.3.

II.2.1 Hybridization

If each of the leads couples to only one impurity level, as is the case in the models described in sections II.1.1-II.1.3, the hybridization term is of the form

$$H_{\text{hyb}} = \sum_q v_q \, d^\dagger_{(\alpha,\sigma)} c_q + \text{h.c.} \tag{2.1}$$

where $q = \{\alpha, k, (\sigma)\}$ combines the lead index α, the energy label k, and a possible spin index σ. Depending on the precise model, the impurity level coupling to lead α can carry a lead or spin index.

In most cases, one is interested in the physics of the impurity only. Based on the equations of motion one can show that the only characteristic of the leads that enters the properties of the impurity is the *"hybridization function"*. For a bath Hamiltonian of the form (1.2) it is given by

$$\Delta_\alpha(\omega) = \sum_k |v_q|^2 \, g_{qq}(\omega), \tag{2.2}$$

where $g_{qq}(\omega)$ is the bare Green's function of bath level q *in absence* of the coupling to the impurity (see section II.2.2 for a definition of the Green's function). Note that if there is a spin degree of freedom in the model, usually neither v_q nor $g_{qq}(\omega)$ depend on spin such that also $\Delta_\alpha(\omega)$ is spin-independent. Therefore, the spin index is dropped on the left-hand side of equation (2.2).

In equilibrium, only the retarded component has to be considered (compare section II.2.2). For the bare Green's function of lead level q one finds

$$g^R_{qq}(\omega) = \lim_{\epsilon \to 0^+} (\omega - \varepsilon_q + \mathrm{i}\epsilon)^{-1} \, . \tag{2.3}$$

As $\Delta^R_\alpha(\omega)$ is an analytic function, it suffices to look at its imaginary part

$$\Gamma_\alpha(\omega) = -\text{Im}\left(\Delta^R_\alpha(\omega)\right) = \sum_k \left|v_q\right|^2 \pi \delta(\omega - \varepsilon_q). \tag{2.4}$$

The real part can be deduced from the Kramers-Kronig relation. Again, the spin index is suppressed for $\Gamma_\alpha(\omega)$. For a continuous bath, the sum over k should be read as an integral $\int \mathrm{d}\varepsilon_q \, \rho_\alpha(\varepsilon_q)$ with $\rho_\alpha(\varepsilon_q)$ being the density of states such that

$$\Gamma_\alpha(\omega) = \pi \rho_\alpha(\omega) \left|v_\alpha(\omega)\right|^2 . \tag{2.5}$$

Typically, in quantum impurity models one is interested in structureless leads and in many cases one simply considers a box distribution,

$$\Gamma_\alpha(\omega) = \Gamma_\alpha \Theta(D - |\omega|), \tag{2.6}$$

with $2D$ being the bandwidth of the lead.

For a numerical description, the bath has to be discretized into a finite number of levels in such a way that the resulting hybridization is a good approximation of the original continuous hybridization function. To this end, the full band $[-D, D]$ is divided into a finite number of energy intervals $I_k = [E_k, E_{k+1}]$. Each energy interval is represented by a single energy $\varepsilon_k \in I_k$. For a linear discretization, where all intervals I_k are of the same size, it is natural to choose ε_k to be in the middle of the energy interval,

$$\varepsilon_k = \tfrac{1}{2}(E_k + E_{k+1})\,. \tag{2.7}$$

However, this is not necessarily the best choice for a nonlinear discretization. In case of a logarithmic discretization, $E_{k+1}/E_k = \Lambda$ with $\Lambda > 1$, a reasonable choice is given by [15]

$$\varepsilon_k = \frac{E_{k+1} - E_k}{\log\left(\frac{E_{k+1}}{E_k}\right)} = E_{k+1}\,\frac{\left(1 - \frac{1}{\Lambda}\right)}{\log \Lambda}\,. \tag{2.8}$$

The couplings v_q are connected to the hybridization $\Gamma_\alpha(\omega)$ by the condition that the weight of the hybridization within one interval I_k in the discrete system should equal the weight of the continuous function $\Gamma_\alpha(\omega)$ in this interval,

$$\int_{I_k} \mathrm{d}\omega\, \Gamma_\alpha(\omega) = \pi v_q^2 \tag{2.9a}$$

which for the box distribution in equation (2.6) sets

$$v_q = \sqrt{\frac{\Gamma_\alpha \delta_k}{\pi}} \quad \text{with } \delta_k = E_{k+1} - E_k. \tag{2.9b}$$

In this work, the total hybridization is defined as the sum over the hybridization of different leads,

$$\Gamma(\omega) = \sum_\alpha \Gamma_\alpha(\omega)\,. \tag{2.10}$$

II.2.2 The Hybridization in Nonequilibrium

For a closed system in equilibrium it suffices to look at the retarded component of the hybridization function, which can immediately be calculated from the Hamiltonians H_{hyb} and H_{bath} as done in section II.2.1. However, for an open system in nonequilibrium one also needs to consider the *Keldysh component* of the hybridization function which essentially adds information on the occupation of the different levels.

Nonequilibrium Green's functions

Green's functions are defined as correlators of the form $\langle B(t_1) C^\dagger(t_2)\rangle$. The Keldysh formalism generalizes the use of such Green's function to nonequilibrium situations. A detailed explanation of this formalism is outside the scope of the present work and the reader is referred to textbook literature, e.g. ro reference [16]. The fundamental difference between equilibrium and nonequilibrium Green's functions stems from the fact that in equilibrium calculations one can use the property that the system's state at $t = -\infty$ is connected to

the state at $t = \infty$ by a simple phase factor, which is not true anymore in the case of nonequilibrium. Therefore, while in equilibrium it suffices to work on a branch going from $-\infty$ to ∞, one needs to work on a *"Keldysh contour"* with a *forward branch* from $-\infty$ to ∞ and a *backward branch* from ∞ to $-\infty$. Distinguishing different cases with t_1 and t_2 being part of either the forward or the backward branch one has to distinguish four different Green's functions. Here the discussion is restricted to the physics of the steady-state, which is translationally invariant in time such that the two time arguments can be reduced to a single argument $t = (t_1 - t_2)$. The *"retarded"*, *"advanced"*, *"lesser"*, and *"greater"* Green's functions are defined as

$$\mathcal{G}^R_{BC}(t) = -\mathrm{i}\theta(t)\,\langle\{B(t), C^\dagger\}\rangle_{\mathrm{NESS}}\,, \tag{2.11a}$$

$$\mathcal{G}^A_{BC}(t) = \mathrm{i}\theta(t)\,\langle\{B(t), C^\dagger\}\rangle_{\mathrm{NESS}}\,, \tag{2.11b}$$

$$\mathcal{G}^<_{BC}(t) = \mathrm{i}\,\langle C^\dagger B(t)\rangle_{\mathrm{NESS}}\,, \tag{2.11c}$$

$$\mathcal{G}^>_{BC}(t) = -\mathrm{i}\,\langle B(t) C^\dagger\rangle_{\mathrm{NESS}}\,, \tag{2.11d}$$

where all expectation values are taken in the nonequilibrium steady-state (NESS) limit.

The four Green's functions are not independent of each other. This can be made explicit by performing the *"Keldysh rotation"* [16]. Apart from $\mathcal{G}^R_{BC}(t,t')$ and $\mathcal{G}^A_{BC}(t,t')$ defined above, on typically uses the *"Keldysh Green's function"*

$$\mathcal{G}^K_{BC}(t) = \mathcal{G}^>_{BC}(t) + \mathcal{G}^<_{BC}(t) = -\,\langle\big[B(t), C^\dagger\big]\rangle\,, \tag{2.12}$$

as a third independent Green's function.

The Fourier transforms of the Green's functions are defined as

$$G^X_{BC}(\omega) = \int_{-\infty}^{\infty} \mathrm{d}t\, \mathrm{e}^{\mathrm{i}\omega t}\, \mathcal{G}^X_{BC}(t), \tag{2.13}$$

with $X \in \{R, A, <, >, K\}$.

The fluctuation-dissipation theorem

In thermal equilibrium the Keldysh Green's function is not independent of the retarded and advanced Green's function. The corresponding relation is known as *"fluctuation-dissipation theorem"* and nicely illustrates that the Keldysh Green's function encodes information on the occupation statistics [16],

$$G^K(\omega) = 2\mathrm{i}(1 - 2f(\omega))\mathrm{Im}\left(G^R(\omega)\right)\,, \tag{2.14}$$

with $f(\omega)$ being the Fermi distribution function in case of a fermionic system.

Hybridization for thermal leads

While in equilibrium calculations only the retarded component of the hybridization is relevant, in nonequilibrium also the Keldysh component has to be considered. For a continuous thermal lead α coupled to a single impurity level the Keldysh component of the hybridization function has to fulfill the fluctuation-dissipation theorem,

$$\Delta^K_\alpha(\omega) = \sum_k |v_q|^2 g^K_{qq}(\omega) = -2\mathrm{i}(1 - 2f_\alpha(\omega))\Gamma_\alpha(\omega). \tag{2.15}$$

II.2.3 Chain Representations

The representation of leads in terms of the energy levels k introduced above is often referred to as *"star geometry"* because each lead level directly couples to the impurity, and only to the impurity, such that a pictorial description resembles the geometry of a star. For many applications, such as the matrix product state calculations presented in the next chapter, it is advantageous to work with a representation in a *"chain geometry"*. In such a geometry only one lead level directly couples to the impurity and the lead levels themselves are a series of chain elements where each lead level in the chain couples to its nearest neighbor only. One possibility to get such a chain is to start with the setup in the star geometry and to perform a *"tridiagonalization"*, mapping the star geometry onto a chain geometry by means of a unitary transformation. However, one can also directly start with a chain and adapt the hoppings and on-site energies such that they fit the desired hybridization of the continuous model. In this context, a frequently used bath representation is the so-called *"tight-binding chain"*. An iterative procedure for constructing a chain representation starting from the continuous hybridization function is defined in the *"open Wilson chain"* approach.

Tridiagonalization

The bath Hamiltonian H_{bath} and the hybridization Hamiltonian H_{hyb} consist of quadratic terms only and can therefore be represented in matrix form,

$$H = \sum_{xx'} h_{xx'} a_x^\dagger a_{x'} \,, \tag{2.16}$$

with $a_x \in \left\{ d_{(\alpha,\sigma)}, c_q \right\}$. In the star geometry the matrix $h_{xx'}$ has the characteristic form given on the left-hand side of equation (2.17). Using standard Lanczos tridiagonalization techniques, one can find a unitary transformation U which maps this star Hamiltonian onto a chain geometry with nearest-neighbor couplings only. This chain Hamiltonian is described by the characteristic tridiagonal matrix form given on the right-hand side of equation (2.17):

$$\begin{pmatrix} * & v_{\alpha 1} & v_{\alpha 2} & v_{\alpha 3} & \dots \\ v_{\alpha 1}^* & \varepsilon_{\alpha 1} & 0 & 0 & \dots \\ v_{\alpha 2}^* & 0 & \varepsilon_{\alpha 2} & 0 & \dots \\ v_{\alpha 3}^* & 0 & 0 & \varepsilon_{\alpha 3} & \dots \\ \dots & \dots & \dots & \dots & \dots \end{pmatrix} \xrightarrow{\text{unitary transformation } U} \begin{pmatrix} * & t_{\alpha 0} & 0 & 0 & \dots \\ t_{\alpha 0}^* & \chi_{\alpha 0} & t_{\alpha 1} & 0 & \dots \\ 0 & t_{\alpha 1}^* & \chi_{\alpha 1} & t_{\alpha 2} & \dots \\ 0 & 0 & t_{\alpha 2}^* & \chi_{\alpha 2} & \dots \\ \dots & \dots & \dots & \dots & \dots \end{pmatrix} . \tag{2.17}$$

The spin index has been dropped for better legibility, and the precise form of the impurity is irrelevant in this reasoning. A sketch of the two geometries is given in figure II.3. In principle, the unitary transformation U is done for different spins independently. However, as the hybridization typically does not depend on spin, the form of the transformation is the same for different spin components. Note that for the chain geometry one often starts

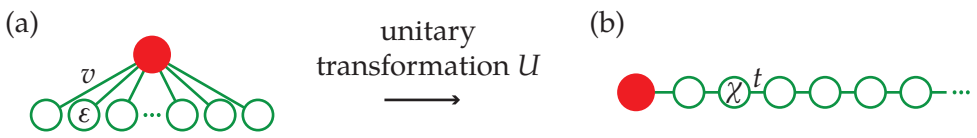

Figure II.3: Sketch of (a) the "star geometry" and (b) the "chain geometry".

the labeling of lead sites with $n = 0$, in particular in the context of NRG, see section III.3. For a particle-hole symmetric bath, the on-site energies in the chain geometry, χ_n, are zero.

Different leads α which couple to different impurity sites $d_{\alpha(\sigma)}$, as e.g. left and right leads in the IRLM (see section II.1.2), have to be tridiagonalized separately into separate chains. One often refers to these different chains as different *"channels"*. Different leads α coupling to the *same* impurity site $d_{(\sigma)}$, can be summarized into one channel. In this case, further simplifications might be possible, see the combination of left and right leads into "even" and "odd" modes in section VI.3.2.

The unitary transformation U mixes the different bath sites, but maps the impurity onto itself. In this new basis, using the new modes $f_{\alpha n(\sigma)} = \sum_k U^{(\alpha)}_{nk} c_{\alpha k(\sigma)}$, the Hamiltonian can be written as

$$H_{\text{hyb}} = \sum_{\alpha(\sigma)} t_{\alpha 0}\, d^\dagger_{(\alpha,\sigma)} f_{\alpha 0(\sigma)} + \text{h.c.}, \tag{2.18a}$$

$$H_{\text{bath}} = \sum_{\alpha(\sigma)} \sum_{n=0}^{\infty} \left(t_{\alpha,n+1} f^\dagger_{\alpha n(\sigma)} f_{\alpha,n+1,(\sigma)} + \text{h.c.} \right) + \chi_{\alpha n} f^\dagger_{\alpha n(\sigma)} f_{\alpha n(\sigma)}. \tag{2.18b}$$

Tight-binding chain

The simplest chain representation of a bath α is given by a chain with on-site energies equal to zero, $\chi_{\alpha n} = 0$, and site-independent hoppings $t_{\alpha n} = -t$ for $n \geq 1$. Only the first hopping, which defines the coupling to the impurity, differs, $t_{\alpha 0} = t'_\alpha$:

$$H_{\text{hyb}} = \sum_{\alpha(\sigma)} t'_\alpha\, d^\dagger_{(\alpha,\sigma)} f_{\alpha 0(\sigma)} + \text{h.c.}, \quad H_{\text{bath}} = -t \sum_{\alpha n(\sigma)} f^\dagger_{\alpha n(\sigma)} f_{\alpha,n+1,(\sigma)} + \text{h.c.} \tag{2.19}$$

It can be shown [17] that such a *tight-binding chain* represents a hybridization of the form

$$\Gamma_\alpha(\omega) = \Theta(2t - |\omega|) \frac{t'^2}{t} \sqrt{1 - \left(\frac{\omega}{2t}\right)^2}. \tag{2.20}$$

From this form it is immediately clear that the bandwidth of the bath is given by $4t$.

In many cases, only the low-energy part of the bath is relevant. In this case, it is irrelevant whether one uses a tight-binding chain or a structureless hybridization as defined in equation (2.6) as long as they are equal at $\omega \approx 0$. The parameter correspondences are:

$$D \leftrightarrow 2t\,, \quad \Gamma_\alpha \leftrightarrow \frac{t'^2}{t}\,. \tag{2.21}$$

Open Wilson chain construction

Another possibility to obtain a chain representation is the open Wilson chain construction [P3]. As depicted in figure II.4(a-b), the idea of this method is to replace the continuous bath with hybridization $\Delta^R(\omega)$ by a chain element coupled to a new continuous bath $\Delta^R_0(\omega)$ in such a way that the resulting hybridization does not change. This is fulfilled if the on-site energy of the new site χ_0, the coupling of the new site to the impurity t_0, and the

hybridization of the new bath $\Delta_0^R(\omega)$ are connected to $\Delta^R(\omega)$ via

$$\Delta_0^R(\omega) = \omega - \chi_0 - \frac{|t_0|^2}{\Delta^R(\omega)} \tag{2.22a}$$

$$\chi_0 = \frac{\int \mathrm{d}\omega\, \omega\Gamma(\omega)}{\int \mathrm{d}\omega\, \Gamma(\omega)} \tag{2.22b}$$

$$|t_0|^2 = \frac{1}{\pi}\int \mathrm{d}\omega\Gamma(\omega)\,, \tag{2.22c}$$

where for each bath the function $\Gamma_x(\omega) = -\mathrm{Im}\left(\Delta_x^R(\omega)\right)$ describes the imaginary part of the analytic function $\Delta_x^R(\omega)$. Note that this definition of $\Gamma(\omega)$ differs by a factor of π from the definition used in reference [P3].

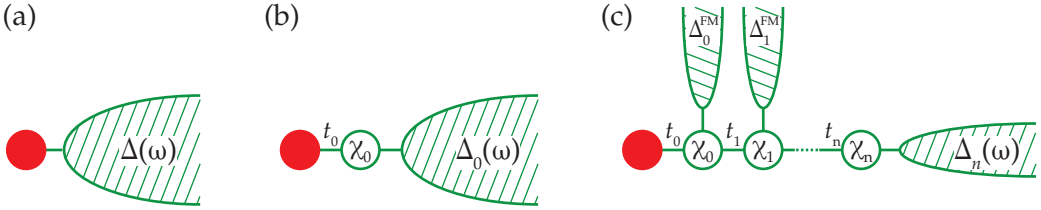

Figure II.4: Sketch of the open Wilson chain construction: (a) The continuous bath couped to the impurity is replaced by (b) an additional site which itself is coupled to a new continuous bath. (c) Each of the newly created baths is split into "fast" and "slow" modes and only the slow modes are used to continue the iteration. The iterative procedure results in a chain representation in which each chain element couples to its nearest neighbors and a fast modes bath. To obtain a finite system, these baths are neglected.

The replacement of baths can be continued iteratively. However, to obtain a suitable discretization, only in the first step the full bath is replaced by a new site. In all later iterations the bath is split into high-energy modes, called *"fast modes"*, and low-energy modes, called *"slow modes"*, $\Delta_n^R(\omega) = \Delta_n^{\mathrm{SM}}(\omega) + \Delta_n^{\mathrm{FM}}(\omega)$. Only the slow modes are replaced to continue the iterative discretization along the chain. The resulting geometry is sketched in figure II.4(c). The choice of splitting the bath $\Delta_n^R(\omega)$ into slow and fast modes, will influence the energy χ_{n+1} and the coupling t_{n+1}. This can, e.g., be used to built up a *"Wilson chain"* with exponentially decaying energy scales, as it is used in the context of NRG, compare section III.3.1. Up to this point, the procedure is still exact. To obtain a finite system the fast mode baths and the very last bath are neglected. This way of constructing the chain representation makes it possible to keep track of the neglected bath modes. This can be used, e.g., to define corrections $\delta\chi_n$ to the on-site energies χ_n resulting from the influence of the fast modes in the case of an asymmetric model. For further details the reader is referred to reference [P3].

In the sense of the above-mentioned iterative procedure, the chain representation in figure II.4(c) can be interpreted as a *continuous fraction expansion*,

$$\Delta^R(\omega) = \cfrac{|t_0|^2}{\omega - \chi_0 - \Delta_0^{\mathrm{FM}}(\omega) - \cfrac{|t_1|^2}{\omega - \chi_1 - \Delta_1^{\mathrm{FM}}(\omega) - \ldots}}\,. \tag{2.23}$$

Hybridization in the IRLM

In section II.1.2 the interacting resonant level model was introduced. Here, the details of the corresponding hybridization are discussed. Starting with a single level coupled to two structureless leads with hybridization $\Gamma_{\alpha,\mathrm{phys}}$, these leads can be represented by two independent chains. The first of these chain elements, $f_{\alpha 0} \equiv d_\alpha$, equals the linear combination of lead modes that directly couples to the impurity, $d_\alpha \propto \sum_k v_{k,\mathrm{phys}} c_q$. In a sense, it represents the lead modes "closest" to the impurity, and the Coulomb repulsion can be introduced between impurity and this first chain element. In many cases, the leads are represented as a tight-binding chain. The hopping between impurity and first chain element is included in the impurity Hamiltonian (1.4a). The hybridization Hamiltonian (1.4b) therefore only needs to represent the remaining chain with all hoppings equal to $-t$. In the sense of the correspondence in equation (2.21), this implies that the value of this "remaining" hybridization Γ_α is given by $\Gamma_\alpha = t = \frac{1}{2}D$.

II.3 Transport in Quantum Dots

A quantum dot is characterized by a strong local confinement of electrons. This results in a series of electronic energy levels which are clearly separated from each other. In a setup known as *"single-electron transistor"* the quantum dot is connected to two electrodes, the *"source"* and the *"drain"*. A finite source-drain voltage V_{SD} induces a current through the quantum dot. Furthermore, a *gate voltage* V_G can be applied, which shifts the position of the energy levels within the quantum dot.

In the following a short introduction into transport properties of such a setup is given. Section II.3.1 introduces the so-called *"Coulomb diamonds"*, which describe the general behavior of the conductance when changing source-drain voltage V_{SD} and gate voltage V_G, while section II.3.2 and II.3.3 focus on a particular parameter regime in which the *"Kondo effect"* becomes visible.

II.3.1 Coulomb Diamonds

To understand transport in a quantum dot, one has to consider the energy which is necessary for an electron to tunnel from the source into the dot and from the dot into the drain. The electrons on the dot repel each other with Coulomb repulsion U. Therefore, the energy cost of adding the nth particle onto the dot, μ_n, strongly depends on the number of electrons on the dot and increases with increasing n. Applying a gate voltage V_G decreases the value of μ_n for all n.

Figure II.5 shows a sketch of the differential transport regimes at low temperature as a function of source-drain voltage $V_{SD} = \frac{1}{\mathrm{e}}(\mu_S - \mu_D)$ and gate voltage V_G: For $V_{SD} = 0$, current can flow only if one of the chemical potentials μ_n is equal to the chemical potentials in source and drain such as, e.g., in (i), where $\mu_N = \mu_S = \mu_D$. In this case the electrons can tunnel through the dot one by one. If $\mu_n \neq \mu_S = \mu_D$ for all n, such as in (ii), where $\mu_{N+1} < \mu_S = \mu_D < \mu_{N+2}$, this tunneling is blocked and no current flows. This is referred to as the regime of *"Coulomb blockade"*. The corresponding region is indicated by the gray *"Coulomb diamonds"*. Each of the diamonds corresponds to a specific number of electrons on the dot. The Coulomb blockade can be lifted by applying a finite source-drain voltage, thereby shifting the chemical potentials of the leads until either μ_D or μ_S equals one of the chemical potentials on the dot, as depicted in (iii) for the case $\mu_D = \mu_{N+1}$. The orange

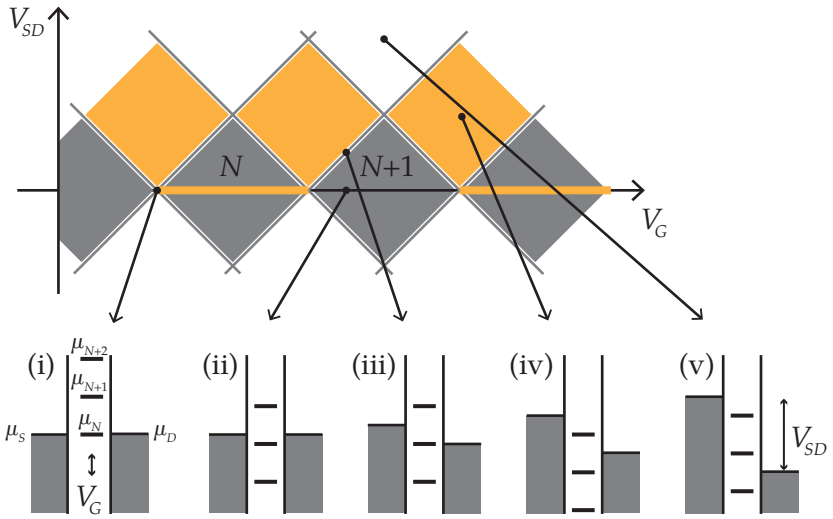

Figure II.5: (a) Sketch of the transport regimes in a quantum dot as a function of V_{SD} and V_G exhibiting the so-called *"Coulomb diamonds"*. Changing V_G the position of the local levels is changed. (i) At $V_{SD} = 0$, current flows only at the specific points where the chemical potential on the dot is equal to the chemical potential of the leads. (ii) Otherwise one is in the regime of Coulomb blockade. (iii-iv) For $V_{SD} \neq 0$, a voltage window $\mu_S - \mu_D$ opens up such that there are larger regimes in which transport can take place via one of the dots many-particle levels. (v) For larger values of V_{SD} more levels can contribute and one is not in the regime of single-particle transport any more. The finite value of the conductance in every second diamond at $V_{SD} = 0$, indicated by the orange lines, corresponds to the Kondo effect explained in the next section.

diamonds indicate this regime of single-electron transport, where one of the levels lies within the voltage window and a current can flow, see also (iv) where $\mu_S > \mu_{N+2} > \mu_D$. When further increasing the source-drain voltage, one leaves the regime of single-electron transport, and more than one level contributes to the current, as depicted in (v).

Around $V_{SD} = 0$, every second Coulomb diamond exhibits a finite current, indicated by the orange lines in figure II.5. This transport cannot be explained via these simple arguments, but it is due to the Kondo effect, which will be described in the next section.

II.3.2 Kondo Effect

From the simple arguments given in the previous section, at $V_{SD} = 0$ one expects the conductance as a function of V_G to be a series of sharp peaks, corresponding to the different many-particle levels of the quantum dot, with the regimes of Coulomb blockade in between. This is indeed what one finds, if the temperature is large enough (but still small compared to the level spacing in the dot), as depicted by the black line in figure II.6. However, at very low temperatures, every second Coulomb blockade valley vanishes and a plateau emerges.

The reason for this is the *"Kondo effect"*. The plateaus in the conductance arise, whenever the occupation of the dot is odd. In this case, there is an electronic level at energy ε_d which is filled with one electron. Adding a second electron with opposite spin results in an additional energy of $\varepsilon_d + U$, where U is the Coulomb repulsion between the two spins. If the Fermi edge lies in between the two "levels" at ε_d and $\varepsilon_d + U$, filling this level is prohibited in terms of the total energy. However, the electron can tunnel through the impurity based on virtual

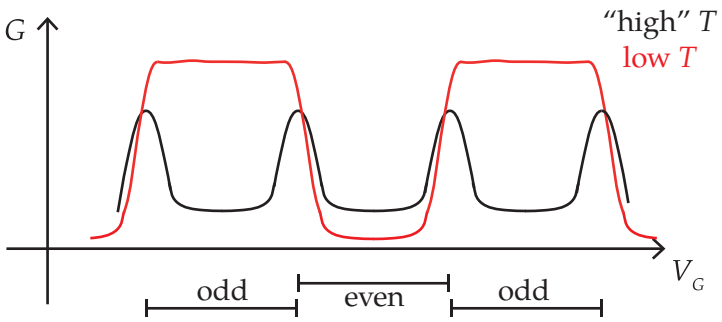

Figure II.6: The differentical conductance at $V_{SD} = 0$ as a function of V_G: For comparatively large temperatures T one finds the regime of Coulomb blockade, interrupted by the peaks in the conductance which correspond to the situations in which one of the local levels is at the Fermi edge. At very low temperature the Coulomb blockade vanishes whenever the occupation of the dot is odd. Instead one finds a Kondo plateau.

states. Two of these virtual states are depicted in figure II.7(a)(ii). As shown in the two examples, the tunneling process from (i) to (iii) can involve a spin flip on the impurity. Many of these processes add up to the Kondo resonance in the local density of states appearing at the Fermi edge as sketched in figure II.7(b). The width of this resonance is given by T_K, an energy known as the *"Kondo scale"* or *"Kondo temperature"*. From these considerations it is obvious that the Kondo effect only appears for an odd number of particles within the quantum dot, i.e., when there is a single *"local moment"* on the dot. This explains why the Kondo effect is only visible in every second Coulomb diamond, see figure II.5, and in every second Coulomb valley, see figure II.6. Due to the spin scattering processes of the Kondo effect, the local spin on the impurity is screened by the spins of the electrons in the leads.

The SIAM captures much of the physics of a quantum dot. However, it considers only a single level ε_d. The effect of further levels in the quantum dot is assumed to be negligible as they are far enough apart. For the regime of very low temperature, where the dot is occupied by a single spin, the Kondo physics can also be described by the Kondo model.

The local density of states in the SIAM can be calculated from

$$A_\sigma(\omega) = -\frac{1}{\pi}\mathrm{Im}\left(G^R_{\sigma\sigma}(\omega)\right) \tag{3.1a}$$

with the retarded Green's function

$$G^R_{\sigma\sigma}(\omega) = -\mathrm{i}\int_0^\infty \mathrm{d}t\, \mathrm{e}^{\mathrm{i}\omega t}\, \langle\{d_\sigma(t), d^\dagger_\sigma\}\rangle\ . \tag{3.1b}$$

In equilibrium such correlators can for example be calculated based on the *"full-density matrix NRG"* introduced in section III.3.4. From this local density of states the conductance at $V_{SD} = 0$ can easily be determined as [18]

$$G = -\tfrac{1}{2}\sum_\sigma \int \mathrm{d}\omega\, \Gamma(\omega) A_\sigma(\omega) \frac{\mathrm{d}f(\omega)}{\mathrm{d}\omega}\,, \tag{3.2}$$

with $f(\omega)$ being the Fermi distribution and $\Gamma(\omega)$ being the hybridization function defined in section II.2.1.

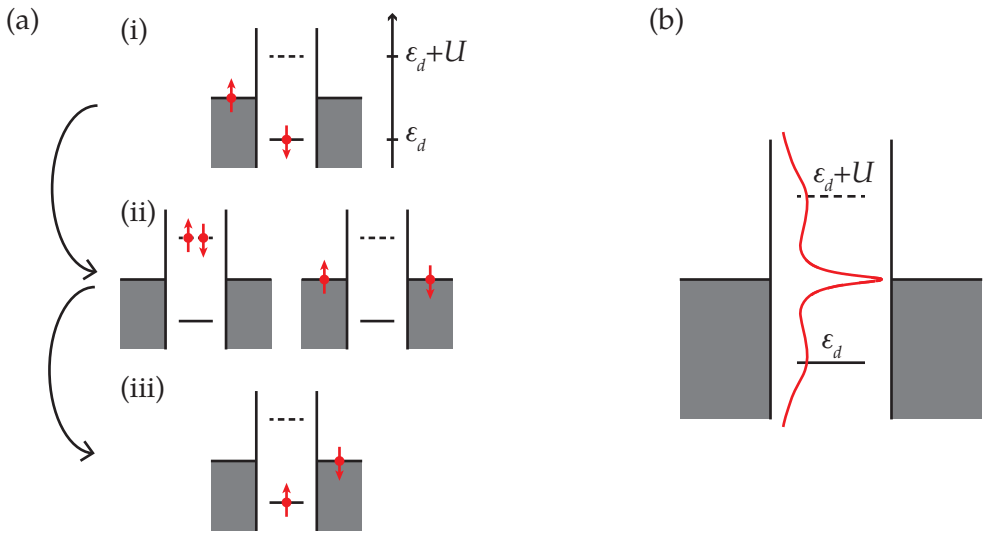

Figure II.7: Sketch of the Kondo effect in the local moment regime: (a) Based on intermediate virtual states in (ii) electrons can tunnel through the quantum dot from (i) to (iii), inducing a spin flip on the local level. (b) Due to this spin scattering states, the local density of states does not only include the two broad peaks corresponding to the two "levels" at ε_d and $\varepsilon_d + U$, but it exhibits an additional strong resonance, responsible for the charge transport and known as the *"Kondo resonance"*.

As a function of temperature, the peak height of the Kondo resonance in the local density of states decreases, see figure II.8(a). Correspondingly, the conductance decreases from its maximal value $\frac{2e^2}{h}$ to zero, see figure II.8(b). In the *"scaling limit"* of large enough U/Γ, the curve $G(T)$ is universal in the sense that for different values of U/Γ the different curves for $G(T)$ collapse to a single curve if all temperatures are given in units of T_K. When applying a finite magnetic field, the Kondo resonance also decreases and splits into two peaks, see figure II.8(c). The distance of the two peaks is approximately set by $2B$, but not exactly given by this value [19, 20] . Corresponding to the decreasing peak height, also $G(B)$ decreases for increasing B, similar to the curve $G(T)$.

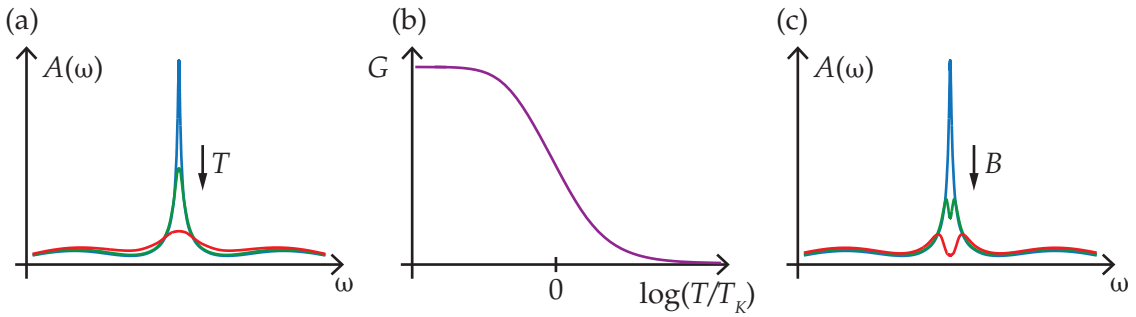

Figure II.8: (a) With increasing temperature T the Kondo resonance in the local density of states decreases. (b) The conductance G as a function of T decreases from its maximal value $2e^2/h$ to zero on a scale given by the Kondo temperature T_K. (c) With increasing magnetic field B the Kondo resonance decreases and splits into two subpeaks.

The exact value of the Kondo scale T_K can be defined in different ways. Very common is the definition via the spin susceptibility χ_S [21],

$$T_K^{(\chi)} = \frac{1}{4\chi_S} . \tag{3.3}$$

For this definition of $T_K^{(\chi)}$, analytic considerations provide the formula valid at the particle-hole symmetric point $\varepsilon_d = -\frac{U}{2}$ [22, 23],

$$T_K^{(\chi)} = \sqrt{\frac{U\Gamma}{2}}\, \mathrm{e}^{\pi\left(\frac{\Gamma}{2U}-\frac{U}{8\Gamma}\right)} . \tag{3.4}$$

Instead, T_K can also be defined via

$$G(T = T_K) = \tfrac{1}{2}G(T = 0) . \tag{3.5}$$

A study based on NRG revealed that for large enough values of U/Γ the two definitions only differ by a few percent [24].

II.3.3 Kondo Effect in Nonequilibrium

During the last twenty years many experiments contributed to a systematical study of Kondo physics [10–12, 25–28]. The most distinctive feature is the zero-bias peak in the conductance as a function of applied source-drain voltage. With increasing temperature the height of this peak decreases as sketched in figure II.9(a). With increasing magnetic field the peak height also starts to decrease, but at some point the peak splits into two peaks, the distance of which scales with the magnetic field as sketched in figure II.9(b).

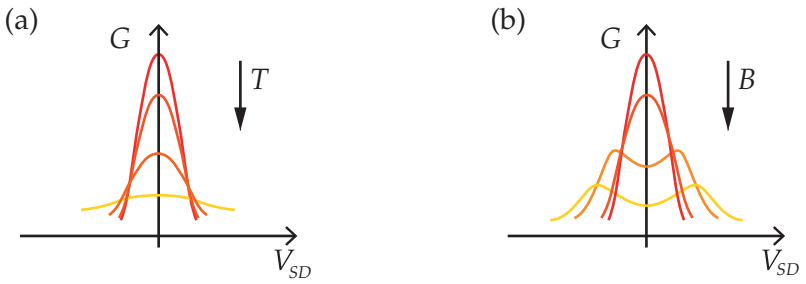

Figure II.9: Sketch of the zero-bias peak found in experiments. The conductance as a function of source-drain voltage shows a sharp peak at $V_{SD} = 0$. (a) With increasing temperature this peak gets less pronounced. (b) With increasing magnetic field the peak decreases and at some point splits into two peaks, the distance of which scales with the magnetic field.

In terms of the local density of states, the applied source-drain voltage means that there is not a single Fermi edge, at which the Kondo resonance develops, compare figure II.8 (b), but the chemical potentials of the two leads differ. Instead, the Kondo resonance splits into two peaks, the position of which is approximately given by the chemical potentials $\mu_{L/R}$ [29]. Thus, at finite magnetic field one even obtains a four-peak structure in the local density of states [P4].

While in experiment these effects have been measured many times, from a theoretical point of view it is still a difficult challenge to describe such nonequilibrium processes. Much work has been devoted to a theoretical description of nonequilibrium Kondo physics [29–40] including perturbative approaches, quantum Monte Carlo, and tensor network methods. The crucial and demanding requirements that a method has to fulfill are:

- It has to be able to capture the many-body properties of the single-impurity Anderson Model or the Kondo model.
- It has to be able to resolve exponentially small energy scales such as the Kondo scale T_K.
- It has to be able to describe steady-state nonequilibrium in the sense of long time scales or a truly open quantum system.

Chapter VI and the publication [P2] in chapter VII present a method that meets all three conditions and is able to describe the zero-bias peak within the single-impurity Anderson model, confirming the behavior found in experiments.

III Matrix Product State Methods

Matrix product state (MPS) methods are an important numerical tool in the description of strongly-correlated quantum systems. Their strength is their capability to capture the many-body physics of such systems in a nonperturbative way. Two very important many-body methods, the density-matrix renormalization group (DMRG) and the numerical renormalization group (NRG) can be phrased in the language of MPS [41–43]. The application of MPS is restricted to quantum states with "low" entanglement. Fortunately, the *"area law"* [44] guarantees that many interesting physical states can be represented in MPS form. This chapter gives a short introduction to the basic concepts of MPS (section III.1) and to two specific MPS methods, which are heavily used in this work, namely the time-dependent density matrix renormalization group (section III.2) and the numerical renormalization group (section III.3). In the end, it briefly reviews the concept of purification in the description of finite temperature states (section III.4). For a broader review on MPS, the reader is referred to reference [41].

III.1 Matrix Product States

Imagine a one-dimensional quantum system represented as a chain. Any quantum state of the system can be written as

$$|\Psi\rangle = \sum_{\sigma_1,\sigma_2,\ldots,\sigma_N} c_{\sigma_1,\sigma_2,\ldots\sigma_N} |\sigma_1\rangle \otimes |\sigma_2\rangle \otimes \cdots \otimes |\sigma_N\rangle \,, \tag{1.1}$$

where for each chain element n the sum runs over the *local state space* $\{|\sigma_n\rangle\}$, which is of dimension d_n. This state can be recast into the form

$$|\Psi\rangle = \sum_{\sigma_1,\sigma_2,\ldots,\sigma_N} \sum_{k_1,k_2,\ldots} A^{[\sigma_1]}_{k_1} A^{[\sigma_2]}_{k_1,k_2} \ldots A^{[\sigma_N]}_{k_{N-1}} |\sigma_1\rangle \otimes |\sigma_2\rangle \otimes \cdots \otimes |\sigma_N\rangle \,, \tag{1.2a}$$

or, when not writing out matrix multiplications explicitly,

$$|\Psi\rangle = \sum_{\sigma_1,\sigma_2,\ldots,\sigma_N} A^{[\sigma_1]} A^{[\sigma_2]} \ldots A^{[\sigma_N]} |\sigma_1\rangle \otimes |\sigma_2\rangle \otimes \cdots \otimes |\sigma_N\rangle \,. \tag{1.2b}$$

Here, $A^{[\sigma_n]}$ is a set of d_n matrices, also named *"A-tensors"*. Pictorial representations of equations (1.1) and (1.2) are given in figure III.1. The index k_n connecting two A-tensors is also referred to as *"bond"*. The index σ_n of the tensor $A^{[\sigma_n]}$ represents the physical state

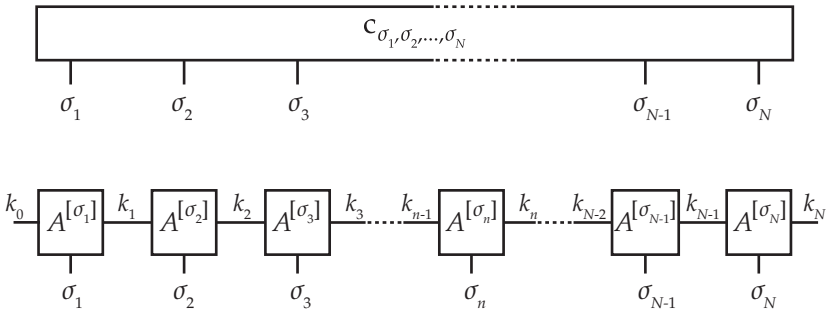

Figure III.1: Illustration of an MPS and the matrices $A^{[\sigma_n]}$: The coefficients $c_{\sigma_1,\sigma_2,\ldots,\sigma_N}$ are decomposed into A-tensors with one tensor for each site corresponding to the chain representation of the Hilbert space.

space of site n and is therefore known as *"physical"* or *"local"* index. For open boundary conditions, the matrices corresponding to the first and the last sites are vectors only. To bring them into the same form as for the other sites, they can obtain a "dummy index" running over a single value, $A^{[\sigma_1]}_{k_1} = A^{[\sigma_1]}_{k_0,k_1}$ with $k_0 \in \{1\}$, and $A^{[\sigma_N]}_{k_{N-1}} = A^{[\sigma_N]}_{k_{N-1},k_N}$ with $k_N \in \{1\}$. In the most general case the matrices corresponding to the first site, $A^{[\sigma_1]}$, are of size $1 \times d_1$, the ones corresponding to the second site, $A^{[\sigma_2]}$, of size $d_1 \times (d_1 \cdot d_2)$, the third of size $(d_1 \cdot d_2) \times (d_1 \cdot d_2 \cdot d_3)$,... In other words the bond dimension scales exponentially with system size such that the decomposition of a general state into MPS form is not possible in practice. Fortunately, for one-dimensional systems the entropy of certain states such as the ground state of a gapped Hamiltonian, fulfills an *area law* [44]: the entanglement entropy of an arbitrary subsystem with the rest of the system does not scale with the volume of this subsystem but with its boundary. For gapless systems there is a further logarithmic correction. This guarantees that for the description of many physically interesting states not the full Hilbert space needs to be taken into account, but these states can be represented in the form (1.2) with matrices of reasonable size.

The following part briefly review different MPS operations (III.1.1), canonical MPS forms (III.1.2), the use of symmetries (III.1.3), and the implementation of a correct fermionic ordering (III.1.4).

III.1.1 MPS Operations

Singular Value Decomposition and Truncation

For any matrix M of size $m \times n$ there exists a decomposition of the form

$$M = USV^\dagger, \tag{1.3}$$

with the following properties [41]:

- U is a matrix of dimension $m \times \min(m,n)$ with $U^\dagger U = \mathbb{1}$.
- $V^\dagger$ is a matrix of dimension $\min(m,n) \times n$ with $V^\dagger V = \mathbb{1}$.
- S is a diagonal matrix of size $\min(m,n) \times \min(m,n)$. Its diagonal elements $s_k = S_{kk}$ are non-negative and referred to as the *"singular values"*.

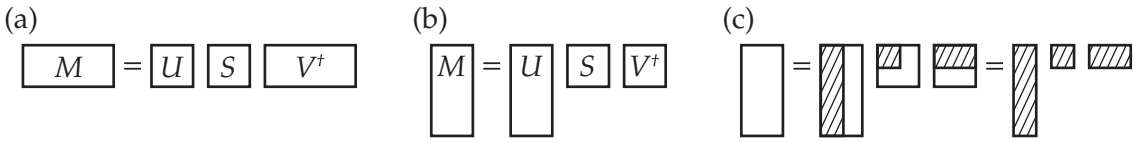

Figure III.2: Sketch of a singular value decomposition of a matrix M of size $m \times n$ (a) for $m < n$ (b) for $m > n$. (c) Truncation in the case $m > n$: keeping only the D largest singular values in the shaded area of S (and therefore keeping only the shaded ares in U and $V^\dagger$), one can compress the matrices U, S, and $V^\dagger$. Analogously the truncation can also be performed for $n \leq m$.

An illustration of the size of these matrices is given in figure III.2(a-b).

With the help of such a *"singular value decomposition"* (SVD) one can insert new bonds into tensors, as illustrated in the following example, the pictorial representation of which is given in figure III.3:

$$A_{ij}^{[\sigma_1,\sigma_2,\ldots,\sigma_N]} = M_{(i,\sigma_1,\ldots\sigma_n),(\sigma_{n+1},\ldots,\sigma_N,j)} = \sum_k \underbrace{U_{(i,\sigma_1,\ldots\sigma_n),k}}_{A_{ik}^{[(\sigma_1,\ldots\sigma_n)]}} \underbrace{S_{kk} V^\dagger_{k,(\sigma_{n+1},\ldots,\sigma_N,j)}}_{A_{kj}^{[(\sigma_{n+1},\ldots\sigma_N)]}}$$
$$= \left(A^{[(\sigma_1,\ldots,\sigma_n)]} A^{[(\sigma_{n+1},\ldots,\sigma_N)]}\right)_{ij}. \tag{1.4}$$

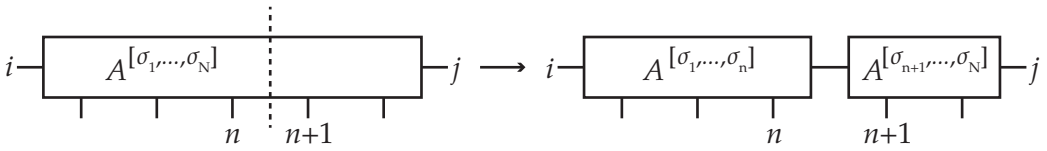

Figure III.3: Making use of an SVD decomposition one can insert additional bonds into tensors.

In particular, it is possible to formally perform the decomposition of $c_{\sigma_1,\sigma_2,\ldots,\sigma_N}$ in equation (1.1) into a tensor representation of the form (1.2) by performing a sequence of SVDs.

Within an SVD it is straightforward to *truncate* the MPS tensors. S is a diagonal matrix of size $\min(m,n)$. Its non-negative diagonal entries s_k can be ordered such that $s_1 \geq s_2 \geq \ldots \geq s_{\min(m,n)}$. Keeping only the $D < \min(m,n)$ largest of these singular values s_k one can restrict the size of the matrix S to $D \times D$, as depicted in figure III.2(c). This immediately restricts the bond connecting the two MPS tensors represented by U and SV to dimension D. In typical applications, D is either a fixed maximal bond dimension, or one keeps all singular values larger than some threshold s_{tol}, $s_D \leq s_{\text{tol}} \leq s_{D+1}$. This threshold is chosen small enough that no relevant information is lost.

Contractions

Two tensors that are connected by a bond can easily be contracted into one by simply carrying out the corresponding matrix multiplication,

$$\left(A^{[(\sigma_1,\ldots,\sigma_n)]} A^{[(\sigma_{n+1},\ldots,\sigma_N)]}\right)_{ij} = \sum_k A_{ik}^{[(\sigma_1,\ldots\sigma_n)]} A_{kj}^{[(\sigma_{n+1},\ldots\sigma_N)]} = A_{ij}^{[\sigma_1,\sigma_2,\ldots,\sigma_N]}. \tag{1.5}$$

The pictorial representation of the contraction of two neighboring sites $A^{[\sigma_n]}$ and $A^{[\sigma_{n+1}]}$ is given in figure III.4(a).

Applying Operators

Applying a local operator which acts on a single site n only, $|\tilde{\Psi}\rangle = \hat{O}^{(n)} |\Psi\rangle$, with

$$\hat{O}^{(n)} = \sum_{\sigma_n, \tilde{\sigma}_n} O^{(n)}_{\tilde{\sigma}_n, \sigma_n} |\tilde{\sigma}_n\rangle \langle \sigma_n| \tag{1.6}$$

changes the A-matrix of the corresponding site

$$\tilde{A}^{[\sigma_n]} = \sum_{\sigma'_n} O^{(n)}_{\sigma_n, \sigma'_n} A^{[\sigma'_n]}, \tag{1.7}$$

see figure III.4(b) for a pictorial representation.

To apply an operator which acts on two neighbouring sites n and $n+1$,

$$\hat{O}^{(n,n+1)} = \sum_{\sigma_n, \tilde{\sigma}_n,} O^{(n,n+1)}_{\tilde{\sigma}_n, \tilde{\sigma}_{n+1}, \sigma_n, \sigma_{n+1}} \left(|\tilde{\sigma}_n\rangle \otimes |\tilde{\sigma}_{n+1}\rangle \right) \left(\langle \sigma_n| \otimes \langle \sigma_{n+1}| \right), \tag{1.8}$$

one has to contract the two sites into one object, as depicted in figure III.4(c). In a second step, one can then redivide this new object into the matrices $\tilde{A}^{[\sigma_n]}$ and $\tilde{A}^{[\sigma_{n+1}]}$ using an SVD.

Analogously, the more sites an operator acts on, the more sites have to be contracted into one tensor. Therefore, applying such an operator becomes numerically costly, if the *non-locality* of the operator gets too strong. For very long-ranged operators it is impossible to perform the application of the operator in this form. Instead, one can decompose these operators into a matrix product operator (MPO), which is the straightforward generalization of MPS from states to operators [41].

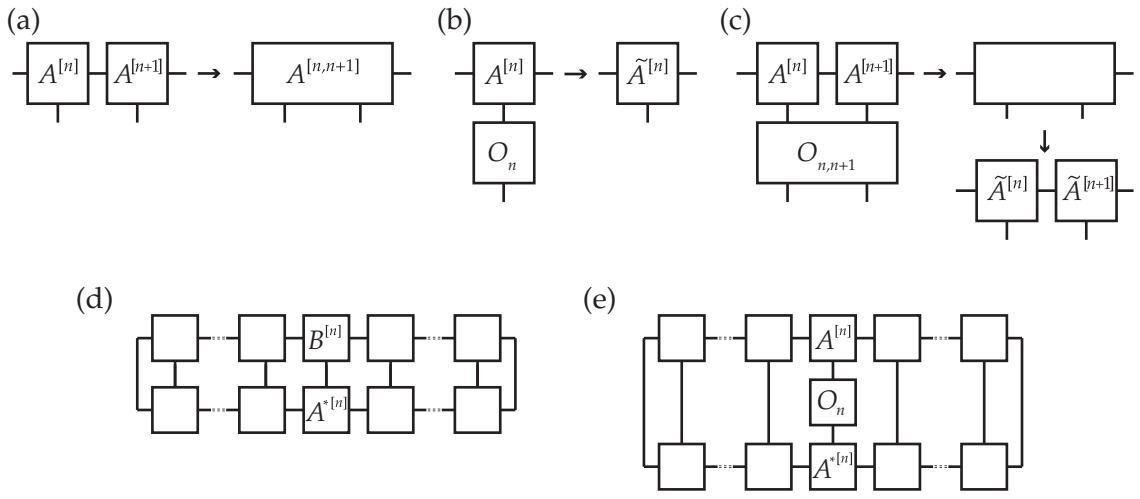

Figure III.4: Pictorial representation of the following MPS operations: (a) contracting two neighboring tensors, (b) applying a local operator, (c) applying a two-site operator, (d) calculating the overlap of two MPS, (e) calculating the expectation value of a local operator.

MPS Overlaps

From equation (1.2) it can directly be deduced that the overlap of two wave functions is given by

$$\langle \Psi_A | \Psi_B \rangle = \sum_{\sigma_1,\sigma_2,\ldots,\sigma_N} A^{*[\sigma_1]} A^{*[\sigma_2]} \ldots A^{*[\sigma_N]} B^{[\sigma_1]} B^{[\sigma_2]} \ldots B^{[\sigma_N]}, \tag{1.9}$$

with the pictorial equivalence given in figure III.4(d).

MPS Expectation Values

With the previous two paragraphs on operators and overlaps it is obvious, how expectation values of the form $\langle \Psi | \hat{O} | \Psi \rangle$ can be calculated. For completeness, the corresponding pictorial representation is given in figure III.4(e) for an operator acting on a single site n.

III.1.2 Canonical Forms

With the help of an SVD one can bring MPS into *canonical forms* [41]. Given an arbitrary MPS in the form (1.2) one can decompose the first tensor $A^{[\sigma_1]}$ into

$$A^{[\sigma_1]}_{lm} = A_{(l,\sigma_1),m} = \sum_k U_{(l,\sigma_1),k} S_{kk} V^\dagger_{k,m}, \tag{1.10}$$

and define new tensors $\tilde{A}^{[\sigma_1]}$ and $\tilde{A}^{[\sigma_2]}$,

$$\sum_m A^{[\sigma_1]}_{lm} A^{[\sigma_2]}_{mn} = \sum_k \underbrace{U_{(l,\sigma_1),k}}_{\tilde{A}^{[\sigma_1]}_{lk}} \underbrace{S_{kk} \sum_m V^\dagger_{k,m} A^{[\sigma_2]}_{mn}}_{\tilde{A}^{[\sigma_2]}_{kn}}. \tag{1.11}$$

By construction the product of $\tilde{A}^{[\sigma_1]}$ and $\tilde{A}^{[\sigma_2]}$ is equal to that of $A^{[\sigma_1]}$ and $A^{[\sigma_2]}$, such that replacing the original A-tensors by the new ones does not change the MPS. The advantage of this new representation is the property that, due to $U^\dagger U = \mathbb{1}$, $\tilde{A}^{[\sigma_1]}$ is orthonormalized in the sense that

$$\sum_{\sigma_1,l} \tilde{A}^{*[\sigma_1]}_{lk} \tilde{A}^{[\sigma_1]}_{lm} = \delta_{km}. \tag{1.12}$$

This is graphically depicted in figure III.5(a). In a next step one can analogously redefine the product $\tilde{A}^{[\sigma_2]} A^{[\sigma_3]}$ to orthonormalize the tensor $\tilde{A}^{[\sigma_2]}$. This procedure can be continued along the chain until all tensors (except for the last) are *"left-orthonormalized"*. If all tensors $\tilde{A}^{[\sigma_1]}$ to $\tilde{A}^{[\sigma_n]}$ are left-orthonormalized, the full block going from site 1 to n reduces to

$$\begin{aligned}
&\sum_k \sum_{\sigma_1,\ldots,\sigma_n} \left(\tilde{A}^{*[\sigma_1]} \tilde{A}^{*[\sigma_2]} \ldots \tilde{A}^{*[\sigma_n]}\right)_{km} \left(\tilde{A}^{[\sigma_1]} \tilde{A}^{[\sigma_2]} \ldots \tilde{A}^{[\sigma_n]}\right)_{kl} \\
&= \sum_{k'k''} \underbrace{\sum_k \sum_{\sigma_1} \tilde{A}^{*[\sigma_1]}_{kk'} \tilde{A}^{[\sigma_1]}_{kk''}}_{=\delta_{k'k''}} \sum_{\sigma_2,\ldots,\sigma_n} \left(\tilde{A}^{*[\sigma_2]} \ldots \tilde{A}^{*[\sigma_n]}\right)_{k'm} \left(\tilde{A}^{[\sigma_2]} \ldots \tilde{A}^{[\sigma_n]}\right)_{k''l} \\
&= \ldots = \sum_k \sum_{\sigma_n} \tilde{A}^{*[\sigma_n]}_{km} \tilde{A}^{[\sigma_n]}_{kl} = \delta_{ml},
\end{aligned} \tag{1.13}$$

with the graphical picture given in figure III.5(b).

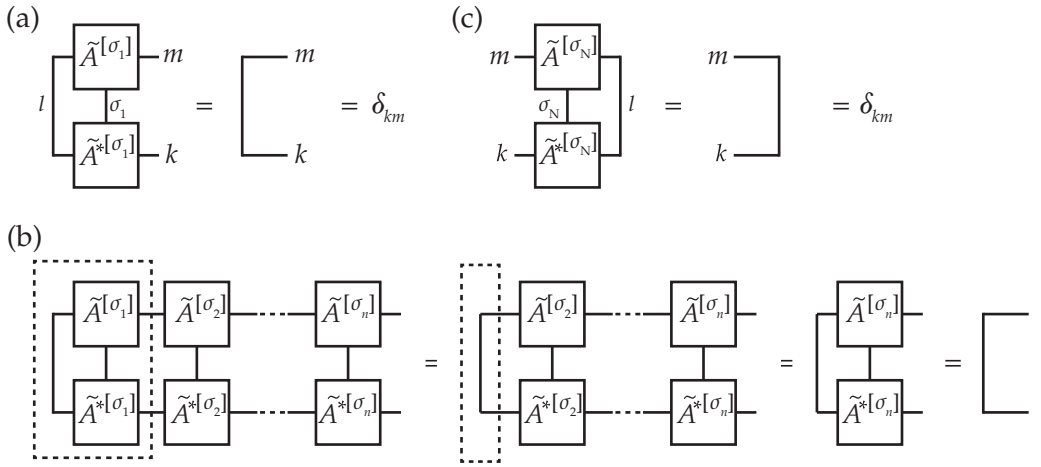

Figure III.5: Graphical representations of (a) equation (1.12), which defines a left-orthonormalized tensor $\tilde{A}^{[\sigma_1]}$, (b) equation (1.13), which illustrates the properties of a set of left-orthonormalized tensors $\tilde{A}^{[\sigma_1]} \dots \tilde{A}^{[\sigma_n]}$, and (c) equation (1.15), which defines a right-orthonormalized tensor $\tilde{A}^{[\sigma_N]}$.

Analogously, the orthonormalization can also be performed starting from the right

$$\sum_m A^{[\sigma_{N-1}]}_{lm} A^{[\sigma_N]}_{mn} = \sum_k \underbrace{\sum_m A^{[\sigma_{N-1}]}_{lm} U_{mk} S_{kk}}_{\tilde{A}^{[\sigma_{N-1}]}_{lk}} \underbrace{V^\dagger_{k,(n,\sigma_N)}}_{\tilde{A}^{[\sigma_N]}_{kn}} \tag{1.14}$$

such that, due to $V^\dagger V = \mathbb{1}$,

$$\sum_{\sigma_N, l} \tilde{A}^{*[\sigma_N]}_{kl} \tilde{A}^{[\sigma_N]}_{ml} = \delta_{km}, \tag{1.15}$$

as depicted in figure III.5(c). Again, this can be continued until all A-tensors (except for the first) are *"right-orthonormalized"*.

Besides this left-canoncial and right-canonical form there are also mixed-canonical forms, where all tensors up to site $n-1$ are left-orthonormalized and all tensors starting from $n+1$ are right-orthonormalized (for any site n).

III.1.3 Symmetries

If the physical model under consideration exhibits symmetries, these symmetries can be exploited to reduce the numerical cost of the MPS calculations. Examples for such symmetries are the conservation of particle number or the spin symmetry. For abelian symmetries the idea is simple: due to the symmetry, the matrices $A^{[\sigma]}$ or operators O can be decomposed into a block diagonal structure with all other coefficients being zero due to symmetry arguments. Any mathematical operation on these matrices can therefore be performed block by block. This strongly reduces the numerical cost. Similar arguments also hold for non-Abelian symmetries [45].

III.1.4 Fermionic Signs

When describing fermionic models one has to take care of the fermionic anticommuation relations: the MPS matrices $A^{[\sigma_n]}$ in equation (1.2) only contain the full information on the state $|\Psi\rangle$ if one restricts to a specific ordering of the fermionic sites in the tensor product, $|\sigma_N\rangle \otimes \cdots \otimes |\sigma_1\rangle$. In the following this is illustrated for an ordering which starts with the first site,

$$|\Psi\rangle = \sum_{\sigma_1,\sigma_2,\ldots,\sigma_N} A^{[\sigma_1]} A^{[\sigma_2]} \ldots A^{[\sigma_N]} |\sigma_N, \ldots, \sigma_2, \sigma_1\rangle\,, \tag{1.16}$$

such that an operator acting on site m has to be interchanged with all sites $l > m$. Creating or annihilating a particle on site m is then given by

$$f_m^{(\dagger)} |\sigma_N, \ldots, \sigma_m, \ldots, \sigma_1\rangle = \sum_{l=m+1}^{N} (-1)^{n_l} |\sigma_N, \ldots, F_m^{(\dagger)} \sigma_m, \ldots, \sigma_1\rangle\,, \tag{1.17}$$

where n_l is the number of fermions on site l. Here, the lowercase letter $f_m^{(\dagger)}$ is used for the physical operator acting on the full Hilbert space and the upper-case letter $F_m^{(\dagger)}$ for the corresponding operator acting on the local state space. Any further indices such as channel or spin labels are supressed. Defining the local operator $Z_l = (-1)^{N_l}$, with N_l the local number operator, one can therefore write the creation/annihilation operator as

$$f_m^{(\dagger)} = \mathbb{1} \otimes \cdots \otimes \mathbb{1} \otimes F_m^{(\dagger)} \otimes Z_{m+1} \otimes \cdots \otimes Z_N. \tag{1.18}$$

The pictorial representation of how to apply this operator is given in figure III.6(a).

Typically, creation and annihilation operators come in pairs. For $m < n$ one obtains

$$f_m^{(\dagger)} f_n^{(\dagger)} = \mathbb{1} \otimes \cdots \otimes \mathbb{1} \otimes F_m^{(\dagger)} \otimes Z_{m+1} \otimes \ldots Z_{n-1} \otimes Z_n F_n^{(\dagger)} \otimes \mathbb{1} \otimes \ldots \mathbb{1}, \tag{1.19}$$

where for the sites $l > n$ it was used that $Z_l^2 = \mathbb{1}$. How to apply this operation is depicted in figure III.6(b). Analogous rule can be found for $n < m$. If $n = m$, no fermionic signs have to be taken into account, because $f_n^{(\dagger)} f_n^{(\dagger)}$ commutes with any other operator.

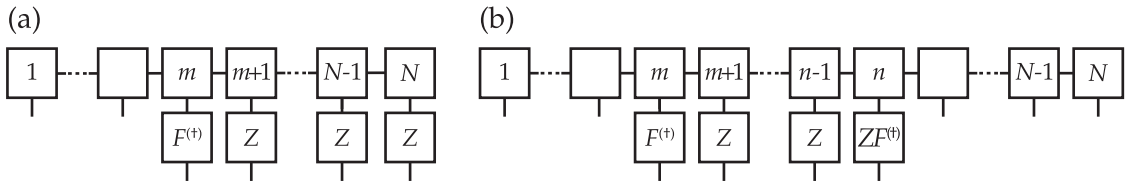

Figure III.6: Pictorial representation of (a) the application of one creator/annihilator and the resulting fermionic signs in equation (1.18) and (b) the application of two creators/annihilators and the resulting fermionic signs in equation (1.19).

If $f_m^{(\dagger)}$ carries further indices, such as channel or spin indices, one also has to ensure a correct ordering of the different operators belonging to the same site m. However, the corresponding fermionic signs can be taken into account *locally* by a proper definition of the operators $f_m^{(\dagger)}$ in the local state space of site m.

III.2 Time-Dependent Density-Matrix Renormalization Group

A frequent task in MPS descriptions of quantum systems is the time evolution of quantum states. Such a time evolution can for example be used to describe quantum quenches. In the context of an imaginary-time evolution, it can also be employed to describe finite temperature states [41]. The following gives a brief introduction to the *"time-dependent density-matrix renormalization group"* (tDMRG), pioneered by A. Daley, C. Kollath, U. Schollwöck, G. Vidal, and by A. Feiguin and S. White [41, 46–48], as one possible way to implement a time evolution within the framework of MPS. For an overview on further techniques to time evolve MPS and the subtle differences, the reader is referred to reference [41]. This section first reviews the underlying Trotter decomposition (III.2.1), before it turns to the actual implementation of the time evolution (III.2.2).

III.2.1 Trotter Decomposition

For a Hamiltonian defined on a chain with on-site and nearest-neighbor terms only, one can decompose the Hamiltonian into terms $H_{n,n+1}$ where each of these terms acts on two neighboring sites n and $n+1$:

$$H = \sum_{n=1}^{N} \varepsilon_n f_n^\dagger f_n + \sum_{n=1}^{N-1} \left(t_n f_n^\dagger f_{n+1} + \text{h.c.} \right) = \sum_{n=1}^{N-1} H_{n,n+1} \,. \tag{2.1}$$

Any further indices, such as spin or channel index, are suppressed. While any term of the form $f_n^\dagger f_{n+1}$ has to be part of the Hamiltonian $H_{n,n+1}$, the definition comes with a certain ambiguity regarding the on-site energies: except for the first and the last site, the on-site energy of site n can either be part of $H_{n-1,n}$ or $H_{n,n+1}$. A balanced variant is to divide the the energy term symmetrically into these two Hamiltonians.

Starting from equation (2.1) one can introduce an "odd" Hamiltonian H_{odd} which contains all contributions $H_{n,n+1}$ with n odd, while the "even" Hamiltonian H_{even} consists of all $H_{n,n+1}$ with n even. Dividing the time evolution operator into N_t time steps, $t = N_t\,\delta t$, one can apply a *"Trotter-Suzuki decomposition"*, also called *"Trotter decomposition"*, to each small time step [41],

$$\mathrm{e}^{-\mathrm{i}H\delta t} = \mathrm{e}^{-\mathrm{i}H_{\text{odd}}\,\delta t}\,\mathrm{e}^{-\mathrm{i}H_{\text{even}}\,\delta t} + O(\delta t^2). \tag{2.2}$$

The term $O(\delta t^2)$ stems from the fact, that $[H_{\text{odd}}, H_{\text{even}}] \sim O(\delta t^2)$. With a slight modification, the Trotter decomposition gets exact up to second order [41]:

$$\mathrm{e}^{-\mathrm{i}H\delta t} = \mathrm{e}^{-\frac{\mathrm{i}}{2}H_{\text{odd}}\,\delta t}\,\mathrm{e}^{-\mathrm{i}H_{\text{even}}\,\delta t}\,\mathrm{e}^{-\frac{\mathrm{i}}{2}H_{\text{odd}}\,\delta t} + O(\delta t^3). \tag{2.3}$$

For the full time evolution operator one obtains

$$\mathrm{e}^{-\mathrm{i}Ht} = \mathrm{e}^{-\mathrm{i}HN_t\delta t} = \mathrm{e}^{-\frac{\mathrm{i}}{2}H_{\text{odd}}\,\delta t}\left(\mathrm{e}^{-\mathrm{i}H_{\text{even}}\,\delta t}\,\mathrm{e}^{-\mathrm{i}H_{\text{odd}}\,\delta t}\right)^{N_t-1}\mathrm{e}^{-\mathrm{i}H_{\text{even}}\,\delta t}\,\mathrm{e}^{-\frac{\mathrm{i}}{2}H_{\text{odd}}\,\delta t} + O(\delta t^3). \tag{2.4}$$

Compared to the decomposition in equation (2.2), the only extra cost for a second-order decomposition is that one of the N_t time steps δt has to be divided into two separate time steps $\delta t/2$ for either the "odd" or the "even" bonds. The different bonds in H_{odd} commute,

so

$$\mathrm{e}^{-\mathrm{i}H_{\mathrm{odd}}\,\delta t} = \exp\left(-\mathrm{i}\sum_{n\ \mathrm{odd}} H_{n,n+1}\,\delta t\right) = \prod_{n\ \mathrm{odd}} \mathrm{e}^{-\mathrm{i}H_{n,n+1}\,\delta t}, \tag{2.5}$$

and analogously for H_{even}. Because all summands in H_{odd} (H_{even}) commute, the order of the different terms $\mathrm{e}^{-\mathrm{i}H_{n,n+1}\,\delta t}$ within the product on the right-hand side of equation (2.5) is irrelevant.

The decomposition in equation (2.3) is not the only possibility to divide the time-evolution operator. A further possibility, which is frequently used and does not rely on the notion of "even" and "odd" is given by

$$\begin{aligned}\mathrm{e}^{-\mathrm{i}H\delta t} = &\left(\mathrm{e}^{-\frac{\mathrm{i}}{2}H_{1,2}\delta t}\,\mathrm{e}^{-\frac{\mathrm{i}}{2}H_{2,3}\delta t}\ldots\mathrm{e}^{-\frac{\mathrm{i}}{2}H_{N-2,N-1}\delta t}\right)\mathrm{e}^{-\mathrm{i}H_{N-1,N}\delta t}\\ &\left(\mathrm{e}^{-\frac{\mathrm{i}}{2}H_{N-2,N-1}\delta t}\ldots\mathrm{e}^{-\frac{\mathrm{i}}{2}H_{2,3}\delta t}\,\mathrm{e}^{-\frac{\mathrm{i}}{2}H_{1,2}\delta t}\right) + O(\delta t^3)\,.\end{aligned} \tag{2.6}$$

III.2.2 Time Evolution

The time evolution in tDMRG relies on the Trotter decomposition in equation (2.4). The operators $\mathrm{e}^{-\mathrm{i}H_{\mathrm{odd}}\,\delta t}$ ($\mathrm{e}^{-\mathrm{i}H_{\mathrm{even}}\,\delta t}$) split into two-site Trotter gates $\mathrm{e}^{-\mathrm{i}H_{n,n+1}\,\delta t}$ with n being odd (even), see equations (2.4)-(2.5). The full time evolution operator $\mathrm{e}^{-\mathrm{i}Ht}$ can therefore be represented in a series of layers consisting of two-site gates as depicted in figure III.7(a).

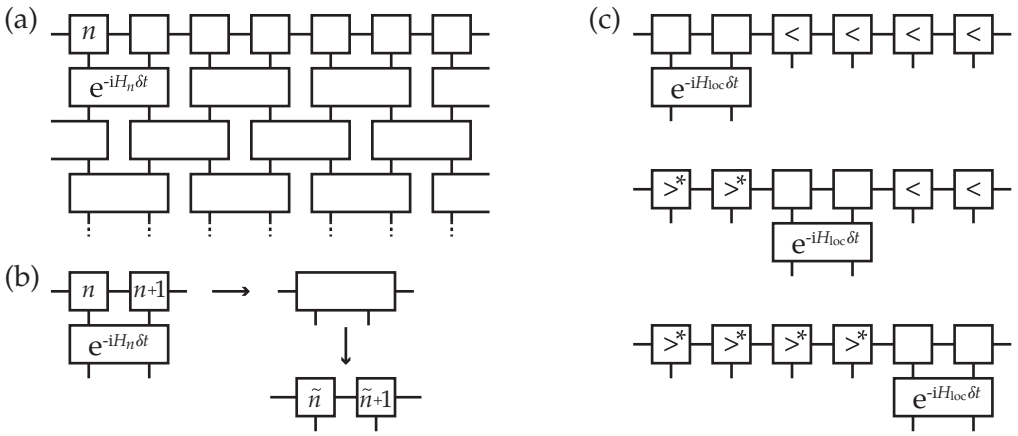

Figure III.7: (a) Due to the Trotter decomposition the time evolution decays into different layers representing $\mathrm{e}^{-\mathrm{i}H_{\mathrm{odd}}\,\delta t}$ and $\mathrm{e}^{-\mathrm{i}H_{\mathrm{even}}\,\delta t}$. (b) Applying a two-site Trotter gate, the two sites are merged and afterwards redivided using an SVD. (c) To ensure a correct orthonormalization for the SVD for each layer one starts e.g. with all tensors right-orthonormalized. Applying the Trotter gates along the chain starting from the left one then ensures a left-orthonormalization of the changed tensors. This implies that also the bonds which are not changed by the time evolution have to be orthonormalized. For the next layer one can start with the left-orthonormalized state applying the Trotter gates starting from the right.

Each of these gates corresponds to a two-site operator of the form (1.8). When applying one of these gates at sites n and $n+1$, the two sites have to be merged and afterwards

redivided using an SVD as depicted in figure III.7(b). Within this SVD one truncates the bonds by keeping only the largest singular values as described in section III.1.1. Besides the Trotter-Suzuki decomposition this is the second approximation that enters the tDMRG time evolution. The truncation of singular values can be biased if the tensors to the left (right) of the decomposed tensor are not left-orthonormalized (right-othonormalized), simply because the weight of the singular values can be shifted to other bonds. To avoid this, one can start the time evolution with a right-orthonormalized state and apply the Trotter gates starting from the left. When performing the SVD one can determine left-orthonormalized tensors, as depicted in figure III.7(c). Additionally, when applying the layer of Trotter gates for the odd (even) bonds, it is necessary to also orthonormalize the intermediate even (odd) bonds. After one sweep along the chain the state is left-orthonormalized. The next sweep can then be performed starting from the right.

Due to a *growth in entanglement* one needs larger and lager bond dimensions with increasing time to guarantee the same accuracy in the SVDs. Therefore, such tDMRG calculations are typically restricted to a finite time window even if the Trotter and the truncation error are tolerable.

Instead of truncating each bond after the application of one Trotter gate, one can also compress states of the form $|\Psi'\rangle = e^{-\mathrm{i}H\delta t}|\Psi\rangle$ using a variational principle [41]. In many cases, this will be more accurate, but also numerically more expensive.

An alternative to the layers of Trotter gates on "odd" and "even" bonds are sweeps back and forth with Trotter gates on each bond based on the Trotter decomposition in equation (2.6).

III.3 The Numerical Renormalization Group

The *"numerical renormalization group"* (NRG) was invented in 1975 by Kenneth G. Wilson to solve the Kondo model [8, 9]. "For his theory for critical phenomena in connection with phase transitions" [49] Wilson was awarded the Nobel Prize in Physics in 1982. Compared to Wilson's original work, further progress has been made in various directions and thereby the range of applicabilty of NRG has widely been extended. This made it possible that during the last decades NRG was used to describe the properties of various impurity models [21]. This brief introduction to the numerical renormalization group explains the basic concepts and the tools used in the present work. For a broader overview and further techniques, see reference [21]. This section first reviews the concept of a Wilson chain (III.3.1), before it describes the iterative diagonalization of the Hamiltonian (III.3.2). A short comment highlights the connection to MPS (III.3.3). Finally, the full-density matrix NRG is introduced as a valuable tool to calculate spectral functions (III.3.4).

III.3.1 Wilson Chain

Starting point for NRG is an impurity model with a Hamiltonian of the form

$$H = H_{\mathrm{imp}} + H_{\mathrm{hyb}} + H_{\mathrm{bath}}. \tag{3.1}$$

The impurity Hamiltonian H_{imp} describes an arbitrary impurity, the bath Hamiltonian H_{bath} a noninteracting fermionic bath, and H_{hyb} a linear hybridization between impurity and bath,

$$H_{\text{hyb}} = \sum_q v_q d^\dagger_{(\alpha,\sigma)} c_q + \text{h.c.}, \quad H_{\text{bath}} = \sum_q \varepsilon_q c^\dagger_q c_q. \tag{3.2}$$

with $q = \{\alpha, k, (\sigma)\}$ labeling the channel α, the different energy levels k and the bath spin if applicable, see section II and, in particular, equations (II.1.2) and (II.2.1). Each value of k represents an energy interval $I_k = [E_k, E_{k+1}]$. The crucial point in NRG is the fact that the discretization of the band is chosen to be *logarithmic*,

$$E_{\pm 1} = \pm D, \quad E_{\pm k} = \pm D\Lambda^{2-k-z}, \quad \text{for } k = 2, 3, \ldots. \tag{3.3}$$

$\Lambda \gtrsim 1$ is the parameter that characterizes the logarithmic discretization, $\Lambda \to 1$ corresponds to the continuum limit. The *z-shift* $z \in [0, 1[$ can be exploited to sample different discretizations systematically in order to reduce discretization artifacts [50–52]. For each of the given energy intervals I_k the corresponding energy ε_q representing the full interval lies within I_k, $E_k < \varepsilon_k < E_{k+1}$. However, the details on how to actually choose these energies to get the best representation of the bath are highly non-trivial [15, 53], see equation (II.2.8) for one common choice.

Figure III.8: Sketch of the logarithmic discretization. The full band $[-D, D]$ is devided into energy intervals, the size of which scales with Λ^{-n}.

This bath representation is mapped onto a chain using the tridiagonalization described in section II.2.3, and the Hamiltonian is expressed in the form

$$H_{\text{hyb}} = \sum_{\alpha(\sigma)} t_{\alpha 0}\, d^\dagger_{(\alpha,\sigma)} f_{\alpha 0(\sigma)} + \text{h.c.}, \tag{3.4a}$$

$$H_{\text{bath}} = \sum_\alpha \sum_{n=0}^{\infty} \left(t_{\alpha,n+1,(\sigma)} f^\dagger_{\alpha n(\sigma)} f_{\alpha,n+1,(\sigma)} + \text{h.c.} \right) + \chi_{\alpha n} f^\dagger_{\alpha n(\sigma)} f_{\alpha n(\sigma)}. \tag{3.4b}$$

Due to the logarithmic discretization in the star geometry the hoppings $t_{\alpha n}$ and the on-site energies $\chi_{\alpha n}$ in the chain geometry will fall off exponentially. For a fermionic model, one obtains

$$t_n, \chi_n \sim \Lambda^{-\frac{n}{2}}. \tag{3.5}$$

Therefore, the beginning of the chain represents the high energy scales. Going further along the chain, one accesses continually smaller energy scales. This is referred to as *"energy scale separation"* and is the key towards an *iterative diagonalization* of the full Hamiltonian. In principle, the value of k can run up to infinity in equation (3.3). In this case also the chain is of infinite length. In practice, one will cut the chain at the smallest energy scale one is interested in. Such a chain representation of the bath with energy scale separation due to the underlying logarithmic discretization is commonly referred to as *"Wilson chain"*.

Instead of constructing the Wilson chain starting from a logarithmic discretization in the star geometry, there are also other possibilities to obtain a chain representation with energy scale separation, e.g., one can use the open Wilson chain construction [P3], see section II.2.3.

III.3.2 Iterative Diagonalization

The idea of NRG is to proceed iteratively on the different energy scales. One starts with the Hamiltonian

$$H_0 = H_{\text{imp}} + H_{\text{hyb}} + \sum_{\alpha(\sigma)} \chi_{\alpha 0} f^\dagger_{\alpha 0(\sigma)} f_{\alpha 0(\sigma)}, \tag{3.6}$$

which can be diagonalized exactly. This Hamiltonian can be seen as the starting point of a series of Hamiltonians defined as

$$H_n = H_{n-1} + \sum_{\alpha(\sigma)} \chi_{\alpha n(\sigma)} f^\dagger_{\alpha n(\sigma)} f_{\alpha n(\sigma)} + \left(t_{\alpha n(\sigma)} f^\dagger_{\alpha,n-1,(\sigma)} f_{\alpha n(\sigma)} + \text{h.c.} \right). \tag{3.7}$$

If one knows the eigenbasis $|h\rangle_n$ for Hamiltonian H_n,

$$H_n |h\rangle_n = E_n(h) |h\rangle_n , \quad h = 1, 2, \dots , \tag{3.8}$$

one can construct a many-body basis

$$\left\{ |s\rangle_{n+1} \right\} = \left\{ |h\rangle_n \right\} \otimes \left\{ |\sigma\rangle_{n+1} \right\} \tag{3.9}$$

with $\left\{ |\sigma\rangle_{n+1} \right\}$ being the local state space of chain site $n+1$. The Hamiltonian H_{n+1} can be expressed and diagonalized in this basis, yielding the eigenbasis $\left\{ |h\rangle_{n+1} \right\}$ and the eigenenergies $E_{n+1}(h)$.

Truncation

Adding an additional site in equation (3.9) increases the size of the current basis by a factor of d, where d is the *"local dimension"* of the added chain element. Going along the chain, the dimension of the many-body basis therefore increases exponentially. To keep the numerics feasible, the state space has to be truncated. To this end, the energy eigenstates $|h\rangle_n$ are ordered such that $E_n(h) \leq E_n(h+1)$. Only the ones with the lowest energies are kept when going to the next iteration,

$$|h\rangle^{\text{K}}_n = |h\rangle_n \text{ with } E^{\text{K}}_n(h) = E_n(h), \quad h = 1, 2, \dots N_{\text{keep}}. \tag{3.10}$$

Analogously, one can define the discarded states

$$|h\rangle^{\text{D}}_n = |h\rangle_n \text{ with } E^{\text{D}}_n(h) = E_n(h), \quad h = N_{\text{keep}} + 1, \dots \tag{3.11}$$

With this truncation one restricts the number of states $|h\rangle_n$ to N_{keep} in equation (3.9),

$$\left\{ |s\rangle^{\text{K}}_{n+1} \right\} = \left\{ |h\rangle^{\text{K}}_n \right\} \otimes \left\{ |\sigma\rangle_{n+1} \right\} \tag{3.12}$$

such that the number of states $|s\rangle^{\text{K}}_{n+1}$ is given by $N_{\text{keep}} \cdot d$, a number that stays constant when continuing the iteration process. This truncation of the highest energy states at iteration n

has a negligible effect on the spectrum of the next iterations. The reason for this is the energy scale separation: the inclusion of a further site corresponds to a perturbation of relative strength $\sqrt{\Lambda}$ [21]. Consequently, The number of kept states per iteration, N_{keep}, has to be chosen larger the smaller the value of Λ.

Scaling

Due to the logarithmic discretization, the hoppings and on-site energies of the chain will decay exponentially as given in equation (3.5). This decrease can be accounted for by scaling the Hamiltonian of iteration $n+1$ by a factor of $\sqrt{\Lambda}$ compared to the previous one,

$$\tilde{H}_n = \Lambda^{\frac{n-1}{2}} H_n, \quad \tilde{E}_n^{(\mathrm{K})}(h) = \Lambda^{\frac{n-1}{2}} E_n^{(\mathrm{K})}(h). \tag{3.13}$$

Furthermore, it is common practice to adjust the reference point of the energy scale after each diagonalization such that the ground state of the current Hamiltonian H_n is given by $E_n^0 = \min(E_n(h)) = 0$.

This scaling procedure at the one hand guarantees the stability of the numerical calculation. On the other hand, it allows an interpretation of the procedure in terms of a renormalization group flow,

$$\tilde{H}_{n+1} = R\left(\tilde{H}_n\right), \tag{3.14}$$

with much physical insight in the evaluation of the corresponding fix points and their crossovers [21].

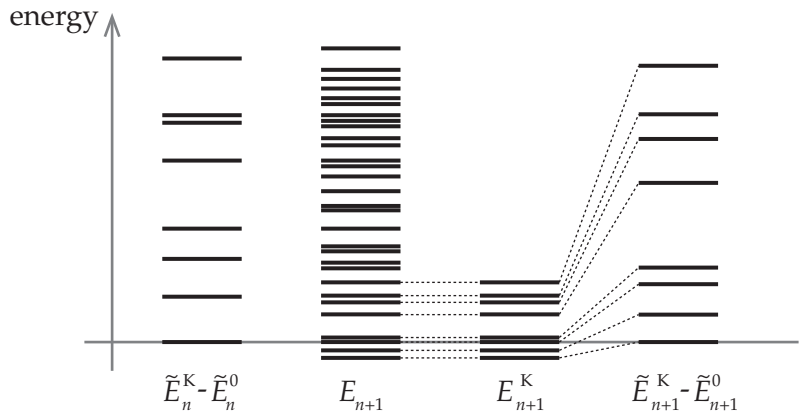

Figure III.9: Sketch of the energy spectra in an NRG iteration step: Starting from $\tilde{E}_n^K$ and the corresponding eigenstates, one can construct the set of states given in equation (3.12) and use it to diagonalize H_{n+1}, yielding the eigenenergies E_{n+1}. The lowest N_{keep} of these eigenenergies are kept in E_{n+1}^{K}. Rescaled and shifted by the lowest energy $\tilde{E}_{n+1}^0$ one ends up with a spectrum comparable to the previous iteration.

Channels

Different *"channels"*, e.g. different physical leads α, are included in a correspondingly larger local state space $|\sigma\rangle$. In this sense, NRG can treat multi-channel models. However, if the

state space $|\sigma\rangle$ is large, a larger number of kept states is required such that, in practice, one is limited to a small number of channels.

III.3.3 MPS Representation

A convenient way to implement the numerical renormalization group is based on its connection to MPS [42, 43]. The eigenstates $|h\rangle_n$ are connected to $|s\rangle_n^K$ via a unitary transformation such that the relation between the states $|h\rangle_n$ and $|h'\rangle_{n-1}^K$ can be written in the form

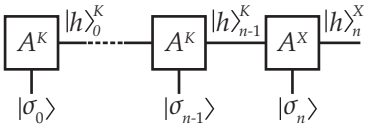

Figure III.10: MPS representation of NRG eigenstates.

$$|h\rangle_n = \sum_s A_{sh}\,|s\rangle_n = \sum_{h',\sigma_n} A_{h'h}^{[\sigma_n]}\,|h'\rangle_{n-1}^{\mathrm{K}} \otimes |\sigma\rangle_n\,. \tag{3.15}$$

The division of $|h\rangle_n$ into kept and discarded states will split the matrix $A_{h'h}^{[\sigma_n]}$ into two parts $A_{h'h}^{K[\sigma_n]}$ and $A_{h'h}^{D[\sigma_n]}$. Starting with $|h\rangle_0 = A_h^{[\sigma_0]}\,|\sigma\rangle_0$ the NRG iterations creates eigenstates of MPS form, as depicted in figure III.10:

$$|h\rangle_n^X = \sum_{\sigma_0,\sigma_1,\ldots,\sigma_n} \left(A^{K[\sigma_0]}A^{K[\sigma_1]}\ldots A^{K[\sigma_{n-1}]}A^{X[\sigma_n]}\right)_h |\sigma_0\rangle \otimes |\sigma_1\rangle \otimes \cdots \otimes |\sigma_n\rangle \tag{3.16}$$

with $X \in \{K, D\}$.

III.3.4 Full-Density-Matrix NRG

For the calculation of correlators, as needed, e.g., for the determination of the impurity's local density of states, it is possible to build up a *full density matrix* (FDM) [54, 55] based on the construction of a *complete basis set* [56].

Complete Basis

F. Anders and A. Schiller have argued [56] that it is possible to construct a basis of approximate eigenstates of the Hamiltonian by considering the discarded NRG states: for each iteration step n all discarded states $|h\rangle_n^D$ are continued to the Hilbert space of the full Hamitonian $H = H_N$ by appending an environment $|e\rangle_n$ that consists of all the degrees of freedom for iterations $n+1$ to N,

$$|he\rangle_n^D = |h\rangle_n^D \otimes |e\rangle_n\,, \tag{3.17}$$

as depicted in figure III.11. These states can be interpreted as approximate eigenstates of the Hamiltonian,

$$H\,|he\rangle_n^D \approx E_n(h)\,|he\rangle_n^D\,. \tag{3.18}$$

Summarizing the states over all iterations n provides a basis of the full Hilbert space,

$$\mathbb{1} = \sum_{nhe} |he\rangle_n^D\ {}_n^D\langle he|\,. \tag{3.19}$$

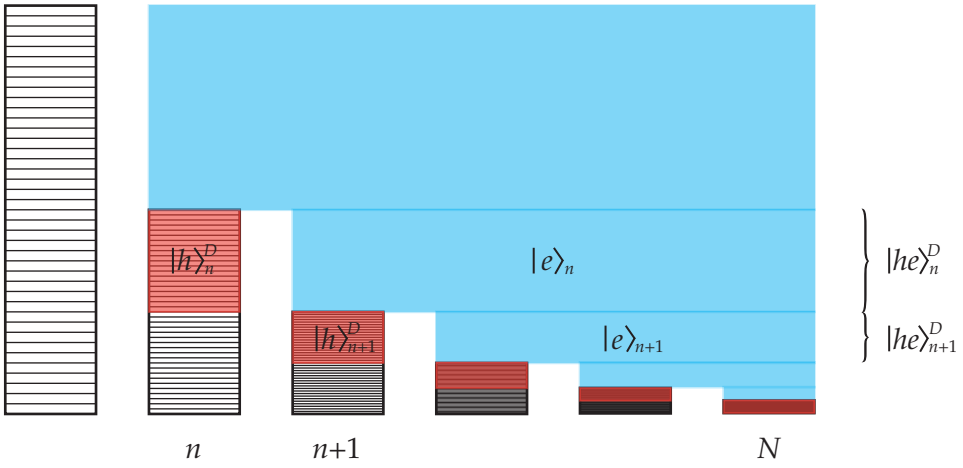

Figure III.11: Sketch of the complete basis of approximate energy eigenstates in the NRG: the discarded states of iteration n are continued to the last iteration N by appending an environment $|e\rangle_n$ representing the Hilbert space of the iterations $n+1$ to N. The set of all these continued states, $|he\rangle_n^D$, represents a basis of the Hamiltonian consisting of approximate energy eigenstates.

For this procedure, the eigenstates of the last iteration N all count as discarded, $|h\rangle_N = |h\rangle_N^D$ for all h. For these states there is no environment $|e\rangle$ that needs to be added, $|he\rangle_N^D = |h\rangle_N^D$.

Full Density Matrix

Within the basis $\left\{|he\rangle_n^D\right\}$ the density matrix takes the simple form [54]

$$\rho = \sum_{ne,h\in D} \frac{1}{Z} \mathrm{e}^{-\beta E_n(h)} \, |he\rangle_n^D \, {}_n^D\langle he| \,, \quad \text{with } Z = \sum_{ne,h\in D} e^{-\beta E_n(h)}. \tag{3.20}$$

For the calculation of correlators in the next paragraph the matrix elements of this density matrix with respect to the discarded and kept states within one Wilson shell n are needed with the environment traced out,

$$\left(M^{(n)}\right)_{hh'}^{XX'} = \sum_e {}_n^X\langle he|\rho|h'e\rangle_n^{X'} \,, \quad X \text{ and } X' \in \{K, D\} \,. \tag{3.21}$$

As a first step towards these elements it is important to clarify the connection between different states $|he\rangle_n^X$:

$${}_n^D\langle he|h'e'\rangle_{n'}^D = \delta_{hh'}\delta_{ee'}\delta_{nn'} \tag{3.22}$$

and

$${}_n^K\langle he|h'e'\rangle_{n'}^D = \begin{cases} \delta_{e(n'),e'} \left(\underbrace{A^{[e_n]}A^{[e_{n+1}]} \ldots A^{[e_{n'-1}]}A^{[e_{n'}]}}_{\left(A^{[e_n \to e_{n'}]}\right)} \right)_{hh'} & \text{if } n' > n \\ 0 \quad \text{else,} \end{cases} \tag{3.23}$$

where $e(n')$ is the part of e that represents the local space of iteration $n'+1 \to N$. The matrices $A^{[\sigma_n]}$ represent the eigenstates of the Hamiltonians H_n as defined in equation (3.15).

From these relations and the form of equation (3.20) it is evident that the matrix elements $\left(M^{(n)}\right)^{XX'}_{hh'}$ are diagonal in X and X',

$$\left(M^{(n)}\right)^{XX'}_{hh'} = \left(R^{(n)}\right)^{X}_{hh'} \delta_{XX'}. \tag{3.24}$$

Moreover, it is obvious that they are diagonal in the DD-sector,

$$\left(R^{(n)}\right)^{D}_{hh'} = \sum_e {}^{D}_{n}\langle he|\rho|h'e\rangle^{D}_{n} = \frac{1}{Z}\,\mathrm{e}^{-\beta E_n(h)}\,\delta_{hh'}\,d^{N-n} = \delta_{hh'}\,\underbrace{d^{N-n}\frac{Z_n}{Z}}_{w_n}\left(\rho^{(nn)}\right)^{DD}_{hh}. \tag{3.25}$$

with $Z_n = \sum_{h\in D} \mathrm{e}^{-\beta E_n(h)}$ and

$$\left(\rho^{(nn)}\right)^{DD}_{hh} = \frac{1}{Z_n}\,\mathrm{e}^{-\beta E_n(h)}. \tag{3.26}$$

The factor $\sum_e {}_n\langle e|e\rangle_n = d^{N-n}$ reflects the degeneracy of the energy $E_n(h)$ in the complete basis set due to the environment $|e\rangle_n$. The KK-sector is much less trivial as it connects different Wilson shells:

$$\begin{aligned}
\left(R^{(n)}\right)^{K}_{hh'} &= \sum_e {}^{K}_{n}\langle he|\rho|h'e\rangle^{K}_{n} = \frac{1}{Z}\sum_e \sum_{\tilde{n}\tilde{e},\tilde{h}\in D} \mathrm{e}^{-\beta E_{\tilde{n}}(\tilde{h})}\ {}^{K}_{n}\langle he|\tilde{h}\tilde{e}\rangle^{D}_{\tilde{n}}\ {}^{D}_{\tilde{n}}\langle\tilde{h}\tilde{e}|h'e\rangle^{K}_{n} \\
&= \frac{1}{Z}\sum_e \sum_{\tilde{n}>n}\sum_{\tilde{e},\tilde{h}\in D} \mathrm{e}^{-\beta E_{\tilde{n}}(\tilde{h})}\,\delta_{e(\tilde{n}),\tilde{e}}\left(A^{[e_n\to e_{\tilde{n}}]}\right)_{h\tilde{h}}\left(A^{*[e_n\to e_{\tilde{n}}]}\right)_{h'\tilde{h}} \\
&= \sum_{\tilde{n}>n,\tilde{h}\in D} \underbrace{d^{N-\tilde{n}}\frac{Z_{\tilde{n}}}{Z}}_{w_{\tilde{n}}} \sum_{\{e_n,e_{n+1},\dots e_{\tilde{n}}\}} \left(A^{[e_n\to e_{\tilde{n}}]}\right)_{h\tilde{h}}\left(\rho^{\tilde{n}\tilde{n}}\right)^{DD}_{\tilde{h}\tilde{h}}\left(A^{*[e_n\to e_{\tilde{n}}]}\right)_{h'\tilde{h}} \\
&= \sum_{\tilde{n}n} w_{\tilde{n}}\left(\rho^{(n\tilde{n})}\right)^{KK}_{hh'}
\end{aligned} \tag{3.27}$$

Correlators

With the full density matrix one can calculate two-point correlators of the form

$$G_{BC}(t) = \langle B(t)C^\dagger\rangle = -\mathrm{i}\Theta(t)\,\mathrm{Tr}\left(e^{\mathrm{i}Ht}Be^{-\mathrm{i}Ht}C^\dagger\rho\right), \tag{3.28a}$$

$$G_{BC}(\omega) = \int_{-\infty}^{\infty} \mathrm{e}^{\mathrm{i}\omega t}\,G_{BC}(t), \tag{3.28b}$$

with operators B and C acting on the impurity. If the eigenstates of the Hamiltonian H are known, $H|n\rangle = E_n|n\rangle$, the correlator can be rewritten as

$$G_{BC}(t) = \sum_{nm} \underbrace{\langle n|B|m\rangle}_{B_{nm}}\,\mathrm{e}^{-\mathrm{i}(E_m-E_n)t}\,\underbrace{\langle m|C^\dagger\rho|n\rangle}_{\left(C^\dagger\right)_{mn}\rho_n}, \tag{3.29a}$$

$$G_{BC}(\omega) = 2\pi\sum_{mn}\frac{1}{Z}e^{-\beta E_n}\delta(\omega-(E_m-E_n))B_{nm}\left(C^\dagger\right)_{mn}, \tag{3.29b}$$

where it was used that the density matrix is diagonal in the energy eigenstates, $\rho_n = \frac{1}{Z}e^{-\beta E_n}$. The form (3.29) is also referred to as *"Lehmann representation"*.

In terms of the complete NRG basis set, one finds

$$G_{BC}(\omega) = 2\pi \sum_{n_i,h_i,e_i} \delta\left(\omega - \Delta E^{h_2,h_1}_{n_2,n_1}\right) {}^{D}_{n_1}\langle h_1 e_1|B|h_2 e_2\rangle^{D}_{n_2}\, {}^{D}_{n_2}\langle h_2 e_2|C^\dagger|h_3 e_3\rangle^{D}_{n_3}\, {}^{D}_{n_3}\langle h_3 e_3|\rho|h_1 e_1\rangle^{D}_{n_1}\,, \tag{3.30}$$

with $\Delta E^{h_2,h_1}_{n_2,n_1} = E_{n_2}(h_2) - E_{n_1}(h_1)$. The sum runs over the discarded states of three different Wilson shells $\{n_1, n_2, n_3\}$. However, it can be reduced to a sum over a *single* Wilson shell,

$$G_{BC}(\omega) = 2\pi \sum_{\substack{n,h_i,e_i \\ \{X_1,X_2,X_3\} \\ \neq\{KKK\}}} \delta\left(\omega - \Delta E^{h_2,h_1}_{nn}\right) {}^{X_1}_{n}\langle h_1 e_1|B|h_2 e_2\rangle^{X_2}_{n}\, {}^{X_2}_{n}\langle h_2 e_2|C^\dagger|h_3 e_3\rangle^{X_3}_{n}\, {}^{X_3}_{n}\langle h_3 e_3|\rho|h_1 e_1\rangle^{X_1}_{n}\,. \tag{3.31}$$

Here, the sum over $\{X_1, X_2, X_3\}$ runs over all combinations of kept (K) and discarded (D) states except for the sector where all three are kept. That this reduction to one Wilson shell is possible, relies on the fact that the kept states of one shell are related to the discarded states of all later shells,

$$\sum_{he} |he\rangle^{K}_{n}\, {}^{K}_{n}\langle he| = \sum_{m>n}\sum_{he} |he\rangle^{D}_{m}\, {}^{D}_{m}\langle he|\,. \tag{3.32}$$

For a detailed derivation the reader is referred to reference [55]. The sum over $\{X_1, X_2, X_3\} \neq \{KKK\}$ immediately reduces to a sum over X_1 and X_2 because the matrix elements of the density matrix are diagonal in the X-sector, see equation (3.24). The operators B and C act on the impurity only. Their matrix elements therefore reduce to

$${}^{X}_{n}\langle he|O|h'e'\rangle^{X'}_{n} = {}^{X}_{n}\langle h|O|h'\rangle^{X'}_{n}\,\delta_{ee'} = \left(O^{(n)}\right)^{XX'}_{hh'}\delta_{ee'} \tag{3.33}$$

In summary, the correlator takes the form

$$G_{BC}(\omega) = 2\pi \sum_{\substack{n,h,h',h'' \\ XX'\neq KK}} \delta\left(\omega - \Delta E^{h''h'}_{nn}\right)\left(B^{(n)}\right)^{XX'}_{h,h'}\left(C^{\dagger(n)}\right)^{X'X}_{h',h''} \underbrace{\sum_{e} {}^{X}_{n}\langle h''e|\rho|he\rangle^{X}_{n}}_{\left(R^{(n)}\right)^{X}_{h''h}=\sum_{m>n} w_m \left(\rho^{(nm)}\right)^{XX}_{h''h}} \tag{3.34}$$

with the matrix elements $\left(R^{(n)}\right)^{X}_{h''h}$ discussed in equations (3.25)-(3.27). A pictorial representation of equation (3.34) is given in figure III.12.

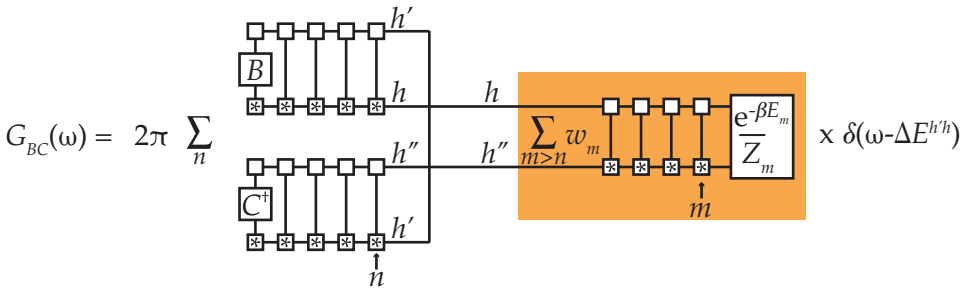

Figure III.12: Pictorial representation of the correlator G_{BC} in equation (3.34)

To determine the correlator $G_{BC}(\omega)$ one therefore starts with an NRG *forward sweep* generating all matrices $A^{[\sigma_n]}$. Afterwards the matrix elements $R^{(n)}$ are calculated in a *backward sweep*. This allows a direct feedback from the physics at low energies to the high-energy sector [55].

Weights w_n

It is instructive to examine the behavior of the weights

$$w_n = \frac{1}{Z} d^{N-n} \sum_{h \in D} e^{-\beta E_n(h)} \tag{3.35}$$

as a function of Wilson shell n. By construction, the eigenenergies $E_n(h)$ scale with $\Lambda^{-n/2}$. Using this, it is straightforward to show [55] that these weights are strongly peaked around the shell n^* which corresponds to the temperature $T = \beta^{-1}$,

$$\Lambda^{-\frac{n^*}{2}} \sim T. \tag{3.36}$$

The factor w_n, therefore, encodes the fact that the part of the Wilson chain corresponding to the energy scales close to the temperature T is the relevant part for the density matrix ρ.

III.4 Purification

At finite temperature the density matrix represents a *mixed state*, but MPS are designed to describe *pure states*. Still, one can describe finite temperature states based on MPS using the concept of *"purification"* [57, 58], which is explained in the following. First, the basic concept of purification is presented (III.4.1). Afterwards it is shown how a finite temperature state can be determined numerically via an imaginary time evolution (III.4.2), and the concept of a backward time evolution in the auxiliary state space is introduced (III.4.3).

III.4.1 Basic Concept

The density matrix is a positive semidefinite Hermitian operator and can therefore be written in the form

$$\rho(t) = X(t)X^\dagger(t). \tag{4.1}$$

For a closed quantum system, instead of describing the full operator $\rho(t)$ one can equally well study the time evolution of $X(t)$. To ensure that $\dot{\rho}(t) = -\mathrm{i}[H, \rho(t)]$, the time evolution of $X(t)$ is of the form

$$X(t) = \mathrm{e}^{-\mathrm{i}Ht} X U(t) \tag{4.2}$$

with $U(t)$ being any unitary transformation, which cancels out in the density matrix (4.1).

The operator $X(t)$ can be represented as a state in an enlarged Hilbert space using

$$X(t) = \sum_{mn} X_{mn}(t) \, |m\rangle \langle n| \tag{4.3a}$$

$$|X(t)\rangle = \sum_{mn} X_{mn}(t) \, |m\rangle |n\rangle_{\text{aux}} \, , \tag{4.3b}$$

with $\{|n\rangle\}$ being the eigenstates of the Hamiltonian H, $H|n\rangle = E_n |n\rangle$, and $X_{mn} = \langle m|X|n\rangle$. The space spanned by the states $\{|n\rangle_{\text{aux}}\}$ is a copy of the original Hilbert space $\{|n\rangle\}$ and referred to as *"auxiliary state space"*, while the original state space $\{|n\rangle\}$ is referred to as *"physical state space"*. At any time t the density matrix $\rho(t)$ can be recovered from $|X(t)\rangle$ using

$$\begin{aligned}\rho(t) &= \text{Tr}_{\text{aux}} \left(|X(t)\rangle \langle X(t)| \right) = \sum_k {}_{\text{aux}}\langle k|X(t)\rangle \langle X(t)|k\rangle_{\text{aux}} = \sum_{mnk} X_{mk}(t) X^*_{nk}(t) \, |m\rangle \langle n| \\ &= \sum_{mn} \left(X(t) X^\dagger(t) \right)_{mn} |m\rangle \langle n| \, . \end{aligned} \tag{4.4}$$

To ensure a density matrix with $\text{Tr}\left(\rho(t)\right) = 1$, the state $|X(t)\rangle$ needs to be normalized to $\langle X(t)|X(t)\rangle = 1$,

$$\text{Tr}\left(\rho(t)\right) = \text{Tr}_{\text{phys+aux}} \left(|X(t)\rangle \langle X(t)| \right) = \langle X(t)|X(t)\rangle = 1. \tag{4.5}$$

The expectation values of an operator A acting on the physical sites is given by

$$\langle A \rangle = \text{Tr}\left(A\rho(t)\right) = \text{Tr}_{\text{phys+aux}} \left(A \, |X(t)\rangle \langle X(t)| \right) = \langle X(t)|A|X(t)\rangle \, . \tag{4.6}$$

III.4.2 Imaginary Time Evolution

The density matrix for a system with chemical potential μ at finite temperature $T = \beta^{-1}$ is given by

$$\rho = Z^{-1} \, \mathrm{e}^{-\beta(H-\mu N)} \tag{4.7}$$

with partition function $Z = \text{Tr}\left(\mathrm{e}^{-\beta(H-\mu N)}\right)$, particle number operator N, and chemical potential μ. The purified state $|X\rangle$ in equation (4.3b) takes the form

$$|X\rangle = Z^{-\frac{1}{2}} \, \mathrm{e}^{-\frac{1}{2}\beta(H-\mu N)} \sum_n |n\rangle |n\rangle_{\text{aux}} = Z^{-\frac{1}{2}} \, \mathrm{e}^{-\frac{1}{2}\beta(E_n - \mu N_n)} \sum_n |n\rangle |n\rangle_{\text{aux}} \, , \tag{4.8}$$

where X_{mn} was chosen to be diagonal and it was assumed that the Hamiltonian conserves the particle number such that the eigenstates of the Hamiltonian have a well-defined number of particles, $N|n\rangle = N_n |n\rangle$.

From equation (4.8) one can immediately deduce that at infinite temperature, $\beta = T^{-1} = 0$, the thermal state is given by the *maximally entangled state*

$$|X_\infty\rangle \propto \sum_n |n\rangle |n\rangle_{\text{aux}} \, . \tag{4.9}$$

If the eigenstates of the Hamiltonian are not known such that at finite temperature ($\beta \neq 0$) the thermal state $|X\rangle$ in equation (4.8) cannot be constructed directly, it can instead be

obtained from the maximally entangled state using an *"imaginary time evolution"*,

$$|X\rangle \propto \mathrm{e}^{-\beta(H-\mu N)/2} \sum_n |n\rangle\,|n\rangle_{\mathrm{aux}} = \mathrm{e}^{-\beta(H-\mu N)/2}\,|X_\infty\rangle\ . \tag{4.10}$$

This imaginary time evolution can be performed in total analogy to real-time evolutions based on MPS methods, see section III.2, but with an imaginary time step $\tau = \mathrm{i}\beta/2$ (assuming $\mu = 0$). The maximally entangled state is maximally entangled in any basis, not only in the eigenbasis of the Hamiltonian [58]. On an MPS chain with local dimensions $\{|\sigma_i\rangle\}$ with additional auxiliary sites $|\sigma_i\rangle_{\mathrm{aux}}$ it is therefore given by

$$|X_\infty\rangle = \prod_i \left(\sum_{\sigma_i} |\sigma_i\rangle\,|\sigma_i\rangle_{\mathrm{aux}} \right)\ . \tag{4.11}$$

III.4.3 Backward Time Evolution

The arbitrary unitary transformation $U(t)$ in equation (4.2) can be interpreted as a time evolution acting on the auxiliary state space,

$$U(t) = \mathrm{e}^{-\mathrm{i}H_{\mathrm{aux}}t}\,, \tag{4.12}$$

such that

$$|X(t)\rangle = \mathrm{e}^{-\mathrm{i}Ht}\,\mathrm{e}^{-\mathrm{i}H_{\mathrm{aux}}t}\,|X(t=0)\rangle\ . \tag{4.13}$$

When time evolving a purified state using MPS methods, it has been argued [59] that this freedom of an arbitrary time evolution on the auxiliary state space can be exploited to reduce the entanglement growth within the MPS. A very good choice in this context is to time-evolve the auxiliary modes *backward in time* [59], in the sense that the "energy" of state $|n\rangle_{\mathrm{aux}}$ is given by *minus* the energy of state $|n\rangle$,

$$H_{\mathrm{aux}} = -E_n\,|n\rangle_{\mathrm{aux}}\,\langle n|_{\mathrm{aux}}\,. \tag{4.14}$$

IV Lindblad-Driven Discretized Leads

Why is the theoretical description of *nonequilibrium steady-state* (NESS) physics in quantum impurity models such a challenge compared to equilibrium situations? The answer lies in the fact that in the case of steady-state nonequilibrium one has to describe transport over a large window of time: particles flow in at the one side of the impurity and out on the other side. This implies that one of the leads loses particles while the number of particles in the other lead increases. However, at the same time, one would like to keep a fixed thermal distribution in the leads. This is impossible in a discrete quantum system. In principle, one can work with discrete leads that are large enough such that the change in the number of particles is irrelevant on the time scales that one is interested in. But in many cases such a system would be too large for a numerical description. Instead, the approach considered in this chapter explicitly works with an *open quantum system*.

In the approach of *"Lindblad-driven discretized leads"* (LDDL) additional dissipative terms in the time evolution of the density matrix render the discrete leads open. These *"Lindblad driving terms"* can actively change the particle number and thereby balance the loss or gain of particles in the two leads. Metaphorically speaking, they act as the "battery" connected to the leads. The price one has to pay to restore the continuous properties of the leads is that the system's time evolution is not given by a Hamiltonian any more, but by a Lindblad equation. Given such a system one cannot work on the level of individual states, but one has to describe the full density matrix.

Figure IV.1 shows a sketch of the basic idea: (a) The physical system consists of an impurity coupled to two continuous thermal leads with different thermal distributions, e.g., due to an applied voltage V. (b) For a numerical description the leads are discretized. In the LDDL approach each discrete lead level couples to an additional continuous Lindblad reservoir. (c) These reservoirs are not described explicitly, but they are traced out and represented in the form of dissipative Lindblad driving terms. By adding particles on the left-hand side and taking out particles on the right-hand side, these terms guarantee the correct occupation statistics of the leads even in the long-time limit, despite a finite current through the impurity.

Section IV.1 gives a short introduction to Lindblad equations. In particular, it describes the idea of the *"quantum regression theorem"* (QRT) on how to calculate correlation functions in a system that time-evolves under Lindbladian dynamics. For fermionic systems, however, the QRT cannot be applied in its standard form, but has to be modified by additional signs accounting for the fermionic anticommutation relations. This is proven in the appendix of the publication [P1]. In addition to this formal proof, section IV.1.2 gives an explicit example

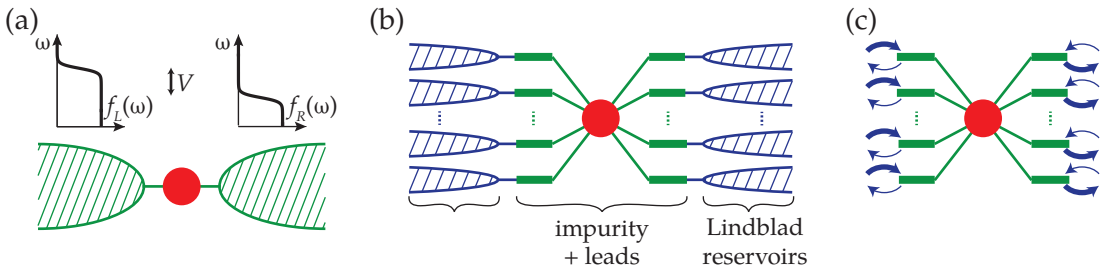

Figure IV.1: Sketch of the idea of LDDL: (a) Left and right leads are continuous thermal leads with different Fermi distributions, e.g. due to an applied voltage V, such that a current flows through the impurity. (b) The leads are represented by the a finite number of lead levels, each of which is coupled to an additional Lindblad reservoir. (c) These reservoirs are described as dissipative Lindblad driving terms, which can explicitly change the number of particles and restore the thermal distribution.

for a single level coupled to a Lindblad reservoir showing why these fermionic signs enter the QRT.

A Lindblad equation for LDDL can be obtained in different ways. In section IV.2 a first approach is presented that relies on a derivation of the Lindblad equation starting from the original impurity model with continuous thermal leads.

In section IV.3 a different logic is pursued: introducing an LDDL Lindblad equation, it is shown for which parameters the continuum limit of this Lindblad equation reproduces the correct hybridization function of a thermal bath. This approach has the advantage of not fixing the Lindblad driving terms from the outset such that it is possible to identify larger parameter regimes that result in a suitable hybridization. In particular, this formal approach sheds light on the connection between discretization parameters, physical parameters, and a reasonable choice for the Lindblad driving terms. Moreover, this analysis allows to identify a representation of the leads for which the Lindblad driving and the Hamiltonian are *local* on an MPS chain simultaneously. This local representation is found to be strongly connected to the concept of purification. We also draw a short comparison between the formal approach and the Lindblad equation determined in section IV.2. Note that more details on the results of the first part of this section (IV.3.1 - IV.3.3) can be found in the article [P1], see chapter V.

Section IV.4 comments on the possibility to derive a representation of LDDL starting from the open Wilson chain construction introduced in section II.2.3.

Finally, section IV.5 gives an overview of different possibilities to solve a Lindblad equation for its steady-state based on MPS methods.

IV.1 Lindblad Equations

Situations of steady-state nonequilibrium physics are important examples of *open quantum systems*. Such an open quantum system S, described by a density matrix ρ_S, can be interpreted as a subpart of a *closed system* consisting of S and an additional environment E. While the full system $S + E$ is governed by Hamiltonian dynamics, this is not true for the subsystem S due to the additional coupling to the environment E. The influence of the environment E on the system S can be captured by additional *dissipative terms* $\mathcal{D}\rho_S$ in the *Liouville equation* for

the time evolution of the density matrix ρ_S,

$$\frac{\mathrm{d}}{\mathrm{d}t}\rho_S = \mathcal{L}\rho_S = -\frac{\mathrm{i}}{\hbar}\left[H_S, \rho_S\right] + \mathcal{D}\rho_S. \tag{1.1}$$

For better legibility, we set $\hbar = 1$ in the remainder of this chapter. In many cases the environment is assumed to be *"Markovian"*, a property which can be paraphrased as "having no memory". It can be shown that for such a Markovian environment any dissipative Liouville equation that preserves the positivity and the trace of the system's density matrix, must be of the form [60]

$$\frac{\mathrm{d}}{\mathrm{d}t}\rho_S(t) = \mathcal{L}\rho_S(t) = -\mathrm{i}\left[H_S + H_{\mathrm{Lamb}}, \rho_S(t)\right] + \frac{1}{2}\sum_y \left(2J_y\,\rho_S(t)\,J_y^\dagger - \left\{J_y^\dagger J_y, \rho_S(t)\right\}\right). \tag{1.2}$$

The class of these master equations is named *"Lindblad equations"* after Göran Lindblad [61, 62]. The operators J_y are referred to as *"Lindblad operators"*. The Hamiltonians H_S and H_{Lamb} are often grouped into one Hamiltonian. However, one should keep in mind that this Hamiltonian is not necessarily equal to the system's Hamiltonian H_S but can contain an additional Lamb shift H_{Lamb}. A detailed derivation of the form of a Lindblad equation based on a microsopic view can, e.g., be found in reference [63]. The strategy of such a microscopic derivation is to start with the full *closed* system consisting of subsystem $S + E$ and to trace out the environment E giving an explicit Lindblad equation for subsystem S. For a specific elementary system, namely for a single level coupled to a fermionic bath, such a derivation is presented in section IV.1.2.

IV.1.1 The Quantum Regression Theorem

Quadratic systems governed by Hamiltonian dynamics are exactly solvable. Analogously, consider a "quadratic Lindblad equation" for which the Hamiltonian is quadratic, $H = H_S + H_{\mathrm{Lamb}} = \sum_{mn} h_{mn} L_m^\dagger L_n$, and the Lindblad operators are linear in either the annihilators, $J_{y1} = \sum_n j_{yn1} L_n$, or the creators, $J_{y2} = \sum_n j_{yn2} L_n^\dagger$. It can easily be shown that for both, fermionic and bosonic systems, $\left[L_i, L_j^\dagger\right]_\pm = \delta_{ij}$, the equations of motion for linear operators take a closed form,

$$\frac{\mathrm{d}}{\mathrm{d}t}\left\langle L_i(t)\right\rangle = \mathrm{Tr}\left(L_i\,\dot{\rho}_S(t)\right) \overset{(1.2)}{=} \sum_k M_{ik}\left\langle L_k(t)\right\rangle, \tag{1.3}$$

where M is a matrix that depends on h_{mn} and the parameters j_{yni} of the Lindblad operators. For two-point correlators, the idea of the *"quantum regression theorem"* (QRT) [60, 63] is to exploit

$$\frac{\mathrm{d}}{\mathrm{d}t}\left\langle L_i(t) L_j^\dagger\right\rangle = \frac{\mathrm{d}}{\mathrm{d}t}\mathrm{Tr}\left(L_i(t)\tilde{\rho}_S\right) = \mathrm{Tr}\left(L_i\dot{\tilde{\rho}}_S(t)\right) \tag{1.4}$$

with $\tilde{\rho}_S = L_j^\dagger \rho_S$. For *bosonic* systems the Lindblad time evolution is also applicable to the density matrix $\tilde{\rho}_S$ such that using equation (1.3)

$$\frac{\mathrm{d}}{\mathrm{d}t}\left\langle L_i(t) L_j^\dagger\right\rangle = \sum_k M_{ik}\left\langle L_k(t) L_j^\dagger\right\rangle. \tag{1.5}$$

However, we found that for *fermionic* systems the time evolution of $\tilde{\rho}_S(t)$ is not given by the Lindblad equation (1.2), but additional signs have to be taken into account due to the fermionic anticommutation relations. This is explained in the article [P1] in detail and made explicit for a specific example in section IV.1.2.

IV.1.2 Single Fermionic Level Coupled to a Lindblad Reservoir

As a simple explicit example, this section shows how a Lindblad equation for a single fermionic level coupled to a thermal Lindblad reservoir can be derived. A very similar discussion for the single level is, e.g., given in reference [64] and a detailed discussion on such microscopic derivations of Lindblad equations for general systems can be found in the literature, see e.g. reference [63]. We review this derivation here to further illustrate the concept of Lindblad equations and, in particular, to point out with the help of this simple example why the fermionic anticommutation relation modify the form of the QRT. This can be seen as an instructive illustration of the more formal proof in the appendix of the paper [P1] in chapter V.

The model considered here is that of a single fermionic level (the system S) coupled to a fermionic thermal bath (the environment E). The Hamiltonian of the full closed quantum system is given by

$$H = \underbrace{\varepsilon_d d^\dagger d}_{H_S} + \underbrace{\sum_k \varepsilon_k c_k^\dagger c_k}_{H_E} + \underbrace{\sum_k \left(v_k d^\dagger c_k + \text{h.c.}\right)}_{H_I} = H_0 + H_I\,. \tag{1.6}$$

Lindblad Equation

Transforming to the interaction picture by defining

$$U(t,t_0) = \mathrm{e}^{-\mathrm{i}H(t-t_0)}\,, \qquad U_0(t,t_0) = \mathrm{e}^{-\mathrm{i}H_0(t-t_0)}\,, \tag{1.7a}$$

$$U_I(t,t_0) = U_0^\dagger(t,t_0)U(t,t_0)\,, \qquad \frac{\mathrm{d}}{\mathrm{d}t}U_I(t,t_0) = -\mathrm{i}\hat{H}_I U_I(t,t_0)\,, \tag{1.7b}$$

$$\hat{A}(t) = U_0^\dagger(t,t_0)AU_0(t,t_0)\,, \tag{1.7c}$$

the time evolution of the density matrix is given by

$$\hat{\rho}(t) = U_0^\dagger(t,t_0)\rho(t)U_0(t,t_0) = U_I(t,t_0)\rho(t_0)U_I^\dagger(t,t_0) \tag{1.8}$$

$$\frac{\mathrm{d}}{\mathrm{d}t}\hat{\rho}(t) = -\mathrm{i}\left[\hat{H}_I(t),\hat{\rho}(t)\right] \quad \Rightarrow \hat{\rho}(t) = \hat{\rho}(0) - \mathrm{i}\int_0^t \mathrm{d}s\,\left[\hat{H}_I(s),\hat{\rho}(s)\right]. \tag{1.9}$$

The integrated form can be inserted back into the differential form. The coupling between reservoir and the system S is assumed to be weak such that the reservoir is only weakly affected by the system. In this case the density matrix can be written as $\hat{\rho}(t) = \hat{\rho}_S(t)\otimes\rho_E$. Tracing out the environment's degrees of freedom and assuming $\mathrm{tr}_E\left[\hat{H}_I(t),\rho(0)\right] = 0$ one obtains

$$\frac{\mathrm{d}}{\mathrm{d}t}\hat{\rho}_S(t) = -\int_0^t \mathrm{d}s\,\mathrm{tr}_E\left[\hat{H}_I(t),\left[\hat{H}_I(s),\hat{\rho}_S(s)\otimes\rho_E\right]\right]. \tag{1.10}$$

For Markovian systems the time scale on which correlations in the reservoir decay is much smaller than the time scale on which the system S varies. This allows to replace $\hat{\rho}_S(s)$ by $\hat{\rho}_S(t)$ such that the time derivative of the density matrix at time t does not depend on $\hat{\rho}_S(s)$ for times s with $s < t$. Furthermore, after a substitution $s \to t - s$ this hierarchy in the time scales allows to replace the upper limit in the integral by ∞,

$$\frac{\mathrm{d}}{\mathrm{d}t}\hat{\rho}_S(t) = -\int_0^\infty \mathrm{d}s\, \mathrm{tr}_E\left[\hat{H}_I(t), \left[\hat{H}_I(t-s), \hat{\rho}_S(t)\otimes\rho_E\right]\right]. \tag{1.11}$$

The four terms of the commutators can be recast into two terms plus their Hermitian conjugate

$$\frac{\mathrm{d}}{\mathrm{d}t}\hat{\rho}_S(t) = -\int_0^\infty \mathrm{d}s\, \mathrm{tr}_E\left(\hat{H}_I(t)\hat{H}_I(t-s)\left(\hat{\rho}_S(t)\otimes\rho_E\right) - \hat{H}_I(t-s)\left(\hat{\rho}_S(t)\otimes\rho_E\right)\hat{H}_I(t)\right) + \text{h.c.} \tag{1.12}$$

With the explicit interaction Hamiltonian of equation (1.6) this reads

$$\hat{H}_I(t) = \sum_k \left(v_k\,\hat{d}^\dagger(t)\hat{c}_k(t) + v_k^*\,\hat{c}_k^\dagger(t)\hat{d}(t)\right) \tag{1.13}$$

$$\begin{aligned}\frac{\mathrm{d}}{\mathrm{d}t}\hat{\rho}_S(t) = -\int_0^\infty \mathrm{d}s\, \mathrm{tr}_E\Bigg(&\sum_{kq}\left(v_k\,\hat{d}^\dagger(t)\hat{c}_k(t) + v_k^*\,\hat{c}_k^\dagger(t)\hat{d}(t)\right)\cdot \\ &\left(v_q\,\hat{d}^\dagger(t-s)\hat{c}_q(t-s) + v_q^*\,\hat{c}_q^\dagger(t-s)\hat{d}(t-s)\right)\left(\hat{\rho}_S(t)\otimes\rho_E\right) \\ &-\sum_{kq}\left(v_k\,\hat{d}^\dagger(t-s)\hat{c}_k(t-s) + v_k^*\,\hat{c}_k^\dagger(t-s)\hat{d}(t-s)\right)\left(\hat{\rho}_S(t)\otimes\rho_E\right)\cdot \\ &\left(v_q\,\hat{d}^\dagger(t)\hat{c}_q(t) + v_q^*\,\hat{c}_q^\dagger(t)\hat{d}(t)\right)\Bigg) + \text{h.c.}\end{aligned} \tag{1.14}$$

When expanding this expression, terms that contain two annihilators $\hat{c}$ or two creation operators $\hat{c}^\dagger$ can be dropped due to $\mathrm{tr}_E(\hat{c}_k\hat{c}_q\rho_E) = 0$ and $\mathrm{tr}_E(\hat{c}_k^\dagger\hat{c}_q^\dagger\rho_E) = 0$. Keeping track of the correct order, one finds

$$\begin{aligned}\frac{\mathrm{d}}{\mathrm{d}t}\hat{\rho}_S(t) = -\int_0^\infty \mathrm{d}s \sum_{kq}\Big(&v_k v_q^*\,\mathrm{tr}_E\left(\hat{c}_k(t)\hat{c}_q^\dagger(t-s)\rho_E\right)\hat{d}^\dagger(t)\hat{d}(t-s)\hat{\rho}_S(t) \\ &+ v_k^* v_q\,\mathrm{tr}_E\left(\hat{c}_k^\dagger(t)\hat{c}_q(t-s)\rho_E\right)\hat{d}(t)\hat{d}^\dagger(t-s)\hat{\rho}_S(t) \\ &- v_k v_q^*\,\mathrm{tr}_E\left(\hat{c}_k(t-s)\rho_E\hat{c}_q^\dagger(t)\right)\hat{d}^\dagger(t-s)\hat{\rho}_S(t)\hat{d}(t) \\ &- v_k^* v_q\,\mathrm{tr}_E\left(\hat{c}_k^\dagger(t-s)\rho_E\hat{c}_q(t)\right)\hat{d}(t-s)\hat{\rho}_S(t)\hat{d}^\dagger(t)\Big) + \text{h.c.}\end{aligned} \tag{1.15}$$

The environment is assumed to be thermal. It therefore fulfills

$$\begin{aligned}\mathrm{tr}_B\left(\hat{c}_k(t)\hat{c}_q^\dagger(t-s)\rho_E\right) &= \mathrm{tr}_B\left(\hat{c}_k^\dagger(t-s)\rho_E\hat{c}_q(t)\right) = \delta_{kq}\,\mathrm{e}^{-\mathrm{i}\varepsilon_k s}\left(1-f(\varepsilon_k)\right) \\ \mathrm{tr}_B\left(\hat{c}_k^\dagger(t)\hat{c}_q(t-s)\rho_E\right) &= \mathrm{tr}_B\left(\hat{c}_k(t-s)\rho_E\hat{c}_q^\dagger(t)\right) = \delta_{kq}\,\mathrm{e}^{\mathrm{i}\varepsilon_k s} f(\varepsilon_k),\end{aligned} \tag{1.16}$$

where $f(\omega)$ is the Fermi distribution characterizing the occupation statistics of the reservoir. With $\hat{d}(t-s) = \hat{d}(t)\,\mathrm{e}^{\mathrm{i}\varepsilon_d s}$ and the hybridization function $\Gamma(\omega) = \sum_k \pi|v_k|^2\delta(\omega-\varepsilon_k)$, one

obtains

$$\frac{\mathrm{d}}{\mathrm{d}t}\hat{\rho}_S(t) = -\int_0^\infty \mathrm{d}s \int_{-\infty}^\infty \mathrm{d}\omega\, \frac{\Gamma(\omega)}{\pi} \Big(\mathrm{e}^{-\mathrm{i}(\omega-\varepsilon_d)s}\,(1-f(\omega)) \left(\hat{d}^\dagger(t)\hat{d}(t)\hat{\rho}_S(t) - \hat{d}(t)\hat{\rho}_S(t)\hat{d}^\dagger(t)\right) + \mathrm{e}^{\mathrm{i}(\omega-\varepsilon_d)s} f(\omega) \left(\hat{d}(t)\hat{d}^\dagger(t)\hat{\rho}_S(t) - \hat{d}^\dagger(t)\hat{\rho}_S(t)\hat{d}(t)\right)\Big) + \mathrm{h.c.} \quad (1.17)$$

The integral can be performed using $\int_0^\infty \mathrm{d}s\ \mathrm{e}^{\pm\mathrm{i}(\omega-\varepsilon_d)s} = \pi\delta(\omega-\varepsilon_d) \pm \mathrm{i}\mathcal{P}\left(\frac{1}{\omega-\varepsilon_d}\right)$,

$$\begin{aligned}\frac{\mathrm{d}}{\mathrm{d}t}\hat{\rho}_S(t) = \Gamma(\varepsilon_d) \Big(&(1-f(\varepsilon_d)) \left(2\hat{d}(t)\hat{\rho}_S(t)\hat{d}^\dagger(t) - \hat{d}^\dagger(t)\hat{d}(t)\hat{\rho}_S(t) - \hat{\rho}_S(t)\hat{d}^\dagger(t)\hat{d}(t)\right) \\ &+ f(\varepsilon_d) \left(2\hat{d}^\dagger(t)\hat{\rho}_S(t)\hat{d}(t) - \hat{d}(t)\hat{d}^\dagger(t)\hat{\rho}_S(t) - \hat{\rho}_S(t)\hat{d}(t)\hat{d}^\dagger(t)\right)\Big) \\ -\mathrm{i}\int_{-\infty}^\infty \mathrm{d}\omega\, \frac{\Gamma(\omega)}{\pi}\mathcal{P}\left(\frac{1}{\omega-\varepsilon_d}\right) \Big(&(1-f(\omega)) \left(\hat{d}^\dagger(t)\hat{d}(t)\hat{\rho}_S(t) - \hat{\rho}_S(t)\hat{d}^\dagger(t)\hat{d}(t)\right) \\ &+ f(\omega) \left(\hat{d}(t)\hat{d}^\dagger(t)\hat{\rho}_S(t) - \hat{\rho}_S(t)\hat{d}(t)\hat{d}^\dagger(t)\right)\Big)\,. \end{aligned} \quad (1.18)$$

And with $\hat{d}(t)\hat{d}^\dagger(t)\hat{\rho}_S(t) - \hat{\rho}_S(t)\hat{d}(t)\hat{d}^\dagger(t) = \left[\hat{d}^\dagger(t)\hat{d}(t), \hat{\rho}_S(t)\right]$ the last two lines can be rewritten as

$$-\mathrm{i}\int_{-\infty}^\infty \mathrm{d}\omega\, \frac{1}{\pi}\Gamma(\omega)\mathcal{P}\left(\frac{1}{\omega-\varepsilon_d}\right) \left[\hat{d}^\dagger(t)\hat{d}(t), \hat{\rho}_S(t)\right] = -\mathrm{i}\left[\hat{H}_{\mathrm{Lamb}}, \hat{\rho}_S(t)\right]\,, \quad (1.19)$$

where $\hat{H}_{\mathrm{Lamb}} = \hat{h}_{\mathrm{Lamb}}\,\hat{d}^\dagger(t)\hat{d}(t)$. If $\Gamma(\omega)$ is symmetric around ε_d, as is often the case in fermionic models in the wide-band limit, $\hat{h}_{\mathrm{Lamb}}$ vanishes. Finally, the time evolution is transformed back to the Schrödinger picture,

$$\begin{aligned}\frac{\mathrm{d}}{\mathrm{d}t}\hat{\rho}_S(t) &= \frac{\mathrm{d}}{\mathrm{d}t}\left(U_0^\dagger(t,t_0)\rho_S(t)U_0(t,t_0)\right) \\ &= U_0(t,t_0)^\dagger \left(\frac{\mathrm{d}}{\mathrm{d}t}\rho_S(t)\right) U_0(t,t_0) + \mathrm{i}U_0^\dagger(t,t_0)\left[H_0,\rho_S(t)\right]U_0(t,t_0) \quad (1.20) \\ \frac{\mathrm{d}}{\mathrm{d}t}\rho_S(t) &= -\mathrm{i}\left[H_0,\rho_S(t)\right] + U_0(t,t_0)\left(\frac{\mathrm{d}}{\mathrm{d}t}\hat{\rho}_S(t)\right)U_0^\dagger(t,t_0) \\ &= -\mathrm{i}\left[H_S + H_{\mathrm{Lamb}},\rho_S(t)\right] + \Gamma(\varepsilon_d)\,(1-f(\varepsilon_d))\left(2d\rho_S(t)d^\dagger - d^\dagger d\rho_S(t) - \rho_S(t)d^\dagger d\right) \\ &\quad + \Gamma(\varepsilon_d)f(\varepsilon_d)\left(2d^\dagger\rho_S(t)d - dd^\dagger\rho_S(t) - \rho_S(t)dd^\dagger\right). \quad (1.21)\end{aligned}$$

This equation is of the Lindbladian form in equation (1.2) with Lindblad operators,

$$\begin{aligned}J_1 &= 2\Gamma(\varepsilon_d)\,(1-f(\varepsilon_d))\ d\,, \\ J_2 &= 2\Gamma(\varepsilon_d)f(\varepsilon_d)\,d^\dagger\,.\end{aligned} \quad (1.22)$$

The information on the frequency dependence of the hybridization is lost, but its overall strength is reflected in the strength of the Lindblad driving. The thermal distribution of the fermionic reservoir is encoded in the relative driving strength of the two Lindblad operators, which are proportional to the annihilator d and the creator $d^\dagger$, respectively.

Quantum Regression Theorem

When considering the quantum regression theorem, compare section IV.1.1, the crucial point in the above derivation of the Lindblad equation is the step leading from equation (1.14) to equation (1.15), in which the density matrix $\hat{\rho}_S$ is interchanged with reservoir operators $\hat{c}^{(\dagger)}_{k/q}$ using

$$\left[\hat{\rho}_S, \hat{c}^{(\dagger)}_{k/q}\right] = 0\,. \tag{1.23}$$

When applying the QRT, the Lindblad equation is assumed to hold also for a density matrix of the form $\tilde{\rho}_S = L^{(\dagger)}\rho_S$, see equations (1.4)-(1.5). However, in case that $L^{(\dagger)}$ and $\hat{c}^{(\dagger)}_{k/q}$ are fermionic operators, one has

$$\left\{\hat{\tilde{\rho}}_S, \hat{c}^{(\dagger)}_{k/q}\right\} = 0 \tag{1.24}$$

such that the last two lines in equation (1.15) gain additional minus signs. Going through the derivation including these additional minus signs, one obtains for the time evolution of $\tilde{\rho}_S$,

$$\begin{aligned}\frac{\mathrm{d}}{\mathrm{d}t}\tilde{\rho}_S(t) = &-\mathrm{i}\left[H_S + H_{\mathrm{Lamb}}, \tilde{\rho}_S(t)\right] \\ &+ \Gamma(\varepsilon_d)\left(1 - f(\varepsilon_d)\right)\left(-2d\,\tilde{\rho}_S(t)d^\dagger - d^\dagger d\,\tilde{\rho}_S(t) - \tilde{\rho}_S(t)d^\dagger d\right) \\ &+ \Gamma(\varepsilon_d) f(\varepsilon_d)\left(-2d^\dagger\tilde{\rho}_S(t)d - dd^\dagger\tilde{\rho}_S(t) - \tilde{\rho}_S(t)dd^\dagger\right),\end{aligned} \tag{1.25}$$

with emphasis on the two minus signs in front of the terms $2d\,\tilde{\rho}_S(t)d^\dagger$ and $2d^\dagger\tilde{\rho}_S(t)d$.

These minus signs can be generalized to arbitrary fermionic systems, see the appendix of [P1] in chapter V for details. This means that fortunately, the idea of calculating correlators by defining the density matrix $\tilde{\rho}_S$ can be extended to quadratic Lindblad equations, but one has to use this modified Lindblad equation for the time evolution of $\tilde{\rho}_S$.

IV.2 Lindblad-Driven Discretized Leads – A First Approach

In section IV.3 it is studied how a Lindblad equation should be chosen to represent Lindblad-driven discretized leads in an impurity model. In order to obtain a more intuitive understanding of the LDDL approach the current section presents a simple explicit derivation of such a Lindblad equation. The result gives a first hint to the form of the Lindblad driving terms. But even more important, it is an instructive illustration for a possible theoretical understanding of the LDDL setup.

When a continuous lead coupled to an impurity is discretized into a finite number of lead levels, each lead level represents a small energy interval of the original continuous bath. The frequency dependence of the hybridization $\Gamma(\omega) = -\mathrm{Im}(\Delta^R(\omega))$ is only kept in a coarse-grained fashion and the continuous properties of the lead are lost. However, in a first step this information can be preserved in the following way: the full hybridization function is decomposed into different energy intervals, $\Delta^R(\omega) = \sum_k \Delta^R_k(\omega)$, as depicted in figure IV.2(a)-(b). Similar to the idea of the open Wilson chain described in section II.2.3, the hybridization of each interval, $\Delta^R_k(\omega)$, is then represented by one lead level k coupled to a new continuous bath $\tilde{\Delta}^R_k(\omega)$, as depicted in figure IV.2(c). This can be done without changing the total hybridization felt by the impurity [P3]. The impurity together with the

lead levels is interpreted as the system S, while the new continuous baths correspond to an environment E. Assuming that only one impurity level d couples to the original lead, the Hamiltonian of system S is given by

$$H_S = H_{\text{imp}} + \sum_k \left(v_k d^\dagger c_k + \text{h.c.}\right) + \sum_k \varepsilon_k c_k^\dagger c_k \,, \tag{2.1}$$

where further indices are suppressed for simplicity. The energies ε_k, the couplings v_k, and

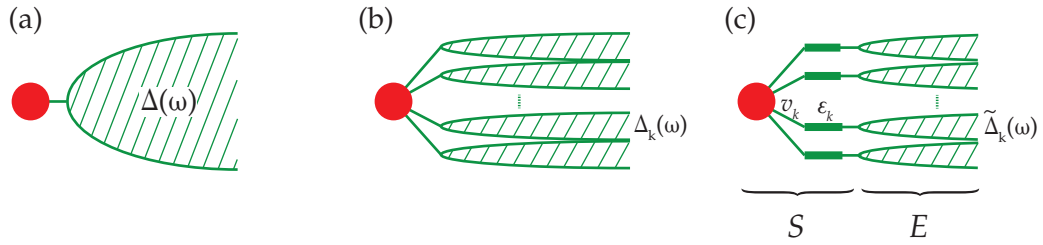

Figure IV.2: Sketch of the LDDL construction: (a) The impurity couples to a continuous thermal bath. (b) This bath can be decomposed into a set of discrete intervals. (c) The continuous bath of each interval is represented by one lead level k which couples to the remaining degrees of freedom. The impurity together with the discrete lead levels are interpreted as the system S, while the remaining baths are summarized into an environment E. The system S itself is *discrete*. But describing the environment E in terms of a Lindblad driving, the leads keep their property of being an *open* quantum system.

the functions $\tilde{\Delta}_k^R(\omega)$ are fixed by the condition that the influence of the lead level coupled to its bath $\tilde{\Delta}_k^R(\omega)$ on the impurity has to be identical to the interval's original contribution to the hybridization, $\Delta_k^R(\omega)$. This is fulfilled if the following relation holds [P3]:

$$\tilde{\Delta}_k^R(\omega) = \omega - \varepsilon_k - \frac{|v_k|^2}{\Delta_k^R(\omega)}, \tag{2.2}$$

with

$$\varepsilon_k = \frac{1}{\pi |v_k|^2} \int_{-\infty}^{\infty} \mathrm{d}\omega\, \omega \Gamma_k(\omega), \quad \text{and} \quad |v_k|^2 = \frac{1}{\pi} \int_{-\infty}^{\infty} \mathrm{d}\omega\, \Gamma_k(\omega). \tag{2.3}$$

Up to this point, this is an *exact* representation of the full original lead. However, there are still continuous baths $\tilde{\Delta}_k^R(\omega)$ involved in the environment E. In the LDDL approach these baths are integrated out and described by Lindblad driving terms acting on the system S. To this end, we ignore the coupling to the impurity because our goal is to find an effective description of Lindblad-driven lead levels such that each interval contributes to the hybridization corresponding to $\Delta_k(\omega)$. This hybridization, however, consists of the *free* correlators, i.e., the correlators of the levels decoupled from the impurity. Tracing out the environment E is analogous to the derivation of a Lindblad equation for a single level given in section IV.1.2. Instead of a level ε_d coupled to a bath with hybridization $\Gamma(\omega)$ in section IV.1.2, we here have levels ε_k coupled to $\tilde{\Gamma}_k(\omega) = -\text{Im}\left(\tilde{\Delta}_k^R(\omega)\right)$. Provided that we can assume a thermal distribution also for the baths $\tilde{\Delta}_k(\omega)$ with Fermi statistics $f(\omega)$, we

obtain two jump operators for each lead level, compare equation (1.22),

$$\begin{aligned} J_{k1} &= 2\gamma_k \left(1 - f(\varepsilon_k)\right) c_k \,, \\ J_{k2} &= 2\gamma_k f(\varepsilon_k)\, c_k^\dagger \,. \end{aligned} \tag{2.4}$$

where $f(\varepsilon_k)$ is the Fermi distribution of the thermal lead and

$$\gamma_k = -\mathrm{Im}\left(\tilde{\Delta}_k^R(\varepsilon_k)\right) = \mathrm{Im}\left(\frac{|v_k|^2}{\Delta_k^R(\varepsilon_k)}\right) . \tag{2.5}$$

The full Lindblad equation is given by

$$\begin{aligned} \frac{\mathrm{d}}{\mathrm{d}t}\rho_S(t) = -\mathrm{i}\left[H_S + H_{\mathrm{Lamb}}, \rho_S(t)\right] &+ \sum_k \gamma_k \left(1 - f(\varepsilon_k)\right) \left(2c_k \rho_S(t) c_k^\dagger - \left\{c_k^\dagger c_k, \rho_S(t)\right\}\right) \\ &+ \sum_k \gamma_k f(\varepsilon_k) \left(2c_k^\dagger \rho_S(t) c_k - \left\{c_k c_k^\dagger, \rho_S(t)\right\}\right) . \end{aligned} \tag{2.6}$$

If the hybridization of the original lead is given by a box distribution, $\Gamma(\omega) = \Gamma\Theta(D - |\omega|)$, and if it is divided into distinct energy intervals,

$$\Gamma_k(\omega) = \begin{cases} \Gamma & \text{for } \omega \in [E_k, E_{k+1}] \\ 0 & \text{elsewhere} \end{cases} \tag{2.7}$$

one obtains

$$|v_k|^2 = \tfrac{1}{\pi}\delta_k \Gamma \quad \text{with } \delta_k = E_{k+1} - E_k, \tag{2.8}$$

$$\varepsilon_k = \tfrac{1}{2}\left(E_k + E_{k+1}\right) . \tag{2.9}$$

The hybridization $\Gamma_k(\omega)$ is symmetric around $\omega = \varepsilon_k$. Therefore, the Lamb shift H_{Lamb} vanishes. Furthermore, this symmetry enforces $\mathrm{Re}(\Delta_k(\varepsilon_k)) = 0$ such that the factor γ_k in the coefficients of the Lindblad driving is given by

$$\gamma_k = \mathrm{Im}\left(\frac{|v_k|^2}{-\mathrm{i}\Gamma}\right) = \frac{\delta_k}{\pi} . \tag{2.10}$$

The form of the Lindblad equation (2.6) is intuitive: the Lindblad operators drive the leads towards occupancy $f(\varepsilon_k)$. To this end, the Lindblad terms representing the annihilators $J \propto c_k$ contribute to the time derivative of $\rho_S(t)$ with weight $1 - f(\varepsilon_k)$, while the creators $J \propto c_k^\dagger$ carry a weight of $f(\varepsilon_k)$. Interestingly, following this result, the overall strength of the Lindblad driving γ_k is proportional to the size of the corresponding energy interval, δ_k, but it does not depend on the strength of the original hybridization Γ.

Note that in section IV.1.2 the bath $\Delta(\omega)$ coupled to the local level was interpreted as the environment E. Here only the baths $\tilde{\Delta}_k(\omega)$ are summarized into the environment E and the Lindblad driving acts on the lead levels instead of directly acting on the impurity. For typical impurity models immediately integrating out the full bath would be too crude. The additional lead levels allow a much better resolution of the bath's properties. This can, e.g., be seen from the fact that for the single level in section IV.1.2 the only information kept from the thermal distribution $f(\omega)$ and the hybridization $\Gamma(\omega)$ are their specific values at $\omega = \varepsilon_d$. In comparison, the LDDL approach in this section keeps the information on $f(\omega)$ and $\Gamma(\omega)$

at many points $\omega = \varepsilon_k$. This idea of a *"buffer zone"* of lead levels which are included into the system S rather than into the environment E has been introduced and used in a series of publications before, see references [65–70].

IV.3 Lindblad-Driven Discretized Leads – A Formal Approach

In this section the LDDL approach is considered in a more formal manner with emphasis on the leads' hybridization function. In particular, this section will turn around the argumentation: instead of starting from a continuous bath and deriving a Lindblad equation from it, we begin with a Lindblad equation and prove how the parameters have to be chosen to regain a valid representation of the original bath.

The only lead property that enters the impurity physics is the hybridization function, see sections II.2.1-II.2.2. Hence, one can use any lead representation as long as it reproduces the original continuous hybridization function to a good approximation. For an open system, however, not only the retarded component of the hybridization has to be considered, but also a correct Keldysh component has to be guaranteed. The idea of the approach in this section is simple: the form of the Hamiltonian of the system S must be such that one recovers the correct retarded component $\Delta^R(\omega)$. At the same time the Lindblad driving has to be chosen such that the leads remain thermal in the sense that the fluctuation-dissipation theorem (II.2.15), which fixes the form of the Keldysh component $\Delta^K(\omega)$, is fulfilled to a good approximation.

The publication [P1] in chapter V, the main results of which are reviewed in the sections IV.3.1-IV.3.3, achieved two important goals: In a first part, it is shown how the hybridization function for Lindblad-driven discretized leads can be determined from the parameters in the Lindblad equation. This tells us how the Lindblad equation has to be chosen such that the LDDL approach provides a suitable representation of thermal leads. In particular, it is proven that the LDDL approach for reasonably chosen parameters is *exact in the continuum limit*. In a second part the insight into the hybridization of leads in the LDDL approach is used to develop an LDDL representation for which the Hamiltonian and the Lindblad driving can be local on the MPS chain *simultaneously*. This lies the foundation for a simpler evaluation of the Lindblad equation based on MPS methods. Section IV.3.4 compares the results of this formal approach to the intuitive picture of section IV.2. Finally, section IV.3.5 comments on the connection between the local LDDL representation and standard purification schemes.

IV.3.1 Quadratic Lindblad Models

We consider a quadratic Lindblad equation,

$$\begin{aligned}\dot{\rho}(t) = -\mathrm{i}\left[\tilde{H}, \rho(t)\right] &+ \sum_{mn} \Lambda^{(1)}_{mn} \left(2L_n \rho(t) L_m^\dagger - \left\{L_m^\dagger L_n, \rho(t)\right\}\right) \\ &+ \sum_{mn} \Lambda^{(2)}_{mn} \left(2L_m^\dagger \rho(t) L_n^\dagger - \left\{L_n L_m^\dagger, \rho(t)\right\}\right) \end{aligned} \tag{3.1}$$

with

$$\tilde{H} = \sum_{mn} \tilde{h}_{mn} L_m^\dagger L_n \,. \tag{3.2}$$

Compared to equation (1.2) we here explicitly distinguish between Lindblad operators that *annihilate* particles and Lindblad operators that *create* particles. In this section, the label S for

the density matrix is dropped because no environment E is defined. We define the Green's functions corresponding to the operators $L_n^{(\dagger)}$,

$$\mathcal{G}^R_{mn}(t) = -\mathrm{i}\Theta(t)\,\langle\{L_m(t), L_n^\dagger\}\rangle_{\mathrm{NESS}} \tag{3.3a}$$
$$\mathcal{G}^A_{mn}(t) = \mathrm{i}\Theta(-t)\,\langle\{L_m(t), L_n^\dagger\}\rangle_{\mathrm{NESS}} \tag{3.3b}$$
$$\mathcal{G}^K_{mn}(t) = -\mathrm{i}\,\langle[L_m(t), L_n^\dagger]\rangle_{\mathrm{NESS}} \tag{3.3c}$$

and their Fourier transforms

$$G^{R/A/K}_{mn}(\omega) = \int_{-\infty}^{\infty} \mathrm{d}t\; \mathrm{e}^{\mathrm{i}\omega t}\, \mathcal{G}^{R/A/K}_{mn}(t)\,. \tag{3.3d}$$

These Green's functions can be determined in analogy to the QRT with the additional signs for the time evolution of a "fermionic" density matrix introduced in the appendix of the paper [P1]. It is shown in the publication [P1] in chapter V that they are given by the following matrix equations

$$G^R(\omega) = \left(\omega - \tilde{h} + \mathrm{i}\,\Lambda^{(+)}\right)^{-1} \tag{3.4}$$
$$G^K(\omega) = -\mathrm{i}\,G^R(\omega) 2\Lambda^{(-)} G^A(\omega). \tag{3.5}$$

with $\Lambda^{(\pm)} = \Lambda^{(1)} \pm \Lambda^{(2)}$, see also reference [71].

IV.3.2 The LDDL Lindblad Equation

Consider a lead Hamiltonian in the star geometry,

$$H_{\mathrm{lead}} = \sum_{\alpha k(\sigma)} \varepsilon_k c^\dagger_{\alpha k(\sigma)} c_{\alpha k(\sigma)} = \sum_q \varepsilon_q c_q^\dagger c_q\,, \tag{3.6}$$

where $q = \{\alpha, k, (\sigma)\}$ labels the lead levels summarizing their lead index α, their energy label k, and a possible spin index σ, compare equation (II.1.2). It can easily be argued (see [P1] in chapter V and compare also section IV.2) that for such a lead Hamiltonian the Lindblad equation in the LDDL approach should take the form

$$\frac{\mathrm{d}}{\mathrm{d}t}\rho(t) = -\mathrm{i}\,[H, \rho(t)] + \sum_q \gamma_q \Big[\big(1 - f_\alpha(\varepsilon_q)\big)\left(2c_q\,\rho(t)c_q^\dagger - \left\{c_q^\dagger c_q, \rho(t)\right\}\right) \\ f_\alpha(\varepsilon_q)\left(2c_q^\dagger\,\rho(t)c_q - \left\{c_q c_q^\dagger, \rho(t)\right\}\right)\Big]\,. \tag{3.7}$$

Here, γ_q is the strength of the Lindblad driving. The Hamiltonian H includes the impurity, the lead Hamiltonian, and the lead-impurity hybridization, compare equation (II.1.1). The hybridization function of the corresponding Lindblad-driven discretized leads follows from the noninteracting lead levels *decoupled* from the impurity but including their Lindblad driving. This is a *quadratic* systems such that the hybridization including its Keldysh component can immediately be deduced using equations (3.4) and (3.5).

In the paper [P1], we find that the hybridization function resulting from the Lindblad equation (3.7) is a sum over peaks representing the different lead levels. However, compared to standard closed systems, where the peaks are sharp delta peaks, these peaks are *broadened* by the Lindblad driving terms into *Lorentz peaks* with a width defined by the driving strength γ_q.

A simplified example of how the level-spacing δ_q and the overall driving strength γ_q influence the hybridization is given in figure IV.3: For a single thermal lead with finite temperature T and hybridization $\Gamma(\omega) = -\mathrm{Im}(\Delta^R(\omega)) = \Gamma\Theta(D - |\omega|)$ it shows the comparison of the continuous hybridization to the corresponding LDDL result. The continuous hybridization is shown in black in all three panels. In addition to $\Gamma(\omega)$ given in the upper part one also needs to consider the Keldysh component given in the lower part. For the continuous lead the Keldysh component is known via the fluctuation-dissipation theorem, see equation (II.2.15), and carries the characteristic form of the Fermi function. The red curves illustrate the form of the hybridization resulting from the LDDL approach for different values of δ and γ. For simplicity, the level-spacing is chosen constant, $\delta_q = \delta$, and also γ_q is chosen q-independent, $\gamma_q = \gamma$. In panel (a) the Lindblad driving strength is smaller than the level-spacing such that the discrete Lorentz peaks get visible corresponding to the discreteness of the leads in the LDDL approach. In panel (b) γ is set equal to δ resulting in a broadening of the peaks, which smoothens the discreteness of the peaks. Still, the hybridization function suffers from finite-size effects in the sense, that the broadened function is not equal to the original continuous hybridization. Only in the continuum limit $\delta \to 0$ the original hybridization can be recovered. This is illustrated in panel (c), where the value of $\gamma = \delta$ is smaller than in panel (b), such that the LDDL hybridization gets closer to that of the original continuous lead.

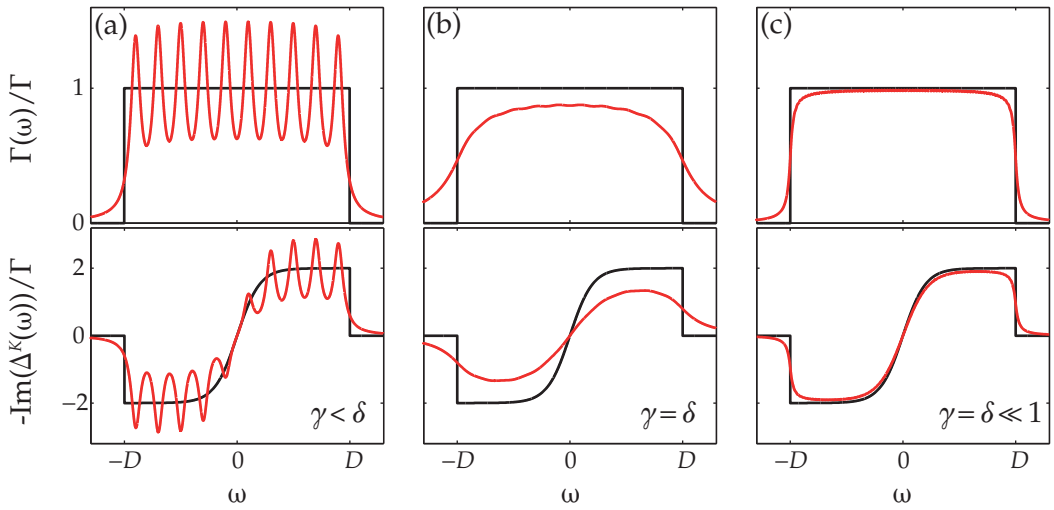

Figure IV.3: Illustration of the hybridization resulting from the Lindblad equation (3.7). The hybridization of a strucureless single thermal lead is shown by the black lines in all three panels. The upper (lower) part of the panels displays the retarded (Keldysh) component of the hybridization. The red curves illustrate the hybridization resulting from the LDDL approach for different values of level-spacing δ and overall Lindblad driving strength γ. In panel (a) γ is smaller than δ such that the discreteness of the lead representation is visible in the form of sharp peaks. In panel (b) γ is equal to δ, such that the peaks are broadened into a smooth curve. However, due to the finite value of δ this smooth function still deviates from the original hybridization. In panel (c) a smaller value of $\gamma = \delta$ is chosen to illustrate that in the continuum limit $\delta \to 0$ the LDDL approach will recover the exact hybridization of the continuous thermal lead.

In summary, one can deduce that one needs

$$\delta_q \lesssim \gamma_q \,. \tag{3.8}$$

At the same time both γ_q and δ_q should be chosen small compared to the physically relevant energy scales. This is immediately clear for the level spacing δ_q. But also γ_q has to be small enough. Otherwise it would smear out the peaks corresponding to the lead level over a range larger than the physically relevant energy scales. A more detailed discussion of the choices for δ_q and γ_q and the hybridization of LDDL is given in publication [P1], see chapter V.

IV.3.3 Local Representation

In the LDDL approach the leads are represented by a finite number of lead levels q coupled to one of the impurity levels with couplings v_q, and a Lindblad driving is used to keep the occupation of the leads at a fixed distribution despite a finite current through the impurity. In this original *star geometry*, the Lindblad driving is *local* in the sense that the Lindblad driving terms do not connect different lead levels directly, see equation (3.7). However, when going over to a *chain geometry* in which the Hamiltonian is local, as discussed in section II.2.3, the Lindblad driving is highly nonlocal rendering MPS based treatments of the Lindblad equation numerically costly. This can immediately be seen from the unitary transformation U, which maps the Hamiltonian onto a chain. Transforming the Lindblad matrices $\Lambda^{(1)}$ and $\Lambda^{(2)}$, the definition of which is given in equation (3.1), according to U, the two matrices, which were diagonal in equation (3.7), acquire a non-diagonal form. The two geometries are depicted in figure IV.4(a).

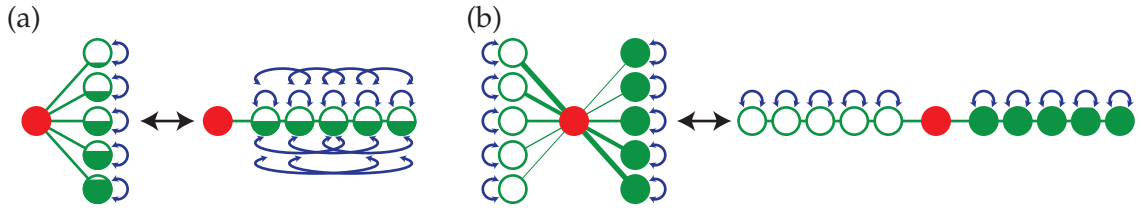

Figure IV.4: (a) In the star geometry the occupation follows a Fermi distribution and the Lindblad driving acts locally. However, when going to the chain geometry, the Lindblad driving is highly non-local. (b) In the new representation each original lead level is replaced by one "hole" and one "particle". The information on the Fermi function is shifted into the couplings to the impurity, $\tilde{v}_{q\eta}$. Because all "holes" ("particles") are driven towards the same occupancy, the Lindblad driving can be chosen such that it *remains local* when going into the chain geometry with separated channels for "holes" and "particles".

In the publication [P1] it is shown that this problem can be overcome by using twice as many lead levels, thereby introducing an additional index $\eta \in \{1,2\}$. Half of the levels ($\eta = 1$) are driven towards occupancy zero, and half of the levels ($\eta = 2$) towards occupancy one,

$$\tilde{\Lambda}^{(1,2)}_{q\eta,q'\eta'} = \delta_{qq'}\delta_{\eta\eta'}\tilde{\lambda}^{(1,2)}_{q\eta} \quad \text{with} \quad \tilde{\lambda}^{(1)}_{q\eta} = \delta_{\eta 1}\gamma_q \quad \text{and} \quad \tilde{\lambda}^{(2)}_{q\eta} = \delta_{\eta 2}\gamma_q. \tag{3.9}$$

This driving does not depend on the Fermi function anymore. Instead, the dependence on

temperature and voltage is shifted into the couplings to the impurity,

$$\tilde{v}_{q,\eta=1} = v_q\sqrt{1-f_\alpha(\varepsilon_q)}, \quad \tilde{v}_{q,\eta=2} = v_q\sqrt{f_\alpha(\varepsilon_q)}. \tag{3.10}$$

This reformulation can be understood as a replacement of each single lead level by one *"hole"*, coupling to the impurity with weight $(1-f_\alpha(\varepsilon_q))$ and driven towards occupancy zero, and one *"particle"*, coupling to the impurity with weight $f_\alpha(\varepsilon_q)$ and driven towards occupancy one.

Why this picture of "holes" and "particles" represents the same physics as the original model can easily be understood in terms of the hybridization: The retarded component is split into

$$\begin{aligned} \Gamma_\alpha(\omega) &= \sum_{\eta\in\{1,2\}} \Gamma_{\alpha\eta}(\omega)\,, \\ \Gamma_{\alpha,1}(\omega) = \Gamma_\alpha(\omega)\,(1-f_\alpha(\omega))\,, &\quad \Gamma_{\alpha,2}(\omega) = \Gamma_\alpha(\omega) f_\alpha(\omega)\,. \end{aligned} \tag{3.11}$$

For a thermal lead, the Keldysh component of the hybridization function has to fulfill the fluctuation-dissipation theorem, compare equation (II.2.15),

$$\begin{aligned} \Delta^K_\alpha(\omega) &= -2\mathrm{i}(1-2f_\alpha(\omega))\Gamma_\alpha(\omega)\,, \\ \Delta^K_{\alpha\eta}(\omega) &= -2\mathrm{i}\left(1-2n_\eta(\omega)\right)\Gamma_{\alpha\eta}(\omega)\,, \end{aligned} \tag{3.12}$$

with $n_\eta(\omega)$ the occupation statistics of "holes" and "particles" in the thermal state. The hybridization function is an additive quantity, so the statistics $n_\eta(\omega)$ have to be chosen such that

$$\Delta^K_\alpha(\omega) = \sum_\eta \Delta^K_{\alpha\eta}(\omega)\,. \tag{3.13}$$

This is fulfilled for an arbitrary Fermi distribution $f_\alpha(\omega)$ if

$$n_1(\omega) = 0 \quad \text{and} \quad n_2(\omega) = 1 \tag{3.14}$$

for all values of ω. Therefore, instead of driving the original level towards an occupation of $f_\alpha(\varepsilon_q)$, we can instead drive the corresponding "hole" and "particle" towards occupation $n_1(\varepsilon_q) = 0$ and $n_2(\varepsilon_q) = 1$.

When choosing γ_q to be q-independent, the Lindblad matrices of this new representation, $\tilde{\Lambda}^{(1,2)}$, considered for each η independently are not only diagonal but even proportional to the identity matrix. Therefore, the Lindblad driving is local in the star geometry and *remains local* under the unitary transformation which maps the Hamiltonian onto the chain geometry, as long as this mapping is performed for "holes" and "particles" independently. Star and chain geometry of this new local setup are sketched in figure IV.4(b).

Note that from a numerical point of view the doubling of lead levels is not as expensive as it seems at first glance due to two reasons: Firstly, many of the new levels will immediately decouple from the model. For very low energies, where the Fermi distribution is equal to one, the "holes" decouple from the impurity due to $\tilde{v}^2_{q,\eta=1} \propto (1-f_\alpha(\varepsilon_q))$, compare equation (3.10). Analogously, for high energies, where the Fermi function is equal to zero, the "particles" decouple due to $\tilde{v}^2_{q,\eta=2} \propto f_\alpha(\varepsilon_q)$. In other words, the doubling of lead levels is only needed where $f_\alpha(\omega) \notin \{0,1\}$. Secondly, in case that two leads with different Fermi

functions $f_L(\omega) \neq f_R(\omega)$ couple to the *same* impurity site, a further simplification becomes possible. While in the original setup the two leads have to be treated independently, the "holes" and "particles" of the two leads in the local representation are subject to the *same Lindblad driving*. This makes it possible, that the "holes" ("particles") of left and right lead corresponding to the same energy ε_k are combined into a single mode

$$\tilde{c}^{(+)}_{k\eta,(\sigma)} \propto \tilde{v}_{Lk\eta,(\sigma)}\tilde{c}_{Lk\eta,(\sigma)} + \tilde{v}_{Rk\eta,(\sigma)}\tilde{c}_{Rk\eta,(\sigma)}. \tag{3.15}$$

The corresponding orthogonal mode $\tilde{c}^{(-)}_{k\eta,(\sigma)}$ decouples from the model. A more detailed discussion on the local representation and the decoupling of modes is given in the paper [P1] in chapter VII.

IV.3.4 Comparison to the First Approach

In section IV.2 we deduced the LDDL Lindblad equation by explicitly integrating out continuous baths, while in section IV.3.2 we started from a Lindblad equation to show for which parameters we regain the correct hybridization function. As is to be expected the two formulations are consistent to a great extent. They both find a Lindblad equation of the form of equation (3.7). But while in the explicit derivation of section IV.2 one obtains

$$\gamma_k = \mathrm{Im}\left(\frac{|v_k|^2}{-\mathrm{i}\Gamma}\right) = \frac{\delta_k}{\pi}, \tag{3.16}$$

the formal approach demands

$$\gamma_k \gtrsim \delta_k. \tag{3.17}$$

In other words, they both find that γ_k scales with the size of the corresponding interval, δ_k. But the formal approach shows that a better convergence to the correct hybridization can be obtained with a stronger smoothening $\gamma_k > \delta_k$, as long as one is still able to choose γ_k small compared to the physically relevant energy scales. Both of the approaches, however, agree that the there is no further dependence of γ_k on other parameters.

IV.3.5 Connection to Purification

The *doubling* of lead levels in the local Lindblad representation introduced in section IV.3.3 is strongly connected to the concept of purification discussed in section III.4. Also in purification the lead levels are doubled. In the latter case this is done to represent a density matrix in the form of an MPS by introducing auxiliary modes next to the physical ones. Within the thermofield approach presented in chapter VI it can be shown that with a simple rotation in the state space of physical and auxiliary levels the purification procedure for a noninteracting thermal lead arrives *exactly* at the picture of "holes" and "particles" used for the local form of our LDDL Lindblad equation. In this sense, the doubling of lead levels introduced in section IV.3.3 to obtain a local chain representation is identical to the thermofield approach.

However, there is one striking point: in purification the doubling of lead levels is undone when recovering the density matrix via a trace over the auxiliary state space, see equation (III.4.4). In contrast, the density matrix ρ in the local representation of our LDDL scheme truly lives in the enlarged Hilbert space. The connection can be explained as follows.

Starting from an impurity model one can purify the leads,

$$\rho = \rho_{\text{imp}} \otimes \rho_{\text{lead}} = \rho_{\text{imp}} \otimes \text{Tr}_{\text{aux}} \left(|\Omega\rangle \langle\Omega| \right) . \tag{3.18}$$

The physics of the impurity does not change if one simply drops the trace over the auxiliary levels,

$$\tilde{\rho} = \rho_{\text{imp}} \otimes |\Omega\rangle \langle\Omega| = \rho_{\text{imp}} \otimes \rho_{\text{lead+aux}}. \tag{3.19}$$

When calculating expectation values of physical operators (which by definition do not act on the auxiliary lead levels), the trace over the auxiliary state space is performed in a natural way,

$$\langle A \rangle = \text{Tr}_{\text{imp+lead+aux}} \left(\tilde{\rho} A \right) = \text{Tr}_{\text{imp+lead}} \left(\rho A \right) . \tag{3.20}$$

The density matrix $\rho_{\text{lead+aux}}$ lives in an enlarged Hilbert space and corresponds to the density matrix used in the LDDL approach. In that sense the representation of the leads in the LDDL setup is in complete analogy to the thermofield approach.

Finally, note that for closed systems it is possible to write down a simple time evolution for $X(t)$ such that the correct time evolution for the density matrix $\rho(t) = X(t)X^\dagger(t)$ is reproduced, see equation (III.4.2). In many purification procedures one therefore works with a description of the operator $X(t)$ only. In the presence of dissipative Lindblad terms, there is, in general, no such simple time evolution for $X(t)$. Instead one has to consider the full density matrix. However, if one is still interested in exploiting the form $\rho(t) = X(t)X^\dagger(t)$ to ensure positivity of the density matrix in MPS calculations despite of truncation errors, one can describe $\rho(t)$ in a "locally purified form", see reference [72].

IV.4 Lindblad-Driven Discretized Leads – An Open Wilson Chain Approach

In section II.2.3 we have argued that within the open Wilson chain construction [P3] it is possible to keep track of the continuous modes that are neglected when discretizing a continuous lead into a finite chain representation. In the resulting geometry each chain site n couples to an additional continuous bath of "fast modes", $\Delta_n^{\text{FM}}(\omega)$, see figure II.4(c). This seems to be a perfect starting point to derive a suitable Lindblad driving for a Wilson chain. One would hope to find a Lindblad equation which is local on the MPS chain while still avoiding the doubling of lead levels introduced in IV.3.3. However, two immediate difficulties arise:

When integrating out the continuous fast mode bath of site n a naive approach would be to neglect the couplings of site n to its neighboring sites. In this case, the derivation of the Lindblad driving terms would be in complete analogy to the calculation for a single level in section IV.1.2. This, however, is not necessarily a well-defined assumption since the couplings to the neighboring sites and to the fast mode bath by construction all live on the same energy scale. On the other hand, when taking into account the couplings between the different sites, the Lindblad driving resulting from the fast modes of site n will essentially act on *all* chain sites. Such a nonlocal Lindblad driving will be difficult to treat within MPS calculations.

The second point one should keep in mind is the structure of the fast modes. Let us illustrate this for a particle-hole symmetric model. For such a model all on-site energies are zero, $\chi_n = 0$. On the other hand, the fast mode bath represents the high energy modes of the bath $\Delta_n(\omega)$, compare section II.2.3. Therefore, its hybridization function is *by definition* only non-zero for the high frequencies. When deriving a Lindblad driving naively, neglecting the coupling to the neighboring chain sites and following the calculation in section IV.1.2, the strength of the Lindblad driving would be zero due to $\gamma_n \propto \Gamma_n^{\mathrm{FM}}(\omega = \chi_n = 0) = 0$. Apparently, the approximations made are too crude. In particular, the description of a bath using Lindblad driving terms is not ideally suited for baths with a strong ω-dependence.

So, while the idea of deriving a Lindblad driving from the fast mode baths is still very appealing, a less naive approach would have to be found.

IV.5 Solving Lindblad Equations based on MPS

Section IV.3 showed how to construct a Lindblad equation for thermal leads in an impurity model in such a way that the Lindblad driving and the Hamiltonian dynamics are local on the underlying MPS chain. This seems to be an ideal starting point for the evaluation of nonequilibrium based on MPS. However, finding the steady state of such a Lindblad equation in an MPS language is highly nontrivial because one has to work with the full density matrix and therefore on the level of *operators*. During the last few years, the solution of Lindblad equations based on MPS has been a topic of great interest. To close this chapter, this section summarizes some of the suggestions on how to tackle this problem, without any claim to exhaustiveness.

An intriguing possibility to avoid working on the level of a full density matrix is the *"quantum trajectory approach"*, in which the density matrix is broken down into an ensemble of stochastically created time-dependent states. In the long-time limit, one can deduce the properties of the steady state. If numerically possible, one can also time-evolve the full density matrix towards its steady state. A further interesting idea is to target the steady state directly, i.e., without calculating the transient behavior, by solving $\mathcal{L}\rho = 0$. The following part gives a short overview of these different approaches.

IV.5.1 The Quantum Trajectory Approach

The basic idea of the so-called *"quantum trajectory approach"* [60, 73–78] is to step down from the level of density matrix operators to the level of quantum states at the price of stochastic averaging. To this end one stochastically generates an ensemble of *"quantum trajectories"* $\{|\phi_n(t)\rangle\}$ such that the density matrix

$$\bar{\rho}_S(t) = \frac{1}{N_{\mathrm{T}}} \sum_{n=1}^{N_T} |\phi_n(t)\rangle \langle\phi_n(t)| \tag{5.1}$$

fulfills the Lindblad equation in the limit of an infinite number of trajectories, $N_T \to \infty$.

The Lindblad equation (1.2) can be rewritten in the form

$$\begin{aligned} \frac{\mathrm{d}}{\mathrm{d}t}\rho_S = \mathcal{L}\rho_S &= -\mathrm{i}\,[H_S + H_{\mathrm{Lamb}}, \rho_S] + \frac{1}{2}\sum_y \left(2J_y\,\rho_S J_y^\dagger - \left\{J_y^\dagger J_y, \rho_S\right\}\right) \\ &= -\mathrm{i}\left(H_{\mathrm{eff}}\,\rho_S - H_{\mathrm{eff}}^\dagger\,\rho_S\right) + \sum_y J_y\,\rho_S J_y^\dagger \end{aligned} \tag{5.2}$$

with an effective non-Hermitian Hamiltonian H_{eff},

$$H_{\text{eff}} = H_S + H_{\text{Lamb}} - \mathrm{i}H_{\text{LB}} = H_S + H_{\text{Lamb}} - \tfrac{\mathrm{i}}{2}\sum_y J_y^\dagger J_y. \tag{5.3}$$

This formulation of the Lindbladian $\mathcal{L}$ suggests a division into two parts: the first part of the second line of equation (5.2) resembles a von-Neumann equation with non-Hermitian Hamiltonian H_{eff}. The second part simulates dissipative processes by introducing so-called *"quantum jumps"*. The different trajectories in the ensemble in equation (5.1) are calculated from a time evolution which is a stochastic combination of these two components, as described in the following.

Effective time evolution

If no quantum jump occurs the trajectory evolves according to

$$|\phi_n(t+\delta t)\rangle = \mathrm{e}^{-\mathrm{i}H_{\text{eff}}\delta t}\,|\phi_n(t)\rangle\,.$$

Due to the non-Hermiticity of H_{eff} the norm of $|\phi_n(t)\rangle$ decreases. For a small time step δt this decrease of the norm squared is given by

$$\begin{aligned}\delta\mathcal{N} &= \langle\phi_n(t+\delta t)|\phi_n(t+\delta t)\rangle - \langle\phi_n(t)|\phi_n(t)\rangle \\ &= \langle\phi_n(t)|\left(1+\mathrm{i}H_{\text{eff}}^\dagger\delta t\right)\left(1-\mathrm{i}H_{\text{eff}}\delta t\right)|\phi_n(t)\rangle - \langle\phi_n(t)|\phi_n(t)\rangle \\ &= \mathrm{i}\delta t\,\langle\phi_n(t)|\left(H_{\text{eff}}^\dagger - H_{\text{eff}}\right)|\phi_n(t)\rangle = -\delta t\,\langle\phi_n(t)|\sum_y J_y^\dagger J_y|\phi_n(t)\rangle\,.\end{aligned} \tag{5.4}$$

This decrease reflects the fact that so far the last term in equation (5.2) has not been considered. In this sense, $\delta\mathcal{N}$ is a measure for the probability of a jump to occur. After the small time step, the state is re-normalized to one.

Quantum jump

If a quantum jump of type y occurs, the trajectory changes to

$$|\phi_n(t+\delta t)\rangle = \frac{J_y\,|\phi_n(t)\rangle}{\sqrt{\langle\phi_n(t)|\,J_y^\dagger J_y|\phi_n(t)\rangle}}\,. \tag{5.5}$$

The probabilities of the different jumps are given by

$$\delta p_y(t) = \delta t\langle\phi_n(t)|\,J_y^\dagger J_y|\phi_n(t)\rangle\,. \tag{5.6}$$

The total probability for one of the jumps can be linked to the norm decrease during the effective time evolution

$$\delta p = \sum_y \delta t\langle\phi_n(t)|\,J_y^\dagger J_y|\phi_n(t)\rangle = -\delta\mathcal{N}. \tag{5.7}$$

Mean density matrix

In the limit of $N_T \to \infty$, this yields for the density matrix $\bar{\rho}(t)$, constructed as given in equation (5.1), [75]:

$$\begin{aligned}\bar{\rho}(t+\delta t) &= \frac{1}{N_T}\sum_n \left(\left(1 - \sum_y \delta p_y(t)\right) \frac{\mathrm{e}^{-\mathrm{i}H_{\mathrm{eff}}\delta t}\,|\phi_n(t)\rangle\,\langle\phi_n(t)|\,\mathrm{e}^{\mathrm{i}H_{\mathrm{eff}}^\dagger \delta t}}{1+\delta\mathcal{N}} \right. \\ &\qquad \left. + \sum_y \delta p_y(t) \frac{J_y\,|\phi(t)\rangle\,\langle\phi(t)|\,J_y^\dagger}{\langle\phi_n(t)|J_y^\dagger J_y|\phi_n(t)\rangle} \right) \\ &= \frac{1}{N_T}\sum_n \left((1-\mathrm{i}H_{\mathrm{eff}}\delta t)\,|\phi_n(t)\rangle\,\langle\phi_n(t)|\left(1+\mathrm{i}H_{\mathrm{eff}}^\dagger\delta t\right) + \delta t \sum_y J_y\,|\phi_n(t)\rangle\,\langle\phi_n(t)|\,J_y^\dagger \right) \\ &= \bar{\rho}(t) - \mathrm{i}\delta t\left(H_{\mathrm{eff}}\,\bar{\rho}(t) - \bar{\rho}(t)H_{\mathrm{eff}}^\dagger\right) + \delta t\sum_y J_y\,\bar{\rho}(t)J_y^\dagger\end{aligned}$$

$$\Rightarrow \frac{\delta\bar{\rho}(t)}{\delta t} = -\mathrm{i}\left(H_{\mathrm{eff}}\,\bar{\rho}(t) - \bar{\rho}(t)H_{\mathrm{eff}}^\dagger\right) + \sum_y J_y\,\bar{\rho}(t)J_y^\dagger. \tag{5.8}$$

The mean density matrix $\bar{\rho}$ therefore fulfills the Lindblad equation (5.2).

If one is interested in the expectation value of an operator A only, the mean density matrix does not need to be constructed explicitly. Instead one can average over the expectation values belonging to the different trajectories,

$$\langle A(t)\rangle = \mathrm{Tr}\left(A\rho(t)\right) = \frac{1}{N_T}\sum_{n=1}^{N_T}\langle\phi_n(t)|A|\phi_n(t)\rangle\ . \tag{5.9}$$

Assuming that the steady state is unambiguous, the initial state for the time evolution of the trajectories, in principle, is arbitrary. For any initial state, the density matrix should approach the steady state in the infinite-time limit. However, a reasonably chosen initial state could shorten the transient behavior.

Note that this stochastic *unraveling* of the Lindblad equation is not unique. In particular, the discrete jumps can be avoided based on *"quantum state diffusion"* [79].

IV.5.2 Time-Evolving the Density Matrix

Perhaps most straightforward is the approach followed e.g. in reference [29], in which the density matrix is simply evolved in time according to the Lindblad equation until one reaches the steady state. Again, provided that the steady state is unambiguous, the initial state, in principle, is arbitrary.

Superfermionic representation

To be able to employ standard MPS time evolution schemes one can use a superfermionic representation [66] which "purifies" the density matrix into an MPS form. As in standard purifications schemes, the Hilbert space represented by the states $\{|n\rangle\}$ is doubled using an additional copy of the Hilbert space represented by the states $\{|\tilde{n}\rangle\}$. However, while for a closed quantum system we introduced the purification of the operator X for which $\rho = XX^\dagger$, compare equation (III.4.3b), for a Lindbladian system one has to consider the full density

matrix. In the superfermionic representation it is given by

$$|\rho(t)\rangle = \rho(t)\,|I\rangle = \sum_{m\tilde{n}} \rho_{mn}(t)\,|m\rangle \otimes |\tilde{n}\rangle\,, \tag{5.10}$$

with the matrix elements $\rho_{mn}(t) = \langle m|\,\rho(t)|n\rangle$. Any expectation value can be calculated using

$$\langle A(t)\rangle = \langle I|A|\,\rho(t)\rangle \tag{5.11}$$

with $|I\rangle = \sum_n |n\rangle \otimes |\tilde{n}\rangle$. The Lindblad equation is recast in the form [66]

$$\mathrm{i}\frac{\mathrm{d}}{\mathrm{d}t}\,|\rho(t)\rangle = \mathcal{L}\,|\rho(t)\rangle \tag{5.12}$$

with a superfermionic Lindbladian $\mathcal{L}$.

A positive approach

Due to truncation errors it is, in general, possible that in this scheme the density matrix does not preserve its positivity. However, it has been shown [72] that this can be overcome using a "locally purified form"

$$\rho(t) = X(t)X(t)^\dagger \tag{5.13}$$

during the above time evolution such that ρ is a positive operator at any time t.

IV.5.3 Directly Targeting the Steady-State

In principle, it is possible that the characterization of the transient behavior requires larger bond dimensions than the steady state itself. The description of these intermediate times can be avoided by targeting the steady state directly. To this end, one searches for a state ρ_{NESS} for which

$$\mathcal{L}\rho_{\mathrm{NESS}} = 0. \tag{5.14}$$

This can be done in two ways:

Minimizing $\mathcal{L}^\dagger\mathcal{L}$: The operator $\mathcal{L}$ in equation (5.14) is non-Hermitian. However, the operator $\mathcal{L}^\dagger\mathcal{L}$ is Hermitian, and in particular it is even semi-positive such that the steady state ρ_{NESS} is given by the groundstate of this operator. This state ρ_{NESS} can therefore be found in analogy to a standard DMRG ground state search as shown in [80].

Targeting $\mathcal{L}\rho = 0$: As an alternative to the groundstate search of $\mathcal{L}^\dagger\mathcal{L}$, it is also possible to determine the null eigenvector of the operator $\mathcal{L}$ variationally [81]. This can be performed, e.g., with the help of the shift-and-invert Arnoldi method, which allows targeting a state with a specific eigenvalue.

V Lindblad-Driven Discretized Leads – Publication

The following article I published together with M. Goldstein, A. Dorda, E. Arrigoni, A. Weichselbaum and J. von Delft. A. Weichselbaum and J. von Delft were important advisors during the whole project. M. Goldstein supported me in the analytic calculations leading to the equations (17) and (25). A. Dorda and E. Arrigoni provided the more formal derivation of the fermionic quantum regression theorem in the appendix, compared to the more illustrative understanding given in IV.1.2. Furthermore, they gave the first hint that it is possible to bring the Lindblad driving into the local form by doubling the number of lead levels.

Lindblad-driven discretized leads for nonequilibrium steady-state transport in quantum impurity models: Recovering the continuum limit

F. Schwarz,[1] M. Goldstein,[2] A. Dorda,[3] E. Arrigoni,[3] A. Weichselbaum,[1] and J. von Delft[1,*]

[1]*Physics Department, Arnold Sommerfeld Center for Theoretical Physics, and Center for NanoScience, Ludwig-Maximilians-Universität, Theresienstraße 37, 80333 München, Germany*

[2]*Raymond and Beverly Sackler School of Physics and Astronomy, Tel Aviv University, Tel Aviv 6997801, Israel*

[3]*Institute of Theoretical and Computational Physics, Graz University of Technology, 8010 Graz, Austria*

(Received 13 April 2016; revised manuscript received 19 September 2016; published 27 October 2016)

The description of interacting quantum impurity models in steady-state nonequilibrium is an open challenge for computational many-particle methods: the numerical requirement of using a finite number of lead levels and the physical requirement of describing a truly open quantum system are seemingly incompatible. One possibility to bridge this gap is the use of Lindblad-driven discretized leads (LDDL): one couples auxiliary continuous reservoirs to the discretized lead levels and represents these additional reservoirs by Lindblad terms in the Liouville equation. For quadratic models governed by Lindbladian dynamics, we present an elementary approach for obtaining correlation functions analytically. In a second part, we use this approach to explicitly discuss the conditions under which the continuum limit of the LDDL approach recovers the correct representation of thermal reservoirs. As an analytically solvable example, the nonequilibrium resonant level model is studied in greater detail. Lastly, we present ideas towards a numerical evaluation of the suggested Lindblad equation for interacting impurities based on matrix product states. In particular, we present a reformulation of the Lindblad equation, which has the useful property that the leads can be mapped onto a chain where both the Hamiltonian dynamics and the Lindblad driving are local at the same time. Moreover, we discuss the possibility to combine the Lindblad approach with a logarithmic discretization needed for the exploration of exponentially small energy scales.

DOI: 10.1103/PhysRevB.94.155142

I. INTRODUCTION

Quantum impurity models describe discrete local quantum degrees of freedom coupled to continuous baths of excitations. They were originally introduced for the description of magnetic impurities in metals, but in the last two decades became highly relevant also for describing transport through quantum dots or nanotubes coupled to metallic leads. While some notable impurity models are integrable, others are not; hence our interest here will be directed towards nonperturbative numerical many-body methods. In experimental work on such systems it is routine to measure the nonlinear current-voltage characteristics. However, numerically calculating such steady-state nonequilibrium properties is a difficult computational problem that is by no means routine. Despite much effort and noteworthy progress for some benchmark problems such as the interacting resonant level model, the Kondo model and the single-level Anderson impurity model [1–7], the theoretical description of steady-state nonequilibrium can still be regarded as a major open challenge for computational treatments of quantum impurity models.

The two key ingredients, local interactions and steady-state transport, in computational practice lead to a set of requirements that are hard to reconcile. (i) The presence of *interactions* means that the models of interest are not quadratic; hence their treatment requires many-body methods. (ii) These methods should be able to reach very *low energy scales* since quantum impurity models often show interesting many-body correlations below a characteristic, exponentially small low-energy scale (e.g., the Kondo temperature for the Kondo or Anderson models). (iii) Steady-state transport means that charge flows at a constant rate in at one side and out on the other. Describing this properly requires dealing with a truly *open* quantum system.

For equilibrium situations, where (iii) is not relevant, two powerful approaches based on matrix product states (MPS) are available, which both use a discretized description of the leads, formulated in terms of one-dimensional chains of finite length. The first is Wilson's numerical renormalization group (NRG) [8,9]. It fulfils the requirement (i) as it is based on an iterative diagonalization of the full many-body Hamiltonian, and it complies with condition (ii) by discretizing the leads on a logarithmic grid capable of resolving exponentially small energy scales. The second method is the density matrix renormalization group (DMRG), which can be used also in situations where a logarithmic discretization is not advisable, albeit at the cost of requiring very long chains to resolve small energy scales. However, both these approaches treat the impurity plus discretized leads as a truly *closed* quantum system and, hence, are fundamentally limited in dealing with the open-system requirement (iii) [10]. Although there are ideas on how to extend the use of NRG to situations of steady-state nonequilibrium [4] and although progress has been made using time-dependent DMRG (tDMRG) approaches [1–3], it would be highly desirable to have a versatile strategy based on MPS methodology that intrinsically overcomes the discrepancy between the numerical need to discretize the leads on the one hand and the requirement of a truly open quantum system on the other hand.

During the last few years, a new scheme has been put forth [11–22] to address this discrepancy. Its main idea is

*Corresponding author: vondelft@lmu.de

to introduce additional continuous reservoirs coupled to the discretized leads to render the system truly open again. Since these additional reservoirs are then described using Lindblad operators, we will call the approach *Lindblad-driven discretized leads* (LDDL). Consider an arbitrary impurity and noninteracting leads enumerated by a lead index α. In the thermodynamic limit, lead α is continuous in energy. This may be coarse-grained in energy using discrete levels q, such that each level q now represents an entire energy interval. The continuum limit will be recovered if each level q is coupled to the remainder of the states in the energy interval it represents, which thus serves as an environmental reservoir for it. Now, for the description of steady-state nonequilibrium physics, one has to ensure that each discretized lead α is held at a fixed temperature T_α and at a fixed chemical potential μ_α. In the LDDL scheme, this is achieved by embedding the system S consisting of impurity and discretized lead levels q into an environment R. This environment consists of one reservoir $\mathcal{R}_q$ for each discrete lead level q, to be associated with the above-mentioned continuum of levels which that level represents, and is described by Lindblad driving terms in the Liouville equation for the density matrix of the subsystem S. The driving rates involved in these Lindblad terms have to be chosen such that the occupation numbers for the lead levels are driven towards the values that they would have if the leads were decoupled from the impurity, namely $f_\alpha(\varepsilon_q)$, where $f_\alpha(\omega)$ is the Fermi distribution characterizing lead α, and ε_q the energy associated with lead level q.

The initial publications utilizing the LDDL scheme presented various pieces of evidence that it offers a viable way for describing nonequilibrium steady-state transport in quantum impurity models. References [12–16] used it as a starting point for analytical methods like perturbative and mean-field approaches or the coupled cluster method in superoperator representations. In these models, the driving rates occurring in the Lindblad equation were viewed as phenomenological parameters, and we adopt the same point of view here. We note, though, that it should be possible to formally derive these driving rates using the reaction coordinate method [23–25]. In Refs. [17–19] the LDDL Lindblad equation was evaluated based on a method established in Ref. [26]. More recently, Refs. [20–22] presented an alternative version of the LDDL approach based on a fit procedure for the Lindblad coefficients. Ideas similar to the LDDL approach have also been applied in the context of spin transport in quantum chains [27–30]. Furthermore, in close relation to the LDDL scheme, Refs. [31,32] suggest the use of discrete modes coupled to a continuum bath to explore analogues of quantum transport in experimental devices that actually have a reduced number of degrees of freedom.

The LDDL approach relies on a decomposition of the bath into a discrete part coupled to the impurity in which many-body effects can be considered, and a continuous remainder which reduces finite-size effects. The same idea also forms the basis of the embedded-cluster approximation [33–35].

Our own long-term interests lie in using the LDDL scheme as starting point for numerical computations that seek to solve the Liouville equation for the many-body density matrix of the system S using MPS methods. Compared to standard equilibrium calculations, where one deals with many-body quantum states, solving the Liouville equation would involve calculating many-body density matrices, and hence be computationally more demanding. Nevertheless, we believe this to be worth the additional effort, because of the direct, explicit way in which the LDDL scheme addresses the open-system requirement (iii). Moreover, there has been much recent progress in MPS-based approaches for solving Liouville equations describing open quantum systems [27,36–43], some of which seem directly suitable for tackling the Lindblad equation arising in the LDDL scheme. In particular, already in 2009, transport in spin chains was described using a matrix product operator (MPO) ansatz combined with Lindblad reservoirs [27]. More recently, an LDDL scheme together with MPOs was used to investigate the nonequilibrium properties of an Anderson impurity [22].

In the present paper, which is intended to set the stage for such future MPS-based works, we address three preliminary but important general questions. (i) How should the Lindblad rates in the LDDL scheme be chosen in order to properly recover the continuum limit? (ii) Is it possible to formulate the Lindblad driving terms in such a way that they remain local when the leads are mapped to chains with local Hamiltonian dynamics? (iii) Can the LDDL scheme be used in conjunction with the logarithmic discretization of lead states needed for the exploration of exponentially small energy scales? Questions (i) and (ii) can actually be addressed fully in the context of purely noninteracting quantum impurity models. The reason is that for any quantum impurity model, with or without local interactions, the lead properties needed to specify the steady-state dynamics are *fully* encoded in the *bare* (i.e., with zero lead-impurity coupling) steady-state correlators of that linear combination of lead operators that couples to the impurity.

To answer question (i), it suffices to identify the Lindblad driving conditions that reproduce the bare steady-state correlators known for continuum leads. Our main conclusion in this regard is, perhaps not surprisingly, that the broadening of the discretized levels generated by the Lindblad driving should be such that the resulting level width for each level is comparable to the level spacing to neighboring lead levels. This result is consistent with the conclusions of previous works utilizing the LDDL scheme, in particular in Ref. [12], which also addressed the question of how to recover the continuum limit. Questions (ii) and (iii) have not received much attention previously. We conclude that both can be answered affirmatively, thus opening the door towards treating LDDL systems using MPS-based methods in the near future.

The rest of this paper is organized as follows: first, considering a completely generic quadratic Lindblad equation (Sec. II), we present a simple derivation of analytical formulas for the system's steady-state correlators. This reproduces results found previously using rather more elaborate methods involving superoperators [20,21]. The derivation offered here is so elementary that we believe it to be of general interest (also beyond the context of quantum impurity models). Second, we use these results to obtain analytical expressions for the steady-state lead correlators. These allow us to identify the choice of Lindblad parameters that ensures that the leads within the LDDL scheme become equivalent to thermal reservoirs in the continuum limit, thus answering question (i) (Secs. III B and III C). As an explicit example of a noninteracting impurity

model, where the full Liouville equation can be solved analytically, we study the nonequilibrium resonant level model (RLM) in some detail (Secs. III D and III E). The results obtained by our elementary treatment are consistent with the ones obtained previously for this model using the superoperator formalism [12] and instructively illustrate under what conditions the continuum limit is recovered. Sections IV and V are devoted to questions (ii) and (iii) regarding local Lindblad driving and logarithmic discretization, respectively. Section VI summarizes our conclusions. Finally, Appendix A discusses some details arising in the context of logarithmic discretization, and in Appendix B, a fermionic version of the quantum regression theorem is derived.

II. GREEN'S FUNCTIONS IN THE LINDBLAD APPROACH

In this section, we introduce Green's functions for systems that evolve in time under Lindbladian dynamics. For quadratic systems, we derive closed expressions for the steady-state Green's functions. This section, therefore, is not restricted to impurity models, but the formulas derived for quadratic models lay the foundation for an analytical exploration of the LDDL scheme presented in Secs. III–V.

A. The Lindblad equation

Consider a system S linearly coupled to a large reservoir R which together form a closed quantum system with Hamiltonian dynamics described by the full Hamiltonian of system and reservoir, H_{full}. Equal-time expectation values are defined by

$$\langle A(t)\rangle = \mathrm{tr}_{S,R}(A(t)\,\rho_{\text{full}}) = \mathrm{tr}_{S,R}(A\,\rho_{\text{full}}(t)), \tag{1}$$

where A acts on the system S, and the time evolution of $A(t)$ and of the full density matrix $\rho_{\text{full}}(t)$ is given by (with $\hbar = 1$)

$$A(t) = e^{iH_{\text{full}}t}\,A\,e^{-iH_{\text{full}}t}, \tag{2a}$$

$$\rho_{\text{full}}(t) = e^{-iH_{\text{full}}t}\,\rho_{\text{full}}\,e^{iH_{\text{full}}t}. \tag{2b}$$

Two-point correlators for operators A and C acting on S are defined as

$$\langle A(t)C\rangle = \mathrm{tr}_{S,R}(A(t)C\,\rho_{\text{full}}) = \mathrm{tr}_{S,R}(A\,\varrho_{C,\text{full}}(t)), \tag{3a}$$

$$\langle C\,A(t)\rangle = \mathrm{tr}_{S,R}(A(t)\rho_{\text{full}}C) = \mathrm{tr}_{S,R}(A\,\varrho'_{C,\text{full}}(t)), \tag{3b}$$

where the C-dependent auxiliary operators $\varrho_{C,\text{full}}(t)$ and $\varrho'_{C,\text{full}}(t)$ are defined by

$$\varrho_{C,\text{full}}(t=0) = C\rho_{\text{full}}, \quad \varrho'_{C,\text{full}}(t=0) = \rho_{\text{full}}C, \tag{4a}$$

$$\varrho^{(\prime)}_{C,\text{full}}(t) = e^{-iH_{\text{full}}t}\,\varrho^{(\prime)}_{C,\text{full}}\,e^{iH_{\text{full}}t}. \tag{4b}$$

If the reservoir R is Markovian, its degrees of freedom can be traced out using quite general assumptions [44]. The resulting equation for the time evolution of the reduced density matrix of system S, $\rho(t) = \mathrm{tr}_R(\rho_{\text{full}}(t))$, known as Lindblad equation [45,46], can always be written in the form [44,47]

$$\dot\rho(t) = \mathcal{L}\rho(t) = -i[H,\rho(t)] + \mathcal{D}\rho(t), \tag{5a}$$

$$\mathcal{D}\rho(t) = \sum_m (2J_m\rho(t)J_m^\dagger - \{J_m^\dagger J_m,\rho(t)\}). \tag{5b}$$

The unitary operator H describes the Hamiltonian part of the dynamics. It is not necessarily equal to that part of the original full Hamiltonian that acts on system S, but can contain additional Lamb shifts [cf. Eq. (11) below]. $\mathcal{D}\rho(t)$ describes the dissipative part of the time evolution. The so-called Lindblad operators J act on system S and are unconstrained otherwise, e.g., are not normalized. Note that the Lindblad equation is only valid for $t > 0$. By construction, it preserves the positivity and the trace of the density matrix.

B. Steady-state Green's functions for quadratic models

For a system with quadratic Hamiltonian governed by Lindbladian dynamics with linear Lindblad operators, it is possible to find closed expressions for steady-state correlation functions, see Eqs. (17) and (25) below. For example, in Refs. [20,21], they were derived using superoperators. Here, we offer a simple complementary derivation which utilizes only elementary definitions.

Our starting point is a quadratic system S coupled linearly to a quadratic reservoir R. We write the Hamiltonian of system S as

$$H = \sum_{mn} h_{mn} L_m^\dagger L_n, \tag{6}$$

with $\{L_m, L_n^\dagger\} = \delta_{mn}$, $\{L_m, L_n\} = 0$. The operators $L_m^{(\dagger)}$ will act as normalized Lindblad operators later on. Furthermore, in contrast to the operators $J_m^{(\dagger)}$ in Eq. (5), we now distinguish explicitly between annihilation (L_m) and creation operators ($L_m^\dagger$). To fully characterize the system's nonequilibrium steady-state (NESS) physics, we will be interested in the retarded, advanced and Keldysh Green's functions of S in the steady state [48,49], $\mathcal{G}^{R/A/K}(t)$, and their Fourier transforms, $G^{R/A/K}(\omega)$, defined as follows:

$$\mathcal{G}^R_{mn}(t) = -i\,\theta(t)\,\langle\{L_m(t), L_n^\dagger\}\rangle_{\text{NESS}}\,, \tag{7a}$$

$$\mathcal{G}^A_{mn}(t) = i\,\theta(-t)\,\langle\{L_m(t), L_n^\dagger\}\rangle_{\text{NESS}}\,, \tag{7b}$$

$$\mathcal{G}^K_{mn}(t) = -i\,\langle[L_m(t), L_n^\dagger]\rangle_{\text{NESS}}\,, \tag{7c}$$

$$G^{R/A/K}_{mn}(\omega) = \int_{-\infty}^{\infty} dt\, e^{i\omega t}\mathcal{G}^{R/A/K}_{mn}(t), \tag{7d}$$

with $\theta(t)$ the Heaviside step function. Since the steady state is translationally invariant in time, these Green's functions satisfy the relations

$$G^{R/A}(\omega) = G^{A/R\dagger}(\omega), \quad \mathcal{G}^K(t) = -\mathcal{G}^{K\dagger}(-t), \tag{8}$$

where matrix notation is understood.

Formally, these correlators can be evaluated by integrating out the reservoir R, leading to the following expressions:

$$G^R_{\text{exact}}(\omega) = \big(\omega - h - \Sigma^R_{\text{exact}}(\omega)\big)^{-1}, \tag{9a}$$

$$G^K_{\text{exact}}(\omega) = G^R_{\text{exact}}(\omega)\Sigma^K_{\text{exact}}(\omega)G^A_{\text{exact}}(\omega). \tag{9b}$$

These express the effect of R on S fully in terms of the retarded and Keldysh component of the self-energy $\Sigma^{R/K}_{\text{exact}}(\omega)$, in which all information about the reservoir is encoded. While for interacting systems the self-energy will contain additional terms due to the interaction, for quadratic systems $\Sigma^{R/K}_{\text{exact}}(\omega)$

simply describes the hybridization between system S and reservoir R and can therefore be calculated explicitly.

Here, we are interested in the less complete description that results from making Markovian approximations in treating the reservoir and encoding its effects only at the level of a Liouville equation for the system density matrix ρ. For a fully quadratic system, the most general form of the resulting Lindblad equation is

$$\dot{\rho}(t) = -i[\tilde{H},\rho(t)] + \sum_{mn} \Lambda^{(1)}_{mn}(2L_n\rho(t)L^\dagger_m - \{L^\dagger_m L_n,\rho(t)\}) + \sum_{mn} \Lambda^{(2)}_{mn}(2L^\dagger_m\rho(t)L_n - \{L_n L^\dagger_m,\rho(t)\}), \tag{10}$$

where the matrices $\Lambda^{(1,2)}$ are Hermitian and positive. The effective Hamiltonian of the system,

$$\tilde{H} = \sum_{mn} \tilde{h}_{mn} L^\dagger_m L_n = \sum_{mn} \left(h_{mn} + \Delta^{\text{Lamb}}_{mn}\right) L^\dagger_m L_n, \tag{11}$$

contains the Lamb shift Δ^{Lamb} corresponding to an effective shift of the energies of the lead levels due to the traced-out reservoirs.

Let us now look at the time dependence of equal-time expectation values $\langle A(t)\rangle$. Tracing out the reservoir in Eq. (1) yields $\langle A(t)\rangle = \text{tr}_S(A\,\rho(t))$, where the time-evolution of the density matrix $\rho(t) = \text{tr}_R(\rho_{\text{full}}(t))$ of the system S is now given by the Lindblad equation (10). Using Eq. (10) and the cyclicity of the trace, the time-evolution of equal-time expectation values is given by

$$\begin{aligned} i\frac{d}{dt}\langle A(t)\rangle &= \langle [A,\tilde{H}](t)\rangle + i\sum_{mn}\Lambda^{(1)}_{mn}\langle (2L^\dagger_m A L_n - \{A, L^\dagger_m L_n\})(t)\rangle \\ &\quad + i\sum_{mn}\Lambda^{(2)}_{mn}\langle (2L_n A L^\dagger_m - \{A, L_n L^\dagger_m\})(t)\rangle\,, \end{aligned} \tag{12}$$

where each argument t refers to the full operator enclosed in the foregoing brackets.

Next, we turn to correlators of the form (3). Tracing out the reservoir yields $\langle A(t)C\rangle = \text{tr}_S(A\,\varrho_C(t))$ with $\varrho_C(t) = \text{tr}_R(\varrho_{C,\text{full}}(t))$. Although $\varrho_{C,\text{full}}(t)$ and $\rho_{\text{full}}(t)$ have the same Hamiltonian dynamics, the Liouville equation for $\varrho_C(t)$ after tracing out the reservoirs differs by sign factors from that of $\rho(t)$. This is due to the fact that the operator C in Eq. (4a) contains an odd number of fermionic operators, so that the standard version of the quantum regression theorem [44,47], which assumes C to be bosonic, does not apply. The fermionic version of this theorem, proven in Appendix B, leads to the following time evolution for $\varrho_C(t)$:

$$\dot{\varrho}_C(t) = -i[\tilde{H},\varrho_C(t)] + \sum_{mn}\Lambda^{(1)}_{mn}(\zeta\, 2L_n\varrho_C(t)L^\dagger_m - \{L^\dagger_m L_n,\varrho_C(t)\}) + \sum_{mn}\Lambda^{(2)}_{mn}(\zeta\, 2L^\dagger_m\varrho_C(t)L_n - \{L_n L^\dagger_m,\varrho_C(t)\}), \tag{13}$$

with $\zeta = +1(-1)$ if C contains an even (odd) number of fermion operators. Using (13) and the cyclicity of the trace, one obtains the following equation for $t > 0$:

$$\begin{aligned} i\frac{d}{dt}\langle A(t)C\rangle &= \langle [A,\tilde{H}](t)\,C\rangle \\ &\quad + i\sum_{mn}\Lambda^{(1)}_{mn}\langle (\zeta\, 2L^\dagger_m A L_n - \{A, L^\dagger_m L_n\})(t)\,C\rangle \\ &\quad + i\sum_{mn}\Lambda^{(2)}_{mn}\langle (\zeta\, 2L_n A L^\dagger_m - \{A, L_n L^\dagger_m\})(t)\,C\rangle. \end{aligned} \tag{14}$$

Analogously, the time dependence of $\langle CA(t)\rangle$ can be obtained using $\langle CA(t)\rangle = \text{tr}(A\varrho'_C(t))$, where $\varrho'_C = \varrho C$ has the same dynamics as ϱ_C, which is given in Eq. (13).

Starting from Eq. (14) and the analogous equation for $\langle CA(t)\rangle$ it is straightforward to set up the equations of motion for nonequilibrium Green's functions. The definitions (7a)–(7d) hold for the full system with Hamiltonian dynamics before tracing out the reservoir R. Therefore they are valid for positive and negative times t. However, the derivation of the Lindblad equation assumes $t > 0$. Thus we will use it to evaluate $\mathcal{G}^R(t)$ and $\mathcal{G}^K(t)$ only for positive times and then use the general relations (8) to obtain results for negative times.

For the equation of motion of the retarded Green's function (7a), one obtains

$$i\frac{d}{dt}\mathcal{G}^R_{mn}(t) = \delta(t)\delta_{mn} + \sum_k (\tilde{h}_{mk} - i\Lambda^{(+)}_{mk})\mathcal{G}^R_{kn}(t), \tag{15}$$

where we defined

$$\Lambda^{(\pm)} = \Lambda^{(1)} \pm \Lambda^{(2)}. \tag{16}$$

Fourier transforming we obtain as final result in matrix notation:

$$G^R(\omega) = (\omega - \tilde{h} + i\Lambda^{(+)})^{-1}. \tag{17}$$

The equation of motion of $\mathcal{G}^K(t)$ for $t > 0$ is given, via Eq. (14) and the corresponding equation for $\langle CA(t)\rangle$, by

$$i\frac{d}{dt}\mathcal{G}^K(t) = (\tilde{h} - i\Lambda^{(+)})\mathcal{G}^K(t), \quad (t > 0), \tag{18}$$

with the formal solution

$$\mathcal{G}^K(t) = \exp(-i\tilde{h}t - \Lambda^{(+)}t)\mathcal{G}^K(0), \quad (t > 0). \tag{19}$$

For negative times, we use Eq. (8) to obtain

$$\mathcal{G}^K(t) = \mathcal{G}^K(0)\exp(-i\tilde{h}t + \Lambda^{(+)}t), \quad (t < 0). \tag{20}$$

To find an expression for $\mathcal{G}^K(0)$, we rewrite it as

$$\mathcal{G}^K(0) = i\mathbb{1} - 2iP(0), \quad P_{mn}(t) = \langle L_m(t)L^\dagger_n(t)\rangle_{\text{NESS}}\,. \tag{21}$$

Since $P_{mn}(t)$ is an equal-time expectation value, its time evolution is described by Eq. (12). Its time derivative is zero in the steady state because then equal-time expectation values are stationary. This implies

$$0 = i\frac{d}{dt}P(t) = [\tilde{h},P(t)] - i\{\Lambda^{(+)},P(t)\} + 2i\Lambda^{(1)}. \tag{22}$$

Evaluated at $t = 0$, this is equivalent to

$$2\Lambda^{(-)} = [\mathcal{G}^K(0),\tilde{h}] + i\{\Lambda^{(+)},\mathcal{G}^K(0)\}. \tag{23}$$

Equation (23) is an implicit relation for $\mathcal{G}^K(0)$. Calculating the Keldysh Green's function in Fourier space we use Eq. (19) for $t > 0$ and Eq. (20) for $t < 0$:

$$\begin{aligned} G^K(\omega) &= \int_{-\infty}^{\infty} dt\, e^{i\omega t} \mathcal{G}^K(t) \\ &= i(\omega - \tilde{h} + i\Lambda^{(+)})^{-1}\mathcal{G}^K(0) - i\mathcal{G}^K(0)(\omega - \tilde{h} - i\Lambda^{(+)})^{-1} \\ &= i(\omega - \tilde{h} + i\Lambda^{(+)})^{-1}[\mathcal{G}^K(0)(\omega - \tilde{h} - i\Lambda^{(+)}) \\ &\quad - (\omega - \tilde{h} + i\Lambda^{(+)})\mathcal{G}^K(0)](\omega - \tilde{h} - i\Lambda^{(+)})^{-1} \\ &= -i(\omega - \tilde{h} + i\Lambda^{(+)})^{-1} 2\Lambda^{(-)} (\omega - \tilde{h} - i\Lambda^{(+)})^{-1}, \end{aligned} \tag{24}$$

where we made use of Eq. (23) in the last step. Comparing this with our result for the retarded Green's function (17), we get as the final result for the Keldysh Green's function

$$G^K(\omega) = -\, i G^R(\omega)\, 2\Lambda^{(-)}\, G^A(\omega), \tag{25}$$

where we exploited the Hermiticity of $\Lambda^{(+)}$.

Let us now compare the results of the Lindblad approach for $G^R(\omega)$ and $G^K(\omega)$, Eqs. (17) and (25), to those of an exact treatment of the full Hamiltonian dynamics, Eqs. (9a) and (9b). We observe that the retarded and Keldysh components of the self-energy, which in the present context of quadratic models describe the hybridization between system S and reservoir R, are replaced by the Lindblad driving rates:

$$\Sigma^R_{\text{exact}}(\omega) \overset{\text{Lindblad}}{\to} \Delta^{\text{Lamb}} - i\Lambda^{(+)}, \tag{26a}$$

$$\Sigma^K_{\text{exact}}(\omega) \overset{\text{Lindblad}}{\to} -2i\Lambda^{(-)}. \tag{26b}$$

Of course, the matrices $\Lambda^{(\pm)}$ are independent of ω and, therefore, a finite number of Lindblad operators cannot capture the full ω dependence of a continuous self-energy $\Sigma_{\text{exact}}(\omega)$ in general. Nevertheless, for quantum impurity models, it will in fact be possible to capture all relevant information from the reservoirs in terms of suitably chosen Lindblad rates.

In thermal equilibrium, $\Sigma^K_{\text{exact}}(\omega)$ and $\Sigma^R_{\text{exact}}(\omega)$ are linked via the fluctuation-dissipation theorem [49]:

$$\Sigma^K_{\text{exact}}(\omega) = 2i(1 - 2f(\omega))\text{Im}\big(\Sigma^R_{\text{exact}}(\omega)\big), \tag{27}$$

with $f(\omega)$ being the Fermi distribution function. Hence, if the Lindblad reservoirs are used to thermalize a system, the ratio of the two matrices $\Lambda^{(\pm)}$ has to encode the details of the occupation numbers as will be elaborated below, see Eq. (39). Let us stress, however, that due to the fact that a finite number of Lindblad operators cannot describe the full ω-dependence of the self-energy, the fluctuation-dissipation theorem is, in general, not obeyed in the Lindblad approach.

Equations (17) and (25) are the main results of this section. They allow steady-state Green's functions for quadratic models characterized by a Lindblad equation to be calculated by simply evaluating matrix equations. These formulas have been found before [20,21] using a superoperator representation. Our derivation has the instructive feature of using only the basic definitions and relations of a Lindblad system together with the definitions of the Green's functions and their time evolution.

III. A LINDBLAD APPROACH TO IMPURITY MODELS

Let us now turn to impurity models. We consider models which consist of an arbitrary impurity coupled to different noninteracting fermionic leads, labeled by α. For convenience, we will include the spin index into the channel index α. For two spinful channels, for example, $\alpha \in \{L\uparrow, L\downarrow, R\uparrow, R\downarrow\}$, where L and R denote the left and right channels, respectively. Our aim is the correct description of all impurity properties in steady-state nonequilibrium that arises when different leads are held at different but fixed temperatures or chemical potentials. We consider a Lindblad approach suitable for such systems and, using the formulas for Green's functions from the previous section, we will explain in which limits our Lindblad approach reproduces the correct impurity physics. The same Lindblad equation has been suggested and used in Refs. [12–17]. We revisit it here to analyze explicitly in which limits the Lindblad equation reproduces an exact representation of a continuous reservoir, and to gain a deeper understanding of the resulting hybridization. This will be helpful in finding a local setup for MPS-based methods in Sec. IV.

A. Hamiltonian for impurity and leads

The Hamiltonian of system S consisting of an impurity, leads, and impurity-lead-hybridization is given by

$$H = H_{\text{imp}} + H_{\text{lead}} + H_{\text{hyb}}. \tag{28}$$

The impurity Hamiltonian H_{imp} does not contain lead operators, but is otherwise arbitrary. In particular, H_{imp} does not need to be a quadratic Hamiltonian but can contain interactions. H_{lead} represents the noninteracting leads

$$H_{\text{lead}} = \sum_{\alpha k} \varepsilon_{\alpha k} c^\dagger_{\alpha k} c_{\alpha k} = \sum_q \varepsilon_q c^\dagger_q c_q, \tag{29}$$

where $q = \{\alpha, k\}$ is a composite index. If $i = 1, \ldots, M_d$ discrete impurity levels couple linearly to these fermionic leads, the general form of the hybridization between the impurity and the leads is given by

$$H_{\text{hyb}} = \sum_{i=1}^{M_d} \sum_q (v_{iq}\, d^\dagger_i c_q + \text{H.c.}). \tag{30}$$

It is well-known that for quantum impurity models all lead properties relevant for determining the impurity self-energy are encoded in the so-called hybridization function, a matrix of dimension M_d, which for one lead α is given by

$$\Delta^{R/K}_{ij,\alpha}(\omega) = \sum_k v_{iq} v^*_{jq}\, g^{R/K}_{qq}(\omega). \tag{31a}$$

Here, $g^{R/K}_{qq}(\omega)$ is the bare Green's function of lead level q in the *absence* of the coupling to the impurity. For the retarded component it suffices to consider only its imaginary part,

$$\Gamma_{ij,\alpha}(\omega) = -\text{Im}\big(\Delta^R_{ij,\alpha}(\omega)\big), \tag{31b}$$

since its real part can be deduced from the Kramers-Kronig relation. Let us also define the total hybridization

$$\Delta^{R/K}_{ij}(\omega) = \sum_\alpha \Delta^{R/K}_{ij,\alpha}(\omega), \quad \Gamma_{ij}(\omega) = \sum_\alpha \Gamma_{ij,\alpha}(\omega). \tag{32}$$

By definition, quantum impurity models assume continuous leads (CL), i.e., they assume the spectrum of lead excitations ε_q to form a continuum. The bare lead correlators are assumed to describe thermal leads and hence have the well-known form

$$g^R_{qq;\mathrm{CL}}(\omega) = (\omega - \varepsilon_q + i\epsilon)^{-1}, \tag{33a}$$

$$g^K_{qq;\mathrm{CL}}(\omega) = -2i(1 - 2f_\alpha(\omega))\pi\, \delta_\epsilon(\omega - \varepsilon_q). \tag{33b}$$

Here, $f_\alpha(\omega) = [e^{(\omega-\mu_\alpha)/T_\alpha} + 1]^{-1}$ is the Fermi function for decoupled lead α at temperature T_α and chemical potential μ_α. (When the energy argument of the Fermi function is discrete, as in $f_\alpha(\varepsilon_q)$, its index α will be understood to be the same as in $q = \{\alpha,k\}$.) In Eq. (33b), we introduced the abbreviation

$$\delta_\epsilon(\omega - \varepsilon_q) = \frac{\epsilon/\pi}{(\omega - \varepsilon_q)^2 + \epsilon^2}, \tag{34}$$

which we will use henceforth for a normalized Lorentz function of width ϵ. When taking the continuum limit, the order of limits is such that the level spacing is sent to zero first, followed by taking ϵ to zero. Thus, in the above Eqs. (33) and (34), ϵ is an infinitesimal parameter, so that $\delta_\epsilon(\omega - \varepsilon_q)$ becomes a true Dirac delta function.

B. Lindblad equation for impurity models

The goal of the LDDL scheme is to mimic the CL description as well as possible while using a finite number of discrete lead levels. [The index q is thus understood to be discrete within the context of the discrete leads (DL) in the LDDL scheme, and continuous only when referring to CL expressions.] However, a finite number of discrete lead levels is only capable of describing steady-state nonequilibrium if some dissipative dynamics is introduced that ensures that the level occupancies $N_{q;\mathrm{DL}}(t) = \langle c^\dagger_q c_q\rangle$ are driven towards the values $f_\alpha(\varepsilon_q)$ characteristic for the bare, uncoupled leads. The LDDL scheme achieves this by coupling each physical lead level q to one auxiliary reservoir $\mathcal{R}_q$, as depicted in Fig. 1, whose properties are tuned such that the dissipative dynamics

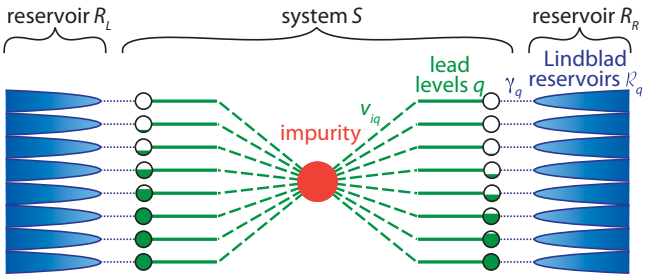

FIG. 1. Schematic depiction of the model for two physical leads $\alpha = \{L,R\}$. Each lead level q couples to the impurity level i with coupling strength v_{iq}. The reservoir $R = R_L + R_R$ consists of one Lindblad reservoir $\mathcal{R}_q$ for each lead level q, whose Lindblad driving rate is chosen such that it tends to drive that level's occupancy towards $f_\alpha(\varepsilon_q)$ (though a small deviation from the latter will be induced by the level-dot coupling, see Sec. III E for details). The value of $f_\alpha(\varepsilon_q)$ is symbolized by the degree of filling of the corresponding open circle. The occupation numbers for the left and right leads differ for a system in nonequilibrium.

of the reservoir-level system (without impurity) drives $N_{q;\mathrm{DL}}(t)$ towards the desired value:

$$\lim_{t\to\infty} N_{q;\mathrm{DL}}(t) = f_\alpha(\varepsilon_q)\,. \tag{35}$$

Technically, we imagine tracing out the auxiliary reservoirs and describing their effects on the discrete levels of the discretized leads using suitably chosen Lindblad terms in a Liouville equation for the system S consisting of impurity plus physical leads. Note that it is not possible to use Lindblad terms to describe the dissipative effects of leads *directly* coupled to the impurity, because this coupling can be strong, so that the leads cannot be treated as a Markovian bath. In contrast, as will become clear later (see Secs. III C and III E), the couplings between the proposed Lindblad reservoirs and the lead levels go to zero in the continuum limit of infinitely many lead levels q. In this case, the approximations made to obtain the Lindblad equation are justified.

We now specify the Lindblad dynamics intended to ensure that the occupation of the lead levels is driven towards the steady-state values of $N_{q;\mathrm{DL}}(t\to\infty) = f_\alpha(\varepsilon_q)$. To this end, we first look at one lead level q without coupling to the impurity ($H_q = \varepsilon_q c^\dagger_q c_q$) but coupled to its Lindblad reservoir $\mathcal{R}_q$. The dissipative terms in the Liouville equation are of the form

$$\begin{aligned}\mathcal{D}\rho(t) = {}&\lambda^{(1)}_q(2c_q\rho(t)c^\dagger_q - \{c^\dagger_q c_q,\rho(t)\})\\ &+ \lambda^{(2)}_q(2c^\dagger_q\rho(t)c_q - \{c_q c^\dagger_q,\rho(t)\}),\end{aligned} \tag{36}$$

where $\lambda^{(1,2)}_q$ is the only entry of the matrix $\Lambda^{(1,2)}$, which in the present context is a 1×1 matrix.

In this case, Eq. (12) (without Lambshift) can be used to determine the time evolution of the occupation number $N_{q;\mathrm{DL}}(t)$:

$$\frac{d}{dt}N_{q;\mathrm{DL}}(t) = 2\lambda^{(2)}_q - 2\big(\lambda^{(1)}_q + \lambda^{(2)}_q\big)N_{q;\mathrm{DL}}(t). \tag{37}$$

The resultant steady-state value of $N_{q;\mathrm{DL}}(t)$ is given by

$$\lim_{t\to\infty} N_{q;\mathrm{DL}}(t) = \frac{\lambda^{(2)}_q}{\lambda^{(1)}_q + \lambda^{(2)}_q}. \tag{38}$$

The requirement in Eq. (35), therefore, leads to

$$\lambda^{(1)}_q = \gamma_q(1 - f_\alpha(\varepsilon_q)) \quad \text{and} \quad \lambda^{(2)}_q = \gamma_q f_\alpha(\varepsilon_q). \tag{39}$$

Here, γ_q is an overall constant on the right-hand side of Eq. (37), showing explicitly that γ_q sets the time scale needed to reach the steady state. The same result has been found previously [12] using a super-fermionic representation. Equation (39) has a structure reminiscent of the fluctuation-dissipation theorem (27), with $\Sigma^{R/K}(\omega)$ replaced by (26) and $f_\alpha(\omega)$ replaced by $f_\alpha(\varepsilon_q)$. This analogy illustrates the limitation of the Lindblad approach due to the finite number of Lindblad operators: while the fluctuation-dissipation theorem contains the full Fermi function $f_\alpha(\omega)$, the Lindblad approach contains only the value at one single frequency, $f_\alpha(\varepsilon_q)$. The fluctuation-dissipation theorem is, therefore, not obeyed by the Lindblad approach in general. Note also that the observation that γ_q sets the relevant time scale in this context is consistent with the fact that γ_q plays the role of a decay rate in the retarded Green's function (17).

This result for a single level serves as motivation for choosing the following Lindblad equation for the full quantum impurity system within the LDDL approach:

$$\begin{aligned}\dot{\rho}(t) = &-i[H,\rho(t)] \\ &+ \sum_q \gamma_q[(1-f_\alpha(\varepsilon_q))(2c_q\rho(t)c_q^\dagger - \{c_q^\dagger c_q,\rho(t)\}) \\ &+ f_\alpha(\varepsilon_q)(2c_q^\dagger\rho(t)c_q - \{c_q c_q^\dagger,\rho(t)\})]. \end{aligned} \tag{40}$$

H is the Hamiltonian of system S, as defined in (28)–(30), and the constants γ_q describe the total strength of the Lindblad driving on the levels q.

The parameters γ_q in Eq. (40) are not yet fixed. In principle, they can be deduced by using the reaction-coordinate method [23–25] to find an effective representation of the decoupled leads in terms of a discrete set of sites, each coupled to its own bath. To this end one divides the support of the hybridization function into different energy intervals, $\Gamma(\omega) = \sum_q \Gamma_q^{(0)}(\omega)$, and uses the reaction coordinate method to replace each of the baths $\Gamma_q^{(0)}(\omega)$ by a new lead level coupled to a new bath $\Gamma_q^{(1)}(\omega)$. One then traces out this new bath and finds the dissipative terms of the Lindblad equation (40), but with derived values of γ_q. These turn out to be proportional to the width (say δ_q) of the energy interval, represented by level q, thus $\gamma_q \sim \delta_q$.

In this paper, we prefer to adopt a more phenomenological point of view, because for a future numerical treatment of the Lindblad setup, it will be useful to be able to treat γ_q as a set of phenomenological parameters. (For example, in Sec. V, we will discuss a logarithmic discretization scheme for which the choice $\gamma_q \sim \delta_q$ is not ideal.) In this phenomenological view, the parameters γ_q can be chosen in whichever way is convenient subject to only one requirement: the resulting hybridization function $\Delta_{ij,\alpha}^{R/K}$ must faithfully represent the original continuum form defined in Eq. (31a). Since the hybridization function (together with the impurity Hamiltonian $H_{\rm imp}$) fully determines the impurity self-energy, this requirement suffices to yield the correct impurity dynamics.

The following subsections will be devoted to exploring how this requirement can be met. Let us here briefly preview our main conclusions. In Sec. III C, we argue that the requirement can be fulfilled by choosing $\delta_q \lesssim \gamma_q$, while keeping γ_q somewhat smaller than all other physical energy scales. In the subsequent Secs. III D and III E, we then illustrate these statements explicitly within the context of the nonequilibrium resonant level model. We find that considerable freedom of choice is available regarding the relation of δ_q to γ_q.

Finally, let us note that the steady-state value of the difference between the actual and desired occupancies of lead level q, say $\delta N_{q;\rm DL} = N_{q;\rm DL} - f_\alpha(\varepsilon_q)$, will in general not be zero, due to the coupling of that level to the impurity. However, we will show in Sec. III E that one can achieve $\delta N_{q;\rm DL} \ll 1$ by choosing $\delta_q \ll \gamma_q$ (for all levels). This in effect corresponds to the continuum limit of infinitely many lead levels with level spacing zero, in which case the Lindblad equation (40) becomes an exact representation of an arbitrary impurity coupled to continuous leads, with Fermi function occupations $f_\alpha(\omega)$. However, we will argue that for the purposes of correctly describing the hybridization function and hence the impurity dynamics it is actually sufficient and computationally much more practical to choose $\delta_q \simeq \gamma_q$ (i.e., to fix their ratio to be of order unity).

C. Hybridization

To demonstrate the suitability of the Lindblad equation (40), it suffices to look at the hybridization functions $\Delta_{ij,\alpha}^{R/K}(\omega)$, which involve only the bare lead Green's functions $g_{qq}^{R/K}(\omega)$. The lead Hamiltonian (29) is quadratic and the Lindblad operators in Eq. (40) linear. Independent of whether or not the impurity contains interactions, we can therefore use the methods established in Sec. II to derive an expression for the hybridization functions within the LDDL setup. We will compare these to the form obtained when using CL expressions.

The matrix equations (17) and (25) for the lead level q decoupled from the impurity but including a Lindblad driving with diagonal matrices $\Lambda_{qq'}^{(\pm)} = \delta_{qq'}\lambda_q^{(\pm)}$ yield the following expressions for the discretized leads:

$$g_{qq;\rm DL}^R(\omega) = (\omega - \varepsilon_q + i\lambda_q^{(+)})^{-1}, \tag{41a}$$

$$g_{qq;\rm DL}^K(\omega) = -2i\frac{\lambda_q^{(-)}}{(\omega-\varepsilon_q)^2 + \lambda_q^{(+)2}}. \tag{41b}$$

Here we have

$$\lambda_q^{(+)} = \gamma_q, \quad \lambda_q^{(-)} = \gamma_q(1-2f_\alpha(\varepsilon_q)) \tag{42a}$$

and therefore,

$$g_{qq;\rm DL}^R(\omega) = (\omega - \varepsilon_q + i\gamma_q)^{-1}, \tag{42b}$$

$$g_{qq;\rm DL}^K(\omega) = -2i(1-2f_\alpha(\varepsilon_q))\pi\,\delta_{\gamma_q}(\omega-\varepsilon_q), \tag{42c}$$

where $\delta_{\gamma_q}(\omega-\varepsilon_q)$ describes a Lorentz function of width γ_q, as defined in Eq. (34).

Comparing $g_{qq}^{R/K}(\omega)$ from the Lindblad approach in Eq. (42) to the corresponding expressions of the continuous leads in Eq. (33), we note that they have precisely the same structure, except that the Lindblad approach introduces an additional broadening γ_q: the infinitesimal broadening ϵ in the retarded Green's function of the continuous model, (33a), is replaced by a finite broadening γ_q in the Lindblad result (42b). Similarly, the Keldysh component (42c) contains a Lorentz peak of width γ_q instead of the δ peak in the result of the continuous model, (33b). Note that the fact that the Fermi functions of Eqs. (33b) and (42c) contain different arguments, is irrelevant because of the δ function in Eq. (33b).

The hybridization $\Delta_{ij,\alpha;\rm DL}^{R/K}(\omega)$ defined in (31a) inherits this broadening from the free Green's functions $g_{qq;\rm DL}^{R/K}(\omega)$. Explicitly, in the Lindblad approach, the negative imaginary part of $\Delta_{ij,\alpha;\rm DL}^R(\omega)$ is a sum over a finite number of Lorentz peaks of width γ_q:

$$\Gamma_{ij,\alpha;\rm DL}(\omega) = \sum_k v_{iq}v_{jq}^*\,\pi\,\delta_{\gamma_q}(\omega-\varepsilon_q). \tag{43}$$

In comparison, for standard continuous leads one obtains a sum over an infinite number of infinitely sharp δ peaks

$$\Gamma_{ij,\alpha;\mathrm{CL}}(\omega) = \sum_k v_{iq} v_{jq}^* \, \pi \, \delta_\epsilon(\omega - \varepsilon_q). \tag{44}$$

(We use the notation $\sum_k$ both when discussing the LDDL approach and for continuous leads, taking it to be understood that the continuum limit is implied for the latter, but not the former.)

Comparing Eqs. (43) and (44), it becomes clear that $\Gamma_{\mathrm{DL}}(\omega)$ will provide a faithful representation of $\Gamma_{\mathrm{CL}}(\omega)$ if two conditions are satisfied. (i) To correctly explore the physical information encoded in $\Gamma_{\mathrm{CL}}(\omega)$, the level spacings δ_q and driving rates γ_q have to be so small that the characteristic spectral features of $\Gamma_{\mathrm{CL}}(\omega)$ are well resolved. (ii) To obtain a smooth function for $\Gamma_{\mathrm{DL}}(\omega)$, free from discretization artifacts, the discrete peak widths must be comparable to or larger than the level spacing,

$$\delta_q \lesssim \gamma_q. \tag{45}$$

Analogously, this also applies to the Keldysh component of the hybridization function, $\Delta^K_{ij,\alpha}(\omega)$.

Let us illustrate this with an example. Consider a single impurity level coupled to one lead with a continuum hybridization function of the form

$$\Gamma_{\mathrm{CL}}(\omega) = \Gamma_0 \, \theta(D - |\omega|). \tag{46a}$$

All energies are expressed in units of the half-band width D. For a continuous lead in thermal equilibrium, the Keldysh component $\Delta^K_{\mathrm{CL}}(\omega)$ is linked to its retarded component by the fluctuation-dissipation theorem [49]

$$\Delta^K_{\mathrm{CL}}(\omega) = 2i(1 - 2f(\omega))\mathrm{Im}\big(\Delta^R_{\mathrm{CL}}(\omega)\big). \tag{46b}$$

In Fig. 2, we show the hybridization function as obtained in the Lindblad approach, which follows from inserting Eq. (42) into Eq. (31). This is done for a linear lead discretization with level spacing δ and choosing the prefactor of the Lindblad driving to be q-independent, $\gamma_q = \gamma$. The black curve represents the exact continuum hybridization (46). The larger γ, the more the Lorentz peaks of Eq. (42) are broadened. If γ/δ becomes too large, this leads to an unwanted smearing of the spectral features. Not illustrated in the figure, but self-evident, is the fact that this smearing can be systematically reduced by reducing the level spacing. Thus requirement (i) can be met by choosing both δ and γ much smaller than the relevant energy scales, here T, while requirement (ii) can be met by choosing $\delta \lesssim \gamma$.

Having illustrated both conditions (i) and (ii), let us remark that for *equilibrium* situations, condition (ii) has a different status than condition (i). Whereas (i) is essential for getting the physics right, (ii) is needed only if one is interested in obtaining spectral properties of the impurity model, such as the local spectral function $A_d(\omega) = -\mathrm{Im}(G^R_{dd}(\omega))$, that are more or less free from discretization artifacts. However, many physical observables, such as the linear conductance $G = (\partial J/\partial V)|_{V=0}$ through the dot or the dot occupation N_d, can be expressed as spectral *integrals* over $A_d(\omega)$ [see Eqs. (56) and (60a) below]. In such cases, there is no need to avoid discretization artifacts; in fact, when using the NRG to calculate equilibrium

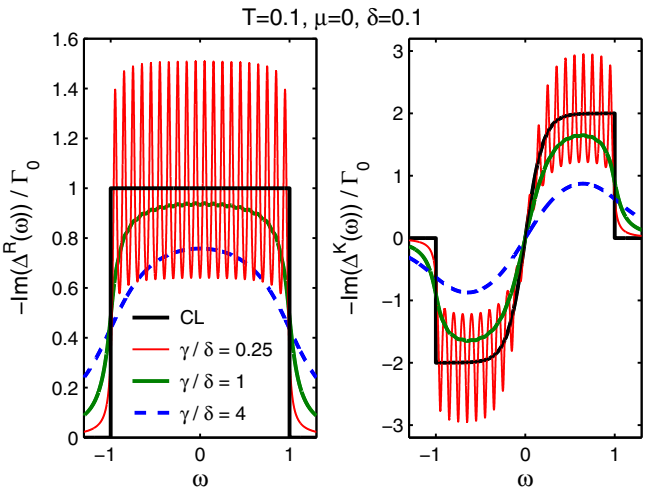

FIG. 2. For a single lead with a continuum hybridization function as defined in Eq. (46), we plot the corresponding Lindblad result based on Eq. (42) and the definition (31) for different values of γ, which was chosen to be independent of q. A linear discretization is used with $M = 2D/\delta$ lead levels for a level spacing of $\delta = 0.1$. We need $v_k = v = \sqrt{\Gamma_0 \delta/\pi}$ to ensure the correct continuum limit $\Delta_{\mathrm{CL}}(\omega)$. The black curve represents the continuum limit (46a) and (46b), respectively. All energies are given in units of D.

spectral functions, it is routine practice to represent $A_d(\omega)$ as a Lehmann sum over infinitely sharp δ peaks. If necessary, it is also known empirically how to smoothen such spectral functions [9,50]. To correspondingly calculate $A_{d;\mathrm{DL}}(\omega)$ in equilibrium using the LDDL approach, it would therefore be entirely possible to choose $\gamma_q \ll \delta_q$; though this would yield a result for $A_{d,\mathrm{DL}}(\omega)$ bearing discretization artifacts, that would not matter, because the function is integrated over anyway.

In contrast, for steady-state nonequilibrium, condition (ii) acquires additional importance, because then the Lindblad driving rates are needed to stabilize the nonequilibrium occupation functions in the leads within the transport window. Technically, they must ensure that the Keldysh component of the hybridization function (which in nonequilibrium is *not* fixed by the fluctuation-dissipation theorem) is faithfully represented as a smooth function *in the transport window*. To this end, it is necessary to choose $\delta_q \lesssim \gamma_q$ within the transport window; as will be illustrated by explicit examples below, the choice $\delta_q \simeq \gamma_q$ actually suffices.

D. Green's functions for the resonant level model

The hybridization function fully encapsulates all lead properties that are relevant for the impurity physics. Hence the previous subsection constitutes a demonstration of the suitability of the suggested Lindblad equation in the context of quantum impurity models. As a check, it is instructive to explicitly calculate the impurity Green's functions for a specific quadratic model within the Lindblad approach using the methods established in Sec. II. The results can be compared to the Green's functions deduced from standard Keldysh techniques using continuous thermal leads.

The simplest quadratic impurity model is the resonant level model (RLM) for spinless fermions,

$$H_{\rm imp} = \varepsilon_d c_d^\dagger c_d,$$
$$H_{\rm hyb} = \sum_{\alpha k} v_{\alpha k} c_d^\dagger c_{\alpha k} + \text{H.c.} = \sum_q v_q c_d^\dagger c_q + \text{H.c.}, \quad (47)$$

where the label d identifies the local level, thus $M_d = 1$ in Eq. (30), and q again abbreviates all lead labels, $q = \{\alpha k\}$. The RLM in the LDDL scheme as well as its continuum limit have been discussed before [12] using superoperators. We revisit it here as an illustrative example of the Green's function formalism derived in Sec. II and to demonstrate once more how the broadening of the Lindblad reservoirs enters the physics.

Because the RLM is quadratic, we can use equations (17) and (25) for the full model including the impurity and immediately write down matrix equations for the retarded Green's functions and the Keldysh Green's functions of the full system S. The lead-lead components of the matrices $\Lambda^{(+)}$ and $\Lambda^{(-)}$ are diagonal, $\Lambda_{qq'} = \delta_{qq'}\lambda_q^{(\pm)}$, with the diagonal elements given by Eq. (42a). As there is no Lindblad driving on the impurity, the matrix elements involving the local level are zero,

$$\Lambda_{dd}^{(\pm)} = \Lambda_{dq}^{(\pm)} = \Lambda_{qd}^{(\pm)} = 0. \quad (48)$$

We first look at the retarded Green's function $\mathcal{G}_{mn}^R(t) = -i\theta(t)\,\langle\{c_m(t), c_n^\dagger\}\rangle$ with $m,n \in \{d,q\}$. The matrix equation (17) can be rewritten as

$$\mathbb{1} = (\omega - h + i\Lambda^{(+)})G_{\rm DL}^R(\omega). \quad (49)$$

Writing out the dd, dq, qd, and qq' components of this matrix equation separately and solving for the different correlators one readily finds

$$G_{dd;\rm DL}^R(\omega) = \left(\omega - \varepsilon_d - \sum_q \frac{|v_q|^2}{\omega - \varepsilon_q + i\gamma_q}\right)^{-1}, \quad (50a)$$

$$G_{dq;\rm DL}^R(\omega) = \left(G_{qd;\rm DL}^A(\omega)\right)^* = \frac{v_q G_{dd;\rm DL}^R(\omega)}{\omega - \varepsilon_q + i\gamma_q}, \quad (50b)$$

$$G_{qq';\rm DL}^R(\omega) = \frac{\delta_{qq'} + v_q^* G_{dq';\rm DL}^R(\omega)}{\omega - \varepsilon_q + i\gamma_q}. \quad (50c)$$

Equation (50a) is consistent with (42b), because the hybridization function $\Delta_{\rm DL}^R(\omega) = \sum_q |v_q|^2 g_{qq;\rm DL}^R(\omega)$ plays the role of the impurity self-energy here.

Equation (25) for the Keldysh Green's function $\mathcal{G}_{mn}^K(t) = -i\,\langle[c_m(t), c_n^\dagger]\rangle$ simplifies due to the diagonal structure of $\Lambda^{(-)}$, leading to

$$G_{dd;\rm DL}^K(\omega) = -i\sum_q G_{dq;\rm DL}^R(\omega)\,2\lambda_q^{(-)}\,G_{qd;\rm DL}^A(\omega) = -2i\left|G_{dd;\rm DL}^R(\omega)\right|^2 \sum_q (1 - 2f_\alpha(\varepsilon_q))|v_q|^2\,\pi\,\delta_{\gamma_q}(\omega - \varepsilon_q), \quad (51a)$$

$$G_{qd;\rm DL}^K(\omega) = -i\sum_{q'} G_{qq';\rm DL}^R(\omega) 2\gamma_{q'}(1 - 2f_{\alpha'}(\varepsilon_{q'}))G_{q'd;\rm DL}^A(\omega), \quad (51b)$$

$$G_{qq';\rm DL}^K(\omega) = -i\sum_{q''} G_{qq''}^R(\omega) 2\gamma_{q''}(1 - 2f_{\alpha''}(\varepsilon_{q''}))G_{q''q';\rm DL}^A(\omega), \quad (51c)$$

where we used Eq. (50b). Analogous to $G_{dd;\rm DL}^K(\omega)$ in Eq. (51a) also $G_{qd;\rm DL}^K(\omega)$ and $G_{qq;\rm DL}^K(\omega)$ may be expressed in terms of $G_{dd;\rm DL}^R(\omega)$ by inserting Eqs. (50) into Eqs. (51b) and (51c).

Let us now compare the $G_{dd}^{R/K}(\omega)$ correlators derived in the Lindblad formalism to the corresponding CL expressions. The latter are given by

$$G_{dd;\rm CL}^R(\omega) = \left(\omega - \varepsilon_d - \sum_q \frac{|v_q|^2}{\omega - \varepsilon_q + i\epsilon}\right)^{-1}, \quad (52)$$

$$G_{dd;\rm CL}^K(\omega)$$
$$= 2i\,\mathrm{Im}\big(G_{dd;\rm CL}^R(\omega)\big)\sum_\alpha (1 - 2f_\alpha(\omega))\frac{\Gamma_{\alpha;\rm CL}(\omega)}{\Gamma_{\rm CL}(\omega)} \quad (53a)$$
$$= -2i\left|G_{dd;\rm CL}^R(\omega)\right|^2 \sum_q (1 - 2f_\alpha(\varepsilon_q))|v_q|^2\,\pi\,\delta_\epsilon(\omega - \varepsilon_q), \quad (53b)$$

with $\Gamma_{\alpha;\rm CL}(\omega)$ defined in (44) and $\Gamma_{\rm CL}(\omega) = \sum_\alpha \Gamma_{\alpha;\rm CL}(\omega)$. Again, in Eqs. (52) and (53), the continuum limit is understood [as described below Eq. (34)]. Comparing (50a) with (52) and (51a) with (53), we see explicitly that the LDDL approach reproduces the correct structure of the Green's functions, but additionally broadens the discrete lead levels to have a finite width γ_q instead of an infinitesimal width ϵ. A similar statement holds also for the $G_{qd}^{R/K}(\omega)$ and $G_{qq'}^{R/K}(\omega)$ Green's functions.

E. Current and occupation functions for the resonant level model

As examples of observables for the RLM, we now calculate the current through the local level, and the occupation number of the local level and the lead levels.

1. Current

To determine an expression for the current through the impurity, we calculate the time derivative of the dot occupation number $N_d = \langle c_d^\dagger c_d\rangle_{\rm NESS}$ using Eq. (12). This derivative is, of course, zero, but one can identify the contributions from the different leads, $e\dot{N}_d = 0 = \sum_\alpha J_\alpha$. The contribution of the dissipative terms to $\dot{N}_d$ vanishes as there is no Lindblad driving

on the impurity itself. Therefore, with $H_{\mathrm{hyb};\alpha} = \sum_k v_q\, c_d^\dagger c_q + \mathrm{H.c.}$, we identify

$$\begin{aligned} J_{\alpha;\mathrm{DL}} &= -ie\,\langle [c_d^\dagger c_d, H_{\mathrm{hyb};\alpha}]\rangle_{\mathrm{NESS}} \\ &= -ie\sum_k (v_q\,\langle c_d^\dagger c_q\rangle_{\mathrm{NESS}} - v_q^*\,\langle c_q^\dagger c_d\rangle_{\mathrm{NESS}}) \\ &= -e\frac{1}{4\pi}\int d\omega \sum_k \left(v_q G^K_{qd;\mathrm{DL}}(\omega) + \mathrm{H.c.}\right). \end{aligned} \tag{54}$$

Assume now that we have two leads, $\alpha = \{L, R\}$, and their hybridizations are multiples of each other, $\Gamma_\alpha(\omega) = a_\alpha \Gamma(\omega)$ with $a_L + a_R = 1$ [51]. We choose the discretization of both channels to be identical, $\varepsilon_{\alpha k} = \varepsilon_k$. This implies $|v_{\alpha k}|^2 = a_\alpha |v_k|^2$ with $|v_k|^2 = |v_{Lk}|^2 + |v_{Rk}|^2$. In this case, it is also appropriate to set $\gamma_{\alpha k} = \gamma_k$. Due to $J_L + J_R = 0$, we can define the current to be $J = J_L = -J_R = (a_R J_L - a_L J_R)$. Using Eqs. (50b), (50c), and (51b), one then finds for the current (with $\hbar$ restored)

$$\begin{aligned} J_{\mathrm{DL}} = -\frac{4e}{h}\int d\omega \sum_k |v_k|^2\, \pi\, \delta_{\gamma_k}(\omega - \varepsilon_k) a_L a_R \\ \times (f_L(\varepsilon_k) - f_R(\varepsilon_k))\mathrm{Im}\big(G^R_{dd;\mathrm{DL}}(\omega)\big). \end{aligned} \tag{55}$$

The corresponding result for continuous leads is given by [52,53]

$$\begin{aligned} J_{\mathrm{CL}} = -\frac{4e}{h}\int d\omega\, \Gamma_{\mathrm{CL}}(\omega) a_L a_R \\ \times (f_L(\omega) - f_R(\omega))\mathrm{Im}\big(G^R_{dd,\mathrm{CL}}(\omega)\big). \end{aligned} \tag{56}$$

We have seen in Sec. III C that γ_k should scale with the width of the energy interval δ_k. Therefore, in the continuum limit of the LDDL approach, the widths of the Lorentz peaks in Eq. (55), γ_k, go to zero. In this case, we can replace $f_\alpha(\varepsilon_k)$ by $f_\alpha(\omega)$ and identify $\sum_k |v_k|^2\, \pi\, \delta_{\gamma_k}(\omega - \varepsilon_k) = \Gamma_{\mathrm{DL}}(\omega)$. Hence, in the continuum limit, the current in the LDDL approach has the same form as the standard CL description, while for a finite number of lead levels we recover the broadening effects discussed before.

Let us illustrate the LDDL current in Eq. (55) with a few numerical examples and compare it to the exact current given by Eq. (56). We consider a symmetric continuum hybridization

$$a_L = a_R = \tfrac{1}{2}, \quad \Gamma_{\mathrm{CL}}(\omega) = \Gamma_0\, \theta(D - |\omega|) \tag{57a}$$

with equal temperature and symmetrically applied voltage

$$T_L = T_R = T, \quad V = (\mu_L - \mu_R) = 2\mu_L. \tag{57b}$$

The values chosen for the different parameters can be found in the figures, where all energies are given in units of D.

In Fig. 3, we analyze how the current through the local level, as given in Eq. (55), depends on the strength of the Lindblad driving. To this end, we discretize linearly with level spacing δ and choose $\gamma_k = \gamma$ to be q-independent. In the left panel, the current is plotted as a function of γ/δ. In this case, curves obtained with different level spacing δ coincide for the decrease in current when γ/δ decreases below $\simeq 1$, indicating that this decrease is a discretization effect. Physically, it is obvious that if γ goes to zero, the Lindblad driving will not be

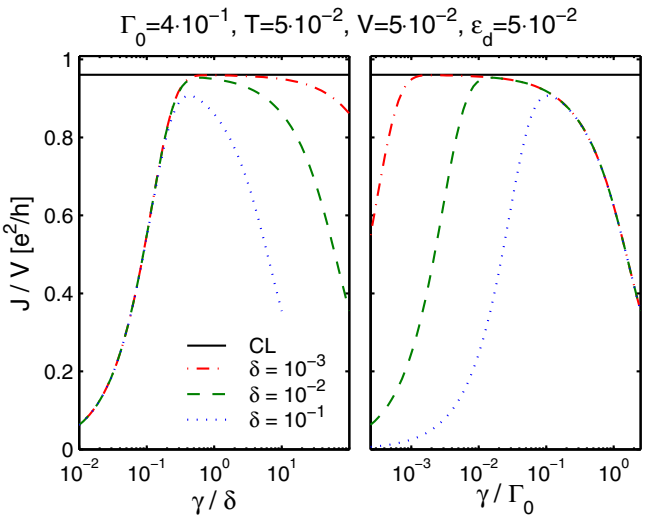

FIG. 3. The current through the local level of the RLM [Eq. (55)] with linearly discretized leads for several values of the level spacing δ. The two panels show the same data, but in the left panel as function of γ/δ and in the right panel as function of γ/Γ_0. This illustrates that the decrease in the current for small values of γ is a discretization effect while the decrease for large γ corresponds to an overdriving of the system. The correct physics can only be obtained if $\delta \lesssim \gamma \ll \Gamma_0$.

able to maintain the occupation of the discretized lead levels at the values of their assigned Fermi functions. Analytically, the decrease in the current can be explained as follows: in Eq. (55) the current is expressed as an integral over the product of two peaked functions [$\mathrm{Im}(G^R_{dd;\mathrm{DL}}(\omega))$ and the explicit sum over k], whose peak positions do not precisely coincide. Therefore, if the peaks become too narrow, the integral goes to zero. To avoid this drop, one would have to broaden at least one of the two functions by hand before calculating the integral or replace the sum over k by its continuum limit, $\Gamma(\omega)(f_L(\omega) - f_R(\omega))$. Such a replacement would enable one, in principle, to use arbitrarily small values of γ in Eq. (55) for the RLM. Note, though, that it will not be possible to send $\gamma \to 0$ in Eq. (55) for more general models because a reliable calculation of the nonequilibrium Green's function $G^R_{dd}(\omega)$ will require γ to remain finite. While for the RLM, the nonequilibrium retarded Green's function is equal to its equilibrium counterpart, this is not true in general. One will therefore need a finite broadening, $\gamma \simeq \delta$, to keep the occupation numbers of the discrete lead levels *close to* the corresponding Fermi distribution (see also Sec. III E) while solving for the steady state of the Lindblad equation and thereby determining the true nonequilibrium Green's function.

The second panel shows the same data as a function of γ/Γ_0. Here, the different curves coincide for the decrease in the current when γ/Γ_0 increases past $\simeq 1$, illustrating that this effect is an inherent property of the Lindblad equation. It corresponds to an overdriving of the system, i.e., the Lindblad reservoirs destroy the coherence and hence suppress the current when $\gamma \gtrsim \Gamma_0$.

If the ratio δ/Γ_0 is small enough, a plateau for $\delta \lesssim \gamma \ll \Gamma_0$ appears and the height of this plateau agrees well with the exact current obtained from Keldysh calculations. In total, the Lindblad driving rates γ_q must be small compared to the

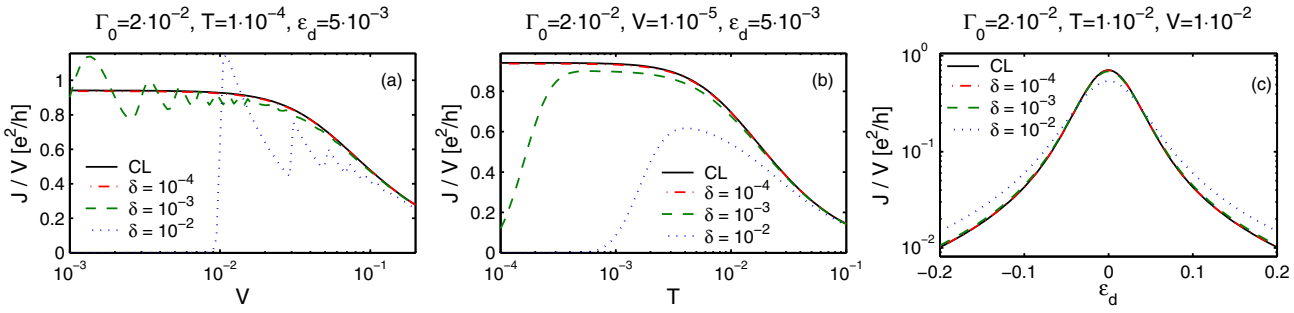

FIG. 4. The current [Eq. (55)] for several different level spacings δ using linearly discretized leads and $\gamma_q = \delta$ as a function (a) of voltage V, (b) temperature T, and (c) the level energy ε_d. For sufficiently small δ, the exact black curve, calculated from the continuum limit of Eq. (56), is reproduced with a deviation of less than one percent. In (a), one can clearly see discretization artifacts for $\delta = 10^{-2}$ and $\delta = 10^{-3}$, which vanish where δ/V gets small enough. Analogously, also in (b), it is apparent that for larger temperatures T, larger level spacings δ can be used, while for small T small level spacings are needed.

physical energy scale Γ_0 but larger or comparable to the level spacing δ_q. On the other hand, the level spacing δ_q has to resolve the energy scale Γ_0, $\delta \lesssim \Gamma_0$. Therefore $\gamma_q = \delta_q$ should always be an appropriate choice and we will use this choice in the following examples.

In Figs. 4(a)–4(c), the value of γ is fixed to $\gamma = \delta$ and the current is plotted as a function of voltage V, temperature T, and level position ε_d, respectively. For small enough level spacing, the deviation from the standard continuum result represented by the black line is less than one percent.

To be more specific, in Fig. 5, we show how the relative error of the current scales with level spacing δ, using $\gamma_k = \delta$. Extrapolating the data points for small δ towards the continuum limit $\delta \to 0$ using a linear fit yields an offset of the order of 10^{-4}, demonstrating that the suggested Lindblad approach becomes exact in the continuum limit.

In order to properly reproduce the dependence of the current on V, T, and Γ_0, the choice of level spacing must satisfy certain conditions. These can be deduced by inspecting Eq. (55), which contains an integral over the product of $\mathrm{Im}(G^R_{dd;\mathrm{DL}}(\omega))$ and $\sum_k |v_k|^2 \pi \delta_{\gamma_k}(\omega - \varepsilon_k) a_L a_R (f_L(\varepsilon_k) - f_R(\varepsilon_k))$. For $\gamma = \delta$, both these functions are smooth. Evidently, δ must be small enough to resolve the ω dependence of $G_{dd}(\omega)$ and $\Gamma(\omega)$. For the RLM, this implies that $\delta \ll \Gamma_0$ is needed. The energy scale on which $(f_L(\varepsilon_k) - f_R(\varepsilon_k))$ varies, is set by temperature and voltage. First, consider the case that temperature is the smallest physical energy scale, $T \ll V, \Gamma_0$. T sets the width of the Fermi function steps. Hence, one might expect that $\delta \lesssim T$ is needed. However, $\delta \lesssim V$ suffices. The reason is that the Fermi functions are multiplied by a smooth function, $\mathrm{Im}(G^R_{dd}(\omega))$, which varies on an energy scale $\Gamma_0 \gg T$; when integrated over, the result is independent of T. Note that for $V \lesssim T$ this temperature independence is lost because then the two steps of $f_L(\omega)$ and $f_R(\omega)$ are not well separated. Next consider the case $V \ll T, \Gamma_0$. Then $(f_L(\omega) - f_R(\omega))$ varies on an energy scale given by temperature T, and the voltage does not need to be resolved. Hence, in summary, δ has to be chosen small enough to resolve all features of the spectral function $\mathrm{Im}(G^R_{dd}(\omega))$ and the larger of the two energy scales V and T.

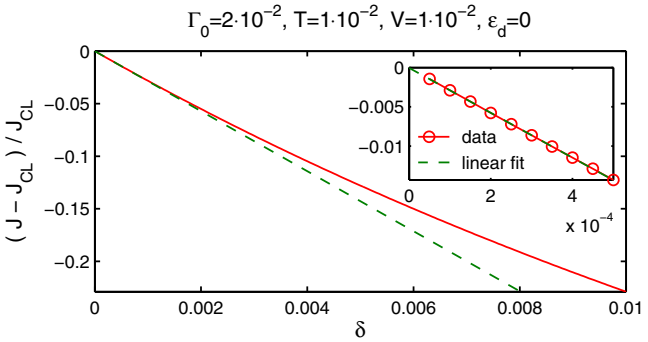

FIG. 5. Relative error of the current for the parameters of Fig. 4(c), at $\varepsilon_d = 0$. A linear fit, obtained from the data shown in the inset, yields an offset smaller than 10^{-4}, showing that the LDDL scheme becomes exact in the continuum limit.

2. *Occupation of local level*

The current is an observable that illustrates the dynamics of the system. As an example of a static property, we next consider the occupation number of the local level, $N_d = \langle c_d^\dagger c_d \rangle_{\mathrm{NESS}}$. Using the Green's functions (50a) and (51a), it is given by

$$\begin{aligned} N_{d;\mathrm{DL}} &= \frac{1}{2} + \frac{1}{2i} \mathcal{G}^K_{dd;\mathrm{DL}}(0) \\ &= \frac{1}{2} + \frac{1}{4\pi i} \int d\omega G^K_{dd;\mathrm{DL}}(\omega) \\ &= \frac{1}{\pi} \int d\omega \left| G^R_{dd;\mathrm{DL}}(\omega) \right|^2 \sum_q f_\alpha(\varepsilon_q) |v_q|^2 \pi \, \delta_{\gamma_q}(\omega - \varepsilon_q), \end{aligned} \tag{58}$$

where we exploited the sum rule

$$\begin{aligned} &- \frac{1}{2\pi} \int d\omega \left| G^R_{dd;\mathrm{DL}}(\omega) \right|^2 \sum_q |v_q|^2 \pi \, \delta_{\gamma_q}(\omega - \varepsilon_q) \\ &= \frac{1}{2\pi} \int d\omega \, \mathrm{Im}\big(G^R_{dd;\mathrm{DL}}(\omega)\big) = -\frac{1}{2}. \end{aligned} \tag{59}$$

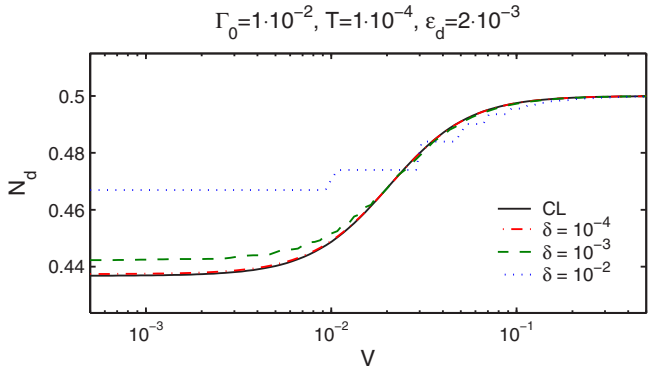

FIG. 6. The occupation number of the local level for the RLM in the Lindblad approach as given by Eq. (58), as function of a symmetrically applied voltage. The discretization was chosen to be linear with different values for the level spacing δ. The black curve represents the continuum limit of Eq. (60). If the level spacing δ is small enough compared to the voltage V, the exact result is recovered. For $\delta = 10^{-2}$, one can clearly see discretization artifacts.

The corresponding result for continuous thermal leads is given by

$$N_{d;\mathrm{CL}} = -\frac{1}{\pi}\int d\omega\, \mathrm{Im}\big(G^R_{dd;\mathrm{CL}}(\omega)\big)\sum_\alpha f_\alpha(\omega)\frac{\Gamma_{\alpha;\mathrm{CL}}(\omega)}{\Gamma_{\mathrm{CL}}(\omega)} \tag{60a}$$

$$= \frac{1}{\pi}\int d\omega \big|G^R_{dd;\mathrm{CL}}(\omega)\big|^2 \sum_\alpha f_\alpha(\varepsilon_q)|v_q|^2\,\pi\,\delta_\epsilon(\omega-\varepsilon_q). \tag{60b}$$

Analogously to the discussion of the current, the comparison of the Lindblad result (58) to (60b) reveals that the LDDL approach in the continuum limit recovers the standard result obtained using continuous thermal leads.

For a symmetric hybridization of the form (57), we illustrate these formulas in Fig. 6 where we plot the occupation of the local level given in (58) as function of voltage. The discretization is again chosen linear for both leads and the Lindblad driving is set to the constant value $\gamma_q = \gamma = \delta$. Again, we find excellent agreement with the continuum results if the level spacing is chosen small enough.

3. Occupation of lead level

Finally, we discuss the steady-state occupation $N_{q;\mathrm{DL}}$ of lead level q. Although our choice for the Lindblad driving rates [Eq. (39)] is designed to drive $N_{q;\mathrm{DL}}$ towards its Fermi distribution value, $N_{q;\mathrm{DL}}$ actually differs slightly from $f_\alpha(\varepsilon_q)$, due to the coupling of level q to the impurity. Using Eqs. (50) and (51), the difference can be calculated analogously to Eq. (58), with the result

$$\delta N_{q;\mathrm{DL}} = N_{q;\mathrm{DL}} - f_\alpha(\varepsilon_q) = -\int\frac{d\omega}{\pi}\,\frac{|v_q|^2\gamma_q(1-2f_\alpha(\varepsilon_q))}{(\omega-\varepsilon_q)^2+\gamma_q^2}\mathrm{Re}\left(\frac{G^R_{dd;\mathrm{DL}}(\omega)}{\omega-\varepsilon_q+i\gamma_q}\right)$$

$$-\int\frac{d\omega}{2\pi}\sum_{q'}\frac{\gamma_{q'}(1-2f_{\alpha'}(\varepsilon_{q'}))|v_q|^2|v_{q'}|^2\left|G^R_{dd;\mathrm{DL}}(\omega)\right|^2}{\big((\omega-\varepsilon_q)^2+\gamma_q^2\big)\big((\omega-\varepsilon_{q'})^2+\gamma_{q'}^2\big)}. \tag{61}$$

For the symmetric two-channel RLM as defined in Eq. (57), assuming that the parameters $\delta_{q'}$ and $\gamma_{q'}$ (for all q') are much smaller than all other energy scales, and $\delta_{q'} \lesssim \gamma_{q'}$, this reduces to

$$\delta N_{q;\mathrm{DL}} \simeq -\frac{|v_q|^2}{2\gamma_q}\frac{\Gamma_0(f_\alpha(\varepsilon_q)-f_{\bar\alpha}(\varepsilon_q))}{(\varepsilon_q-\varepsilon_d)^2+\Gamma_0^2}, \tag{62}$$

with $\bar\alpha = R(L)$ if $\alpha = L(R)$. In this case, therefore, the deviation is nonzero in the transport window where $f_\alpha \neq f_{\bar\alpha}$, and vanishes completely only for a system in equilibrium.

Equation (61) is also true for more general impurity models (with $G_{dd;\mathrm{DL}}(\omega)$ depending on the precise form of H_{imp}). It can be shown that the scaling of $\delta N_{q,\mathrm{DL}}$ with $|v_q|^2/\gamma_q$ found in Eq. (62) holds independent of the form of the impurity, again assuming $\delta_{q'}$ and $\gamma_{q'}$ small enough and $\delta_{q'} \lesssim \gamma_q$. For typical impurity models, $|v_q|^2$ is a smooth function of q whose magnitude scales with the size of the corresponding energy interval, $|v_q|^2 \sim \delta_q$. Therefore, if one sends both δ_q and γ_q to zero while keeping $\delta_q \simeq \gamma_q$ (i.e., fixing their ratio to be of

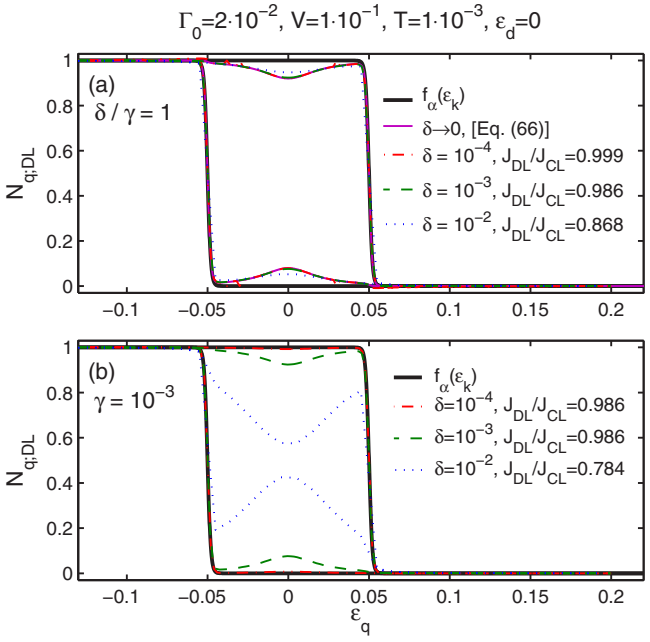

FIG. 7. The occupation numbers $N_{q;\mathrm{DL}}$ for the left and right channels of a symmetric RLM as defined in Eq. (57), choosing a linear discretization with level spacing $\delta_q = \delta$ and q-independent broadening $\gamma_q = \gamma$. In (a), we show $N_{q;\mathrm{DL}}$ for several values of δ at a fixed ratio $\delta/\gamma = 1$. If the level spacing is small enough, the exact current is reproduced, although $N_{q;\mathrm{DL}}$ deviates from the Fermi distribution by a nonzero amount $\delta N_{q;\mathrm{DL}}$, which for small enough δ is given by Eq. (62). In (b), γ is kept fixed at a value that can resolve the physical relevant energy scales (here Γ_0 and V) while δ is varied. Reducing δ, $N_{q;\mathrm{DL}}$ approaches the Fermi distribution, but as soon as δ becomes $\lesssim \gamma$ the accuracy of J_{DL} (taking J_{CL} as reference) does not improve.

order unity), then $\delta N_{q;\mathrm{DL}}$ does not vanish. This is depicted in panel (a) of Fig. 7.

If one insists on having $\delta N_{q;\mathrm{DL}} \ll 1$, one may achieve this by choosing $\delta_q \ll \gamma_q$ (thus ensuring $|v_q|^2/\gamma_q \ll 1$) while keeping γ_q somewhat smaller than all other energy scales. In fact, this corresponds to the order of limits used to recover the case of continuous thermal leads: first the level spacing is sent to zero and the number of lead levels to infinity while keeping the level broadening fixed and nonzero; and only subsequently the level broadening is taken to be infinitesimally small—its only trace in the description of continuous leads is the infinitesimal damping factor $i\epsilon$ in energy denominators, e.g. in Eq. (52). Thus, for continuous leads one indeed has $\delta N_{q;\mathrm{CL}} = 0$, as depicted in panel (b) of Fig. 7. The physical reason for this is that if the leads form a true continuum, i.e., the width of each lead level is larger than the level spacing, the effect of a single dot level on the occupation of each individual lead level is negligibly small.

Note, however, that for numerical computations it would be impractical to use $\delta_q \ll \gamma_q$, since this would require using many more lead levels than for the case $\delta_q \simeq \gamma_q$. Moreover, when one's interest is focused only on impurity properties, it is actually *not necessary* to achieve $\delta N_{q;\mathrm{DL}} \ll 1$: in that case, the precise value of $\delta N_{q;\mathrm{DL}}$ is irrelevant, as long as the hybridization function is represented faithfully and is smooth within the transport window. Indeed, we have shown in Sec. III C that this *can* be achieved when using $\delta_q \simeq \gamma_q$, by simply taking both to be somewhat smaller than all other physically relevant energy scales.

IV. LOCAL CHAIN REPRESENTATION OF THE LINDBLAD EQUATION

The resonant level model is a quadratic model that can be solved analytically. If the impurity contains interactions and many-particle physics becomes relevant, one can still use the suggested LDDL approach as it reproduces the correct bare hybridization function. However, in general, the Lindblad equation cannot be solved for its steady state analytically.

A versatile tool for numerical representations of many-particle quantum states are the so-called matrix product states (MPS) and matrix product operators (MPO) [54]. Only recently the idea to solve Lindblad equations numerically based on MPS/MPO has gained attention: One possibility is the explicit time-evolution of the full density matrix [22,37]. Alternatively, one can step down from the level of density matrices to the level of quantum states at the price of stochastic averaging as in the stochastic quantum trajectory approach [36,40,42,43,47,55]. Which of the two methods is numerically less expensive strongly depends on the model and its specific parameters [56]. To avoid the explicit time-evolution one can also target the steady state directly by solving $\dot{\rho}(t) = \mathcal{L}\rho(t) = 0$ [38,39].

MPS/MPO methods presuppose models having the structure of one-dimensional quantum chains. If we would write our proposed Lindblad setup as a chain by simply representing each level $q = \{\alpha k\}$ by one chain site, this would result in a highly nonlocal model, in which each and every chain site couples to the impurity. This nonlocality would render standard MPS/MPO techniques, e.g., for the time-evolution of a state or operator, numerically costly.[1] In this section, our goal is therefore to reformulate our Lindblad scheme in such a way that the Hamiltonian and the Lindblad driving terms are local when the leads are represented by chains of the type needed for MPS/MPO calculations, where "local" means that the matrices h and $\Lambda^{(1,2)}$ only connect sites on the chains that are very close to each other or are diagonal altogether.

For equilibrium calculations, it is well-known from NRG how to map the Hamiltonian of a noninteracting discretized lead onto a chain in such a way that the resulting Hamiltonian is local [8,9] using a unitary transformation of the form $c_q = \sum_l U_{ql} c'_l$. For our nonequilibrium LDDL scheme, however, a problem arises: under such a transformation the Lindblad matrices $\Lambda^{(1,2)}$ which in our original formulation are local ($\Lambda^{(1,2)}_{qq'} = \delta_{qq'}\lambda^{(1,2)}_q$, i.e., involving no driving terms that combine c_q and $c^\dagger_{q'}$ for $q \neq q'$), would become strongly nonlocal. The reason is that the transformed Lindblad matrices,

$$\Lambda'^{(1,2)}_{ll'} = \sum_q U^*_{ql} \Lambda^{(1,2)}_{qq'} U_{q'l'}, \tag{63}$$

would not be diagonal, because the old Lindblad matrices $\Lambda^{(1,2)}$, though diagonal, depend on q, e.g., due to the dependence of the diagonal elements $\lambda^{(1,2)}_q$ on the Fermi function $f_\alpha(\varepsilon_q)$.

This problem can be circumvented if the original Lindblad rates γ_q are q-independent. To this end, we will formulate an equivalent new Lindblad equation that reproduces the same hybridization function as the one suggested in Sec. III, but is based on new Lindblad matrices $\tilde{\Lambda}^{(1,2)}$ that are proportional to the identity matrix in their q indices. They are thus not only local but also invariant under arbitrary unitary transformations acting on the index q. This invariance makes it possible to map the leads onto a chain on which the Hamiltonian is local, without losing the locality of the dissipative Lindblad terms. We will thus refer to the new scheme as "local setup," and to the original one as "nonlocal setup." The cost for achieving locality is that each physical lead is replaced by two auxiliary leads. However, depending on the precise form of the impurity model, some linear combinations of auxiliary lead modes may decouple, thus lowering the cost again.

Before presenting the technical details of the local setup, let us describe its main idea. The Lindblad setup we are aiming for must have Lindblad matrices $\tilde{\Lambda}^{(1,2)}$ that are proportional to the identity matrix in their q indices. They thus cannot contain any information about Fermi functions. Moreover, the occupation number towards which such matrices drive any level q is actually independent of q [see Eq. (38)]. The levels in the local scheme thus cannot correspond to physical levels; instead, they have the status of auxiliary levels, and Fermi-function information *will have to be encoded in their coupling strengths to the impurity*. To see heuristically how such a Lindblad driving can still be used to mimic thermal leads, we note that a physical level with occupancy $f_\alpha(\varepsilon_q)$ is *empty* with probability $1 - f_\alpha(\varepsilon_q)$ and *filled* with probability

[1] In specific contexts, the added costs of this nonlocality may be offset by lower entanglement, see Ref. [57].

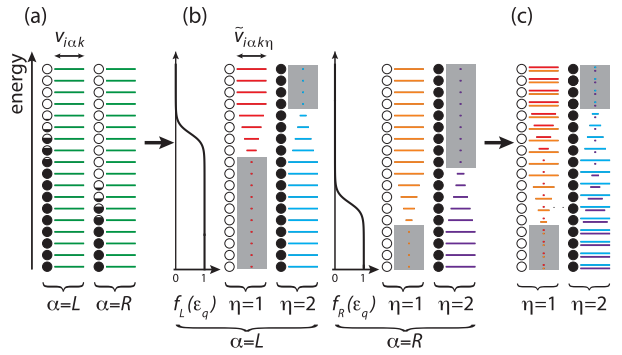

FIG. 8. Schematic depiction of the level-doubling construction scheme for two leads, $\alpha = L$ and R, assuming constant values of $v_{i\alpha k}$. (a) Original levels of the left and right leads, described by $c^{(\dagger)}_{\alpha k}$ operators. (b) After level doubling, each lead α is represented by two sets of auxiliary levels, distinguished by $\eta = 1$ and 2 and Lindblad-driven towards occupancy 0 and 1, respectively. These levels are described by $\tilde{c}^{(\dagger)}_{\alpha k\eta}$ operators, whose coupling strengths $\tilde{v}_{i\alpha k\eta}$ (indicated by the width of the horizontal lines) depend on the Fermi function $f_\alpha(\varepsilon_q)$ of that lead (depicted by smooth black curves). For $\eta = 1$ (or 2), all those auxiliary levels decouple for which $f_\alpha(\varepsilon_q) \approx 1$ (or 0), indicated by grey shading. (c) For a model involving just a single impurity level, only certain linear combinations of L and R auxiliary lead operators, the $\tilde{b}^{(\dagger)}_{k\eta}$ operators of Eq. (71a), couple to the impurity; they are depicted here by double lines representing the couplings $\tilde{v}_{Lk\eta}$ and $\tilde{v}_{Rk\eta}$, with grey shading indicating vanishing couplings.

$f_\alpha(\varepsilon_q)$. Now, occupancies of empty or filled *are* describable using q-independent diagonal Lindblad matrices, at the cost of introducing a new index, $\eta = 1$ or 2, to distinguish the two cases. (The matrices $\tilde{\Lambda}^{(1,2)}$ are then proportional to the identity in their q indices for each η independently. When mapping the system onto a chain the unitary transformation therefore must not mix different η, but treat $\eta = 1$ and $\eta = 2$ as two independent channels.) In the local setup, we thus "double" all levels: each physical level q from the nonlocal setup, having energy ε_q and impurity coupling strength $|v_{iq}|^2$, is replaced by a pair of two auxiliary levels, $q \to \{q\eta\}$ with $\eta \in \{1,2\}$, both with the same energy ε_q. We take the auxiliary level with $\eta = 1$ to have coupling strength $|v_{iq}|^2[1 - f_\alpha(\varepsilon_q)]$ while being Lindblad-driven towards occupancy *zero*, and the auxiliary level with $\eta = 2$ to have coupling strength $|v_{iq}|^2 f_\alpha(\varepsilon_q)$ while being Lindblad-driven towards occupancy *one*. This level-doubling construction is depicted schematically in Figs. 8(a) and 8(b). As will be shown below, the local setup leads to the same hybridization function as the nonlocal one, and hence describes the same impurity physics.

The Hamiltonian and Lindblad equation of the local setup have the same structure as for the nonlocal one [cf. Eqs. (28) to (30) and (40)], but with q replaced by $\{q\eta\}$ and making new choices for the couplings and Lindblad driving rates. Explicitly, the Hamiltonian and impurity-lead couplings now take the form

$$H = H_{\rm dot} + \sum_{q\eta}\left[\sum_{i=1}^{M_d}(\tilde{v}_{iq\eta}d_i^\dagger \tilde{c}_{q\eta} + \text{H.c.}) + \varepsilon_q \tilde{c}^\dagger_{q\eta}\tilde{c}_{q\eta}\right], \quad (64)$$

$$\tilde{v}_{iq,\eta=1} = v_{iq}\sqrt{(1 - f_\alpha(\varepsilon_q))}, \quad \tilde{v}_{iq,\eta=2} = v_{iq}\sqrt{f_\alpha(\varepsilon_q)}. \quad (65)$$

As before, the Lindblad matrices are chosen diagonal, with $\tilde{\Lambda}^{(1,2)}_{q\eta,q'\eta'} = \delta_{qq'}\delta_{\eta\eta'}\tilde{\lambda}^{(1,2)}_{q\eta}$ and the Lindblad equation reads

$$\dot{\rho}(t) = -i[\tilde{H},\rho(t)] + \sum_{q\eta}\big[\tilde{\lambda}^{(1)}_{q\eta}(2\tilde{c}_{q\eta}\rho(t)\tilde{c}^\dagger_{q\eta} - \{\tilde{c}^\dagger_{q\eta}\tilde{c}_{q\eta},\rho(t)\}) + \tilde{\lambda}^{(2)}_{q\eta}(2\tilde{c}^\dagger_{q\eta}\rho(t)\tilde{c}_{q\eta} - \{\tilde{c}_{q\eta}\tilde{c}^\dagger_{q\eta},\rho(t)\})\big]. \quad (66)$$

Since we want to drive the auxiliary levels with $\eta = 1(\eta = 2)$ towards occupancy zero (one), they should be Lindblad-driven only by annihilation (creation) operators, respectively. Using the same Lindblad rates γ_q for both, we thus choose

$$\tilde{\lambda}^{(1)}_{q\eta} = \delta_{\eta,1}\,\gamma_q, \quad \tilde{\lambda}^{(2)}_{q\eta} = \delta_{\eta,2}\,\gamma_q. \quad (67)$$

The rates $\tilde{\lambda}^{(\pm)}_{q\eta} = \tilde{\lambda}^{(1)}_{q\eta} \pm \tilde{\lambda}^{(2)}_{q\eta}$ are then given by

$$\tilde{\lambda}^{(+)}_{q\eta} = \gamma_q, \quad (68a)$$

which is independent of η, and

$$\tilde{\lambda}^{(-)}_{q\eta} = \begin{cases} +\gamma_q, & \text{for } \eta = 1, \\ -\gamma_q, & \text{for } \eta = 2. \end{cases} \quad (68b)$$

To see that the effect of the leads on the impurity is indeed the same in the local and nonlocal schemes, we note that level-doubling replaces the original hybridization function, given by Eq. (31a), by

$$\tilde{\Delta}^{R/K}_{ij,\alpha}(\omega) = \sum_{k\eta}\tilde{v}_{iq\eta}\tilde{v}^*_{jq\eta}\,\tilde{g}^{R/K}_{q\eta,q\eta}(\omega), \quad (69)$$

where the correlators $\tilde{g}^{R/K}_{q\eta,q\eta}(\omega)$ are given by Eq. (41) with q replaced by $\{q\eta\}$ and $\lambda^{(\pm)}$ by $\tilde{\lambda}^{(\pm)}$. Equation (69) yields expressions identically equal to the original hybridization (31a). For the retarded component, this follows from

$$\sum_\eta \tilde{v}_{iq\eta}\tilde{v}^*_{jq\eta} = v_{iq}v^*_{jq}. \quad (70a)$$

Similarly, the Keldysh component is the same as the original one since

$$\sum_\eta \tilde{\lambda}^{(-)}_{q\eta}\tilde{v}_{iq\eta}\tilde{v}^*_{jq\eta} = \lambda^{(-)}_q v_{iq}v^*_{jq}. \quad (70b)$$

The last equation explicitly shows how, when passing from the nonlocal to the local setup, the Fermi-function information encoded in the Lindblad rates $\lambda^{(-)}_q$ of the former is shifted into the couplings $\tilde{v}_{iq\eta}$ of the latter. This is illustrated schematically in Fig. 8(b).

For a uniform discretization in energy space, the rates γ_q can be chosen independent of q. Hence, the level-doubled Lindblad matrices $\tilde{\Lambda}^{(1,2)}$ for each $\eta = 1,2$ are separately proportional to the identity. Thus they will remain so under the linear transformations used to map impurity models to quantum chains, provided that these transformations do not mix the two "channels" $\eta = 1$ and $\eta = 2$. We have thus found what we were looking for: an LDDL scheme reproducing the correct hybridization with Lindblad driving terms that will remain local when the leads are represented in terms of chains.

At first glance, the local setup comes at a high price, namely twice as many lead levels as before, due to the additional label η. This, however, is not the full truth: for all levels with energies

$|\varepsilon_k - \mu_\alpha| \gg T_\alpha$, the value of the Fermi function $f_\alpha(\varepsilon_q)$ will be either one or zero. Therefore, by Eq. (65) either $\tilde{v}_{iq,\eta=1}$ or $\tilde{v}_{iq,\eta=2}$ will vanish, implying that one of the two corresponding auxiliary modes, with either $\eta = 1$ or 2, will decouple from the impurity [indicated by grey shading in Fig. 8(b)]. Thus the number of impurity-coupled auxiliary levels in each lead is actually equal to the number of original levels throughout the energy ranges where the Fermi function equals 1 or 0, and twice that number only in the intermediate range that encompasses the step in $f_\alpha(\varepsilon_k)$. In particular, for $T \to 0$, this intermediate range shrinks to zero.

Moreover, the local setup results in a further major simplification stemming from the fact that its Lindblad rates $\tilde{\lambda}^{(1,2)}$ are independent of α: depending on the exact form of the impurity and the coupling to the impurity, certain linear combinations of auxiliary modes from *different* leads may decouple. We illustrate this for the case of two spinless leads $\alpha = \{L, R\}$ coupled to one spinless impurity level, using the same discretization for the two leads, $\varepsilon_{\alpha k} = \varepsilon_k$. For such a model, the index $i = 1 = d$ can be dropped in the coupling matrix elements. Hence we can combine the auxiliary modes $\{Lk\eta\}$ and $\{Rk\eta\}$ by defining

$$\tilde{b}_{k\eta} = \frac{1}{\sqrt{\sum_\alpha |\tilde{v}_{\alpha k\eta}|^2}} (\tilde{v}_{Lk\eta}\tilde{c}_{Lk\eta} + \tilde{v}_{Rk\eta}\tilde{c}_{Rk\eta}), \tag{71a}$$

$$\tilde{b}'_{k\eta} = \frac{1}{\sqrt{\sum_\alpha |\tilde{v}_{\alpha k\eta}|^2}} (\tilde{v}_{Rk\eta}\tilde{c}_{Lk\eta} - \tilde{v}_{Lk\eta}\tilde{c}_{Rk\eta}). \tag{71b}$$

Only the $\tilde{b}_{k\eta}$ modes couple to the impurity, whereas the $\tilde{b}'_{k\eta}$ modes do not. This is completely analogous to what is done for such models in equilibrium calculations. In nonequilibrium, however, where $f_L \neq f_R$, such a transformation would not have been useful if performed in the original nonlocal setup, because the original Lindblad rates $\lambda^{(1,2)}$ actually depend on f_α, so that transforming them using (71) would generate a coupling between the modes $\tilde{b}_{k\eta}$ and $\tilde{b}'_{k\eta}$ via the dissipative Lindblad terms. In the local setup, however, where the $\tilde{\lambda}^{(1,2)}$ are independent of α, no such coupling is generated, so that the $\tilde{b}'_{k\eta}$ modes decouple altogether. We are thus left with only two impurity-coupled auxiliary channels, with modes $\tilde{b}_{k1}$ and $\tilde{b}_{k2}$, but they have a completely different interpretation than the two physical leads from which we started, with modes c_{kL} and c_{kR}. This is illustrated in Fig. 8(c): it depicts the linear combinations $\tilde{b}_{k\eta}$ in Eq. (71) that couple to the impurity using double lines. The modes $\tilde{b}'_{k\eta}$ are omitted as they decouple from the model.

Figures 8(c) and 8(a) together nicely summarize the level count of impurity-coupled auxiliary versus original levels. Within the dynamical window, defined by the energy range in which $f_L(\varepsilon_q) \neq f_R(\varepsilon_q)$, the number of impurity-coupled auxiliary lead levels in the local setup [Figs. 8(c)] is the same as the number of physical lead levels in the original nonlocal setup [Figs. 8(a)], corresponding to a full two-channel calculation. Outside the dynamical window, where $f_L(\varepsilon_q) = f_R(\varepsilon_q) = 1$ (or 0), the auxiliary levels corresponding to $\eta = 1$ (or 2) decouple from the impurity (as indicated by grey shading), hence here the number of impurity-coupled auxiliary levels equals half the number of original levels. This reduction of levels is easily understood considering that outside the dynamical window we effectively have an equilibrium situation (in that $f_L(\varepsilon_q) = f_R(\varepsilon_q)$ there) and can therefore use the same decoupling transformation as that used routinely in equilibrium calculations. Note also that in the special case of $T = 0$, the modes $\tilde{b}_{k\eta}$ within the dynamical window are identical to either $\tilde{c}_{Lk\eta}$ or $\tilde{c}_{Rk\eta}$.

Of course, such a decoupling of modes is not guaranteed to occur in general for multi-level models. For example, it does not happen for a model with more than one impurity level where each impurity level couples differently to the leads.

The operators from the original nonlocal and new local setups, $c_{\alpha k}$ and $\tilde{c}_{\alpha k\eta}$, are obviously not related by any unitary transformation (after all, they even differ in number). Expressions for the currents into the leads α therefore have to be found using the new Lindblad equation in the local chain representation. Given the fact that the lead index α is still a well-defined quantity, this can straightforwardly be done by evaluating $e\dot{N}_d = 0 = \sum_\alpha J_\alpha$ analogously to Sec. III E, resulting in expressions analogous to Eq. (54), with $q \to q\eta$ and $\sum_k \to \sum_{k\eta}$. For the above example of one spinless local mode coupled to two spinless leads, the expectation values $\langle \tilde{c}^\dagger_{\alpha k\eta} c_d \rangle_{\text{NESS}}$ needed for the evaluation of the current can then be expressed in terms of $\langle \tilde{b}^\dagger_{k\eta} c_d \rangle_{\text{NESS}}$:

$$\langle \tilde{c}^\dagger_{\alpha k\eta} c_d \rangle_{\text{NESS}} = \frac{1}{\sqrt{\sum_\alpha |\tilde{v}_{\alpha k\eta}|^2}} \tilde{v}_{\alpha k\eta} \langle \tilde{b}^\dagger_{k\eta} c_d \rangle_{\text{NESS}}, \tag{72}$$

where we used the fact that the mode $\tilde{b}'_{k\eta}$ decouples from the impurity level, $\langle \tilde{b}'^\dagger_{k\eta} c_d \rangle_{\text{NESS}} = 0$.

For the RLM it is straightforward to verify that Eqs. (17) and (25) yield the same results for $G^R_{dd}(\omega)$ and $G^K_{dd}(\omega)$ when evaluated within the local setup as in the original nonlocal setup [Eqs. (50a) and (51a)]. Analogously, also the results for the current (55) and the occupation of the local level (58) can easily be reproduced.

Let us note that this concept of representing thermal leads by "holes" and "particles" with couplings that depend on the Fermi function has also be found using the thermofield approach [58].

V. LOGARITHMIC-LINEAR DISCRETIZATION

In quantum impurity models, it is often of great interest to consider a wide range of different energy scales, e.g., for models exhibiting Kondo physics. Within the numerical renormalization group, one therefore uses a logarithmic discretization, $\varepsilon_k \sim \pm D\Lambda^{-k}$ with $\Lambda > 1$. This leads to a very efficient description of the renormalization of impurity properties, since much fewer discrete levels are needed to reach low energy scales than when discretizing linearly. For such a logarithmic discretization, it is necessary to have an explicit energy reference, the physics around which is resolved in greater detail. In equilibrium, this reference point is defined by the chemical potential. In contrast, in situations of steady-state nonequilibrium, there is not one single Fermi edge, but a dynamical window that needs to be described accurately, defined by the energy range contributing to transport. Within this window a logarithmic discretization does not seem to be appropriate. Therefore a more flexible discretization scheme is desirable [59–61]. Here, we advocate the use of

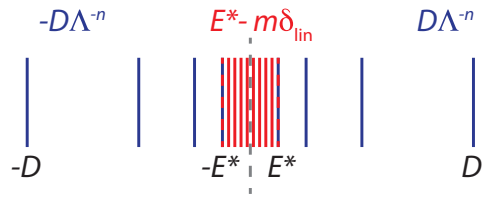

FIG. 9. Sketch of the suggested discretization: the high-energy intervals are discretized logarithmically, while a window $[-E^*, E^*]$ large enough compared to the dynamical window is discretized linearly.

a "logarithmic-linear" discretization scheme which is linear within a window sufficiently large compared to the dynamical window and logarithmic for energies outside this range, similar to the approach used in Ref. [62]. The underlying rationale is that within the dynamical window there is no energy scale separation. Therefore the discretization should not introduce any artificial structure to the calculation, and thus be uniform. Here, we assume a symmetric setup and therefore a symmetric range $[-E^*, E^*]$ that is discretized linearly with level spacing $\delta_{\rm lin}$, as depicted in Fig. 9.

We have argued above that the strength of the Lindblad driving γ_q for a given lead level should be comparable to or larger than the width δ_q of the corresponding energy interval. Furthermore, γ_q needs to be q-*in*dependent to permit the mapping onto a local chain that we suggested in Sec. IV. This seems to be incompatible with the logarithmic discretization scheme, since the latter features energy intervals whose widths depend on q. Note, though, that the logarithmically discretized regime by construction describes excitations on energy scales much larger than the energy scales on which transport takes place. These excitations are not affected by nonequilibrium physics but are only involved in renormalization effects, which (as we know from the success of NRG) are well described even if these levels are not broadened at all. In other words, the condition $\delta_q \simeq \gamma_q$ is not needed for energy scales far outside the transport window, but only for levels that are involved in dissipative effects. We may thus use a Lindblad driving $\gamma_q = \gamma = \delta_{\rm lin}$ for the logarithmically discretized states as well, although this is much smaller than the widths of the corresponding energy intervals. Note that this implies that, if one solves the Lindblad equation numerically using time evolution or some optimization scheme, the starting state should be chosen close enough to the steady state (which for the high-energy states means low enough in energy), because high-energy modes are barely damped. Also, as mentioned earlier, the Lindblad driving does not need to broaden the peak structure arising from the discretization. If needed, this broadening of the discrete peak structure can be done by hand after solving the Lindblad equation, analogously to the broadening in equilibrium NRG calculations [9,50].

Below, we will discuss the implications of the choice $\gamma_q = \gamma = \delta_{\rm lin}$ within the RLM, bearing in mind a caveat: for the RLM the nonequilibrium Green's function $G^R_{dd}(\omega)$ is equal to its equilibrium pendant, which is not true for general interacting impurity models. Therefore the RLM does not allow a fully general check whether the choice $\gamma_q = \gamma = \delta_{\rm lin}$ is able to capture all nonequilibrium properties of the high-energy states occurring in this Green's function. This will be left for future studies.

In Figs. 10(a) and 10(b), we plot the current for the spinless RLM as given in Eq. (55) again using the symmetric setup defined in (57) with the same discretization for both leads. Here, however, we use the suggested discretization with energy intervals $[\pm\Lambda^{-(n-1)}, \pm\Lambda^{-n}]$ for $n = 1, \ldots, N_{\log}$, where $N_{\log}$ is defined by $\Lambda^{-N_{\log}} = E^*$. The window $[-E^*, E^*]$ is discretized linearly using $2N_{\rm lin}$ energy intervals of size $\delta_{\rm lin} = E^*/N_{\rm lin}$. For the prefactor of the Lindblad driving we use $\gamma_q = \gamma = \delta_{\rm lin}$ for both the logarithmically and the linearly discretized energy intervals. The current is plotted for different values of $N_{\log}$ corresponding to different values of E^*. The level spacing is kept approximately the same, which means that more levels are needed for larger E^*. Evidently, if E^* is large enough and $\delta_{\rm lin}$ small enough, it is possible to reproduce the value for the current that one obtains in calculations using continuous thermal leads. Furthermore, the two plots illustrate which energy range should be resolved linearly: In the first panel, we have $T \ll V$. Here, the dynamical window is defined by the two chemical potentials and the full current is only recovered if $E^* \gtrsim 1.2\mu_L = -1.2\mu_R$. In the second panel, temperature becomes the relevant energy scale due to $T \gg V$,

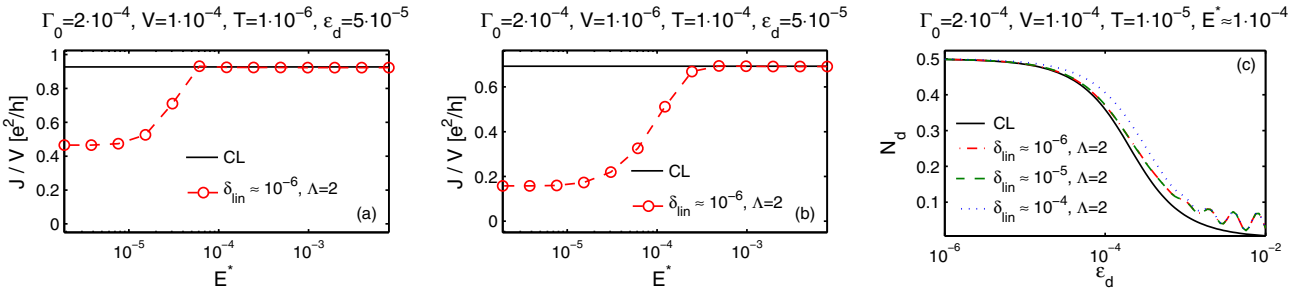

FIG. 10. (a) and (b) show the current through the local level of the RLM as given by Eq. (55) using a discretization, which is linear within the dynamical window $[-E^*, E^*]$ and logarithmic outside as a function of E^*. In (a), the voltage is large compared to temperature and the correct value for the current can only be obtained if $E^* \gtrsim 1.2\mu_L = -1.2\mu_R$. In (b), temperature is larger than voltage and $E^* \gtrsim 4T$ is needed. In (c), the occupation of the local level in the RLM as given by Eq. (58) is shown as a function of the level position ε_d, again using the logarithmic-linear discretization. For $\varepsilon_d \gtrsim E^*$ we see deviations from the CL result, see Appendix A for details. For all three panels, $\Lambda = 2$ and we used $\gamma_q = \gamma = \delta_{\rm lin}$ for the linear and the logarithmic states. The number of lead levels is approximately given by $M_{\rm lin} = 2E^*/\delta_{\rm lin}$ plus $M_{\log} = -2\log(E^*)/\log(\Lambda)$.

the two Fermi functions differ in an energy range defined by temperature, and therefore $E^* \gtrsim 4 \cdot T$ is needed.

Figure 10(c) shows the occupation number of the local level given in (58) as function of the level position ε_d. Only positive values of ε_d are considered. The occupation for negative level position ε_d can be deduced from this data by $N_d(-\varepsilon_d) = 1 - N_d(\varepsilon_d)$. This relation can be shown both for the Lindblad result (58) as well as for the result of continuous leads (60). Here, the suggested discretization only works well for $\varepsilon_d \lesssim E^*$. For $\varepsilon_d \gtrsim E^*$, the Lindblad result for the occupation number deviates from the value obtained for continuous leads. This deviation is independent of δ_{lin} and shows oscillations that correspond to the logarithmically discretized lead levels. This indicates that the error stems from the logarithmically discretized part of the lead.

At first glance, it is not surprising that an error arises when ε_d becomes so large that it falls within the logarithmic discretized part of the spectrum. In this case, the energy range around ε_d where the relevant physics takes place is not sufficiently resolved. Note though that for large ε_d standard NRG calculations using a logarithmic discretization for the full energy range are able to determine the equilibrium occupation number with a much higher accuracy than the LDDL approach with logarithmic-linear discretization. Therefore a detailed analysis of how this error comes about and how its effects can be minimized is offered in Appendix A.

Let us finally comment on the use of the numerical renormalization group within the LDDL setup. Applying the mapping onto a local chain as described in Sec. IV, the hoppings corresponding to the logarithmically discretized energy range will fall off exponentially, as for standard NRG Wilson chains [8,9]. Thus it should be possible to construct an effective many-body basis for this part of the chain using NRG [63,64]. Assuming that the nonequilibrium at low energy scales does not affect the high-energy physics, standard NRG truncation of this basis is justified. For the treatment of the linearly discretized dynamical window there is no energy-scale separation and other MPS techniques such as tDMRG [65–67] have to be used. This approach is in close analogy to the hybrid NRG-DMRG approach of Ref. [61].

VI. CONCLUSION AND OUTLOOK

In summary, we have explored the suitability of Lindblad-driven discretized leads for the description of nonequilibrium steady-state physics in models in which a correlated impurity is coupled to noninteracting leads and each lead is independently held at a fixed chemical potential and temperature. For quadratic models governed by Lindbladian dynamics we have introduced a simple approach to calculate steady-state Green's functions. We have shown that the additional Lindblad reservoirs introduce a broadening for the discretized lead levels and that the Lindblad rates can be tuned to provide an exact representation of thermal reservoirs in the continuum limit. The approach, therefore, is appropriate for the description of steady-state nonequilibrium of arbitrary impurities of the kind that arises due to an applied voltage or temperature difference. For the quadratic resonant level with applied voltage, we analytically calculated the current through the local level and the occupation of the local level within the Lindblad setup and found perfect agreement with the results that one obtains using standard calculations for continuous thermal leads.

To explore heat current due to an applied temperature difference, one could study how the energies of the leads change due to their coupling to the impurity, starting from $\dot{H}_{L/R}$ to define left and right energy currents, in a manner similar to the definitions used here for the charge current.

Finally, we presented first steps towards a future numerical determination of the steady state using MPS/MPO methods, showing how the leads can be represented in terms of chains with the desirable property that both the Lindblad driving terms and the Hamiltonian dynamics are local. We also advocated the use of a logarithmic-linear discretization scheme in this context that should permit the exploration of exponentially small energy scales.

Our analysis shows that the LDDL approach constitutes a promising starting point for a systematic treatment of quantum impurity models in steady-state nonequilibrium using MPS/MPO-based numerical approaches. Future work will have to explore which of these approaches targeting the steady-state solution of the Lindblad equation turns out to be the most efficient.

ACKNOWLEDGMENTS

We acknowledge fruitful discussions with I. Weymann, T. Prosen and H. Kim. This work was supported by the German-Israeli-Foundation through I-1259-303.10. F.S., A.W., and J.v.D. were also supported by the Deutsche Forschungsgemeinschaft through SFB631, SFB-TR12, and NIM. A.W. was also supported by WE4819/1-1 and WE4819/2-1. M.G. was also supported by the Israel Science Foundation (Grant No. 227/15) and the US-Israel Binational Science Foundation (Grant No. 2014262). A.D. and E.A. were supported by the Austrian Science Fund (FWF): P24081 and P26508, and by NAWI Graz.

APPENDIX A: DETAILED ERROR ANALYSIS FOR THE LOGARITHMIC-LINEAR DISCRETIZATION DISCUSSED IN SEC. V

In Sec. V, we have seen that for a discretization that is logarithmic for high energies and linear within the dynamical window, the occupation of the local level in the RLM calculated using the LDDL scheme deviates from the exact continuum result. This error appears if the position of the local level ε_d lies within the logarithmically discretized energy range. Moreover, this error is independent of δ_{lin} and shows oscillations that correspond to the logarithmically discretized lead levels.

To understand where this deviation comes from, we divide the integrand in Eq. (58) into two parts, $|G^R_{dd;\text{DL}}(\omega)|^2$ and $\sum_q f_\alpha(\varepsilon_k)|v_q|^2\,\delta_{\gamma_q}(\omega-\varepsilon_k)$. These functions have to be compared to $|G^R_{dd;\text{CL}}(\omega)|^2$ and $\sum_\alpha f_\alpha(\omega)\Gamma_{\alpha;\text{CL}}(\omega)$ in Eq. (60). Assume now that $\varepsilon_d \gg E^*$. In this case, $G^R_{dd;\text{DL}}(\omega)$ is nonzero mainly for $\omega > E^*$. In this ω region, the sum over q consists of tails of Lorentz peaks stemming from the lead levels with ε_k below or within the dynamical window only, while the contribution of all other levels is exponentially suppressed by $f_\alpha(\varepsilon_k) \approx 0$. Hence, for $\omega > E^*$, the sum over q in Eq. (58) is

polynomially suppressed by the small peak width γ, whereas the corresponding expression for continuous leads in (60) is *exponentially* suppressed by the Fermi functions $f_\alpha(\omega)$. The small but finite overlap of the Lorentz tails with the function $|G^R_{dd;\mathrm{DL}}(\omega)|^2$ in (58), which does not exist in the exact formula (60), is the explanation for the deviation of the Lindblad result from the CL value.

But why is this error independent of $\gamma = \delta_{\mathrm{lin}}$, although the Lorentz tails obviously scale with γ? The answer lies in the peak structure of $|G^R_{dd;\mathrm{DL}}(\omega)|^2$. For $|\omega| > E^*$, the lead is logarithmically discretized and the Lindblad broadening $\gamma = \delta_{\mathrm{lin}}$ is small compared to the size of the underlying energy intervals. Therefore $|G^R_{dd;\mathrm{DL}}(\omega)|^2$ contains sharp peaks in this ω region and the peak widths scale with γ. However, because $G^R_{dd;\mathrm{DL}}(\omega)$ is a physical Green's function, the area beneath the real and imaginary parts of this function is represented correctly and therefore independent of γ. Assuming that the peaks are well separated, this implies, that the integral over $|G^R_{dd;\mathrm{DL}}(\omega)|^2$ scales approximately with γ^{-1} in this logarithmically discretized region. Decreasing $\delta_{\mathrm{lin}} = \gamma$, therefore, does not reduce the error in the occupation number, because, while the sum over the tails of the Lorentz functions scales with γ, the area of $|G^R_{dd;\mathrm{DL}}(\omega)|^2$ scales with γ^{-1}, leaving the total error approximately the same.

In contrast, if ε_d lies within the dynamical window, the main contribution of $|G^R_{dd;\mathrm{DL}}(\omega)|^2$ (and therefore the main contribution of the integrand) lies within the linearly discretized window. Here, the peaks of $|G^R_{dd;\mathrm{DL}}(\omega)|^2$ strongly overlap and therefore the integral over $|G^R_{dd;\mathrm{DL}}(\omega)|^2$ is γ-independent. In other words, the integrand is represented as a smooth function within the linearly discretized window. Hence, if $\delta_{\mathrm{lin}} = \gamma$ is small enough to resolve all relevant features, the integrand coincides with the exact CL integrand and no error is observed.

The occupation of the local level for negative ε_d can be deduced by $N_d(-\varepsilon_d) = 1 - N_d(\varepsilon_d)$. Therefore, for $\varepsilon_d \ll -E^*$, an error analogous to that for $\varepsilon_d \gg E^*$ occurs.

One possibility to avoid the error is to replace the sum over q by its continuum counterpart: $\sum_q f_\alpha(\varepsilon_k)|v_q|^2\,\pi\delta_{\gamma_q}(\omega - \varepsilon_k) \to \sum_\alpha f_\alpha(\omega)\Gamma_{\alpha;\mathrm{CL}}(\omega)$. This is equivalent to using the standard form of the occupation number given by the continuum limit of Eq. (60a) but with the exact Green's function replaced by the Green's function deduced from Lindblad formalism. In general, i.e., also for interacting models, which cannot be solved analytically, this procedure corresponds to deducing only the Green's function from the Lindblad approach and then calculating the occupation number using standard Green's function techniques. (Note, though, that numerically evaluating $G^R_{dd;\mathrm{DL}}(\omega)$ can be computationally more demanding than simply evaluating expectation values. For example, this is the case in the quantum trajectory approach.)

Why does the error not occur for a linear discretization? In fact, it does, but can be scaled down using more lead levels. When discretizing the full bandwidth $[-D, D]$ linearly, $|G^R_{dd;\mathrm{DL}}(\omega)|^2$ is represented by a smooth function within the full band, because the Lindblad broadening is comparable to the size of the energy intervals everywhere. The area beneath $|G^R_{dd;\mathrm{DL}}(\omega)|^2$, therefore, does not depend on γ, while the contribution of the Lorentz tails for large ω can be reduced using a smaller value of $\delta = \gamma$. (Note that the number of lead levels q that we sum over, scales with $\delta^{-1} \sim \gamma^{-1}$. However, this γ dependence is canceled by the γ dependence of $|v_q|^2$, which scales with $\delta \sim \gamma$. Therefore the scaling of $\sum_q f_\alpha(\varepsilon_k)|v_q|^2\,\pi\delta_{\gamma_q}(\omega - \varepsilon_k)$ with γ stemming from the Lorentz tails is preserved.) Nonetheless, also for a linear discretization, it could be advisable to replace the sum over q by its continuum representation as described above to reduce the error for a fixed number of states.

Another question arising immediately is why this kind of error is not visible in the current. If we look at Eq. (55) we find two major differences compared to the analysis of the occupation number above. First, the sum over the lead levels $\sum_k |v_k|^2\,\pi\delta_{\gamma_k}(\omega - \varepsilon_k)(f_L(\varepsilon_k) - f_R(\varepsilon_k))$ contains the difference of Fermi functions instead of a sum. This implies that only the lead levels corresponding to the linearly discretized dynamical window contribute, while the contribution of the logarithmically discretized intervals is exponentially suppressed. Nevertheless, the tails of the Lorentz peaks in this sum leak out to high values of $|\omega|$, whereas in the formula for continuous thermal leads contributions from this ω range are exponentially suppressed. The second and relevant difference is the fact that, while the sum over k is multiplied by $|G^R_{dd;\mathrm{DL}}(\omega)|^2$ in the formula for the occupation of the local level, it is multiplied by $\mathrm{Im}(G^R_{dd;\mathrm{DL}}(\omega))$ in the formula for the current. Both functions are strongly peaked in the logarithmically discretized region, but as explained above, the integral over $\mathrm{Im}(G^R_{dd;\mathrm{DL}}(\omega))$ is independent of γ, whereas the integral over $|G^R_{dd;\mathrm{DL}}(\omega)|^2$ scales with γ^{-1}. Due to this difference, the error in the occupation number is independent of γ while the error in the current is proportional to γ and can therefore be reduced using smaller $\delta_{\mathrm{lin}} = \gamma$. But again, for fixed δ_{lin}, it could be possible to reduce the error of the Lindblad result by using the continuum analog of the sum over k, analogously to what was described for the occupation number above.

APPENDIX B: QUANTUM REGRESSION THEOREM FOR FERMION OPERATORS

In this Appendix, we derive the Lindblad equation Eq. (13) for $\varrho_C(t)$, in which the operator C from Eq. (4a) contains an odd number of fermionic operators. It is an extension of the so-called quantum regression theorem (QRT) [44,47,68] to the case of fermionic operators [69].

1. Time evolution of reduced density matrix

We start by showing that in the fermionic case the density matrix itself obeys the same Lindblad equation (10) as for bosons. The usual derivation of the Lindblad equation within the Born-Markov approximation (BMA) [44,47,68][2] starts from a system-reservoir Hamiltonian in the form of a sum of tensor products of operators acting on the system and reservoir separately. For the fermionic case, however, one generally has

[2]The same derivation applies for the so-called singular-coupling limit [44,47,68].

a system-reservoir Hamiltonian of the form

$$H_{S,R} = \sum_{\alpha} r_\alpha s_\alpha + \text{H.c.}, \tag{B1}$$

where r_α (s_α) are reservoir (system) operators containing an odd number of fermionic operators, i.e.,

$$\{s_\alpha, r_\beta\} = 0\,. \tag{B2}$$

Since the operators r_α and s_α *anti*commute, (B1) cannot be interpreted as a tensor product between operators acting independently on the reservoir ($\mathcal{H}_R$) and system ($\mathcal{H}_S$) Hilbert spaces. For the sake of clarity, in the present Appendix it will be convenient to distinguish between when a particular operator, such as, e.g., s_α acts on the reservoir-system product Hilbert space $\mathcal{H}_{RS}$ or just on one of the two separate spaces. In the latter case, we will add a hat ("ˆ") to the operator. (In the main text, we do not use hats because there nearly all operators act on the system's Hilbert space and the few exceptions can easily be recognized from the context.) For definiteness, we adopt the convention that product states in $\mathcal{H}_{RS}$ are understood in the following order:

$$|R\rangle \otimes |S\rangle\,, \tag{B3}$$

where $|R\rangle \in \mathcal{H}_R$ and $|S\rangle \in \mathcal{H}_S$. Due to the properties of fermion operators we, thus, have the relation

$$s_\alpha = (-1)^{\hat{N}_R} \otimes \hat{s}_\alpha, \tag{B4}$$

$$r_\alpha = \hat{r}_\alpha \otimes \hat{\mathbb{I}}_S, \tag{B5}$$

where $N_R = \hat{N}_R \otimes \hat{\mathbb{I}}_S$ is the operator counting the number of fermions in the reservoir. With this notation, (B1) can be written in tensor form as

$$H_{S,R} = \sum_{\alpha} \hat{R}_\alpha \otimes \hat{s}_\alpha\,. \tag{B6}$$

where we have introduced

$$\hat{R}_\alpha \equiv \hat{r}_\alpha (-1)^{\hat{N}_R}\,. \tag{B7}$$

In this form, it is possible to directly apply the standard BMA derivation of the Lindblad equation [44,47,68]. According to that derivation, the expression for its coefficients depend on the Fourier transforms of the unperturbed reservoir correlation functions [44,47,68]

$$C_{\alpha,\beta}(t) = \text{tr}_R(\hat{R}^\dagger_\alpha(t)\hat{R}_\beta\hat{\rho}_R), \tag{B8}$$

with $\hat{R}_\alpha(t) = e^{i\hat{H}_R t}\hat{R}_\alpha e^{-i\hat{H}_R t}$. The only requirement is that one starts with a reservoir-system Hamiltonian in the form of a tensor product. These correlation functions can be rewritten as

$$\begin{aligned} C_{\alpha,\beta}(t) &= \text{tr}_R((-1)^{\hat{N}_R(t)}\,\hat{r}^\dagger_\alpha(t)\hat{r}_\beta\,(-1)^{\hat{N}_R}\hat{\rho}_R) \\ &= \text{tr}_R(\hat{r}^\dagger_\alpha(t)\hat{r}_\beta\hat{\rho}_R), \end{aligned} \tag{B9}$$

where we have used the fact $(-1)^{\hat{N}_R}$ commutes with the reservoir Hamiltonian[3] and, therefore, it is time independent. This means that the Lindblad equation controlling the time dependence of the *reduced density matrix* of fermionic systems has the same form as for bosonic ones, including its coefficients $C_{\alpha,\beta}$.

2. Time evolution of fermionic operators

The situation is different when considering correlation functions for operators of the system, defined as

$$G_{\beta,\alpha}(t) \equiv \text{tr}_{\text{full}}(s^\dagger_\beta(t)\,s_\alpha\rho_{\text{full}}) = \text{tr}_{\text{full}}(s^\dagger_\beta(s_\alpha\rho_{\text{full}})_t), \tag{B10}$$

where $(\dots)_t = e^{-iH_{\text{full}}t}(\dots)e^{iH_{\text{full}}t}$ indicates density-matrix-type time evolution as in Eq. (4b). The standard QRT [44,47,68] states that, within the BMA assumptions, the time evolution of operators of the form $\hat{\varrho}_C(t) = \text{tr}_R(C\rho_{\text{full}})_t$ are governed by the same Lindblad equation as $\hat{\rho}(t)$, namely (5). However, this theorem holds for operators C of the form $C = \hat{\mathbb{I}}_R \otimes \hat{X}_S$. As discussed above, due to the fermionic anticommutation rules, s_α does not have this form. However, it is possible to transcribe Eq. (B10) into a form in which the standard QRT can be applied by using the following scheme to keep track of fermionic sign factors:

$$\begin{aligned} G_{\beta,\alpha}(t) &= \text{tr}_{\text{full}}(s^\dagger_\beta(-1)^N((-1)^N s_\alpha\rho_{\text{full}})_t) \\ &= \text{tr}_{\text{full}}(S^\dagger_\beta(-1)^{N_S}((-1)^{N_S} S_\alpha\rho_{\text{full}})_t) \\ &= \text{tr}_S(\hat{s}^\dagger_\beta(-1)^{\hat{N}_S}\,\text{tr}_R((-1)^{N_S} S_\alpha\rho_{\text{full}})_t), \end{aligned} \tag{B11}$$

where $N_S = \hat{\mathbb{I}}_R \otimes \hat{N}_S$ counts the number of particles in the system. In the first line we exploited the fact that the operator for the total number of particles in system and reservoir, $N = N_S + N_R$, commutes with H_{full}. In the second line, we introduced the operator

$$S_\alpha \equiv (-1)^{N_R}\,s_\alpha = \hat{\mathbb{I}}_R \otimes \hat{s}_\alpha\,, \tag{B12}$$

which *commutes* with the reservoir operators r_β. Equation (B11) can be now cast in the form

$$G_{\beta,\alpha}(t) = \text{tr}_S(\hat{s}^\dagger_\beta\hat{\varrho}_\alpha(t)), \tag{B13}$$

where we introduced

$$\begin{aligned} \hat{\varrho}_\alpha(t) &\equiv (-1)^{\hat{N}_S}\,\text{tr}_R((-1)^{N_S}\,S_\alpha\,\rho_{\text{full}})_t \\ &= (-1)^{\hat{N}_S}\,\text{tr}_R((\hat{\mathbb{I}}_R \otimes (-1)^{\hat{N}_S}\,\hat{s}_\alpha)\,\rho_{\text{full}})_t, \end{aligned} \tag{B14}$$

which for $t = 0$ reduces to $\hat{s}_\alpha$ applied to the reduced system density matrix:[4]

$$\hat{\varrho}_\alpha(0) = \text{tr}_R(S_\alpha\rho_{\text{full}}) = \hat{s}_\alpha\hat{\rho}. \tag{B15}$$

Now, the operator multiplied to ρ_{full} in the last line in (B14) has the required form $\hat{\mathbb{I}}_R \otimes \hat{X}_S$, so that, within the usual BMA assumptions, the QRT applies to the time dependence of the reservoir trace in (B14). Therefore the time evolution of $\hat{\varrho}_\alpha(t)$

[3] This would hold for a superconductor as well.

[4] As for the bosonic case, ρ can be previously have been time evolved up to a certain time t_1, which in steady state would be $t_1 = \infty$.

yields

$$\frac{d}{dt}\hat{\varrho}_\alpha(t) = (-1)^{\hat{N}_S}\mathcal{L}(\mathrm{tr}_R((-1)^{N_S}S_\alpha\rho_{\mathrm{full}})_t) \equiv \underline{\mathcal{L}}(\hat{\varrho}_\alpha(t)). \quad \text{(B16)}$$

Here, $\underline{\mathcal{L}}$ differs from Eq. (5) by having a minus sign in front of the $2\hat{J}_m\hat{\rho}(t)\hat{J}_m^\dagger$ term, whenever $\hat{J}_m$ is a fermionic operator. For the quadratic system discussed in Sec. II, this leads to Eq. (13).

[1] E. Boulat, H. Saleur, and P. Schmitteckert, Phys. Rev. Lett. **101**, 140601 (2008).
[2] J. Eckel, F. Heidrich-Meisner, S. G. Jakobs, M. Thorwart, M. Pletyukhov, and R. Egger, New J. Phys. **12**, 043042 (2010).
[3] F. Heidrich-Meisner, A. E. Feiguin, and E. Dagotto, Phys. Rev. B **79**, 235336 (2009).
[4] F. B. Anders, Phys. Rev. Lett. **101**, 066804 (2008).
[5] F. Reininghaus, M. Pletyukhov, and H. Schoeller, Phys. Rev. B **90**, 085121 (2014).
[6] G. Cohen, E. Gull, D. R. Reichman, and A. J. Millis, Phys. Rev. Lett. **112**, 146802 (2014).
[7] A. E. Antipov, Q. Dong, and E. Gull, Phys. Rev. Lett. **116**, 036801 (2016).
[8] K. G. Wilson, Rev. Mod. Phys. **47**, 773 (1975).
[9] R. Bulla, T. A. Costi, and T. Pruschke, Rev. Mod. Phys. **80**, 395 (2008).
[10] A. Rosch, Eur. Phys. J. B **85**, 6 (2012).
[11] A. A. Dzhioev and D. S. Kosov, J. Chem. Phys. **135**, 174111 (2011).
[12] A. A. Dzhioev and D. S. Kosov, J. Chem. Phys. **134**, 044121 (2011).
[13] A. A. Dzhioev and D. S. Kosov, J. Chem. Phys. **134**, 154107 (2011).
[14] A. A. Dzhioev and D. S. Kosov, J. Phys.: Condens. Matter **24**, 225304 (2012).
[15] A. A. Dzhioev and D. S. Kosov, J. Phys. A **47**, 095002 (2014).
[16] A. A. Dzhioev and D. S. Kosov, J. Phys. A **48**, 015004 (2015).
[17] S. Ajisaka, F. Barra, C. Mejía-Monasterio, and T. Prosen, Phys. Rev. B **86**, 125111 (2012).
[18] S. Ajisaka, F. Barra, C. Mejía-Monasterio, and T. Prosen, Phys. Scr. **86**, 058501 (2012).
[19] S. Ajisaka and F. Barra, Phys. Rev. B **87**, 195114 (2013).
[20] E. Arrigoni, M. Knap, and W. von der Linden, Phys. Rev. Lett. **110**, 086403 (2013).
[21] A. Dorda, M. Nuss, W. von der Linden, and E. Arrigoni, Phys. Rev. B **89**, 165105 (2014).
[22] A. Dorda, M. Ganahl, H. G. Evertz, W. von der Linden, and E. Arrigoni, Phys. Rev. B **92**, 125145 (2015).
[23] A. W. Chin, A. Rivas, S. F. Huelga, and M. B. Plenio, J. Math. Phys. **51**, 092109 (2010).
[24] R. Martinazzo, B. Vacchini, K. H. Hughes, and I. Burghardt, J. Chem. Phys. **134**, 011101 (2011).
[25] M. P. Woods, R. Groux, A. W. Chin, S. F. Huelga, and M. B. Plenio, J. Math. Phys. **55**, 032101 (2014).
[26] T. Prosen, J. Stat. Mech. (2010) P07020.
[27] T. Prosen and M. Žnidarič, J. Stat. Mech. (2009) P02035.
[28] T. Prosen, J. Phys. A **48**, 373001 (2015).
[29] T. Prosen and E. Ilievski, Phys. Rev. Lett. **107**, 060403 (2011).
[30] T. Prosen and B. Žunkovič, New J. Phys. **12**, 025016 (2010).
[31] A. Bermudez, M. Bruderer, and M. B. Plenio, Phys. Rev. Lett. **111**, 040601 (2013).
[32] A. Bermudez and T. Schaetz, New J. Phys. **18**, 083006 (2016).
[33] V. Ferrari, G. Chiappe, E. V. Anda, and M. A. Davidovich, Phys. Rev. Lett. **82**, 5088 (1999).
[34] G. Chiappe and J. A. Vergés, J. Phys.: Condens. Matter **15**, 8805 (2003).
[35] E. V. Anda, G. Chiappe, C. A. Büsser, M. A. Davidovich, G. B. Martins, F. Heidrich-Meisner, and E. Dagotto, Phys. Rev. B **78**, 085308 (2008).
[36] A. J. Daley, Adv. Phys. **63**, 77 (2014).
[37] A. H. Werner, D. Jaschke, P. Silvi, M. Kliesch, T. Calarco, J. Eisert, and S. Montangero, Phys. Rev. Lett. **116**, 237201 (2016).
[38] J. Cui, J. I. Cirac, and M. C. Bañuls, Phys. Rev. Lett. **114**, 220601 (2015).
[39] E. Mascarenhas, H. Flayac, and V. Savona, Phys. Rev. A **92**, 022116 (2015).
[40] A. J. Daley, J. M. Taylor, S. Diehl, M. Baranov, and P. Zoller, Phys. Rev. Lett. **102**, 040402 (2009).
[41] H. Pichler, A. J. Daley, and P. Zoller, Phys. Rev. A **82**, 063605 (2010).
[42] A. Kantian, M. Dalmonte, S. Diehl, W. Hofstetter, P. Zoller, and A. J. Daley, Phys. Rev. Lett. **103**, 240401 (2009).
[43] P. Barmettler and C. Kollath, Phys. Rev. A **84**, 041606 (2011).
[44] H.-P. Breuer and F. Petruccione, *The Theory Of Open Quantum Systems* (Oxford University Press, Oxford, 2002).
[45] G. Lindblad, Commun. Math. Phys. **48**, 119 (1976).
[46] G. Lindblad, Commun. Math. Phys. **65**, 281 (1979).
[47] C. W. Gardiner and P. Zoller, *Quantum Noise* (Springer, Berlin, 2000).
[48] H. J. Haug and A.-P. Jauho, *Quantum Kinetics in Transport and Optics of Semiconductors* (Springer, Berlin, 1997).
[49] A. Kamenev, *Field Theory of Non-Equilibrium Systems* (Cambridge University Press, Cambridge, 2011).
[50] A. Weichselbaum and J. von Delft, Phys. Rev. Lett. **99**, 076402 (2007).
[51] S. G. Jakobs, Ph.D. thesis, Aachen, 2010.
[52] Y. Meir and N. S. Wingreen, Phys. Rev. Lett. **68**, 2512 (1992).
[53] A.-P. Jauho, N. S. Wingreen, and Y. Meir, Phys. Rev. B **50**, 5528 (1994).
[54] U. Schollwöck, Ann. Phys. **326**, 96 (2011).
[55] M. B. Plenio and P. L. Knight, Rev. Mod. Phys. **70**, 101 (1998).
[56] L. Bonnes and A. M. Läuchli, arXiv:1411.4831.
[57] F. A. Wolf, I. P. McCulloch, and U. Schollwöck, Phys. Rev. B **90**, 235131 (2014).
[58] I. de Vega and M.-C. Bañuls, Phys. Rev. A **92**, 052116 (2015).
[59] D. Bohr and P. Schmitteckert, Phys. Rev. B **75**, 241103 (2007).
[60] D. Bohr, P. Schmitteckert, and P. Wölfle, Europhys. Lett. **73**, 246 (2006).
[61] F. Güttge, F. B. Anders, U. Schollwöck, E. Eidelstein, and A. Schiller, Phys. Rev. B **87**, 115115 (2013).
[62] A. Weichselbaum, F. Verstraete, U. Schollwöck, J. I. Cirac, and J. von Delft, Phys. Rev. B **80**, 165117 (2009).
[63] F. B. Anders and A. Schiller, Phys. Rev. Lett. **95**, 196801 (2005).
[64] F. B. Anders and A. Schiller, Phys. Rev. B **74**, 245113 (2006).

[65] A. J. Daley, C. Kollath, U. Schollwöck, and G. Vidal, J. Stat. Mech. (2004) P04005.
[66] S. R. White and A. E. Feiguin, Phys. Rev. Lett. **93**, 076401 (2004).
[67] G. Vidal, Phys. Rev. Lett. **93**, 040502 (2004).
[68] H. J. Carmichael, *Statistical Methods in Quantum Optics: Master Equations and Fokker-Planck Equations*, Texts and monographs in physics, Vol. 1 (Springer, Singapore, 2002).
[69] G. Schaller, *Open Quantum Systems Far from Equilibrium*, Lecture Notes in Physics, Vol. 881 (Springer, Heidelberg, 2014).

VI A Quench Approach

This chapter focuses on a quench approach to describe nonequilibrium steady-state transport in impurity models. Instead of extending the system to an *open system* using Lindblad driving, as explained in chapter IV, we work on a *closed system* and accept the fact that we are limited to a finite time window before finite-size effects set in. A description and the definitions of our setup is given in section VI.1. Into our quench calculations we include two important ideas: Based on the *"thermofield approach"* we use a convenient way to describe the thermal state of the leads in terms of *"holes"* and *"particles"*, similar to the lead representation presented in section IV.3.3. This results in an MPS representation of low entanglement, see section VI.2. Furthermore we meet the challenge of describing nonequilibrium at exponentially small energy scales by the use of a hybrid NRG-tDMRG approach, see section VI.3. We implement the quench calculations using the QSpace library, a powerful library for MPS operations, which can exploit Abelian as well as non-Abelian symmetries. Based on these quenches including the above-mentioned concepts we are able to calculate nonequilibrium steady-state currents for the interacting resonant level model, see section VI.4, and the single-impurity Anderson model, see section VI.5. For the latter we are able to describe the zero-bias peak in the conductance at zero temperature, its behavior with increasing temperature, and its splitting due to a finite magnetic field. Most of these results have been published in the article [P2], which is presented in chapter VII. In a last part of the present chapter, we compare our method to the auxiliary master equation approach, see section VI.6.

For better legibility, we set $\hbar = e = k_B = \mu_B = 1$ in this chapter.

VI.1 Quenches in Impurity Models

The basic idea of quenches used to calculate the transport properties of impurity models is simple [38–40, 82, 83] and depicted in figure VI.1: starting with the two leads decoupled from the impurity and held at different chemical potential, the coupling to the impurity is switched on at time $t = 0$. After a transient behavior, the current J through the impurity will approach its steady-state value before at some point in time finite-size effects set in. The initial state of the impurity is not relevant in this reasoning. However, it can have strong influence on the transient behavior. Note that the exact procedure of the quench is not unique, see, e.g., reference [83]. For example, in many cases the coupling between impurity and leads is included when determining the initial state. The time evolution can, e.g., be performed using the time-dependent density-matrix renormalization group, compare section III.2. Typically, these calculations will be limited by the entanglement growth before finite size effects become relevant.

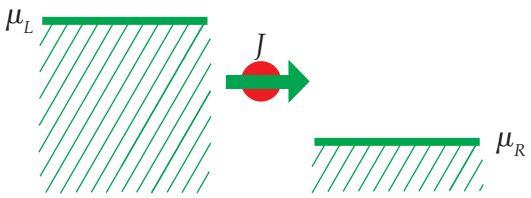

Figure VI.1: Sketch of the quantum quench idea: Starting with two leads decoupled from the impurity and fixed at different chemical potentials, $\mu_L = -\mu_R$, the coupling to the impurity is switched on at time $t = 0$ and a current J starts to flow, which after a transient time approaches the steady-state value.

Our setup includes two leads, $\alpha \in \{L, R\}$. Due to an applied voltage V the chemical potentials in the two leads differ, $\mu_L = -\mu_R = \frac{V}{2}$. For both leads we assume the same temperature $T_\alpha = T = \beta^{-1}$. In the initial state the occupation of the leads has to represent the Fermi distribution

$$f_\alpha(\omega) = \left(1 + \mathrm{e}^{\beta(\omega - \mu_\alpha)}\right)^{-1} . \tag{1.1}$$

The leads are discretized into energy levels k with a corresponding energy ε_k, such that each lead level can be characterized by an index $q = \{\alpha, k, (\sigma)\}$, with σ a potential spin index,

$$H_{\text{lead}} = \sum_{\alpha k(\sigma)} \varepsilon_k c^\dagger_{\alpha k(\sigma)} c_{\alpha k(\sigma)} = \sum_q \varepsilon_q c^\dagger_q c_q \,, \tag{1.2}$$

compare equation (II.1.2).

In this work we consider two different impurity models, the interacting resonant level model and the single-impurity Anderson model, which are introduced in sections II.1.2 and II.1.3. For both models, tDMRG quench calculations have been performed before [38–40, 82, 84]: in particular, P. Schmitteckert calculated full current-voltage characteristics in the IRLM [82], and, among others, F. Heidrich-Meisner, A. Feiguin, and E. Dagotto, pioneered the description of the SIAM based on tDMRG quenches [38].

At zero temperature, the initial state can be found using a DMRG ground state search, a strategy followed in many cases. We, however, adopt a different strategy: for the noninteracting leads in the star geometry, the initial state can be found from analytic arguments. In the *thermofield approach* [85–87] it can be written as a simple product state, see section VI.2. This procedure eliminates the need for an initial DMRG run, comes with a lower entanglement, and can be generalized to finite temperatures. We perform the time evolution of the quench using a hybrid NRG-tDMRG approach [88, 89] based on matrix product states, see section VI.3 for details.

VI.2 The Thermofield Approach

Within the thermofield approach [85–87, 90] a particularly simple representation of the thermal state of the noninteracting leads is found. It involves a *purification* of the density matrix such that it is possible to represent also finite temperature states as an MPS, compare section III.4. But even at $T = 0$ one profits from a thermofield representation of the leads because the thermal state is represented as a *product state* such that one starts the quench with the lowest possible entanglement.

That the thermofield approach itself is a suitable tool in the description of open quantum systems based on MPS was discussed in reference [87] and also employed in reference [91].

Our approach to the thermofield is motivated by the picture of "holes" and "particles" introduced in the context of Lindblad-driven discretized leads in section IV.3.3. To recover this lead representation in terms of empty and filled modes, we modify previous formulations of the thermofield approach regarding its quantum numbers. In particular, this yields the benefit of maintaining particle number conservation.

In section VI.2.1 it is shown how a density matrix of a thermal noninteracting system can be purified analytically. In addition to this purification, in the thermofield approach, one performs a rotation within the state space of physical and auxiliary modes. This is described in section VI.2.2. Section VI.2.3 clarifies the connection to standard purification used in finite temperature DMRG calculations. Finally, section VI.2.4 comments on the transfer of a thermofield representation in the star geometry to a chain representation.

VI.2.1 Purification for a Noninteracting Thermal Lead

The density matrix of a thermal system with temperature $T = \beta^{-1}$ and chemical potential μ is given by

$$\rho(\beta,\mu) = Z^{-1}(\beta,\mu)\, \mathrm{e}^{-(E_n-\mu N_n)}\, |n\rangle\langle n| \tag{2.1}$$

with parition function $Z(\beta,\mu)$, Hamiltonian H, and particle number operator N,

$$Z(\beta,\mu) = \mathrm{tr}\left(\mathrm{e}^{-\beta(H-\mu N)}\right), \quad H|n\rangle = E_n|n\rangle\,, \quad \text{and} \quad N|n\rangle = N_n|n\rangle\,. \tag{2.2}$$

Here, it was assumed that the Hamiltonian preserves the particle number such that H and N can be diagonalized simultaneously. In the purified form as defined in equation (III.4.3b), the *thermal state* is given by

$$|\Omega\rangle = \sum_{n_1 n_2} g_{n_1 n_2}(\beta,\mu)\, |n_1\rangle |n_2\rangle\,, \tag{2.3}$$

with $g_{n_1 n_2}(\beta,\mu)$ chosen such that one recovers the density matrix $\rho(\beta,\mu)$ via

$$\rho(\beta,\mu) = \mathrm{Tr}_{n_2}\left(|\Omega\rangle\langle\Omega|\right) = \sum_{n_2}\langle n_2|\Omega\rangle\langle\Omega|n_2\rangle = \sum_{n_1,n_1'}\sum_{n_2} g_{n_1 n_2}(\beta,\mu) g^*_{n_1' n_2}(\beta,\mu)\, |n_1\rangle\langle n_1'|\,, \tag{2.4}$$

where the trace runs over the auxiliary modes n_2, see section III.4. Comparing equation (2.4) to equation (2.1) one finds the condition

$$\sum_{n_2} g_{n_1 n_2}(\beta,\mu) g^*_{n_1' n_2}(\beta,\mu) = \frac{1}{Z(\beta,\mu)}\, \mathrm{e}^{-\beta\left(E_{n_1}-\mu N_{n_1}\right)}\, \delta_{n_1 n_1'}\,. \tag{2.5}$$

At this point one could simply choose $g_{n_1 n_2}(\beta,\mu)$ to be diagonal, $g_{n_1 n_2}(\beta,\mu) \propto \delta_{n_1 n_2}$. Any other choice is connected to this diagonal form via a unitary transformation in the auxiliary state space. However, we explicitly keep this freedom of a unitary transformation and we will exploit it below to ensure particle number conservation for our numerics.

For the non-interacting thermal leads in the star geometry, the form of $|\Omega\rangle$ can be found analytically. Because the different lead levels q are decoupled from each other, compare

equation (1.2), one can treat each single fermionic mode independently,

$$|\Omega\rangle = \Pi_q \, |\Omega\rangle_q \ . \tag{2.6}$$

The mode q is represented by the annihilation and creation operators $c_q^{(\dagger)} \equiv c_{q1}^{(\dagger)}$ and the corresponding auxiliary mode by $c_{q2}^{(\dagger)}$. The contribution of the these modes to the Hamiltonian is given by $H_q = \varepsilon_q \, c_{q1}^\dagger c_{q1}$. The full enlarged Hilbert space can be divided into the subspaces corresponding to the different fermionic modes. As a basis for each of these subspaces one can use

$$\left\{ |0,0\rangle_q \, , |0,1\rangle_q \, , |1,0\rangle_q \, , |1,1\rangle_q \right\} \ , \tag{2.7}$$

with $|0,0\rangle_q$ being the vacuum in this subspace, $|0,1\rangle_q = c_{q2}^\dagger \, |0,0\rangle_q$, $|1,0\rangle_q = c_{q1}^\dagger \, |0,0\rangle_q$ and $|1,1\rangle_q = c_{q1}^\dagger c_{q2}^\dagger \, |0,0\rangle_q$.

The weights $g_{n_1,n_2}(\beta,\mu)$ of the different states within the thermal state $|\Omega\rangle_q$ have to fulfill equation (2.5). For the single mode q one obtains for the right-hand side of equation (2.5):

$$Z\left(\beta,\mu_\alpha\right) = 1 + \mathrm{e}^{-\beta(\varepsilon_q - \mu_\alpha)} = \left(1 - f_\alpha(\varepsilon_q)\right)^{-1} , \tag{2.8}$$

and

$$\frac{1}{Z(\beta,\mu)} \, \mathrm{e}^{-\beta\left(E_{n_1} - \mu N_{n_1}\right)} = \begin{cases} Z(\beta,\mu)^{-1} = 1 - f_\alpha(\varepsilon_q) & \text{if} \quad |n_1\rangle = |0\rangle \\ Z(\beta,\mu)^{-1} \, \mathrm{e}^{-\beta\left(\varepsilon_q - \mu\right)} = f_\alpha(\varepsilon_q) & \text{if} \quad |n_2\rangle = |1\rangle \end{cases} \tag{2.9}$$

with the Fermi distribution $f_\alpha(\omega)$. An obvious possibility is to choose $g_{n_1 n_2}(\beta,\mu_\alpha)$ to be diagonal such that the states

$$|0,0\rangle_q \text{ and } |1,1\rangle_q \text{ carry the weights } \left|g_{|0,0\rangle_q}\right|^2 = (1 - f_\alpha(\varepsilon)) \text{ and } \left|g_{|1,1\rangle_q}\right|^2 = f_\alpha(\varepsilon) \tag{2.10}$$

leaving the states $|0,1\rangle_q$ and $|1,0\rangle_q$ with weight zero, $g_{|0,1\rangle_q} = g_{|1,0\rangle_q} = 0$. However, equally well one can choose the states

$$|0,1\rangle_q \text{ and } |1,0\rangle_q \text{ to carry the weights } \left|g_{|0,1\rangle_q}\right|^2 = (1 - f_\alpha(\varepsilon)) \text{ and } \left|g_{|1,0\rangle_q}\right|^2 = f_\alpha(\varepsilon) \tag{2.11}$$

leaving the states $|0,0\rangle_q$ and $|1,1\rangle_q$ with weight zero, $g_{|0,0\rangle_q} = g_{|1,1\rangle_q} = 0$.

The two versions are equivalent in the sense that one transforms into the other by interchanging $c_{q2} \leftrightarrow c_{q2}^\dagger$. The first choice in equation (2.10) seems more obvious because the auxiliary mode is a simple copy of the physical mode in terms of the occupation number. It is often used in the literature [86, 87]. However, the second option, equation (2.11), has one big advantage: the two states that contribute to the thermal state have the same overall particle number. This turns out to be key in retaining particle number conservation in the rotation described next.

VI.2.2 Rotation

In the thermofield approach one further simplifies the form of the thermal state by rotating the basis in equation (2.7) such that the thermal state is equal to one of the new rotated basis states and thus a product state. In the following, we first introduce a specific form of

this rotation. This brings us to an interpretation of the lead levels in terms of *"holes"* and *"particles"*. Furthermore, we discuss the implications of the rotation on the choice of the Hamiltonian in the auxiliary state space. For completeness, we finally add the form of the generator representing the suggested rotation.

We want to map the thermal state $|\Omega\rangle_q$ onto a product state. For the choice of $g_{n_1,n_2}(\beta,\mu)$ given in equation (2.11) the two states contributing to the thermal state, $|0,1\rangle_q$ and $|1,0\rangle_q$, have the same particle number. Therefore, one can perform the rotation such that it preserves the number of particles. To this end, the thermal state in the new basis with rotated operators $\tilde{c}_{q1}$ and $\tilde{c}_{q2}$ needs to be either $|\tilde{0},\tilde{1}\rangle_q$ or, equivalently, $|\tilde{1},\tilde{0}\rangle_q$.

Explicitly, the rotation is given by

$$\begin{aligned}\tilde{c}_{q1} &= \cos\theta_q\, c_{q1} - \sin\theta_q\, c_{q2}\\ \tilde{c}_{q2} &= \sin\theta_q\, c_{q1} + \cos\theta_q\, c_{q2}\,,\end{aligned} \tag{2.12a}$$

where

$$\cos\theta_q = \sqrt{1-f_\alpha(\varepsilon_q)}\,,\quad \sin\theta_q = \sqrt{f(_\alpha\varepsilon_q)}\,. \tag{2.12b}$$

This rotation maps the thermal state of the single mode onto

$$\begin{aligned}|\Omega\rangle_q &= \sqrt{1-f_\alpha(\varepsilon_q)}\,|0,1\rangle_q + \sqrt{f_\alpha(\varepsilon_q)}\,|1,0\rangle_q = \left(\cos\theta_q\, c^\dagger_{q2} + \sin\theta_q\, c^\dagger_{q1}\right)|0,0\rangle_q\\ &= \tilde{c}^\dagger_{q2}\,|0,0\rangle_q = |\tilde{0},\tilde{1}\rangle_q\,.\end{aligned} \tag{2.12c}$$

"Holes" and "particles"

By construction one has

$$\tilde{c}_{q1}\,|\Omega\rangle_q = 0 \quad\text{and}\quad \tilde{c}^\dagger_{q2}\,|\Omega\rangle_q = 0\,. \tag{2.13}$$

In other words, the mode $\tilde{c}_{q1}$ ($\tilde{c}_{q2}$) is empty (filled) in the thermal state. Due to this property, we refer to these modes as *"hole"* and *"particle"*, respectively. The occupation of the new lead levels in the thermal state is trivial. The information on the Fermi distribution $f_\alpha(\omega)$ was shifted from the occupation numbers to the basis, which depends on $f_\alpha(\omega)$ via the rotation (2.12). This is reflected in the hybridization: The original lead mode c_{q1} is coupled to the impurity. This coupling v_q to an impurity level is transformed into

$$H_{\mathrm{hyb},q} = \left(v_q\, d^\dagger c_{q1} + \mathrm{h.c.}\right) = \sum_{i\in\{1,2\}}\left(\tilde{v}_{qi}\, d^\dagger \tilde{c}_{qi} + \mathrm{h.c.}\right) \tag{2.14}$$

with couplings $\tilde{v}_{qi}$ *that depend on the Fermi occupation functions*,

$$\tilde{v}_{q1} = v_q\sqrt{1-f_\alpha(\varepsilon_q)}\,,\quad \tilde{v}_{q2} = v_q\sqrt{f_\alpha(\varepsilon_q)}\,. \tag{2.15}$$

From equations (2.13) and (2.15) one obtains a simple physical picture of the thermofield approach: instead of representing $|\Omega\rangle_q$ as a fermionic mode occupied with probability $f_\alpha(\varepsilon_q)$, one represents the mode as a combination of an empty "hole" $\tilde{c}_{q1}$ coupled to the impurity with weight $(1-f_\alpha(\varepsilon_q))$ and a filled "particle" $\tilde{c}_{q2}$ coupled to the impurity with weight $f_\alpha(\varepsilon_q)$. All information on the occupation statistics is contained in the rotated couplings. The state $|\Omega\rangle_q$ itself is a simple product state. In particular, this means that the full thermal state

$|\Omega\rangle = \Pi_q |\Omega\rangle_q$ is a *product state* consisting of empty and filled modes.

This picture of "holes" and "particles" is in complete analogy to the lead representation used for the local form of a Lindblad equation in section IV.3.3, compare also the discussion in section IV.3.5.

In contrast, for the choice in equation (2.10) the two states contributing to the thermal state, $|0,0\rangle_q$ and $|1,1\rangle_q$, have a different particle number. Therefore, the rotation onto a single state inevitably violates particle number conservation. In this case, the particle number of the thermal state in the rotated basis is irrelevant and one typically rotates the system such that the thermal state is given by the vacuum in the new basis. This is equivalent to the rotation given in equation (2.12) but with $c_{q2} \leftrightarrow c_{q2}^\dagger$ and $\tilde{c}_{q2} \leftrightarrow \tilde{c}_{q2}^\dagger$, thus mixing annihilators and creators. In the Hamiltonian this loss of particle number conservation becomes explicit in the hybridization with the impurity, which includes terms of the form $\tilde{v}_{q2}\, d\tilde{c}_{q2}$ and $\tilde{v}_{q2}\, d^\dagger \tilde{c}_{q2}^\dagger$. Also from the physical picture it is clear that a mode with occupation $f_\alpha(\varepsilon_q)$ cannot be represented by a vacuum without violating particle number conservation.

Note that the Hamiltonian in the thermofield approach seems to depend on voltage and temperature due to the couplings $\tilde{v}_{qi}$ in equation (2.15). However, this is not the case. It is merely the *choice of basis* which depends on the Fermi function, as can be seen from equation (2.14), where the expression after the first equal sign is manifestly independent of the Fermi function.

Energy terms in the auxiliary state space

The energy term of the auxiliary site, in principle, can be chosen arbitrarily:

$$H_{q,\mathrm{tot}} = H_q + \tilde{H}_{q,\mathrm{aux}} = \varepsilon_{q1} c_{q1}^\dagger c_{q1} + \varepsilon_{q2} c_{q2}^\dagger c_{q2} \tag{2.16}$$

with $\varepsilon_{q1} = \varepsilon_q$. However, if $\varepsilon_{q2} \neq \varepsilon_{q1}$, the rotation (2.12) results in a direct coupling between the "hole" $\tilde{c}_{q1}$ and the "particle" $\tilde{c}_{q2}$. To avoid such terms, we set $\varepsilon_{q2} = \varepsilon_q$, such that

$$H_{q,\mathrm{tot}} = \sum_{i\in\{1,2\}} \varepsilon_{qi}\, c_{qi}^\dagger c_{qi} = \sum_{i\in\{1,2\}} \varepsilon_{qi}\, \tilde{c}_{qi}^\dagger \tilde{c}_{qi}\,. \tag{2.17}$$

Again, with the choice given in equation (2.10) and rotating to the vacuum, one gets equivalent results, but with $c_{q2} \leftrightarrow c_{q2}^\dagger$ and $\tilde{c}_{q2} \leftrightarrow \tilde{c}_{q2}^\dagger$. In this case one therefore uses $\varepsilon_{q2} = -\varepsilon_q$.

Generator

Let us for completeness add the form of the rotation in equation (2.12) in terms of a generator G_q,

$$\begin{aligned} \tilde{c}_{q1} &= \mathrm{e}^{-\mathrm{i}G_q}\, c_{q1}\, \mathrm{e}^{\mathrm{i}G_q} \\ \tilde{c}_{q2} &= \mathrm{e}^{-\mathrm{i}G_q}\, c_{q2}\, \mathrm{e}^{\mathrm{i}G_q} \end{aligned} \tag{2.18}$$

with

$$G_q = \mathrm{i}\theta_q (c_{q1}^\dagger c_{q2} - c_{q2}^\dagger c_{q1}) \tag{2.19}$$

and θ_q defined in equation (2.12b). Due to

$$\begin{aligned}\left(c_{q1}^\dagger c_{q2} - c_{q2}^\dagger c_{q1}\right)^{2n} \quad |0,\tilde{1}\rangle_q &= (-1)^n\,|0,\tilde{1}\rangle_q \\ \left(c_{q1}^\dagger c_{q2} - c_{q2}^\dagger c_{q1}\right)^{2n+1} |0,\tilde{1}\rangle_q &= (-1)^n\,|1,\tilde{0}\rangle_q\end{aligned} \tag{2.20}$$

one finds

$$\mathrm{e}^{-\mathrm{i}G_q}\,|0,\tilde{1}\rangle_q = \sum_{n=0}^{\infty}\frac{1}{n!}\theta^n\left(c_{q1}^\dagger c_{q2} - c_{q2}^\dagger c_{q1}\right)^n |0,\tilde{1}\rangle_q = \cos\theta_q\,|0,\tilde{1}\rangle_q + \sin\theta_q\,|1,\tilde{0}\rangle_q = |\Omega\rangle_q \tag{2.21}$$

This equation simply recovers the statement, that the thermal state $|\Omega\rangle_q$ in the rotated basis is a simple product state of a "hole" and a "particle".

The Hamiltonian $H_q = \varepsilon_q\, c_{q1}^\dagger c_{q1}$ does not commute with the generator G_q. However, if the Hamiltonian includes an additional energy term with the same energy ε_q also for the auxiliary mode, $H_{q,\mathrm{tot}} = \sum_{i\in\{1,2\}} \varepsilon_{qi}\, c_{qi}^\dagger\, c_{qi}$, it does commute with G_q,

$$\left[H_{q,\mathrm{tot}}, G_q\right] = 0\,. \tag{2.22}$$

This is just another way of writing equation (2.17).

VI.2.3 Connection to Finite-Temperature Purification in DMRG

The thermofield approach can essentially be interpreted as standard finite-temperature purification applied to a thermal *non-interacting* system as presented in section III.4 together with the rotation in the local space of physical and auxiliary mode. To make this even more explicit, this section points out some of the connections to section III.4. In particular, it is shown that the choice of the Hamiltonian in the auxiliary state space defined in equation (2.16) is equivalent to the backward time evolution proposed in section III.4.3

Recovering the Thermofield Approach

For the non-interacting fermionic system with modes q the maximally entangled state representing infinite temperature $\beta = 0$ is given by

$$|X_\infty\rangle \propto \prod_q \left(|0,0\rangle_q + |1,1\rangle_q\right). \tag{2.23}$$

The imaginary time evolution (compare section III.4.2) can be performed analytically and the thermal state at temperature $T = \beta^{-1}$ and chemical potential μ_α is found to be

$$\begin{aligned}|\Omega\rangle \propto \mathrm{e}^{-\beta(H-\mu_\alpha N)/2}\prod_q \left(|0,0\rangle_q + |1,1\rangle_q\right) &\propto \prod_q \left(|0,0\rangle_q + \mathrm{e}^{-\beta\left(\varepsilon_q-\mu_\alpha\right)/2}\,|1,1\rangle_q\right) \\ &\propto \prod_q \left(\sqrt{1-f(\varepsilon_q)}\,|0,0\rangle_q + \sqrt{f(\varepsilon_q)}\,|1,1\rangle_q\right).\end{aligned} \tag{2.24}$$

The physical Hamiltonian is given by

$$H = \sum_q \varepsilon_q c_q^\dagger c_q\,. \tag{2.25}$$

Choosing the backward time evolution as defined in section III.4.3, the Hamiltonian in the auxiliary space is set to

$$H_{\text{aux}} = -\sum_q \varepsilon_q c^\dagger_{q,\text{aux}} c_{q,\text{aux}} \,. \tag{2.26}$$

Restoring particle number conservation

The thermal state $|\Omega\rangle$ formulated as in equation (2.24) is ill-defined with respect to the particle number. This can be fixed by the replacement $c_{q,\text{aux}} \to a^\dagger_{q,\text{aux}}$. For the states $|0\rangle_{\text{q,aux}}$ and $|1\rangle_{\text{q,aux}}$ this yields

$$\begin{aligned} c^\dagger_{q,\text{aux}} c_{q,\text{aux}} |0\rangle_{\text{q,aux}} = 0 \quad &\to \left(1 - a^\dagger_{q,\text{aux}} a_{q,\text{aux}}\right) |0\rangle_{\text{q,aux}} = 0 \\ &\to a^\dagger_{q,\text{aux}} a_{q,\text{aux}} |0\rangle_{\text{q,aux}} = |0\rangle_{\text{q,aux}} \,, \qquad (2.27a) \\ c^\dagger_{q,\text{aux}} c_{q,\text{aux}} |1\rangle_{\text{q,aux}} = |1\rangle_{\text{q,aux}} \quad &\to \left(1 - a^\dagger_{q,\text{aux}} a_{q,\text{aux}}\right) |1\rangle_{\text{q,aux}} = |1\rangle_{\text{q,aux}} \\ &\to a^\dagger_{q,\text{aux}} a_{q,\text{aux}} |1\rangle_{\text{q,aux}} = 0 \,. \qquad (2.27b) \end{aligned}$$

In that sense these states are relabeled as

$$|0\rangle_{\text{q,aux}} \to |1_a\rangle_{\text{q,aux}} \,, \tag{2.28a}$$

$$|1\rangle_{\text{q,aux}} \to |0_a\rangle_{\text{q,aux}} \,. \tag{2.28b}$$

Expressed in these new modes $a_{\text{q,aux}}$ the thermal state has a well-defined particle number,

$$|\Omega\rangle = \prod_q \left(\sqrt{1 - f(\varepsilon_q)}\, |0, 1_a\rangle_q + \sqrt{f(\varepsilon_q)}\, |1, 0_a\rangle_q \right). \tag{2.29}$$

The auxiliary Hamiltonian in equation (2.26) transforms into

$$H_{\text{aux}} = -\sum_q \varepsilon_q c^\dagger_{q,\text{aux}} c_{q,\text{aux}} = \sum_q \varepsilon_q a^\dagger_{q,\text{aux}} a_{q,\text{aux}} + \text{const.} \tag{2.30}$$

When performing the time evolution, the constant term in H_{aux} results in a global phase and can therefore be dropped. The energies of the new modes $a_{q,\text{aux}}$ are equivalent to the energies of the corresponding physical modes c_q, although the starting point was a *backward* time evolution in the auxiliary state space. The difference in sign is due to the redefinition of $c_{q,\text{aux}} \to a^\dagger_{q,\text{aux}}$ in the auxiliary state space. Starting from equation (2.29) one can now perform the rotation in equation (2.12).

This derivation illustrates that the energy terms chosen in equation (2.16) are equivalent to the standard backward time evolution presented in section III.4.3. Note though that the choice in equation (2.16) was motivated by the fact that only these energy terms are able to keep "holes" and "particles" separate after the rotation (2.12) in the sense of equation (2.17).

VI.2.4 Chain Geometry

The above description of the thermofield approach is based on the star geometry. For MPS calculations, in most cases, it is desirable to transform into a chain representation of the leads. In doing so, one would like to retain the property that the thermal state is a simple product state. This is, of course, not given for an arbitrary tridiagonalization. However, it can be

guaranteed if the unitary transformation does not mix "holes" with "particles". If "holes" and "particles" are treated as separated channels with independent tridiagonalizations, the unitary transformation for the "holes" mixes only empty lead levels, and the transformation for the "particles" only fully filled lead levels. Therefore, these channels will also be empty and fully filled in the thermal state in the chain geometry. In order for this to work, it is crucial that the Hamiltonian does not mix "holes" and "particles". This is only the case if one chooses the energy terms of the auxiliary modes equal to those of the physical modes as given in equation (2.17). Note that the tridiagonalization works with the modified couplings between impurity and "holes" and "particles", $\tilde{v}_{qi}$, and therefore depends on the Fermi distribution function.

VI.3 A hybrid NRG-tDMRG approach

In many impurity models, there are different energy scales that are of relevance. For example, in the SIAM, one is interested in resolving the physics occurring at the Kondo scale, which scales exponentially with the interaction strength U/Γ,

$$T_K \propto \mathrm{e}^{-\frac{\pi}{8}\frac{U}{\Gamma}}, \tag{3.1}$$

see equation (II.3.4). To characterize the full properties of such a model, a method must be able to describe these exponentially small energy scales.

In equilibrium calculations the numerical renormalization group meets this challenge using a renormalization procedure: The energy scale separation of the Wilson chain, which relies on a logarithmic discretization of the leads, see section III.3.1, makes it possible to resolve the different energy scales iteratively starting at high energies. However, in non-equilibrium there is not one single Fermi edge the physics around which can be resolved in more and more detail. Instead, there are two different Fermi edges in the two leads, which define a transport window. Within this window a logarithmic discretization is not appropriate.

On the other hand, the time-dependent density matrix renormalization group, which is typically based on a linear discretization, has successfully been used to describe non-equilibrium situations at energy scales close to the bandwidth.

The hybrid NRG-tDMRG strategy adopted here was developed by F. Güttge, F. Anders, U. Schollwöck, E. Eidelstein, and A. Schiller [88, 89]. It combines a logarithmic discretization for high-energy scales with a linear discretization within the transport window. NRG is used to integrate out the high-energy modes, thereby renormalizing the problem down to an effective bandwidth which is set by the size of the transport window. This renormalized impurity model is then treated using tDMRG.

The main advantage of this procedure becomes obvious in the quench calculation. In a tDMRG calculation the size of the individual Trotter time steps has to be chosen small compared to the largest energy scale involved. Typically, it is therefore of the order of $\delta t_D \sim D^{-1}$. By truncating the high-energy modes one renormalizes the impurity down to an effective bandwidth D^* such that one can use time steps of the order of $\delta t_{D^*} \sim D^{*-1}$, which can be orders of magnitudes larger than δt_D, $\delta t_{D^*} \gg \delta t_D$. This enables us to reach much longer time scales.

We implement our MPS calculations based on the QSpace library [45, 55, 92] and exploit the particle number conservation and for the SIAM also the conservation of the z-component of the spin, S_z.

Section VI.3.1 introduces a suitable discretization in the star geometry and the corresponding parameters. Section VI.3.2 shows how the discretized system can be brought into a suitable MPS chain geometry. In section VI.3.3 it is discussed how the high-energy scales can be integrated out based on NRG, before section VI.3.4 introduces the actual quench time evolution based on tDMRG. Finally, section VI.3.5 focuses on the evaluation of expectation values, in particular the current, in the MPS geometry.

VI.3.1 Discretization

The bandwidth $[-D, D]$ is discretized into intervals $I_k = [E_k, E_{k+1}]$. Our aim is to find a suitable discretization which is logarithmic for high energies and linear within the transport window. The size of this transport window $[-D^*, D^*]$ is fixed by the physical parameters. To obtain a reasonably smooth discretization one can define the energies E_k by evaluating a sufficiently smooth function $\mathcal{E}(x)$ at the positions $x_k = [..., -1+z, z, 1+z, 2+z, ...]$, $E_k = \mathcal{E}(x_k)$. The parameter z defines a z-shift in complete analogy to standard NRG calculations, compare section III.3.1. Here, the function $\mathcal{E}(x)$ is constructed such that it meets the following requirements:

- Within the transport window $[-D^*, D^*]$ it ensures a strictly linear level-spacing δ. This is fulfilled, if $\mathcal{E}(x) - \mathcal{E}(x-1) = \delta$, where $|\mathcal{E}(x)| < D^*$.
- To approach a logarithmic discretization for high energies, the function $\mathcal{E}(x)$ needs to scale exponentially, $\mathcal{E}(x+1)/\mathcal{E}(x) = \Lambda$ for $\mathcal{E}(x) \gg D^*$, and $\mathcal{E}(x)/\mathcal{E}(x+1) = \Lambda$ for $\mathcal{E}(x) \ll -D^*$, with $\Lambda > 1$.
- The transition from the logarithmic to the linear part should be smooth in the sense that $\mathcal{E}(x)$ and its first derivative are continuous.

One such function $\mathcal{E}(x)$ is given by

$$\mathcal{E}(x) = \begin{cases} \delta \cdot x\,, & \text{for } |x| \leq x^*\,, \\ \frac{\delta}{\log(\Lambda)} \sinh(\ln(\Lambda)(x \mp x^*)) \mp \delta \cdot x^*\,, & \text{for } x \gtrless \pm x^*\,. \end{cases}$$

Each interval I_k is represented by an energy ε_k. The choice of these energies strongly affects the quality of the lead representation. Different alternatives have been discussed in the context of NRG [15, 53]. Motivated by Eq. (44) in Ref. [15], here the energies ε_k are chosen as

$$\varepsilon_n = \begin{cases} \frac{E_{k+1}-E_k}{\ln(E_{k+1}/E_k)}, & \text{if } |E_k|\,, |E_{k+1}| > D^* \\ \frac{1}{2}\left(E_k + E_{k+1}\right), & \text{else.} \end{cases} \tag{3.2}$$

For $|E_k| > D^*$, but close to D^*, one finds $E_{k+1} - E_k \approx \delta$. Furthermore the level-spacing δ will typically be small compared to the size of the transport window, $\delta/D^* \ll 1$, and therefore $\delta/E_k \ll 1$. In this case,

$$\varepsilon_k = \frac{\delta}{\ln\left(1 + \frac{\delta}{E_k}\right)} \overset{\delta \ll E_k}{\approx} E_k + \frac{1}{2}\delta \approx \frac{1}{2}\left(E_k + E_{k+1}\right). \tag{3.3}$$

In that sense the continuous behavior of the function $\mathcal{E}(x)$ is also transfered to the energies ε_k.

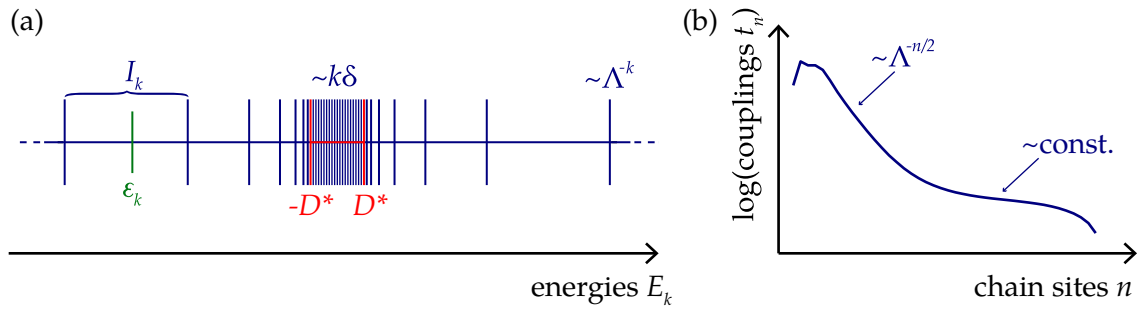

Figure VI.2: (a) Sketch of the discretization with linearly discretized transport window $[-D^*, D^*]$ and logarithmic discretization for high energies. To each interval I_k an energy $\varepsilon_k$is assigned. (b) After tridiagonalizing the Hamiltonian the couplings t_n decay exponentially for the first part of the chain, which corresponds to the energy scales outside the transport window. For the second part of the chain corresponding to the energy scales within the transport window, the couplings are all of the same order. For the very first couplings close to the impurity one finds additional features. At the end of the chain finite-size effects get visible.

A sketch of a combined linear-logarithmic discretization into intervals I_k is given in figure VI.2(a).

When a structureless lead discretized like this is mapped onto a chain, as described in section II.2.3, the couplings t_n decay exponentially in the first part of the chain, which corresponds to the logarithmically discretized intervals outside the transport window. For energy scales inside the transport window represented by the later part of the chain, the couplings will all be of the same order, as sketched in figure VI.2(b). For the quench calculations presented in [P2], the hybridization is divided into "holes" and "particles" before mapping the leads onto the chain and therefore depends on temperature and voltage. Still, the exponential decay in the couplings t_n and the saturation to a constant value can always be recovered.

This discretization has four variable parameters: (i) the parameter of the logarithmic discretization, Λ, (ii) the energy scale D^*, which defines the crossover from linear to logarithmic discretization, (iii) the level spacing of the linear discretized part, δ, and (iv) the z-shift z. Typical values for Λ are $2 \leq \Lambda \leq 3$. The smaller Λ the better is the resolution for high energies, but the worse is the energy scale separation in the Wilson chain, so that more states have to be kept in the renormalization procedure, compare sections III.3 and VI.3.3. The size of the transport window $[-D^*, D^*]$ depends on physical parameters such as voltage and temperature. For the typical scenario of an applied voltage V between two leads of equal temperature T, a simple definition of the transport window is given by the energy range, in which the Fermi functions of the two leads differ. For a symmetrically applied voltage $V = 2\mu$, one can simply choose D^* as the energy at which both Fermi functions drop to a value smaller than some threshold ϵ,

$$\max\left(f_L(D^*), f_R(D^*)\right) = \left(1 + \mathrm{e}^{\beta(D^*-\mu)}\right)^{-1} \stackrel{!}{=} \epsilon\,, \tag{3.4}$$

with $\beta = T^{-1}$. Solving for D^* one obtains

$$D^* = \mu + T\log\left(\epsilon^{-1} - 1\right)\,. \tag{3.5}$$

For zero temperature, this sets D^* equal to the chemical potential $\mu = \frac{V}{2}$. For finite temperature and a small voltage $V \to 0$, D^* scales with temperature. E.g., for $\epsilon = 10^{-3}$ one obtains $D^* \approx 7T$. The level spacing δ has to resolve the physics of the transport window. The number of levels per lead within the transport window is given by $N_{\mathrm{TW}} = 2D^*/\delta$. Therefore, values of the order of $\delta = \frac{1}{20}D^*$ seem to be appropriate. In most cases, we found our results to be reasonably smooth with no need for a z-shift.

As an alternative to the discretization presented in this chapter, one could exploit the idea of open Wilson chains [P3], compare section II.2.3: in this approach one does not need to fix the energy intervals I_k in the star geometry. Instead, one sets the desired values of the couplings *on the chain* and iteratively constructs a Wilson chain with exactly these couplings. The onsite energies of the chain elements follow in a natural way. This ensures a smooth behavior of the couplings on the chain and, in particular, it renders the ad-hoc definition of the energies ε_k in equation (3.2) unnecessary. However, there is one crucial point. In models like the SIAM, where left and right leads couple to the same impurity level, one would like to combine left and right leads into one channel in such a way that half of the modes decouple, see section VI.3.2 for details. At the same time, it is necessary to keep track of left and right leads independently, if one wants to calculate the current in the form of an expectation value, see section VI.3.5. This is straightforward for a discretization in the star geometry and a tridiagonalization onto the chain. But it turns out to be less trivial for the open Wilson chain construction.

VI.3.2 The MPS Geometry

To calculate the quench dynamics based on NRG and tDMRG, we need to bring the system into a chain geometry. In the following we describe the setup used for the calculations presented in sections VI.4-VI.5 and the paper [P2] in chapter VII, respectively. We start in the star geometry and perform the purification in the sense of the thermofield approach. Furthermore, in this geometry we identify decoupling lead levels. For specific models one can further reduce the number of lead levels by combining lead levels of the left and right leads. Finally, we perform the unitary transformations which map the system onto a chain.

The star geometry

We start from the lead Hamilonian in equation (1.2) with a flat hybridization for the two leads, $\Gamma_\alpha(\omega) = \Gamma_\alpha \Theta(D - |\omega|)$. The impurity Hamiltonian and the hybridization term of the IRLM and the SIAM are defined in equations (II.1.4) and (II.1.5), respectively.

The bandwidth $[-D, D]$ is discretized into energy intervals I_k represented by energies ε_k. Within the transport window $[-D^*, D^*]$ the discretization is linear, while for high energies a logarithmic discretization is used, as described in section VI.3.1. The coupling between lead level $q = \{\alpha, k, (\sigma)\}$ and the impurity is given by $v_q = \sqrt{\Gamma_\alpha \delta_k / \pi}$ with δ_k being the size of interval I_k, see equation (II.2.9). A sketch of this *"star geometry"* is shown in figure VI.3.

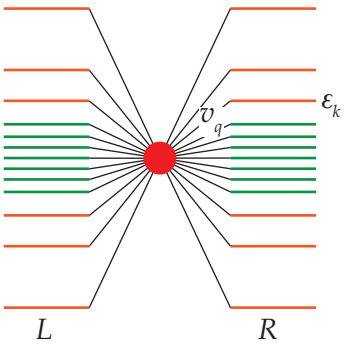

Figure VI.3: Sketch of the star geometry. Different colors are used for the logarithmically and the linearly discretized energy range.

Purification

In the thermofield approach each mode c_q with energy ε_k and coupling v_q is replaced by two modes $\tilde{c}_{qi}$, referred to as "hole" ($i = 1$) and "particle" ($i = 2$), with temperature and voltage dependent couplings, $\tilde{v}_{q1} = v_q\sqrt{1 - f_\alpha(\varepsilon_q)}$ and $\tilde{v}_{q2} = v_q\sqrt{f_\alpha(\varepsilon_q)}$, see section VI.2 and in particular equation (2.15).

Decoupling "hole" and "particle" modes

For energies outside the transport window $[-D^*, D^*]$, the Fermi functions are either one or zero,

$$f_\alpha(\varepsilon_k) \approx 1 \quad \text{if } \varepsilon_k < -D^*, \tag{3.6a}$$
$$f_\alpha(\varepsilon_k) \approx 0 \quad \text{if } \varepsilon_k > D^*. \tag{3.6b}$$

This implies

$$\tilde{v}_{q1} \approx 0 \quad \text{if } \varepsilon_k < -D^*, \tag{3.7a}$$
$$\tilde{v}_{q2} \approx 0 \quad \text{if } \varepsilon_k > D^*. \tag{3.7b}$$

In other words, for high energies the "particles" decouple from the impurity, while for low energies, the "holes" decouple, as illustrated in figure VI.4. This decoupling of modes reflects the fact, that the doubling of lead levels in the purification procedure is only necessary within the transport window, where the Fermi functions differ from zero and one.

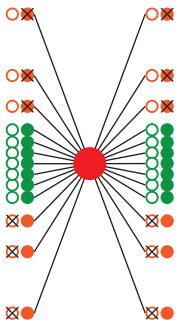

Figure VI.4: After the purification each lead level is described by one "hole" and one "particle", illustrated by empty and filled circles. The "holes" at negative energies with large absolute value decouple, while for the "particles" the modes with large positive energies decouple, as indicated by the black crosses.

For temperature $T = 0$, also in the transport window half of the modes decouple because the Fermi function is equal to one for one of the leads and equal to zero for the other lead. When combining left and right leads as described in the following section, this decoupling of modes within the transport window brings no further reduction of modes. However, for models like the IRLM, in which the combination of left and right leads is not possible, this could be used to further reduce the number of lead levels. So far, we did not exploit this in our calculations.

Combination of the left and right leads

If the impurity consists of only one single site, it is standard in equilibrium calculations to combine left and right lead into a single channel. Similarly, for the SIAM we here define new modes $\tilde{c}^{(\pm)}_{ki}$ such that

$$\begin{aligned} H_{\text{hyb}} + H_{\text{lead}} &= \sum_{qi} \left(\tilde{v}_{qi}\, d^\dagger_\sigma \tilde{c}_{qi} + \text{h.c.} \right) + \sum_{qi} \varepsilon_k \tilde{c}^\dagger_{qi}\, \tilde{c}_{qi} \\ &= \sum_{k\sigma i} \left(\tilde{v}^{(+)}_{ki}\, d^\dagger \tilde{c}^{(+)}_{k\sigma i} + \text{h.c.} \right) + \sum_{k\sigma i} \varepsilon_k \left(\tilde{c}^{(+)\dagger}_{k\sigma i}\, \tilde{c}^{(+)}_{k\sigma i} + \tilde{c}^{(-)\dagger}_{k\sigma i}\, \tilde{c}^{(-)}_{k\sigma i} \right) \end{aligned} \tag{3.8}$$

where

$$\tilde{v}_{ki}^{(+)} = \sqrt{|\tilde{v}_{Lki}|^2 + |\tilde{v}_{Rki}|^2} \tag{3.9a}$$

$$\tilde{c}_{k\sigma i}^{(+)} = \frac{1}{\tilde{v}_{ki}^{(+)}} \left(\tilde{v}_{Lki}\, \tilde{c}_{Lk\sigma i} + \tilde{v}_{Rki}\, \tilde{c}_{Rk\sigma i} \right), \tag{3.9b}$$

$$\tilde{c}_{k\sigma i}^{(-)} = \frac{1}{\tilde{v}_{ki}^{(+)}} \left(-\tilde{v}_{Rki}^{*}\, \tilde{c}_{Lk\sigma i} + \tilde{v}_{Lki}^{*}\, \tilde{c}_{Rk\sigma i} \right). \tag{3.9c}$$

Only the *"even modes"* $\tilde{c}_{k\sigma i}^{(+)}$ couple to the impurity. The *"odd modes"* $\tilde{c}_{k\sigma i}^{(-)}$ completely decouple from the model and can therefore be ignored. In standard quench approaches it would not be possible to use this reduction of modes because for the initial state one has to use different chemical potentials for left and right leads. However, in the thermofield approach the information on the chemical potential was transfered to the couplings $\tilde{v}_{qi}$. Note that the transformation in equation (3.9) is done for "holes" and "particles" independently. Mixing "holes" and "particles" would destroy the simple product form of the thermal state $|\Omega\rangle$.

This combination of left and right leads into "even" and "odd" modes does not work for the IRLM. In the SIAM, the choice of the "even" modes is such that $\tilde{c}_{k\sigma i}^{(+)}$ exactly represents the combination of $\tilde{c}_{Lk\sigma i}$ and $\tilde{c}_{Rk\sigma i}$ that couples to d_σ. In the IRLM, however, left and right leads couple to different lead levels d_α, making it necessary that both, $\tilde{c}_{Lki}$ and $\tilde{c}_{Rki}$, are described explicitly.

In principle, one could perform the combination of left and right leads on the level of hybridization functions,

$$\tilde{\Gamma}_i(\omega) = \sum_\alpha \tilde{\Gamma}_{\alpha i}(\omega) \tag{3.10}$$

with the hybridizations for "holes" and "particles"

$$\tilde{\Gamma}_{\alpha 1}(\omega) = \tilde{\Gamma}_\alpha(\omega)(1 - f_\alpha(\omega)) \quad \text{and} \quad \tilde{\Gamma}_{\alpha 2}(\omega) = \tilde{\Gamma}_\alpha(\omega) f_\alpha(\omega)\,. \tag{3.11}$$

However, for the definition of the current in terms of expectation values it is necessary to keep track of the contributions of the different physical leads. Therefore, we prefer to formulate the combination of left and right leads in terms of a unitary transformation, compare section VI.3.5. The necessity to keep track of left and right leads is also what hinders us to directly work on a chain, e.g., by treating $\tilde{\Gamma}_{\alpha i}(\omega)$ using the open Wilson chain approach as presented in section II.2.3. This restriction can immediately be dropped if the current is calculated via the dot's spectral function. However, we have not calculated spectral functions so far and, therefore, are forced to determine the current via expectation values.

Tridiagonalization of "holes" and "particles"

In section VI.2.4 it was argued that "holes" and "particles" should be tridiagonalized into separate channels because only in this case the thermal state of the leads keeps its simple form also in the chain geometry. For the IRLM, one therefore needs four independent unitary transformations $U^{(\alpha i)}$, with $\{\alpha i\} \in \{L1, L2, R1, R2\}$, tridiagonalizing the modes $\tilde{c}_{qi}$ with couplings $\tilde{v}_{qi}$ and energies ε_k to new modes $f_{\alpha n i}$ with chain hoppings $t_{\alpha n i}$ and on-site energies $\chi_{\alpha n i}$, as described in section II.2.3,

$$f_{\alpha n i} = \sum_k U_{nk}^{(\alpha i)} \tilde{c}_{\alpha k i}\,, \tag{3.12}$$

For the SIAM, we combine the left and right leads, as described in equation (3.9). Therefore, only two unitary transformations are needed, $U^{(i)}$ with $i \in \{1, 2\}$, tridiagonalizing the modes $\tilde{c}^{(+)}_{k\sigma i}$ with couplings $\tilde{v}^{(+)}_{ki}$ and energies ε_k,

$$f_{n\sigma i} = \sum_k U^{(i)}_{nk} \tilde{c}^{(+)}_{k\sigma i} \,. \tag{3.13}$$

The resulting geometry is depicted in figure VI.5 with (a) four channels of the IRLM and (b) two channels in the SIAM. The first part of the chains represents the high-energy scales of the leads. In this energy range, for the "holes" ("particles") only the positive (negative) energies contribute to the hybridization, while the negative (positive) energies decouple from the impurity, see equation (3.7). Therefore, the couplings in this sector of the chain decay with Λ^{-n}. For these energy scales, which are effectively in equilibrium, the purification of the thermofield approach has replaced a standard Wilson chain with couplings $t_n \sim \Lambda^{-n/2}$ by two chains for "holes" and "particles" with couplings $t_n \sim \Lambda^{-n}$.

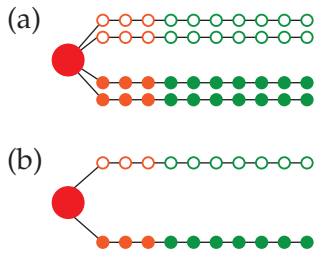

Figure VI.5: Sketch of the chain geometry after tridiagonalization. "Holes" and "particles" are kept in separate channels. The beginning of the chains corresponds to the logarithmically discretized sector, the later part to the transport window. (a) In models like the IRLM, where left and right leads have to be treated separately, one has four separate chains. (b) In models like the SIAM, where left and right leads, can be combined one has two channels.

VI.3.3 Renormalization

Using the numerical renormalization group one can integrate out the high energy scales and bring the problem down to an effective bandwidth D^* [88, 89]. In practice, this is done by diagonalizing the Hamiltonian of the first chain elements based on the standard NRG truncation, see section III.3 for details. The lowest eigenstates of the last NRG iteration equal the low-energy sector of the full NRG basis of approximate energy eigenstates, compare section III.3.4. These states, therefore, represent a basis of the low-energy sector of the first part of the chain and can be interpreted as the basis of the effective local dimension of a *renormalized impurity*.

In the following we comment on the number of sites treated with NRG. Moreover, we explain how for the NRG sector "holes" and "particles" can be recombined to guarantee a well-defined NRG calculation and how operators can be expressed in the effective basis of the renormalized impurity.

Identifying the NRG sector

The number of chain elements treated with NRG could in principle be determined from the number of lead levels that lie outside the transport window in the star geometry. However, it can equally well be determined in the chain geometry. The criteria used are: (i) The decay of the hoppings should be strong enough to ensure that the truncation within NRG is well-defined. (ii) The hoppings and the absolute values of the on-site energies should be

larger than D^*. By construction the two conditions are approximately equivalent.

Including "too many" lead levels into the sector described by NRG makes the truncation within NRG ill-defined because the hoppings in the chain at some point go over from the exponential decay into a constant behavior and energy-scale separation is not guaranteed any longer. Moreover, for the definition of the initial state of the quench we assume that for this NRG part the thermal state is equal to the ground state, see the next paragraph for details. This is only a well-defined assumption if we do not reach into the transport window. Including "not enough" lead levels into the NRG sector makes the quench calculation more costly because larger energy scales are involved such that smaller Trotter time steps are required. For our calculations in the SIAM, see section VI.5, we typically performed the renormalization such that the largest kept many-body energy E_{trunc} is of the order of $E_{\text{trunc}} = 5D^* - 20D^*$, corresponding to 500-700 eigenstates.

Recombination of "holes" and "particles"

From a technical point of view, one could perform the NRG run with two channels, one for the "holes" and one for the "particles". However, from a physical point of view it is unfavorable to describe "holes" and "particles" in different channels because then any particle-hole excitation is separated into different Wilson chains with energy scale separation. Therefore, we recombine "holes" and "particles" within the high-energy sector which we want to describe based on NRG. This corresponds to a further tridiagonalization,

$$\tilde{f}_{x\tilde{n}} = \sum_{ni} \tilde{U}^{(x)}_{\tilde{n},(ni)} f_{x,(ni)} \,, \tag{3.14}$$

with x being a placeholder for all remaining channel indices: in case of the IRLM, the tridiagonalization is performed for the two leads separately, $x = \alpha$, while for the SIAM one has an additional spin index, $x = \sigma$, but $\tilde{U}$ itself does not depend on this spin index.

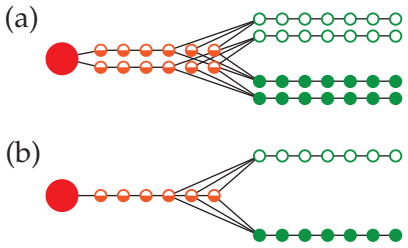

Figure VI.6: Sketch of the recombination of "holes" and "particles" for the high-energy modes. Due to this further transformation a small non-locality arises. (a) In the IRLM one has to keep left and right leads independent. (b) For the SIAM, where left and right leads can be combined, one obtains one channel in the NRG sector, which strongly resembles a standard Wilson chain.

The resulting geometry is depicted in figure VI.6(a) for the IRLM and in VI.6(b) for the SIAM. In terms of the Hamiltonian, the tridiagonalization takes the form (suppressing the index x):

$$\begin{pmatrix} * & t_{1,i=1} & 0 & \dots & t_{1,i=2} & 0 & \dots \\ t^*_{1,i=1} & \chi_{1,i=1} & t_{2,i=1} & \dots & 0 & 0 & \dots \\ 0 & t^*_{2,i=1} & \chi_{2,i=1} & \dots & 0 & 0 & \dots \\ \dots & \dots & \dots & \dots & 0 & 0 & \dots \\ t^*_{1,i=2} & 0 & 0 & \dots & \chi_{1,i=2} & t_{2,i=2} & \dots \\ 0 & 0 & 0 & \dots & t^*_{2,i=2} & \chi_{2,i=2} & \dots \\ \dots & \dots & \dots & \dots & \dots & \dots & \dots \end{pmatrix} \longrightarrow \begin{pmatrix} * & \tilde{t}_1 & 0 & \dots & & & \\ \tilde{t}^*_1 & \tilde{\chi}_1 & \tilde{t}_2 & 0 & \dots & & \\ 0 & \tilde{t}^*_2 & \tilde{\chi}_2 & \tilde{t}_3 & 0 & \dots & \\ \dots & 0 & \tilde{t}^*_3 & \tilde{\chi}_3 & \tilde{t}_4 & 0 & \dots \\ \dots & & & \dots & & & \dots \\ & & & & & & \end{pmatrix} \tag{3.15}$$

Before this tridiagonalization, the Hamiltonian consists of two channels for "holes" and "particles", colored green and red in equation (3.15). Each of the channels is in a chain geometry, but as they both couple to the same impurity (indicated by the "*"), the total Hamiltonian is not tridiagonal. After tridiagonalization there is only one chain left, which is twice as long. For a symmetric model, the new on-site energies $\tilde{\chi}_n$ are zero. And, while the hoppings and energies of "holes" and "particles" decay as Λ^{-n}, the new hoppings $\tilde{t}_n$ scale as $\Lambda^{-n/2}$. In this sense, the new geometry resembles a standard Wilson chain introduced in section III.3.1, and the NRG run is essentially that of an equilibrium calculation. This reflects the fact that the high-energy modes are effectively in equilibrium and not affected by temperature and voltage, which per definition act on a lower energy scale.

As depicted in figure VI.6, the recombination of "holes" and "particles" into one chain introduces a non-locality: Because the first "hole" and "particle" sites of the transport window originally couple to the last elements of the NRG sector, f_{xNi}, they couple to a linear combination of modes $\tilde{f}_{xn}$ after the unitary transformation. For the time evolution of the quench this non-locality is not problematic because any linear combination of operators acting on the different sites of the renormalized impurity can be expressed within the effective NRG basis, see below. However, the nonlocal couplings are subject to truncation in NRG. For couplings that extend over a long part of the chain, this would introduce a relevant error. Fortunately, the energy scale separation of the Wilson chain ensures that this non-locality stretches only over a few sites such that the error due to truncation is tolerable.

We argued before that "holes" and "particles" should be kept in separate channels, see section VI.2.4. The reason is that only in this case one immediately knows how the thermal state looks like in the chain geometry (all "hole" modes empty, all "particle" modes filled). After the recombination we expect the new sites to be approximately half-filled and the thermal state is not a simple product state any more. However, this does not matter because these high-energy modes are effectively in equilibrium and are not influenced by temperature and voltage. Therefore, for these high-energy modes to be "thermal", one can equally well take the groundstate of this part of the chain, which is known from the NRG calculation.

Operators in the effective basis

The states kept in the last NRG iteration represent an effective low-energy basis for the first part of the chain, consisting of approximate eigenstates of the Hamiltonian, see section III.3. This effective basis can be interpreted as the local state space of the renormalized impurity. We order our matrix product state such that the renormalized impurity is located in the middle with the channel of "holes" to the left, and the channel of "particles" to the right, as depicted in figure VI.7(a).

Any operator, local or non-local, that acts on the sites included in the renormalized impurity, can be expressed in the effective NRG basis. Typically, the operator is known in the local basis $\{|\Sigma\rangle = |\sigma_1\rangle \otimes |\sigma_2\rangle \otimes \cdots \otimes |\sigma_N\rangle\}$

$$O = \sum_{\Sigma,\Sigma'} O_{\Sigma,\Sigma'} |\Sigma\rangle \langle\Sigma'| \quad \text{with} \quad O_{\Sigma,\Sigma'} = \langle\Sigma| O |\Sigma'\rangle \ . \tag{3.16}$$

The connection between this local basis $\{|\Sigma\rangle\}$ and the basis of NRG states $\{|n\rangle\}$ is given by the A-matrices of the NRG run, the definition of which is given in section III.3.3,

$$\langle\Sigma|n\rangle = \sum_{|\tilde{\sigma}\rangle} \left(A^{[\tilde{\sigma}_1]} \ldots A^{[\tilde{\sigma}_N]}\right)_n \langle\Sigma|\tilde{\sigma}_1 \otimes \cdots \otimes \tilde{\sigma}_N\rangle = \left(A^{[\sigma_1]} \ldots A^{[\sigma_N]}\right)_n \ . \tag{3.17}$$

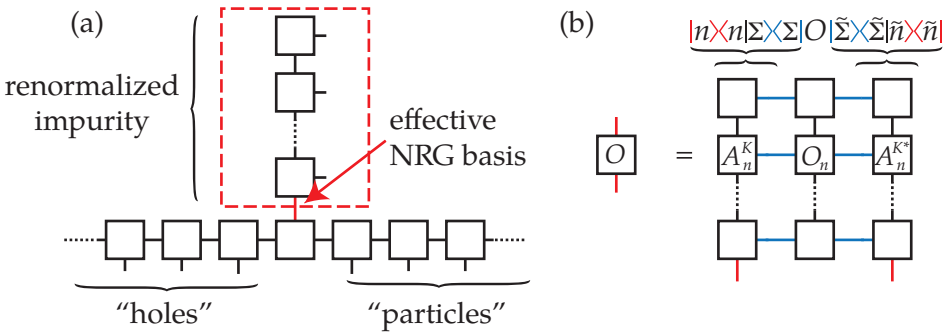

Figure VI.7: Sketch of the renormalized impurity and its operators: (a) The NRG run provides an effective basis for the renormalized impurity, which we can interpret as the local dimension of one MPS chain. This impurity is located in the middle of our MPS chain. We arrange the channel for the "holes" to the left of the impurity, and the channel for the "particles" to the right. (b) Any operator acting within the state space of the renormalized impurity can be expressed in the effective basis using the A-matrices of the NRG run.

To represent O in the effective basis one therefore sandwiches the operator between the A-matrices of the NRG run, as depicted in figure VI.7(b) to obtain

$$O = \sum_{n,n'} O_{n,n'} \, |n\rangle \langle n'| \quad \text{with} \quad O_{nn'} = \langle n| \, O \, |n'\rangle = \sum_{\Sigma,\Sigma'} \langle n|\Sigma\rangle \, O_{\Sigma,\Sigma'} \, \langle \Sigma'|n'\rangle \; . \tag{3.18}$$

When representing fermionic operators O in the basis $\{|n\rangle\}$ care has to be taken to include the correct fermionic signs, as described in section III.1.4. For the MPS including the renormalized impurity we define the fermionic ordering along the chain as described in section III.1.4. The fermionic signs for the sites within the renormalized impurity can be accounted for *locally* using a corresponding definition of all operators in the effective basis. Within the renormalized impurity we use an ordering along the Wilson chain.

VI.3.4 tDMRG Quench

The time evolution of the quench is performed based on matrix product states. The following section explains details on the initial state and the time evolution. Furthermore, it suggests to switch on the coupling between impurity and thermal leads slowly to smoothen the behavior of the time evolution.

Initial state

In the initial state of the quench the leads are thermal and fixed at different chemical potentials. Within the thermofield approach this corresponds to the state in which all "hole" modes are empty and all "particle" modes are filled,

$$|\psi_{\text{ini}}\rangle = |0\rangle \otimes |0\rangle \otimes \ldots \otimes |0\rangle \otimes |\phi_{\text{ini}}\rangle \otimes |1\rangle \otimes |1\rangle \otimes \ldots \otimes |1\rangle \; . \tag{3.19}$$

On our MPS, this initial state is a simple product state. As the energy scales summarized in the renormalized impurity are large compared to voltage and temperature, a suitable initial state for the impurity, $|\phi_{\text{ini}}\rangle$, is the ground state of the NRG run. Equally well, one could use any other state whose energy is small compared to the size of the transport window.

Depending on the precise model, the initial state may break symmetries of the Hamiltonian. In particular, using conservation numbers such as charge or z-component of the spin as abelian quantum numbers in the MPS tensors can make it difficult to respect the symmetries. E.g., as we include the same number of "holes" and "particles" into the renormalized impurity, the total number of sites in the Wilson chain, including the impurity, is odd. This makes it impossible to preserve the particle-hole symmetry of the Hamiltonian in the IRLM. One could think of using the sum over two degenerate ground states with different quantum numbers as the initial state to restore the symmetry. Equivalently, one could perform two independent quenches with different quantum numbers and average over the result. Also quasi-degenerate states could be considered. Knowing the symmetries of the Hamiltonian, which should be reflected in the steady-state, it is also possible to simply symmetrize the result of a single quench. So far, in our calculations we tolerated the symmetry breaking and discussed its consequences, see the appendix of the paper [P2].

Time evolution

On the MPS, one can perform a standard time evolution based on the time-dependent density-matrix renormalization group and a standard second-order Trotter decomposition, as explained in section III.2. Technically, one could do this using the fixed truncated effective basis for the impurity site in the middle of the chain. However, the hopping from the renormalized impurity to its neighboring sites would then be exponentiated within a truncated basis. To avoid this, we introduce one *"flexible site"*, as depicted in Figure S3 of [P2] in chapter VII: if the renormalized impurity contains the first N sites in the sense of the Hamiltonian H_N in section III.3, we continue the Wilson chain by one further site consisting of one "hole" and one "particle". In the resulting basis, we can exponentiate the Hamiltonian H_{N+1}, including the coupling between sites N and $N+1$. This is justified in the sense of a standard NRG iteration step. To describe the couplings between sites $N+1$ and the remaining "holes" and "particles", the site $N+1$ can be reinstated into the channels of "holes" and "particles", compare the appendix of [P2] for details. When interchanging different sites in this procedure, fermionic swap gates [93] can be used to guarantee the correct ordering in terms of fermionic signs.

The size of the Trotter time steps should be small compared to the energy scales involved. Without renormalization of the impurity, this means that δt scales with D^{-1}. After renormalization the relevant energy scale is given by D^{*-1}. A good point of reference is given by the largest many-body energy kept in the NRG run, $\delta t \sim E_{\text{trunc}}^{-1}$, compare section VI.3.3. In our calculations a proportionality constant of $0.5 - 1$ turned out to be a suitable choice. After applying a Trotter gate, the singular values of the corresponding bond are truncated. The threshold used in our calculation varied between $\varepsilon_{\text{tol}} = 2 \cdot 10^{-4} - 10^{-3}$. For an analysis of the error in our time evolution see figure S5 of the appendix of the paper [P2] in chapter VII. The calculation is stopped when a maximal bond dimension D_{max} is reached. In our calculations for the SIAM we used values for D_{max} up to 450. At first glance, this does not seem to be much, but one has to bear in mind that the local dimension of the impurity has a local dimension of $d \approx 500 - 700$.

For the second order Trotter decomposition we use the form given in equation (III.2.3). Calculating many subsequent time steps the half-time steps for the even or odd layers in the beginning and at the end of each time step can be combined into one, as given in equation (III.2.4). Whenever expectation values are calculated in between, this procedure has to be interrupted and the half-time steps have to be performed explicitly.

Switching on the coupling between impurity and thermal leads

The initial state corresponds to a state in which the thermal leads are *decoupled* from the impurity. At time $t = 0$, the coupling between thermal leads and impurity is switched on such that a current starts flowing through the impurity. Instead of this sudden quench, one can switch on the coupling over a small time window $[0, t_{\text{ramp}}]$. This kind of *"ramping"* can smoothen the behavior of the expectation values with time. The exact implementation of this ramping does not seem to have much influence on the results. We divide the interval $[0, t_{\text{ramp}}]$ into N small intervals and increase the coupling stepwise $\eta_n = \eta \frac{n}{N}$ with η being the full coupling in the final Hamiltonian.

VI.3.5 Expectation Values

During the time evolution one would like to keep track of different expectation values such as the current and the dot occupation. However, it is not necessary to calculate the expectation value after each Trotter time step. Instead one can define an arbitrary time window of N Trotter time steps, $\Delta t = N\delta t$, and evaluate the expectation values at the times $t_n = n\,\Delta t$. The calculation of expectation values based on MPS is straightforward, compare section III.1.1.

The quench provides the time evolution of the considered quantity. From this time dependence one can deduce a reasonable steady-state mean in the limit of large enough times t.

In the following we briefly comment on three physical quantities, their definitions and the connection between them: the current, the conductance, and the dot occupation.

Current and Conductance

The current through the impurity can be defined by looking at the change in the dot occupation: particles flow into the impurity from the one lead and out to the other lead. In the steady state the net change in the dot occupation is zero because all expectation values should be stable in this state. However, one can still identify the contributions from the different leads.

For the IRLM one finds

$$\begin{aligned}\sum_\alpha J_\alpha^{(\text{IRLM})} &= e\,\langle \dot{n}_C\rangle = -\frac{\mathrm{i}}{\hbar}\,\langle [n_C, H]\rangle = -\frac{\mathrm{i}}{\hbar}\sum_\alpha \left(t'\,\langle d_C^\dagger d_\alpha\rangle - \text{h.c.}\right)\\ &= -\frac{\mathrm{i}}{\hbar}\sum_\alpha \left(2\mathrm{i}t'\mathrm{Im}\left(\langle d_C^\dagger d_\alpha\rangle\right)\right) = \sum_\alpha \frac{2e}{\hbar}\mathrm{Im}\left(t'\,\langle d_C^\dagger d_\alpha\rangle\right)\,, \qquad (3.20)\end{aligned}$$

$$J_\alpha^{(\text{IRLM})} = \frac{2e}{\hbar}\mathrm{Im}\left(t'\,\langle d_C^\dagger d_\alpha\rangle\right)\,. \qquad (3.21)$$

In the hybrid NRG-tDMRG approach (see section VI.3) the operator $d_C^\dagger d_\alpha$ can be expressed in the effective basis of the renormalized impurity and the corresponding expectation value can easily be evaluated in terms of a local operator, compare section III.1.1. Care has to be taken in the definition of the operator $d_C^\dagger d_\alpha$ within the effective basis because it has to include fermionic signs, as described in section III.1.4.

For the SIAM analogously one obtains

$$J_\alpha^{(\mathrm{SIAM})} = \frac{2e}{\hbar}\sum_{k\sigma}\mathrm{Im}\left(v_q\,\langle d^\dagger c_q\rangle\right) = \frac{2e}{\hbar}\sum_{k\sigma}\sum_i \mathrm{Im}\left(\tilde{v}_{qi}\,\langle d^\dagger \tilde{c}_{qi}\rangle\right)\,, \tag{3.22}$$

where we used $v_q c_q = \sum_i \tilde{v}_{qi}\tilde{c}_{qi}$ to describe the current in terms of "holes" and "particles". In this model, we combine left and right leads into "even" and "odd" modes $\tilde{c}^{(\pm)}_{k\sigma i}$ as defined in equation (3.9). The modes $\tilde{c}_{qi}$ can be expressed in terms of the modes $\tilde{c}^{(\pm)}_{k\sigma i}$,

$$\tilde{c}_{qi} = \frac{1}{\tilde{v}^{(+)}_{ki}}\left(\tilde{v}^*_{\alpha k\sigma i}\tilde{c}^{(+)}_{k\sigma i} \mp \tilde{v}_{\bar{\alpha}k\sigma i}\tilde{c}^{(-)}_{k\sigma i}\right) \tag{3.23}$$

with the minus (plus) sign and $\bar{\alpha} = R$ ($\bar{\alpha} = L$) for $\alpha = L$ ($\alpha = R$). The modes $\tilde{c}^{(-)}_{k\sigma i}$ decouple from the model, therefore

$$\langle d^\dagger \tilde{c}^{(-)}_{k\sigma i}\rangle = 0\,, \tag{3.24}$$

such that

$$J_\alpha^{(\mathrm{SIAM})} = \frac{2e}{\hbar}\sum_{k\sigma i}\frac{|\tilde{v}_{qi}|^2}{\tilde{v}^{(+)}_{ki}}\mathrm{Im}\left(\langle d^\dagger \tilde{c}^{(+)}_{k\sigma i}\rangle\right)\,. \tag{3.25}$$

To express J_α in terms of the operators corresponding to the local state space of our MPS chain, two tridiagonalizations have to be considered: firstly the one, which maps the modes $\tilde{c}^{(+)}_{k\sigma i}$ onto a chain, see equation (3.13), and secondly the recombination of "holes" and "particles" in the NRG sector, see equation (3.14),

$$\begin{aligned}\tilde{c}^{(+)}_{k\sigma i} &= \sum_n \left(U^{(i)\dagger}\right)_{kn} f_{n\sigma i}\\ &= \sum_{n\notin\mathrm{NRG}}\left(U^{(i)\dagger}\right)_{kn} f_{n\sigma i} + \sum_{n\in\mathrm{NRG}}\sum_{\tilde{n}}\left(U^{(i)\dagger}\right)_{kn}\left(\tilde{U}^\dagger\right)_{(ni,\tilde{n})}\tilde{f}_{\tilde{n}\sigma}\,.\end{aligned} \tag{3.26}$$

Using this connection, the expectation values $\langle d^\dagger \tilde{c}^{(+)}_{k\sigma i}\rangle$ in equation (3.25) can be calculated from $\langle d^\dagger f_{n\sigma i}\rangle$ and $\langle d^\dagger \tilde{f}_{\tilde{n}\sigma}\rangle$. However, due to the combination of left and right leads into "even" and "odd" modes, compare section VI.3.2, the current is a nonlocal quantity in the sense that all these expectation values are needed. The terms $\langle d^\dagger \tilde{f}_{\tilde{n}\sigma}\rangle$ can be calculated within the effective basis (again including the use of fermionic signs). For the $\langle d^\dagger f_{n\sigma i}\rangle$ only the operator $d^\dagger$ is represented in the effective basis while $f_{n\sigma i}$ acts on the corresponding MPS site. Here, the fermionic signs taking into account the sites in the renormalized impurity are included in the definition of the operator $d^\dagger$ in the effective basis. The fermionic signs of the remaining MPS sites are treated as explained in section III.1.4.

Interestingly, the symmetrized current,

$$J_{(\sigma)}(t) = \frac{1}{2}\left(J_{L(\sigma)}(t) - J_{R(\sigma)}(t)\right) \tag{3.27}$$

converges faster than the currents $J_{L(\sigma)}$ and $J_{R(\sigma)}$ converge separately. In our quench calculations we therefore consider the symmetrized current $J_{(\sigma)}(t)$. For the SIAM, one could instead also consider the mean over the spin, $J_\alpha(t) = \frac{1}{2}\left(J_{\alpha\uparrow}(t) + J_{\alpha\downarrow}(t)\right)$. In our calculation

we have done both, the mean over channels and the sum over spins,

$$J(t) = J_\uparrow(t) + J_\downarrow(t) = \frac{1}{2}\sum_\sigma \left(J_{L\sigma}(t) - J_{R\sigma}(t)\right) . \tag{3.28}$$

To deduce a steady-state value J we take the mean of $J(t)$ over the "last part" of the time-window accessible by tDMRG. For high voltages, where the current shows strong oscillations with period $\frac{4\pi}{V}$, this typically includes the last period. For low voltages, the current $J(t)$ varies around a well-defined plateau after a transient behavior. Examples for the behavior of $J(t)$ can be found in figure S4 of the publication [P2] in chapter VII.

The conductance we deduce from

$$G(V) = \frac{\mathrm{d}J(V)}{\mathrm{d}V} \approx \frac{J(V_1) - J(V_2)}{V_1 - V_2} \quad \text{with } V = \frac{1}{2}(V_1 + V_2) \tag{3.29}$$

and V_1 and V_2 "close" to each other. For $V_1 \approx V_2$, the curves $J(t)$ for $V = V_1$ and $V = V_2$ show a similar behavior with time t. Therefore, we choose the time window over which the mean is taken to deduce $J(V)$ very similar in both cases. This can strongly reduce the error because we concentrate on the *difference* in the two curves, and thereby reduce the influence of fluctuations in the curves $J(t)$.

Dot Occupation

The operator counting the number of particles on the impurity acts locally within the basis of the renormalized impurity. It is therefore simple to evaluate. In the IRLM we consider the dot occupation of the central impurity site, $N_d = \langle n_C \rangle$. In the SIAM we investigate the spin-resolved occupation of the impurity site $N_{d\sigma} = \langle n_\sigma \rangle$.

The time derivative of the dot occupation is immediately connected to the left and right currents,

$$\dot{N}_{d(\sigma)} = \frac{1}{e}\left(J_{L(\sigma)} + J_{R(\sigma)}\right) \tag{3.30}$$

In the steady state one expects $J_{L(\sigma)} = -J_{R(\sigma)}$ and $\dot{N}_{d(\sigma)} = 0$. However, the symmetrized current in equation (3.27) converges faster than $J_{L(\sigma)}$ and $J_{R(\sigma)}$, and consequently also faster than the dot occupation, compare figure S4 in the appendix of paper [P2]. Especially for large voltages it can therefore be difficult to deduce a steady-state value for $N_{d\sigma}$, compare also section VI.5.2.

For the reults on the SIAM in section VI.5 we only consider the particle-hole symmetric case, for which the total dot occupation is always given by $N_d = N_{d\uparrow} + N_{d\downarrow} = 1$. However, for finite magnetic field, $B \neq 0$, the magnetization $M = N_{d\uparrow} - N_{d\downarrow}$ is nontrivial and depends on the voltage, see section VI.5.2.

VI.4 Results on the Interacting Resonant Level Model

We used the interacting resonant level model as a nontrivial benchmark for our method, see section II.1.2 for a definition of the Hamiltonian and the parameters. For this model the current as a function of voltage has been calculated numerically based on DMRG quench calculations [82, 84] and for a specific value of the interaction U also analytically based on the Bethe ansatz [82]. For large voltages the current shows a regime of negative differential

conductance, i.e., the current decreases with increasing voltage. The Bethe ansatz result for the current as a function of voltage is universal in the sense that the curve retains its shape for different hoppings t' as long as both, current and voltage, are scaled in units of an energy scale T_B that depends on t'. We recalculated the curve for the current versus voltage found in [82]. In particular, we demonstrated that our method is able to treat low-energy scales using small values of the coupling t', and thus small values of the scale T_B. Our benchmark data together with a more detailed analysis can be found in figure 2 of the paper [P2] in chapter VII.

VI.5 Results on the Single-Impurity Anderson Model

Our main focus lies in the description of nonequilibrium Kondo physics in the single-impurity Anderson model. For an introduction to Kondo physics and a definition of the single-impurity Anderson model and its parameters see chapter II. Section VI.5.1 shows our results on the zero-bias peak in the conductance and its behavior with temperature and magnetic field. Section VI.5.2 comments on the possibility to determine the magnetization of the dot in case of a finite magnetic field B. It is expected that the form of the zero-bias peak is universal for different values of interaction U, as long as U is large enough. This is referred to as the *"scaling limit"*. However, it is not clear how reliably this limit of large U can be realized in experiment. Therefore, section VI.5.3 discusses the dependence of the conductance on a finite value of U.

VI.5.1 The Zero-Bias Peak

The main characteristics of Kondo physics in a quantum dot is the zero-bias peak in the conductance. On the Kondo scale the conductance as a function of voltage decreases from its maximal value to zero. In the Kondo limit $U \to \infty$, this is a universal curve in units of T_K.

Figure VI.8 shows our results for the differential conductance $g(T, V) = \left(2e^2/h\right)^{-1} G(T, V)$ with $G = \mathrm{d}J/\mathrm{d}V$ at the particle-hole symmetric point. With one exception in figure VI.8(a) we have chosen $U/\Gamma = 12$ and $\Gamma = 10^{-3}D$, resulting in a Kondo temperature of $T_K = 2.61 \cdot 10^{-5}D$, such that $U/T_K \approx 460$. This figure is part of the paper published under the reference [P2]. The different panels show (a) the zero bias peak, (b) its temperature dependence, (c) its splitting with finite magnetic field, and (d) an analysis of the peak position for finite magnetic field. An analysis of the error in our data can be found in the appendix of reference [P2].

Non-interacting case

As a very first check the inset of figure VI.8(a) displays the current as a function of voltage in the case of $U = 0$, thus in the absence of Kondo physics. These curves can be benchmarked against analytic results and show nice agreement for both, zero temperature and finite temperature.

The zero-bias peak

Figure VI.8(a) displays the conductance as a function of voltage at temperature $T = 0$, $g(0, V)$, for two different values of U/Γ. As long as both curves agree one describes the scaling limit. Thus, the two curves illustrate that we are in the scaling limit up to voltages that are clearly beyond $V \sim T_K$. Because we apply the voltage symmetrically, this curve is

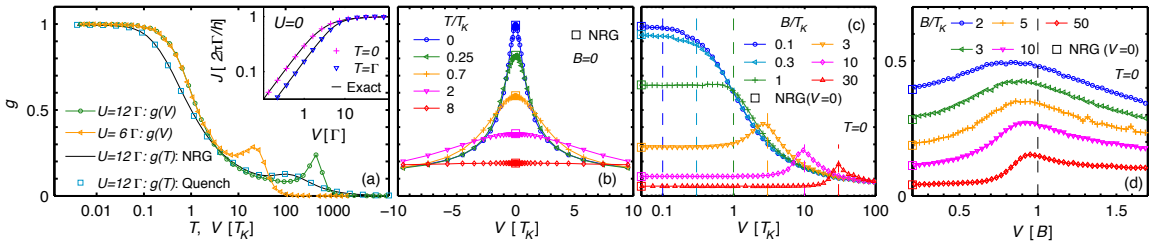

Figure VI.8: [This figure is taken from our publication: Phys. Rev. Lett **121** (2018), 137702, see reference [P2]]. (a) The conductance as a function of temperature at voltage $V = 0$ and as a function of voltage at temperature $T = 0$. (b) The conductance as function of voltage for different temperatures T. (c) The conductance as function of voltage for different values of the magnetic field B. The dashed lines indicate the point at which $V = B$. (d) Similar data as in (c), but with voltage given in units of B to allow a closer look on the peak position.

symmetric around zero, and only data points for $V > 0$ are shown. An interesting point of comparison for this zero-bias peak is given by the conductance as a function of temperature in the limit of zero voltage, $g(T, 0)$. The latter curve is an equilibrium property and can also be deduced from FDM-NRG, compare section III.3.4. Figure VI.8(a) shows $g(0, T_K)$ twice, once calculated using NRG, and once calculated based on our quench approach. The agreement of the two methods is a further benchmark for the validity of our method in the limit of small voltage. The voltage-dependent curve $g(0, V)$ is expected to lie above the temperature-dependent curve $g(T, 0)$. This is known, e.g., from experiment [28]. An immediate measure for the distance of the two curves is the value of $g(0, V = T_K)$, where T_K is defined via $g(T = T_K, 0) = \frac{1}{2}$. We find $g(0, T_K) \approx 0.60 \pm 0.02$, while previous non-exact approaches obtained $g(0, T_K) \approx \frac{2}{3}$ [33, 34], see also the paper [P2] presented in chapter VII.

The temperature dependence

For $U/\Gamma = 12$, figure VI.8(b) shows the zero-bias peak for different values of temperature T. Only the data points for $V > 0$ were calculated, while the data points at $V < 0$ follow from symmetry. The zero-bias peak decreases with increasing temperature, in agreement with many experiments [10–12, 26–28]. The values at $V = 0$ can again be deduced from FDM-NRG and nicely coincide with the quench result. This is equivalent to the agreement in the two curves for $g(T, 0)$ in panel (a).

The splitting due to a finite magnetic field

For finite magnetic field the zero-bias peak is known to split into two peaks at $V \approx \pm B$ [10, 11, 25, 27]. Our result for this splitting is shown in figure VI.8(c) for $U/\Gamma = 12$ and different values of the magnetic field B. Again, for $V = 0$ one can compare to data obtained from NRG which nicely agrees with our quench data.

Figure VI.8(d) shows similar data as figure VI.8(c), but on a linear voltage scale and in units of the magnetic field B. This way of illustrating the peak reveals that the peak position is somewhat below $V = B$ for smaller magnetic fields, but clearly moves towards $V = B$ for larger magnetic fields.

VI.5.2 Magnetization

In addition to the current further expectation values can be considered. One interesting example is the magnetization $M = N_{d\uparrow} - N_{d\downarrow}$ in the case of a finite magnetic field. Let us, therefore, reconsider the case of $B \neq 0$ given in figure VI.8(c). From exactly the same quenches, one can not only deduce the current, but also the spin-resolved dot occupation and, therefore, the magnetization M. However, while the symmetrized current in equation (3.27) converges in the accessible time window, this is not necessarily true for the dot occupation, see also the corresponding discussion in section VI.3.5.

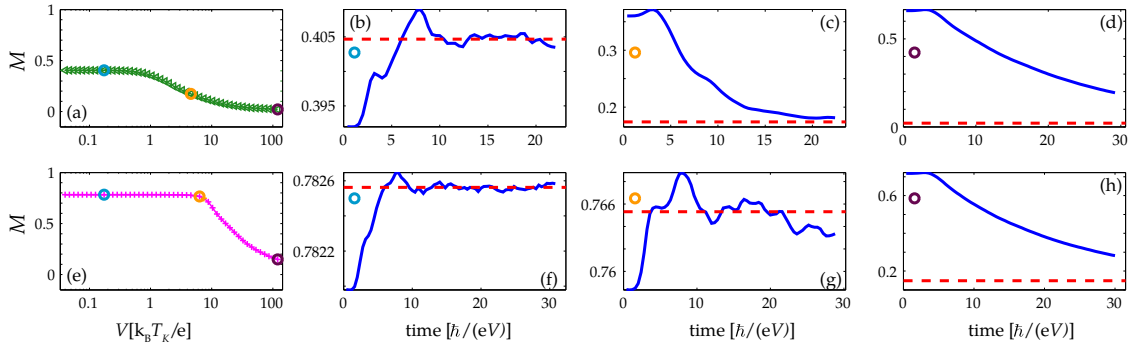

Figure VI.9: Examples for the time dependence of the magnetization in the quench calculations: Panel (a) and (e) show an estimate of the magnetization as a function of voltage for $B = T_K$ and $B = 10T_K$, respectively. Panels (b-d) and (f-h) display the underlying behavior of $M(t)$. For the small voltages in panel (b) and (f), respectively, one can average over a steady-state plateau. For high voltages, as in panel (d) and (h), the magnetization is not converged. An estimate for a steady-state value can be deduced by fitting an exponential decay. Panel (c) and (g) display examples of intermediate voltages.

Let us illustrate this with a few examples, given in figure VI.9. While panel (a) and (e) show an estimate of the magnetization as a function of voltage for $B = T_K$ and $B = 10T_K$, respectively, panels (b-d) and (f-h) show examples of the underlying time-resolved magnetization $M(t) = N_{d\uparrow}(t) - N_{d\downarrow}(t)$. For small voltages, as, e.g., in panel (b) and (f), the curves develop a plateau around which the curves fluctuate and a well-defined mean can be deduced. For high voltages, as, e.g., in panel (d) and (h) one finds a curve which is domninated by an exponential decay. When zooming in, further small fluctuations get visible. In these cases one can deduce the magnetization from an exponential fit. For intermediate voltages, such as, e.g., in panels (c) and (g), one possibly sees neither a nice plateau nor a clear exponential decay. In all of the six panels showing the time-dependence, the red line shows an estimate for the value of the magnetization in the steady-state.

For a correct evaluation of the magnetization one would need to improve the calculations. Possibly, it could be of some advantage to weaken the criteria regarding truncation or the number of lead levels to reach longer time scales. Moreover, employing methods such as linear prediction [94] could improve the quality of the extrapolation.

Nevertheless, figure VI.10 shows an estimate of the magnetization as a function of voltage for four of the parameter sets of figure VI.8(c), obtained either by taking the mean over a late time window of $M(t)$ or via an exponential fit in the case of large voltages. For small voltages we recover the magnetization found by FDM-NRG and indicated by the squares. For voltages comparable to the magnetic field the magnetization starts to decrease until it would finally reach a value of $M = 0$ in the limit of large V.

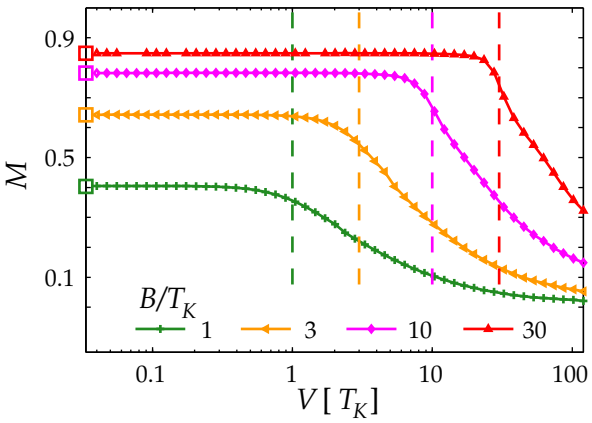

Figure VI.10: Estimate for the magnetization M as a function of voltage for different values of the magnetic field B. The colored dashed lines indicate the position of $V = B$. The magnetization decreases from its equilibrium value to zero on a scale given by $V \approx B$.

VI.5.3 Universality of the Conductance

The physics of the Kondo effect is known to be universal in the sense that in the scaling limit of $U/\Gamma \to \infty$ the results are independent of the exact value of U/Γ when scaling all energies in units of T_K. However, in experiments this scaling limit may not always be realized. Therefore, it is interesting to study the behavior of the conductance for different values of U/Γ.

In figure 3(a) of the publication [P2] two different values of U/Γ were used, $U/\Gamma = 12$ and $U/\Gamma = 6$. In this section, we consider two further ratios, namely $U/\Gamma = 4.5$ and $U/\Gamma = 2$.

The Kondo temperature T_K scales exponentially with U/Γ, $T_K \propto \exp\left(-\frac{\pi U}{8\Gamma}\right)$, compare equation (II.3.4). For the four values of U/Γ considered in this section, the values of T_K, defined via $G(T = T_K) = \frac{1}{2}G_0$, are given in table VI.1. In section II.3.2 we introduced a second definition of the Kondo scale using the zero-field susceptibility. For the value of this energy $T_K^{(\chi)}$ an analytic formula has been found, see equation (II.3.4). Table VI.1 shows the tendency that the difference in the two definitions is smaller for large values of U/Γ.

U/Γ	T_K/Γ	U/T_K	$T_K/T_K^{(\chi)}$
2	0.86	2.33	0.86
4.5	0.41	10.96	1.13
6	0.23	26.41	1.07
12	0.026	459.98	1.04

Table VI.1: Values of the Kondo scale T_K for different ratios of U/Γ.

Figure VI.11(a) displays the differential conductance as a function of temperature T at voltage $V = 0$ with temperature scaled in units of T_K. Analogously, panel (b) displays the conductance as a function of voltage at zero temperature, again with voltage scaled in units of T_K. For small temperatures and voltages, respectively, one clearly finds the universality of the curves in the sense that the different curves for different ratios U/Γ coincide. However, this is only true as long as we can guarantee $V \ll U$. For convenience, the value of U is indicated by the dashed lines in figure VI.11. Due to the exponential scaling of T_K, the ratio of U/T_K strongly increases with increasing U/Γ, compare table VI.1. For large values of U/Γ one can therefore describe the universal curve up to much higer values of T/T_K and V/T_K.

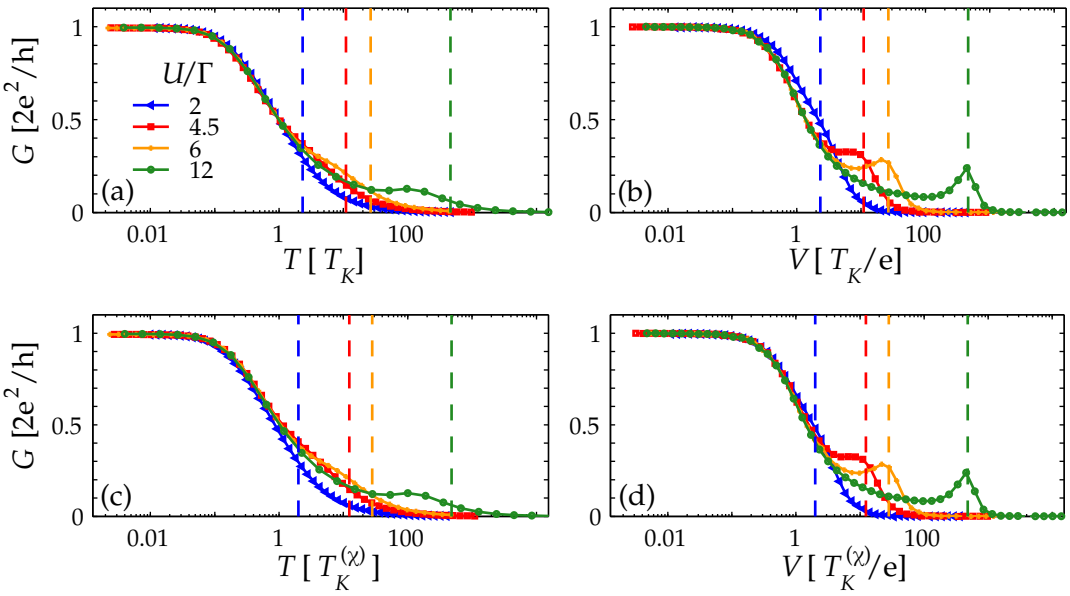

Figure VI.11: Conductance versus (a) temperature and (b) voltage for different values of U/Γ. While $U/\Gamma = 6$ and $U/\Gamma = 12$ show the same behavior up to voltages of the order T_K, one can clearly see deviations around $V \sim T_K$ in case of $U/\Gamma = 2$. The lower panels (c) and (d) show the same data as (a) and (b), but with temperature and voltage scaled in units of $T_K^{(\chi)}$ instead of T_K.

The two panels (a) and (b) in figure VI.11 should not be interpreted independently of each other: the value of T_K is defined via $G(T = T_K) = \frac{1}{2}G_0$. If the finite value of U has a strong effect on the behavior of $G(T/T_K)$ already around $T = T_K$, the definition of T_K is influenced by this nonuniversality. This has then immediate consequences for the curve $G(V/T_K)$ in figure VI.11(b), where the voltage is given in units of T_K. The nonuniversality of the definition of T_K is also reflected in the fact that the value of T_K deviates much stronger from $T_K^{(\chi)}$ in the case of small U/Γ compared to the case of larger U/Γ, see table VI.1. To make this point more explicit, panels (c) and (d) show the same data as (a) and (b), but with temperature and voltage scaled in units of $T_K^{(\chi)}$. Especially for $U/\Gamma = 2$, the scaling with $T_K^{(\chi)}$ results in stronger deviations in the temperature-dependent curves, but better agreement in $G(V/T_K^{(\chi)})$.

Typically one is interested in the behavior of the conductance around $T \sim T_K$ and $V \sim T_K$, respectively. From the figures we deduce that for voltages up to $V = T_K$, a value of $U/\Gamma = 6$ suffices to describe the universal scaling limit. Even $U/\Gamma = 4.5$ seems to capture the scaling limit in this case. However, for smaller values of U/Γ, here illustrated by $U/\Gamma = 2$, significant deviations become visible.

This kind of analysis is very important for experiments. In typical experiments, it is much easier to change the source-drain voltage over a large parameter range than to vary the temperature. Therefore, it has been proposed to determine T_K not from $G(T)$ but from the curve $G(V)$ [28]. Our work is a huge step towards the realization of this suggestion as it can provide the theoretical connection between equilibrium properties such as $G(T)$ and the curve $G(V)$, compare also the discussion of the value of $G(V = T_K)$ in the paper [P2]. Moreover, our method is able to characterize these properties even away from the scaling limit making it possible to compare to experiments with smaller values of U/Γ.

VI.6 Comparison to the Auxiliary Master Equation Approach

The steady-state nonequilibrium of the SIAM has been studied with a variety of different numerical methods. In a joint work on the "nonequilibrium Kondo effect in a magnetic field" [P4], we compared our quench method to the *"auxiliary master equation approach"* (AMEA).

VI.6.1 Auxiliary Master Equation Approach

The auxiliary master equation approach [P4, 29, 71, 95] relies on a Lindblad equation. For a fixed number of lead levels, it uses the parameters of the Hamiltonian and the Lindblad driving terms as fit parameters to obtain a good representation of the thermal leads in terms of the retarded and the Keldysh components of the hybridization function. To this end the equations (17) and (25) of the article in chapter V are used (see also reference [71]), which for a quadratic Lindblad equation connect the Green's functions of the lead levels to the parameters of the Lindblad equations. The fitting procedure is performed with some restrictions concerning the locality of the Lindblad driving [95]. Typically, within this fitting procedure left and right leads are combined into one hybridization function. This renders it impossible to express the current in terms of expectation values. But because AMEA is able to capture the dot's spectral function, the current can instead be calculated via the Meir-Wingreen formula [P4, 18],

$$J = \int \mathrm{d}\omega\, A(\omega)\,\big(f_R(\omega) - f_L(\omega)\big)\,\Gamma(\omega)\,, \tag{6.1}$$

with $A(\omega) = \frac{1}{2}\left(A_\uparrow(\omega) + A_\downarrow(\omega)\right)$ and $\Gamma(\omega) = -\mathrm{Im}\left(\Delta^R(\omega)\right)$.

The Lindblad equation obtained from the fitting procedure is used to time-evolve an arbitrary initial state towards the system's steady state. The time evolution is performed based on MPS. To represent the density matrix in the form of an MPS, the superfermionic representation is employed, see section IV.5.2 for details.

VI.6.2 Comparison

In our joint work [P4] both methods, our quench approach and AMEA, were used to determine the current as a function of voltage in the SIAM for different magnetic fields. With $U/\Gamma = 6$, the interaction was large enough to describe the scaling limit for a large parameter regime, compare also section VI.5.3. For both methods, $\Gamma = 0.1D$ was used with $2D$ being the band width of the leads. The Kondo scale is given by $T_K \approx 0.2\Gamma \approx 0.03U$. The temperature was set to $T = 0.05\Gamma \approx 0.25T_K$. To study the split of the Kondo peak in the conductance for large enough B, the magnetic field was varied between $B = 0.2\Gamma$ up to $B = 2\Gamma$, corresponding to $B \approx T_K - 10T_K$, The two methods show nice agreement, thereby confirming the validity of both approaches.

Comparing our quench approach and AMEA applied to the SIAM one finds the following strengths and weaknesses:

- AMEA is able to capture the dot's spectral function in the nonequilibrium SIAM. For slightly different than the above parameters it has even been achieved to resolve the four-peak structure of the spectral function expected in the case of finite voltage and finite magnetic field, see figure 2 of reference [P4] for details. In particular, when considering the method as an impurity solver for the dynamical mean field theory

in nonequilibrium [71, 96], this possibility to calculate spectral functions is essential. Methodologically, it would also be possible to calculate spectral functions in the quench setup. But the numerical cost would be higher compared to the determination of expectation values, so at the moment it is unclear whether it would be numerically feasible in practice.

- Our quench approach has the advantage of an explicit renormalization of the impurity. Therefore, it is more flexible regarding the treatment of small energy scales. In principle, one would like to enforce $D \gg U \gg \Gamma \gg T_K$, which is only possible if one is able to describe a large energy regime. This gets particularly interesting, when describing large voltages and large magnetic fields. For example, for the parameter set in our joint work [P4], the largest voltage is equal to $V = 0.5\,D$ and the largest magnetic field corresponds to $B = 2\Gamma = \frac{1}{3}U$ such that the results could be influenced by the finite band with and the finite value of U. In comparison, in the paper [P2] presented in chapter VII we could easily use $\Gamma = 10^{-3}\,D$ and $U/\Gamma = 12$, resulting in a value of the Kondo scale as small as $T_K \approx 0.026\Gamma \approx 2.61 \cdot 10^{-5}\,D$, compare also table VI.1. So far, there are also no AMEA results on temperature $T = 0$, although with temperatures clearly below the Kondo temperature it reaches deep into the Kondo regime.

VII A Quench Approach – Publication

The following article I published together with Ireneusz Weymann, Jan von Delft, and Andreas Weichselbaum. Ireneusz Weymann guided me in the very beginning of the project, while Jan von Delft and Andreas Weichselbaum were important advisors to me throughout. In particular, Andreas Weichselbaum made his QSpace library available to me, a powerful library for MPS calculations and, in particular, the numerical renormalization group, which can exploit Abelian as well as non-Abelian symmetries [45, 55, 92].

Nonequilibrium Steady-State Transport in Quantum Impurity Models: A Thermofield and Quantum Quench Approach Using Matrix Product States

F. Schwarz,[1] I. Weymann,[2] J. von Delft,[1] and A. Weichselbaum[1,3,*]

[1]*Physics Department, Arnold Sommerfeld Center for Theoretical Physics, and Center for NanoScience, Ludwig-Maximilians-Universität, Theresienstraße 37, 80333 München, Germany*

[2]*Faculty of Physics, Adam Mickiewicz University, Umultowska 85, 61-614 Poznań, Poland*

[3]*Department of Condensed Matter Physics and Materials Science, Brookhaven National Laboratory, Upton, New York 11973-5000, USA*

(Received 28 August 2017; revised manuscript received 21 December 2017; published 26 September 2018)

The numerical renormalization group (NRG) is tailored to describe interacting impurity models in equilibrium, but it faces limitations for steady-state nonequilibrium, arising, e.g., due to an applied bias voltage. We show that these limitations can be overcome by describing the thermal leads using a thermofield approach, integrating out high energy modes using NRG, and then treating the nonequilibrium dynamics at low energies using a quench protocol, implemented using the time-dependent density matrix renormalization group. This yields quantitatively reliable results for the current (with errors $\lesssim 3\%$) down to the exponentially small energy scales characteristic of impurity models. We present results of benchmark quality for the temperature and magnetic field dependence of the zero-bias conductance peak for the single-impurity Anderson model.

DOI: 10.1103/PhysRevLett.121.137702

Introduction.—A major open problem in the theoretical study of nanostructures, such as quantum dots or nanowires, is the reliable computation of the nonlinear conductance under the conditions of nonequilibrium steady-state (NESS) transport. These are open quantum systems featuring strong local interactions, typically described by quantum impurity models such as the interacting resonant level model (IRLM), the Kondo model (KM), or the single-impurity Anderson model (SIAM). Much work has been devoted to studying the NESS properties of such models using a variety of methods [1–15], leading to a fairly good qualitative understanding of their behavior. The interplay of strong correlations, NESS driving, and dissipative effects leads to a rich and complex phenomenology. In particular, for the KM and SIAM, the nonlinear conductance exhibits a striking zero-bias peak, the so-called Kondo peak, characterized by a small energy scale, the Kondo temperature T_K, that weakens with increasing temperature and splits with increasing magnetic field, in qualitative agreement with experiments [16–22]. However, a full, quantitative description of the NESS behavior of such models under generic conditions has so far been unfeasible: none of the currently available approaches meet the threefold challenge of (i) treating interactions essentially exactly, (ii) resolving very small energy scales, and (iii) incorporating NESS conditions.

This Letter presents an approach that does meet this challenge. (i) To deal with interactions, we use numerical matrix product state (MPS) methods. (ii) We use the numerical renormalization group (NRG) [23,24] to integrate out high-energy modes, leading to a renormalized impurity problem [25] whose reduced effective bandwidth, D^*, is set by a transport window defined by the voltage bias (V) and the temperature (T). This considerably enlarges the window of accessible time scales, which scale as $1/D^*$, and thus it enables us to treat arbitrary voltages. (iii) We then study the transport properties of the renormalized problem using a quench protocol where we abruptly switch on the impurity-lead coupling and compute the subsequent time evolution of the current, $J(t)$, using the time-dependent density-matrix renormalization group (TDMRG) [26–29]. Whereas similar

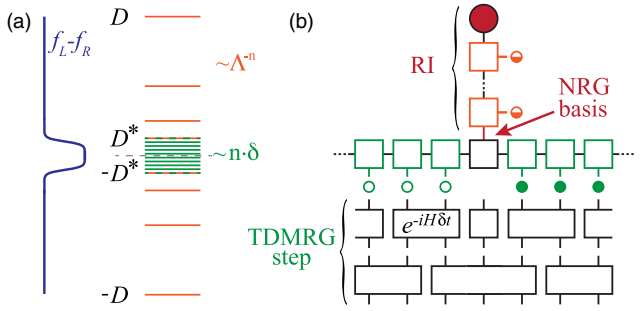

FIG. 1. (a) The discretization combines a log-sector for high energy excitations with a lin-sector for the TW. (b) The log-sector is treated using NRG. Here, "holes" and "particles" are recombined. The effective low-energy basis of NRG is used as the local state space of one MPS chain element. For the lin-sector, holes (empty at $t = 0$) and particles (filled at $t = 0$) are treated separately. On the chain including the RI, we do a TDMRG calculation based on a Trotter decomposition in "odd" and "even" bonds [37].

protocols [5,15,30,31] typically work at $T = 0$, we consider nonequilibrium thermal leads for arbitrary T, using the thermofield approach [32–36] to describe them with a pure product state in an enlarged Hilbert space.

We benchmark our approach using the IRLM, finding excellent agreement with exact Bethe-ansatz predictions for the NESS current. We then turn to the SIAM. For the linear conductance, we reproduce equilibrium NRG results. For the nonlinear conductance, we study the evolution of the zero-bias peak with T and magnetic field.

Setup.—We consider impurities coupled to two thermal leads, labeled $\alpha \in \{L, R\}$ and characterized by Fermi functions $f_\alpha(\omega) = (e^{(\omega-\mu_\alpha)/T}+1)^{-1}$, where $\mu_{L/R} = \pm V/2$. (We set $e = \hbar = k_B = 1$.) We study two different models, the spinless IRLM with a three-site impurity and Coulomb repulsion U between neighboring sites, and the SIAM with Coulomb repulsion U between different spins and a Zeeman splitting due to a magnetic field B. The impurities of these models are described by

$$H^{(\mathrm{I})}_{\mathrm{imp}} = \varepsilon_d \hat{n}_C + U(\hat{n}_L + \hat{n}_R - 1)\hat{n}_C + (t' d_C^\dagger d_L + t' d_C^\dagger d_R + \mathrm{H.c.}) \tag{1}$$

$$H^{(\mathrm{S})}_{\mathrm{imp}} = \varepsilon_d(\hat{n}_{d\uparrow} + \hat{n}_{d\downarrow}) + U\hat{n}_{d\uparrow}\hat{n}_{d\downarrow} - \frac{B}{2}(\hat{n}_{d\uparrow} - \hat{n}_{d\downarrow}), \tag{2}$$

where $\hat{n}_i = d_i^\dagger d_i$, for $i \in \{L, R, C, d\uparrow, d\downarrow\}$. In this Letter, we focus on the particle-hole symmetric case ($\varepsilon_d = 0$ for the IRLM and $\varepsilon_d = -(U/2)$ for the SIAM). The leads are assumed to be noninteracting,

$$H^{(\mathrm{I/S})}_{\mathrm{lead}} = \sum_{\alpha(\sigma)k} \varepsilon_k c^\dagger_{\alpha(\sigma)k} c_{\alpha(\sigma)k} \equiv \sum_q \varepsilon_q c_q^\dagger c_q, \tag{3}$$

with spin index $\sigma \in \{\uparrow, \downarrow\}$ for the SIAM, $q \equiv \{\alpha, (\sigma), k\}$ a composite index, and k a label for the energy levels. The impurity-leads hybridization is given by

$$H^{(\mathrm{I/S})}_{\mathrm{hyb}} = \sum_q (v_q d^\dagger_{\alpha/\sigma} c_q + \mathrm{H.c.}), \tag{4}$$

where in the IRLM the left (right) impurity site d_L (d_R) couples to the modes c_{Lk} (c_{Rk}), respectively, while in the SIAM the two spin states d_σ couple to the lead modes $c_{\alpha\sigma k}$ spin-independently, $v_q = v_{\alpha k}$. The couplings v_q induce an impurity-lead hybridization $\Gamma_\alpha(\omega) = \pi \sum_k |v_q|^2 \delta(\omega - \varepsilon_q)$, chosen such that they represent a box distribution $\Gamma_\alpha(\omega) = \Gamma_\alpha \Theta(D - |\omega|)$ in the continuum limit with half-bandwidth $D := 1$ set as the unit of energy, unless specified otherwise. For the IRLM, we set $\Gamma_L = \Gamma_R = 0.5D$ corresponding to the hopping element of a tight-binding chain with half-bandwidth D, and for the SIAM, we likewise choose $\Gamma_L = \Gamma_R$ and define the total hybridization $\Gamma = \Gamma_L + \Gamma_R$.

Strategy.—We describe the thermal leads decoupled from the impurity using the thermofield approach [32–35]. The impurity-lead coupling induces nonequilibrium processes, which occur on energy scales corresponding to the *transport window* (TW), defined as the energy range in which $f_L(\omega) \not\approx f_R(\omega)$. Energy scales far outside of this TW are effectively in equilibrium, and we therefore integrate them out using NRG, whereas we describe the nonequilibrium physics within the TW using TDMRG quench. We implement both the NRG and TDMRG using MPS techniques. We use a logarithmically discretized sector (log-sector), representing the energy range of the leads outside of the TW, and a linearly discretized sector (lin-sector) within the TW, as depicted in Fig. 1(a). The transition from the logarithmic to the linear discretization can be smoothed [37]. To simplify the MPS calculation, we map the leads onto a chain, with on-site and nearest-neighbor terms only, by tridiagonalizing the Hamiltonian. Integrating out the log-sector using NRG we get a *renormalized impurity* (RI) [25] and a reduced effective bandwidth, $2D^*$, of order of the size of the TW. This enables us to treat transport on energy scales much smaller than D. In particular, we can study arbitrary ratios of V/T_K in the SIAM, even if $T_K \ll D$. We then turn on the coupling between the log-sector and lin-sector by performing a TDMRG quench, starting from an initial state $|\Psi_{\mathrm{ini}}\rangle = |\phi_{\mathrm{ini}}\rangle \otimes |\Omega_{\mathrm{lin}}\rangle$, where $|\phi_{\mathrm{ini}}\rangle$ describes the initial state of the RI, and $|\Omega_{\mathrm{lin}}\rangle$ is a *pure product state* describing the lin-sector of the thermal leads in the thermofield approach. To describe steady-state properties, we time-evolve $|\Psi_{\mathrm{ini}}\rangle$ until expectation values are stationary up to oscillations around their mean value. Since the effective bandwidth relevant for this TDMRG calculation is given by D^*, not D, exponentially large time scales of order $1/D^* \gg 1/D$ are accessible.

Thermofield description of decoupled leads.—In the context of MPS methods, the thermofield description [32–35] of the decoupled leads has two advantages: finite temperature states are represented as pure states, and thermal leads are described by a simple product state.

Akin to purification [29], we double our Hilbert space by introducing one auxiliary mode c_{q2} (not coupled to the system) for each lead mode $c_{q1} = c_q$. In this enlarged Hilbert space, we define a pure state $|\Omega\rangle$ such that the thermal expectation value of an operator A acting on the original physical lead is given by $\langle A\rangle = \langle\Omega|A|\Omega\rangle$. This state can be written as [37]

$$|\Omega\rangle = \prod_q \underbrace{\left(\sqrt{1-f_q}|0,1\rangle_q + \sqrt{f_q}|1,0\rangle_q\right)}_{\equiv |\tilde{0},\tilde{1}\rangle_q}, \tag{5}$$

with $f_q = f_\alpha(\varepsilon_q)$, where $|0,1\rangle_q$ and $|1,0\rangle_q$ are defined by $c_{q1}|0,1\rangle_q = c^\dagger_{q2}|0,1\rangle_q = c^\dagger_{q1}|1,0\rangle_q = c_{q2}|1,0\rangle_q = 0$ for all q. We map $|\Omega\rangle$ to a pure product state using the rotation

$$\begin{pmatrix} \tilde{c}_{q1} \\ \tilde{c}_{q2} \end{pmatrix} = \begin{pmatrix} \sqrt{1-f_q} & -\sqrt{f_q} \\ \sqrt{f_q} & \sqrt{1-f_q} \end{pmatrix} \begin{pmatrix} c_{q1} \\ c_{q2} \end{pmatrix}. \quad (6)$$

Having $\tilde{c}_{q1}|\Omega\rangle = \tilde{c}^{\dagger}_{q2}|\Omega\rangle = 0$, the modes $\tilde{c}_{q1}$ ($\tilde{c}_{q2}$) can be interpreted as holes (particles) which are empty (filled) in the thermal state, respectively. Since in Eq. (5) we constructed $|\Omega\rangle$ to be an eigenstate of the particle number operator, it remains so in the rotated basis. The physical and auxiliary modes are decoupled in the unrotated basis; hence we are free to choose an arbitrary Hamiltonian (and hence time evolution) for the auxiliary modes [47]. We choose their single-particle energies equal to those of the physical modes, $\varepsilon_{q2} = \varepsilon_q$, in order to ensure that the resulting total lead Hamiltonian is diagonal in j in both the original *and* the rotated basis:

$$\mathcal{H}_{\text{lead}} \equiv H_{\text{lead}} + H_{\text{aux}} = \sum_{qj} \varepsilon_q c^{\dagger}_{qj} c_{qj} = \sum_{qj} \varepsilon_q \tilde{c}^{\dagger}_{qj} \tilde{c}_{qj}. \quad (7)$$

Equation (4) is rotated into $H^{(\text{I/S})}_{\text{hyb}} = \sum_{qj} (\tilde{v}_{qj} d^{\dagger}_{\alpha/\sigma} \tilde{c}_{qj} + \text{H.c.})$, whose couplings, $\tilde{v}_{q1} = v_q \sqrt{1-f_q}$ and $\tilde{v}_{q2} = v_q \sqrt{f_q}$, now *explicitly depend* on the Fermi function and encode all relevant information about temperature and voltage.

For the SIAM, we use a specific linear combination of $\tilde{c}_{Lk\sigma i}$ and $\tilde{c}_{Rk\sigma i}$ modes, $\tilde{C}_{k\sigma i} \propto \sum_{\alpha} \tilde{v}_{\alpha k\sigma i} \tilde{c}_{\alpha k\sigma i}$, because the modes orthogonal to these [37] decouple. Mixing left and right lead modes is possible despite the nonequilibrium situation, because the difference in chemical potentials is accounted for by the V-dependent couplings $\tilde{v}_q$. In the IRLM, this reduction of modes is not possible because left and right lead couple to different impurity sites.

NRG renormalization of the impurity.—As is standard for NRG, we map the leads (in the thermofield representation) from the original "star geometry" to a chain geometry. To ensure that $|\Omega\rangle$ remains a product state, we perform the corresponding unitary transformation for holes and particles independently. This results in a chain consisting of two channels $i \in \{1, 2\}$ for the SIAM, and four for the IRLM due to the additional lead index $\alpha \in \{L, R\}$. The first part of the chain corresponds to the log-sector, the later part to the lin-sector. The hoppings within the log-sector decay as Λ^{-n}, because for each lead level q within the log-sector of the original star geometry, either $\tilde{c}_{q1}$ or $\tilde{c}_{q2}$ decouples from the RI due to $f_q \in \{0, 1\}$. For NRG calculations, it is unfavorable to describe holes and particles in separate chains, because then particle-hole excitations involve opposite levels of different chains. For that reason, we recombine the holes and particles of the log-sector into one chain using a further tridiagonalization. In the IRLM, this is done for each lead α independently. After that, the log-sector resembles a standard Wilson chain with hoppings that scale as $\Lambda^{-n/2}$, reflecting the fact that the log-sector is effectively in equilibrium. A sketch of the different geometries can be found in Fig. S2 of Ref. [37].

Using NRG, we find an effective low-energy many-body basis for the log-sector, which we interpret as the local state space of a RI, and we treat it as one chain element of our MPS chain. Coupled to this RI, we have the lin-sector of the leads, represented as two separate chains for holes and particles, as shown in the upper part of Fig. 1(b).

TDMRG quench.—We choose the initial state for the quench as the product state $|\Psi_{\text{ini}}\rangle = |\phi_{\text{ini}}\rangle \otimes |\Omega_{\text{lin}}\rangle$. This implies that for the lin-sector, we start with the state in which all holes (particles) are empty (filled). As the initial state of the RI, $|\phi_{\text{ini}}\rangle$, we choose a ground state of the NRG basis (in principle, one can choose any of the low-energy basis states whose excitation energy is well within the TW). We then switch on the coupling between the RI and the leads, smoothly over a short time window. The system time-evolves under the Hamiltonian $\hat{H} = H_{\text{imp}} + H_{\text{hyb}} + H_{\text{lead}} + H_{\text{aux}}$, $|\Psi(t)\rangle = e^{-i\hat{H}t}|\Psi_{\text{ini}}\rangle$. We perform the time evolution using TDMRG based on a second order Trotter decomposition, as depicted in Fig. 1(b), with a Trotter time step of order $1/D^*$. (Technical details can be found in Sec. S-3.C of Ref. [37].) The fact that this initial lead state is entanglement-free is advantageous for reaching comparatively long times. We extract NESS information from $\langle A(t)\rangle = \langle\Psi(t)|A|\Psi(t)\rangle$ within a window of intermediate times, large enough for post-quench transients to no longer dominate, but well below the recurrence time, where finite-size effects set in. We compute the current through the impurity site (SIAM) or the central impurity site (IRLM), respectively, using $J = \frac{1}{2}(J_L - J_R)$, where J_L (J_R) is the current that flows into the site from the left (right), respectively [37]. We are able to track the time evolution up to times of order $1/D^*$. Since $D^* \sim \max(V, T)$, this suffices to describe particle transport for any choice of V or T. However, processes on much smaller energy scales cannot necessarily be resolved (see Sec. S-4.C of [37] for details).

Interacting resonant level model.—We benchmark our method for the IRLM, for which Ref. [15] computed the steady-state current at $T = 0$ both numerically, using DMRG quenches, and analytically, using the exact Bethe ansatz. A universal scaling of the current-voltage characteristics was found at the self-dual point of the model, with the corresponding energy scale T_B scaling as $(t')^{3/4}$. (These results were very recently confirmed by Ref. [48].) Figure 2 presents a comparison of our data with the analytical expression for the universal scaling curve given in [15], for the current as function of voltage at $T = 0$ at the self-dual point $U \approx D$ and $\varepsilon_d = 0$. The agreement is excellent for a large range of t' values. For each value of t', T_B was used as a fit parameter; the resulting T_B values, shown in the inset, agree nicely with the scaling predicted in [15]. Using the fitted values of T_B, all data points deviate by less than 2% from the Bethe results. Our use of NRG to renormalize

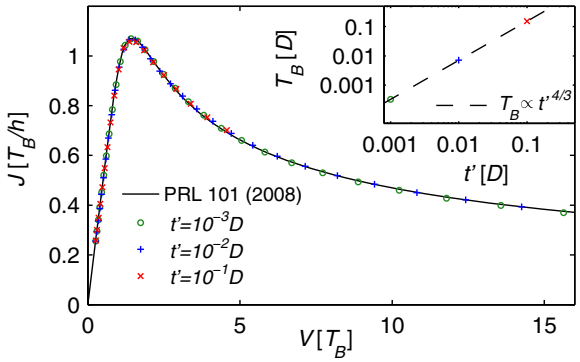

FIG. 2. Universal scaling of current vs voltage for the IRLM at the self-dual point for $T = 0$, in units of the energy scale $T_B(t')$, with negative differential conductance at large voltages, in excellent agreement with analytical results (solid curve, [15]). The inset shows the scaling of T_B with $(t')^{3/4}$.

the impurity enables us to study values of t' up to a hundred times smaller than the values used in [15], giving us access to much smaller values of T_B and larger V/T_B ratios.

Single-impurity Anderson model.—For the SIAM, a natural first check is the noninteracting case, $U = 0$, which is exactly solvable, but its treatment in MPS numerics does not differ from the case $U \neq 0$. The inset of Fig. 3(a) displays the current over voltage for two different temperatures, showing good agreement between our MPS numerics and exact predictions, thus providing direct evidence for the validity of our approach. For $U \neq 0$, our method yields quantitative agreement with previous numerical results obtained in the regime $V \gtrsim \Gamma$ [6,7], see Sec. S-6 of Ref. [37] for details. Furthermore, we find good agreement with the auxiliary master equation approach for arbitrary voltages, see Ref. [49] for details.

The main panel of Fig. 3(a) focuses on the differential conductance $g(T,V) = (\partial J(T,V)/\partial V)/(2e^2/h)$ for strong interactions. As a consistency check, we compare our results for $g(T,0)$ with the linear conductance computed using FDM-NRG [51]. We find excellent agreement over a large range of temperatures. From this data, we define the Kondo temperature T_K via the condition $g(T_K,0) \equiv \frac{1}{2}$.

We also show $g(0,V)$ over a wide voltage range in Fig. 3(a). In agreement with experiment [22] and other theoretical work [8], this curve lies above $g(T,0)$. The difference can be quantified by the value of $g(0,T_K)$, a universal number characterizing NESS transport for the SIAM, whose precise value is not yet known with quantitative certainty. Our method, which we trust to be quantitatively reliable, yields $g(0,T_K) \approx 0.60 \pm 0.02$ in the Kondo limit of $U/\Gamma \gg 1$, where the estimated error bar of about 3% is likely conservative (cf. [37]). For comparison, (nonexact) analytical calculations for the Kondo model yielded $g(0,T_K) \approx 2/3$ [8,9].

Figures 3(b)–3(d) show our quantitative description of the T- and B-dependence of the zero-bias peak in the Kondo limit ($U/\Gamma = 12$). With increasing T at $B = 0$, the zero-bias peak decreases [Fig. 3(b)], as observed in numerous experiments [17–22]. For finite B, the zero-bias peak splits into two sub-peaks at $V \approx \pm B$ [Fig. 3(c)]. A more detailed analysis of the value of B, at which the peak begins to split [52,53], is given in Sec. S-7 of Ref. [37]. In Fig. 3(d), the peak position with respect to B is resolved in more detail, with the voltage given in units of B. While for $B \approx 2T_K$ the peak position is roughly at $V/B \approx 0.83$, it quickly tends towards $V/B = 1$ for larger magnetic fields. Our study thus quantitatively confirms that the large-field peak-to-peak splitting for the nonlinear conductance is $\approx 2B$, as observed in several experiments [16,17,20]. This is also found in independent calculations [49] using the approach of Ref. [13].

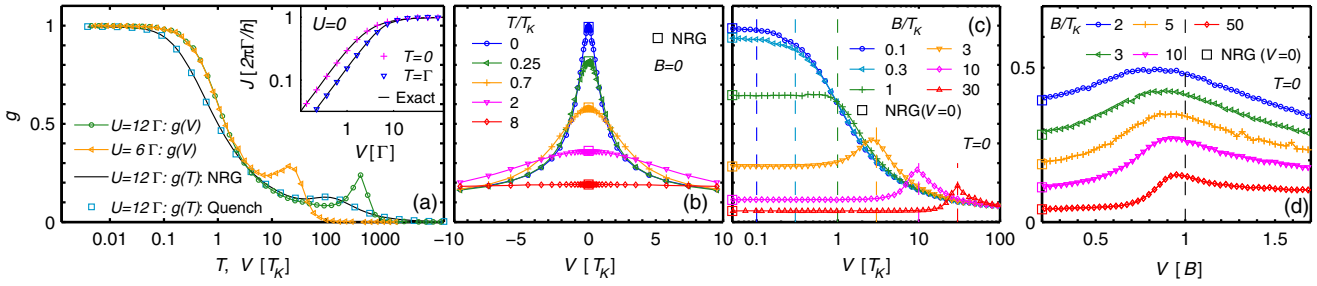

FIG. 3. Numerical results for the SIAM with $\Gamma = 10^{-3}$. For $U = 12\Gamma$, used in (b)–(d), we find $T_K = 2.61 \times 10^{-5}$. [This implies $T_K = 1.04 T_K^{(\chi)}$, where $T_K^{(\chi)} = (1/4\chi_s) = (U\Gamma/2)^{\frac{1}{2}} e^{\pi[(\Gamma/2U)-(U/8\Gamma)]}$ is an alternative definition of the Kondo temperature based on the Bethe-ansatz result [50] for the static spin susceptibility χ_s, at $B = T = 0$]. (a) Conductance vs V and T: squares show quench results in linear response as function of T, $g(T,0)$, in good agreement with the NRG results (solid line). Dots and triangles show quench results for the nonlinear conductance vs V at $T = 0$ for two different values of U. Inset: current vs V for $U = 0$ on a log-log scale, for two different temperatures, showing excellent agreement with analytical results. (b) Disappearance of the Kondo resonance in $g(T,V)$ with increasing T at $B = 0$, with $g(T,-V) = g(T,V)$, by symmetry. (c) Splitting of the resonance in $g(0,V)$ for finite B. Two subpeaks emerge at $V \approx \pm B$, as marked by the dashed lines. (d) Similar data as in (c) but plotted vs V/B and on a linear scale. For $B = 2T_K$, the peak position in the conductance $g(0,V)$ is still slightly below B, but for a higher magnetic field, the peak clearly moves towards $V/B \approx 1$. In (b)–(d), the squares indicate the NRG result for $V = 0$.

Summary and outlook.—We have combined the thermofield approach with a hybrid NRG-TDMRG quench strategy to reach a longstanding goal: a versatile, flexible, and *quantitatively reliable* method for studying quantum impurity models in steady-state nonequilibrium. Because of these features, our scheme has the potential of developing into the method of choice for such settings, in the same way as NRG is the method of choice for equilibrium impurity models. Indeed, various quantitative benchmark tests have confirmed the accuracy of our scheme, and it can easily be applied to other models and setups. For example, a generalization to a finite temperature difference between the left and right lead would be straightforward. It would also be interesting to use our setup for quantitative studies of the nonequilibrium two-channel Kondo physics measured in [54], or to study impurity models with superconducting leads, since the hybrid NRG-TDMRG approach is ideally suited for dealing with the bulk gap.

Methodologically, our setup can straightforwardly be extended to study NESS physics, without resorting to a quench strategy, by including Lindblad driving terms in the Liouville equation, which are *local* on the MPS chain [55]. Although the direct time-evolution of such Lindblad equations based on tensor networks seems feasible [56], one could try to avoid the real-time evolution altogether, and target the steady-state directly, by looking for the density matrix that fulfills $\dot{\rho} = 0$ [57,58].

We thank F. Heidrich-Meisner and P. Werner for providing the reference data in Fig. S6. We acknowledge useful discussions with E. Arrigoni, M.-C. Bañuls, B. Bruognolo, A. Dorda, D. Fugger, M. Goldstein, and H. Schöller. This work was supported by the German-Israeli-Foundation through I-1259-303.10 and by the DFG through the excellence cluster NIM. A. W. was also supported by DFG WE4819/1-1 and WE4819/2-1. I. W. was supported by National Science Centre in Poland through the Project No. DEC-2013/10/E/ST3/00213.

*andreas.weichselbaum@lmu.de

[1] A. Rosch, J. Paaske, J. Kroha, and P. Wölfle, Nonequilibrium Transport Through a Kondo Dot in a Magnetic Field: Perturbation Theory and Poor Man's Scaling, Phys. Rev. Lett. **90**, 076804 (2003).

[2] S. Kehrein, Scaling and Decoherence in the Nonequilibrium Kondo Model, Phys. Rev. Lett. **95**, 056602 (2005).

[3] F. B. Anders, Steady-State Currents Through Nanodevices: A Scattering-States Numerical Renormalization-Group Approach to Open Quantum Systems, Phys. Rev. Lett. **101**, 066804 (2008).

[4] S. Kirino, T. Fujii, J. Zhao, and K. Ueda, Time-dependent DMRG study on quantum dot under a finite bias voltage, J. Phys. Soc. Jpn. **77**, 084704 (2008).

[5] F. Heidrich-Meisner, A. E. Feiguin, and E. Dagotto, Real-time simulations of nonequilibrium transport in the single-impurity Anderson model, Phys. Rev. B **79**, 235336 (2009).

[6] J. Eckel, F. Heidrich-Meisner, S. G. Jakobs, M. Thorwart, M. Pletyukhov, and R. Egger, Comparative study of theoretical methods for non-equilibrium quantum transport, New J. Phys. **12**, 043042 (2010).

[7] P. Werner, T. Oka, M. Eckstein, and A. J. Millis, Weak-coupling quantum Monte Carlo calculations on the Keldysh contour: Theory and application to the current-voltage characteristics of the Anderson model, Phys. Rev. B **81**, 035108 (2010).

[8] M. Pletyukhov and H. Schoeller, Nonequilibrium Kondo Model: Crossover from Weak to Strong Coupling, Phys. Rev. Lett. **108**, 260601 (2012).

[9] S. Smirnov and M. Grifoni, Keldysh effective action theory for universal physics in spin-$\frac{1}{2}$ Kondo dots, Phys. Rev. B **87**, 121302 (2013).

[10] G. Cohen, E. Gull, D. R. Reichman, and A. J. Millis, Green's Functions from Real-Time Bold-Line Monte Carlo Calculations: Spectral Properties of the Nonequilibrium Anderson Impurity Model, Phys. Rev. Lett. **112**, 146802 (2014).

[11] A. E. Antipov, Q. Dong, and E. Gull, Voltage Quench Dynamics of a Kondo System, Phys. Rev. Lett. **116**, 036801 (2016).

[12] F. Reininghaus, M. Pletyukhov, and H. Schoeller, Kondo model in nonequilibrium: Interplay between voltage, temperature, and crossover from weak to strong coupling, Phys. Rev. B **90**, 085121 (2014).

[13] A. Dorda, M. Ganahl, H. G. Evertz, W. von der Linden, and E. Arrigoni, Auxiliary master equation approach within matrix product states: Spectral properties of the nonequilibrium Anderson impurity model, Phys. Rev. B **92**, 125145 (2015).

[14] S. G. Jakobs, V. Meden, and H. Schoeller, Nonequilibrium Functional Renormalization Group for Interacting Quantum Systems, Phys. Rev. Lett. **99**, 150603 (2007).

[15] E. Boulat, H. Saleur, and P. Schmitteckert, Twofold Advance in the Theoretical Understanding of far-from-Equilibrium Properties of Interacting Nanostructures, Phys. Rev. Lett. **101**, 140601 (2008).

[16] D. C. Ralph and R. A. Buhrman, Kondo-Assisted and Resonant Tunneling via a Single Charge Trap: A Realization of the Anderson Model Out of Equilibrium, Phys. Rev. Lett. **72**, 3401 (1994).

[17] D. Goldhaber-Gordon, H. Shtrikman, D. Mahalu, D. Abusch-Magder, U. Meirav, and M. A. Kastner, Kondo effect in a single-electron transistor, Nature (London) **391**, 156 (1998).

[18] S. M. Cronenwett, T. H. Oosterkamp, and L. P. Kouwenhoven, A tunable Kondo effect in quantum dots, Science **281**, 540 (1998).

[19] F. Simmel, R. H. Blick, J. P. Kotthaus, W. Wegscheider, and M. Bichler, Anomalous Kondo Effect in a Quantum Dot at Nonzero Bias, Phys. Rev. Lett. **83**, 804 (1999).

[20] W. G. van der Wiel, S. D. Franceschi, T. Fujisawa, J. M. Elzerman, S. Tarucha, and L. P. Kouwenhoven, The Kondo effect in the unitary limit, Science **289**, 2105 (2000).

[21] A. V. Kretinin, H. Shtrikman, D. Goldhaber-Gordon, M. Hanl, A. Weichselbaum, J. von Delft, T. Costi, and D. Mahalu, Spin-$\frac{1}{2}$ Kondo effect in an InAs nanowire quantum dot: Unitary limit, conductance scaling, and Zeeman splitting, Phys. Rev. B **84**, 245316 (2011).

[22] A. V. Kretinin, H. Shtrikman, and D. Mahalu, Universal line shape of the Kondo zero-bias anomaly in a quantum dot, Phys. Rev. B **85**, 201301 (2012).

[23] K. G. Wilson, The renormalization group: Critical phenomena and the Kondo problem, Rev. Mod. Phys. **47**, 773 (1975).

[24] R. Bulla, T. A. Costi, and T. Pruschke, Numerical renormalization group method for quantum impurity systems, Rev. Mod. Phys. **80**, 395 (2008).

[25] F. Güttge, F. B. Anders, U. Schollwöck, E. Eidelstein, and A. Schiller, Hybrid NRG-DMRG approach to real-time dynamics of quantum impurity systems, Phys. Rev. B **87**, 115115 (2013).

[26] G. Vidal, Efficient Simulation of One-Dimensional Quantum Many-Body Systems, Phys. Rev. Lett. **93**, 040502 (2004).

[27] A. J. Daley, C. Kollath, U. Schollwöck, and G. Vidal, Time-dependent density-matrix renormalization-group using adaptive effective Hilbert spaces, J. Stat. Mech. (2004) P04005.

[28] S. R. White and A. E. Feiguin, Real-Time Evolution Using the Density Matrix Renormalization Group, Phys. Rev. Lett. **93**, 076401 (2004).

[29] U. Schollwöck, The density-matrix renormalization group in the age of matrix product states, Ann. Phys. (Amsterdam) **326**, 96 (2011).

[30] A. Branschädel, G. Schneider, and P. Schmitteckert, Conductance of inhomogeneous systems: Real-time dynamics, Ann. Phys. (Amsterdam) **522**, 657 (2010).

[31] L. G. G. V. D. da Silva, F. Heidrich-Meisner, A. E. Feiguin, C. A. Büsser, G. B. Martins, E. V. Anda, and E. Dagotto, Transport properties and Kondo correlations in nanostructures: Time-dependent DMRG method applied to quantum dots coupled to Wilson chains, Phys. Rev. B **78**, 195317 (2008).

[32] Y. Takahashi and H. Umezawa, Thermo field dynamics, Collective Phenomena **2**, 55 (1975).

[33] S. M. Barnett and B. J. Dalton, Liouville space description of thermofields and their generalisations, J. Phys. A **20**, 411 (1987).

[34] A. Das, Topics in finite temperature field theory," in *Quantum Field Theory—A 20th Century Profile*, edited by A. N. Mitra (Hindustan Book Agency, New Delhi, 2000) pp. 383–411.

[35] I. de Vega and M.-C. Bañuls, Thermofield-based chain-mapping approach for open quantum systems, Phys. Rev. A **92**, 052116 (2015).

[36] C. Guo, I. de Vega, U. Schollwöck, and D. Poletti, Stable-unstable transition for a Bose-Hubbard chain coupled to an environment, Phys. Rev. A **97**, 053610 (2018),

[37] See Supplemental Material at http://link.aps.org/supplemental/10.1103/PhysRevLett.121.137702, which includes Refs. [38–46], for details.

[38] V. L. Campo and L. N. Oliveira, Alternative discretization in the numerical renormalization-group method, Phys. Rev. B **72**, 104432 (2005).

[39] R. Žitko, Adaptive logarithmic discretization for numerical renormalization group methods, Comput. Phys. Commun. **180**, 1271 (2009).

[40] A. Weichselbaum, Discarded weight and entanglement spectra in the numerical renormalization group, Phys. Rev. B **84**, 125130 (2011); Tensor networks and the numerical renormalization group, Phys. Rev. B **86**, 245124 (2012); Non-Abelian symmetries in tensor networks: A quantum symmetry space approach, Ann. Phys. (Amsterdam) **327**, 2972 (2012).

[41] P. Corboz, R. Orús, B. Bauer, and G. Vidal, Simulation of strongly correlated fermions in two spatial dimensions with fermionic projected entangled-pair states, Phys. Rev. B **81**, 165104 (2010).

[42] G. Schneider and P. Schmitteckert, Conductance in strongly correlated 1D systems: Real-time dynamics in DMRG, arXiv: cond-mat/0601389.

[43] P. Wang and S. Kehrein, Flow equation calculation of transient and steady-state currents in the Anderson impurity model, Phys. Rev. B **82**, 125124 (2010).

[44] T. Barthel, U. Schollwöck, and S. R. White, Spectral functions in one-dimensional quantum systems at finite temperature using the density matrix renormalization group, Phys. Rev. B **79**, 245101 (2009).

[45] P. Schmitteckert, Calculating Green functions from finite systems, J. Phys. Conf. Ser. **220**, 012022 (2010).

[46] M. Hanl and A. Weichselbaum, Local susceptibility and Kondo scaling in the presence of finite bandwidth, Phys. Rev. B **89**, 075130 (2014).

[47] C. Karrasch, J. H. Bardarson, and J. E. Moore, Finite-temperature dynamical density matrix renormalization group and the Drude weight of spin-1/2 chains, Phys. Rev. Lett. **108**, 227206 (2012).

[48] K. Bidzhiev and G. Misguich, Out-of-equilibrium dynamics in a quantum impurity model: Numerics for particle transport and entanglement entropy, Phys. Rev. B **96**, 195117 (2017).

[49] D. M. Fugger, A. Dorda, F. Schwarz, J. von Delft, and E. Arrigoni, Nonequilibrium Kondo effect in a magnetic field: auxiliary master equation approach, New J. Phys. **20**, 013030 (2018).

[50] P. B. Wiegmann and A. M. Tsvelick, Exact solution of the Anderson model: I, J. Phys. C **16**, 2281 (1983); A. M. Tsvelick and P. B. Wiegmann, Exact solution of the Anderson model. II. Thermodynamic properties at finite temperatures, J. Phys. C **16**, 2321 (1983).

[51] A. Weichselbaum and J. von Delft, Sum-Rule Conserving Spectral Functions from the Numerical Renormalization Group, Phys. Rev. Lett. **99**, 076402 (2007).

[52] M. Filippone, C. P. Moca, A. Weichselbaum, J. von Delft, and C. Mora, At which magnetic field, exactly, does the Kondo resonance begin to split? a Fermi liquid description of the low-energy properties of the Anderson model, Phys. Rev. B **98**, 075404 (2018).

[53] A. Oguri and A. C. Hewson, Higher-Order Fermi-Liquid Corrections for an Anderson Impurity Away from Half Filling, Phys. Rev. Lett. **120**, 126802 (2018); Higher-order Fermi-liquid corrections for an Anderson impurity away from half filling: Equilibrium properties, Phys. Rev. B **97**, 045406 (2018); Higher-order Fermi-liquid corrections for an Anderson impurity away from half filling: Nonequilibrium transport, Phys. Rev. B **97**, 035435 (2018).

[54] Z. Iftikhar, S. Jezouin, A. Anthore, U. Gennser, F. D. Parmentier, A. Cavanna, and F. Pierre, Two-channel Kondo

effect and renormalization flow with macroscopic quantum charge states, Nature (London) **526**, 233 (2015).

[55] F. Schwarz, M. Goldstein, A. Dorda, E. Arrigoni, A. Weichselbaum, and J. von Delft, Lindblad-driven discretized leads for nonequilibrium steady-state transport in quantum impurity models: Recovering the continuum limit, Phys. Rev. B **94**, 155142 (2016).

[56] A. H. Werner, D. Jaschke, P. Silvi, M. Kliesch, T. Calarco, J. Eisert, and S. Montangero, Positive Tensor Network Approach for Simulating Open Quantum Many-Body Systems, Phys. Rev. Lett. **116**, 237201 (2016).

[57] J. Cui, J. I. Cirac, and M. C. Bañuls, Variational Matrix Product Operators for the Steady State of Dissipative Quantum Systems, Phys. Rev. Lett. **114**, 220601 (2015).

[58] E. Mascarenhas, H. Flayac, and V. Savona, Matrix-product-operator approach to the nonequilibrium steady state of driven-dissipative quantum arrays, Phys. Rev. A **92**, 022116 (2015).

Nonequilibrium Steady-State Transport in Quantum Impurity Models: a Thermofield and Quantum Quench Approach using Matrix Product States

Supplementary Material

F. Schwarz,[1] I. Weymann,[2] J. von Delft,[1] and A. Weichselbaum[1,3]

[1] *Physics Department, Arnold Sommerfeld Center for Theoretical Physics, and Center for NanoScience, Ludwig-Maximilians-Universität, Theresienstraße 37, 80333 München, Germany*
[2] *Faculty of Physics, Adam Mickiewicz University, Umultowska 85, 61-614 Poznań, Poland*
[3] *Department of Condensed Matter Physics and Materials Science, Brookhaven National Laboratory, Upton, New York 11973-5000, USA*

This supplementary material goes into the details of the numerical calculations. In section S-1 we describe the thermofield in more detail. In section S-2 we describe the discretization we use for the leads. In section S-3 we give some technical details for the MPS implementation. Section S-4 discusses how to determine expectation values, and section S-5 uses an example to illustrate the accuracy of our approach. Section S-6 compares our results for the SIAM at high voltages to previous results, and section S-7 addresses the question of determining the magnetic field at which the Kondo resonance begins to split.

S-1. THE THERMOFIELD APPROACH

The thermofield approach [32–35] used in the main text is a convenient way to represent a thermal state as a pure quantum state in an enlarged Hilbert space with the useful property that this pure state can be expressed as a simple product state. Here, we summarize the analytic details of this approach. For a schematic depiction of its main steps, see Fig. S1.

The density matrix of a thermal state is given by

$$\rho = \tfrac{1}{Z(\beta)} e^{-\beta H} = \sum_n \underbrace{\tfrac{e^{-\beta E_n}}{Z(\beta)}}_{\equiv \rho_n} |n\rangle \langle n| \tag{S1}$$

with $\beta = 1/T$, $Z(\beta) = \mathrm{tr}\left(e^{-\beta H}\right)$, and $H|n\rangle = E_n |n\rangle$.

Akin to purification [29], one can represent this thermal state as pure state $|\Omega\rangle$ in an enlarged Hilbert space: one doubles the Hilbert space by introducing the auxiliary state space $\{|n_2\rangle\}$, which is a copy of the original Hilbert space $\{|n\rangle\} \equiv \{|n_1\rangle\}$ and defines,

$$|\Omega\rangle = \sum_{n_1,n_2} f_{n_1,n_2}(\beta)\, |n_1\rangle \otimes |n_2\rangle \tag{S2}$$

such that the density matrix ρ can be recovered as

$$\begin{aligned}\rho =& \mathrm{Tr}_{\mathrm{aux}}\left(|\Omega\rangle\langle\Omega|\right) = \sum_{n_2} \langle n_2|\Omega\rangle \langle\Omega|n_2\rangle \\ =& \sum_{m_1,n_1} \underbrace{\sum_{n_2} f^*_{m_1 n_2}(\beta) f_{n_1 n_2}(\beta)}_{\equiv \rho_{n_1,m_1}} |n_1\rangle\langle m_1| \,.\end{aligned} \tag{S3}$$

Thermal equilibrium requires

$$\rho_{n_1,m_1} = \tfrac{e^{-\beta E_{n_1}}}{Z(\beta)} \delta_{m_1 n_1} \,. \tag{S4}$$

Eq. (S3) implies that the thermal expectation value of any operator A is given by

$$\langle A\rangle_\beta = \langle\Omega|A|\Omega\rangle \,. \tag{S5}$$

For noninteracting systems we can look at each single fermionic mode q separately with Hamiltonian $H_q = \varepsilon_q c_q^\dagger c_q$. The orthonormal basis of our enlarged Hilbert space with modes $c_{q1} = c_q$ and c_{q2} is given by:

$$\left\{ |0,0\rangle_q, |0,1\rangle_q, |1,0\rangle_q, |1,1\rangle_q \right\} . \tag{S6}$$

It follows from Eq. (S4) that the cumulative weight of the first two states (where the physical mode is empty) is $(1-f_q)$ with $f_q = (1+e^{\beta(\varepsilon_q - \mu_\alpha)})^{-1}$, while the weight of the other two (where the mode is filled) is f_q.

Within the space of the four states in (S6) one can perform a rotation such that one of the new basis states carries the full weight in the thermal state, while the other three do not contribute. This can be exploited to represent $|\Omega\rangle$ as a simple product state. By choosing $f^{(q)}_{00} = f^{(q)}_{11} = 0$ (implying $f^{(q)}_{01}(\beta) = \sqrt{1-f_q}$ and $f^{(q)}_{10}(\beta) = \sqrt{f_q}$) and rotating such that $|\Omega\rangle = \prod_q |\tilde{0},\tilde{1}\rangle_q$, we can ensure that this rotation preserves particle number conservation.

The rotated modes are of the form

$$\begin{pmatrix} \tilde{c}_{q1} \\ \tilde{c}_{q2} \end{pmatrix} = \begin{pmatrix} \cos\theta_q & -\sin\theta_q \\ \sin\theta_q & \cos\theta_q \end{pmatrix} \begin{pmatrix} c_{q1} \\ c_{q2} \end{pmatrix} \tag{S7}$$

where the angle θ_q is defined by

$$\begin{aligned} \sin\theta_q &= f^{(q)}_{10} = \sqrt{f_q} \,, \\ \cos\theta_q &= f^{(q)}_{01} = \sqrt{1-f_q} \,. \end{aligned} \tag{S8}$$

By construction, we then have

$$|\Omega\rangle = \prod_q \underbrace{\left(\sqrt{1-f_q}\,|0,1\rangle_q + \sqrt{f_q}\,|1,0\rangle_q\right)}_{=:\,|\tilde{0},\tilde{1}\rangle_q} \tag{S9}$$

and therefore

$$\tilde{c}_{q1}\,|\Omega\rangle = \tilde{c}^{\dagger}_{q2}\,|\Omega\rangle = 0\,. \tag{S10}$$

Let us conclude with a few further remarks: In the literature [34, 35], one typically transforms to a basis in which $|\Omega\rangle$ is the vacuum of the enlarged Hilbert space.

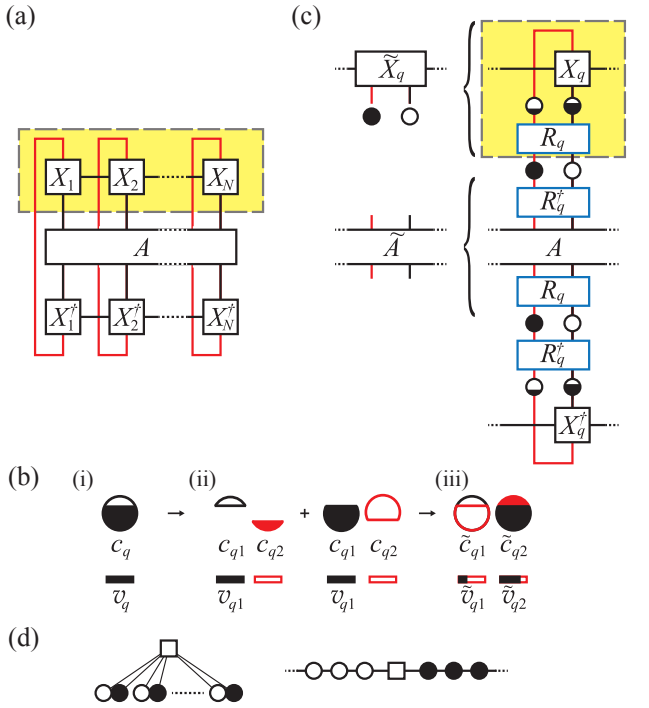

Figure S1. (a) Schematic MPS representation of the expectation value $\langle A\rangle = \mathrm{tr}(\rho A)$ rewritten in the form $\langle\Omega|A|\Omega\rangle$, where the state $|\Omega\rangle$ with its physical and auxiliary local modes is indicated by the dashed box. (b) Starting from (i) a thermal level occupied with probability f_q we represent the state (ii) as a linear combination $|\Omega\rangle$ of states in which the physical mode is empty or filled, weighting the two contributions corresponding to the Fermi function. We choose the auxiliary mode to be filled (empty) when the physical mode is empty (filled) [see Eq. (S9)]. (iii) The rotation R_q in Eq. (S7), combining the physical mode c_{q1} and the auxiliary mode c_{q2}, yields modes that are empty or filled with probability one, but their coupling to the impurity $\tilde{v}_{qi}$ depends on f_q. (c) Schematic depiction of the thermofield basis transformation for a single fermionic level q. Operators $\tilde{A}$ act on the state $|\Omega\rangle$ represented in the new rotated basis consisting of "holes" and "particles" in terms of the tensors $\tilde{X}_q$. (d) Both purification and local level rotation are set up in the star geometry, where each "free" lead mode couples to the impurity only. We then go over to the chain geometry by tridiagonalizing the modes $\tilde{c}_{qi}$ such that the resulting Hamiltonian consists of nearest-neighbor terms only. We do this for the holes $\tilde{c}_{q1}$ and the particles $\tilde{c}_{q2}$ separately. Since both channels are product states of either completely filled or completely empty levels, a unitary one-particle basis transformation, as provided by the tridiagonalization performed separately within each channel only, necessarily preserves this structure.

This corresponds to the approach presented here, but with the role of $\tilde{c}_{q2}$ and $\tilde{c}^{\dagger}_{q2}$ interchanged. In this case, the rotation in Eq. (S7) takes the standard form of a Bogoliubov transformation. Using this basis, it would not be necessary to keep the rotated modes in separate channels when going over to an MPS chain. However, the mapping onto a single chain (i) does not eliminate any degrees of freedom, and (ii) comes at the price of loosing particle number conservation. Therefore, for the sake of numerical efficiency, we preferred to keep the two channels separate. The only drawback of the latter approach appears to be that particle and hole excitations are locally separated along the chain geometry which, eventually, may make the accurate description of the long-time behavior more challenging.

The thermofield approach is closely related to the purification approach often used in MPS studies of finite-temperature systems. In particular, both approaches involve doubling the degrees of freedom, introducing an auxiliary mode for each physical mode. But while the latter typically describes interacting systems, the thermofield approach corresponds to its application to non-interacting thermal leads. In many applications of purification, the formulation is chosen such that auxiliary and physical modes are in the same state for the maximally entangled state at infinite temperature. For the thermal state of noninteracting leads at finite temperature, this would correspond to a choice of diagonal $f^{(q)}_{mn}$ in our statement below Eq. (S6), such that

$$|\tilde{\Psi}\rangle = \sqrt{\rho_0}|0,0\rangle + \sqrt{\rho_1}|1,1\rangle \tag{S11a}$$

for each single-particle lead level. In comparison to that, we exploit the freedom of unitary transformations in the auxiliary state space and use a number eigenstate instead,

$$|\Psi\rangle = \sqrt{\rho_0}|0,1\rangle + \sqrt{\rho_1}|1,0\rangle\,. \tag{S11b}$$

Evidently, Eq. (S11b) can be mapped onto Eq. (S11a) by a particle-hole transformation for the auxiliary degrees of freedom. (In an MPS diagram such as Fig. S1(c), this would amount to flipping the direction of the arrow of all lines [40] representing auxiliary degrees of freedom.) Since such a particle-hole transformation would map our H_{aux} onto $-H_{\mathrm{aux}}$, the scheme used here is reminiscent of the purification scheme employed in [47], who used opposite signs for the physical and auxiliary mode Hamiltonians in order to improve numerical efficiency.

Note also that in the present work we purify the thermal leads and do not have an auxiliary degree of freedom for the impurity itself. The reason for this is simple: in the initial state we want to enforce a specific thermal distribution on the occupation statistics of the leads. This carries over to a specific connection between the auxiliary and the physical degrees of freedom in the leads. In contrast, the impurity can be in any state at the beginning of our quench. In particular, one can choose the initial state of the impurity such that the auxiliary mode

for the impurity simply decouples. Also the Hamiltonian dynamics does not connect the auxiliary mode to the rest of the system, so we do not need to describe the auxiliary degree of freedom for the impurity at any time.

Finally, we note that the present scheme of simulating a thermal yet closed system can be extended to open systems. In a previous work [55] we had also introduced a lead representation in terms of "holes" and "particles", yet formulated a description of nonequilibrium steady-state transport through a localized level using Lindblad-driven discretized leads. There we demonstrated, that such a Lindblad driving in effect broadens the discrete levels of discretized leads in such a way that they faithfully mimic the properties of continuous leads. In the basis of "holes" and "particles" this Lindblad driving takes a remarkably simple form and, in particular, it is *local* on the chain underlying the MPS. By adding such a Lindblad driving to the time evolution, it should be possible to describe even longer time scales. However, the price one would have to pay, is a time evolution that is not described by Hamiltonian dynamics but by a Lindblad equation.

S-2. LOG-LINEAR DISCRETIZATION

We want to coarse-grain, i.e. discretize the full band of bandwidth $[-D, D]$ into N energy intervals $[E_n, E_{n+1}]$ in such a way that the width of the energy intervals scales linearly within the transport window (TW) $[-D^*, D^*]$ and logarithmically for energies outside, with a sufficiently smooth transition between the linear sector (lin-sector) and the logarithmic sector (log-sector). Related ideas have been considered in [25, 45]. The three relevant parameters for our discretization are: (i) the level-spacing δ within the lin-sector; (ii) the parameter $\Lambda > 1$ defining the logarithmic discretization in the log-sector (typically $\Lambda \gtrsim 2$; see below); and (iii) the energy scale D^* at which the transition between the lin-sector and the log-sector takes place. To construct such a log-linear discretization we define a continuous function $\mathcal{E}(x)$ which is evaluated at the points $x_n = n + z$ with $n \in \mathbb{Z}$ and $z \in [0, 1)$ to obtain the energies $E_n = \mathcal{E}(x_n)$. This function $\mathcal{E}(x)$ has to fulfill $\mathcal{E}(x+1) - \mathcal{E}(x) = \delta$ for $|\mathcal{E}(x+1)| < D^*$ and $\frac{\mathcal{E}(x+1)}{\mathcal{E}(x)} = \Lambda$ $\left(\frac{\mathcal{E}(x)}{\mathcal{E}(x+1)} = \Lambda\right)$ for $\mathcal{E}(x) \gg D^*$ ($\mathcal{E}(x) \ll -D^*$), respectively. Furthermore, we demand the function and its first derivative to be continuous. We construct such a function by inserting a linear section into the logarithmic discretization described by the sinh() function,

$$\mathcal{E}(x) = \begin{cases} \delta \cdot x & \text{if } |x| \leq x^* \\ \delta \cdot \left(\frac{\sinh[(x \mp x^*)\log\Lambda]}{\log(\Lambda)} \pm x^*\right) & \text{if } x \gtrless \pm x^* \end{cases} \quad \text{(S12)}$$

with $x^* = D^*/\delta$. Fixing the three parameters δ, Λ and D^* fully fixes the form of the function $\mathcal{E}(x)$. The only free parameter left is the parameter $z \in [0, 1)$, whose role is fully analogous to the z-shift in NRG calculations [38, 39].

The outermost intervals are limited by the bandwidth $E_1 = -D$, $E_{N+1} = D$. If one of these outermost intervals gets narrow compared to the adjoining interval, one can simply join these two intervals into one for the sake of energy scale separation within NRG.

The discretization is therefore determined by four parameters: Λ, D^*, δ, and z. The parameter Λ characterizes the logarithmic discretization for the log-sector. It has to be small enough to capture the relevant high-energy physics, but large enough to ensure energy scale separation in the NRG calculation. For our calculations, we typically choose $2 \lesssim \Lambda \lesssim 3$. D^* is the energy scale that defines the size of the TW. If $T \lesssim V$, it is approximately set by the chemical potential $V/2$. If $T \gtrsim V$, temperature will define the size of the TW and the edges of the window will be smeared out. We chose D^* as the energy at which the Fermi function of the channel with positive chemical potential ($\mu = V/2$) has decreased to a value of 10^{-3}, implying $D^* = V/2$ for $T = 0$ and $D^* \approx 7T$ for $V \ll T$. The level spacing δ in the lin-sector sets the time-scale accessible by the quench calculations before finite size effects get visible. Typically, we set $\delta = D^*/20$, such that we have approximately forty energy intervals within the TW. In all our calculations, we used $z = 0$.

To each of the intervals $[E_n, E_{n+1}]$ we assign an energy ε_n representing the energy of the interval. In the context of NRG, different methods have been developed to optimize this energy [38, 39]. Motivated by Eq. (44) in Ref. [38], we choose a simplified version, namely

$$\varepsilon_n = \begin{cases} \frac{E_{n+1} - E_n}{\ln(E_{n+1}/E_n)}, & \text{if } |E_n|, |E_{n+1}| > D^* \\ \frac{1}{2}(E_n + E_{n+1}), & \text{else.} \end{cases} \quad \text{(S13)}$$

When $|E_n|$ approaches $|D^*|$ from above, our log-linear discretization approaches a linear discretization, with $E_{n+1} - E_n = \delta$. In this case,

$$\varepsilon_n = \frac{\delta}{\ln(1 + \frac{\delta}{E_n})} \overset{\delta \ll E_n}{\approx} E_n + \frac{\delta}{2} \approx \frac{1}{2}(E_n + E_{n+1}), \quad \text{(S14)}$$

which matches the definition of ε_n for $|E_n|, |E_{n+1}| < D^*$ in Eq. (S13). In this sense the smooth behavior of the energies E_n defining the discretization intervals leads to a reasonably smooth transition from the log-sector to the lin-sector also in the energies ε_n.

S-3. DETAILS ON THE MPS CALCULATION

All our MPS calculations were built on top of the QSpace tensor library that can exploit abelian as well as non-abelian symmetries on a generic footing [40]. For the SIAM, standard particle-hole symmetry is defined by the spinor $\hat{\psi}^\dagger \equiv (c_\uparrow^\dagger, s c_\downarrow)$, which interchanges holes and particles (up to a sign s) while simultaneously also reverting spin $\sigma \in \{\uparrow, \downarrow\}$ [40]. This symmetry acts independently of the SU(2) spin symmetry, and hence is preserved even if $B \neq 0$. In our simulations, however, we

only exploit U(1) spin and U(1) particle-hole symmetry, since (i) we are also interested in finite magnetic field B, which breaks spin SU(2) symmetry, and (ii) finite bias voltage V breaks particle-hole symmetry in the leads.

A. The MPS geometry

The starting point is the star geometry with the two leads, $\alpha \in \{L, R\}$, discretized in energy with lead levels $q = \{\alpha, (\sigma), k\}$, as depicted in Fig. S2(a). Note that we do not include the chemical potential into the energies ε_q. Together with left/right symmetry for the leads, this implies $\varepsilon_{\alpha(\sigma)k} = \varepsilon_k$. In the thermofield approach the lead levels q are doubled and rotated to "holes" and "particles", represented by the operators $\tilde{c}_{qi}$, as depicted in Fig. S2(b).

a. Decoupling modes: For the positive (negative) high energies in the log-sector the "particle" modes $\tilde{c}_{q2}$ (the "hole" modes $\tilde{c}_{q1}$) are already decoupled due to $f_q = 0$ ($f_q = 1$) without any further rotation. Hence the doubling of levels is not required there.

Furthermore, in the SIAM, we can combine the "holes" and "particles" separately from the left lead with those from the right lead into new modes,

$$\tilde{C}_{k\sigma i} = \tfrac{1}{\mathcal{N}} \sum_{\alpha} \tilde{v}_{\alpha k\sigma i} \tilde{c}_{\alpha k\sigma i} \ , \quad \left(\mathcal{N}^2 \equiv \sum_{\alpha'} \ |v_{\alpha' k\sigma i}|^2\right) \tag{S15a}$$

yielding the geometry in Fig. S2(c). The modes orthogonal to these,

$$\tilde{C}^{(\perp)}_{k\sigma i} = \tfrac{1}{\mathcal{N}} \left(\tilde{v}^*_{Lk\sigma i} \tilde{c}_{Rk\sigma i} - \tilde{v}^*_{Rk\sigma i} \tilde{c}_{Lk\sigma i}\right) , \tag{S15b}$$

decouple from the impurity. In matrix notation, temporarily suppressing the global index set $k\sigma i$ for readability, this can be written as

$$\begin{pmatrix} \tilde{C} \\ \tilde{C}^{(\perp)} \end{pmatrix} = \tfrac{1}{\mathcal{N}} \begin{pmatrix} \tilde{v}_L & \tilde{v}_R \\ -\tilde{v}^*_R & \tilde{v}^*_L \end{pmatrix} \begin{pmatrix} \tilde{c}_L \\ \tilde{c}_R \end{pmatrix} \tag{S16a}$$

with inverse relations,

$$\begin{pmatrix} \tilde{c}_L \\ \tilde{c}_R \end{pmatrix} = \tfrac{1}{\mathcal{N}} \begin{pmatrix} \tilde{v}^*_L & -\tilde{v}_R \\ \tilde{v}^*_R & \tilde{v}_L \end{pmatrix} \begin{pmatrix} \tilde{C} \\ \tilde{C}^{(\perp)} \end{pmatrix} \tag{S16b}$$

The decoupling of the orthogonal modes is in complete analogy to standard equilibrium calculations in the SIAM [24]. In our setup it carries over to the nonequilibrium situation, because the difference in the chemical potential of the two physical leads is shifted into the couplings $\tilde{v}_{qi}$. In the IRLM, this combination of left and right lead modes is not possible, because the two leads couple to two different impurity sites, in full analogy to standard equilibrium calculations.

The above analysis leads to the remarkable conclusion that the numerical effort for the description of the spinless IRLM is comparable to that of the spinful SIAM.

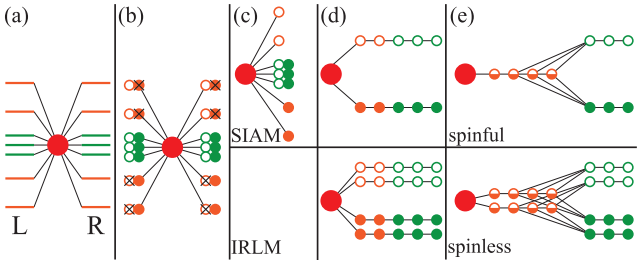

Figure S2. Sketch of the different discrete site geometries. (a) We start with two channels $\alpha \in \{L, R\}$ in the star geometry, with the two colors representing the log-sector and the lin-sector. (b) Within the thermofield approach each level is exactly represented by one "hole" and one "particle". However, for the positive (negative) energies in the log-sector the "particles" ("holes") decouple from the impurity due to $f_q = 0$ ($1 - f_q = 0$), respectively. (c) For the SIAM, only specific linear combinations of left and right lead modes couple to the impurity, while the corresponding orthogonal modes decouple see Eqs. (S15) (d) Tridiagonalizing "holes" and "particles" into separate channels, we get two channels in the chain geometry for the SIAM (upper part) and four in the IRLM (lower part), for which we still distinguish between left and right leads. The couplings in the log-sector for each channel decay as Λ^{-n} (e) Recombination of holes and particles within log-sector into one channel using another tridiagonalization since for NRG it is unfavorable to have "holes" and "particles" in separate channels. The couplings in this altered channel setup decay as $\Lambda^{-n/2}$, which resembles equilibrium NRG. However, the first site of the lin-sector in the chain geometry now couples to a range of sites of towards the end of the log-sector. Nevertheless, energy scale separation ensures that this nonlocality is restricted to only a few sites.

The additional cost involved for the SIAM for treating two states is compensated by the simplification that left and right lead modes can be combined because they couple to the same impurity site.

b. Tridiagonalization: When going over to a chain geometry, the corresponding tridiagonalization is performed for "holes" and "particles" independently (treating them as different "channels"), in order to maintain the property that the thermal state $|\Omega\rangle$ is a simple product state while also preserving charge conservation: if for the state $|\Omega\rangle$ a channel is completely empty (filled) in the star geometry, it will remain a completely empty (filled) channel also in the chain geometry. For the IRLM, since the left and right leads have to be represented as separate channels, we tridiagonalize the modes $\tilde{c}_{qi}$ into the four channels $\{\alpha i\}$ with $\alpha \in \{L, R\}$ and $i \in \{1, 2\}$ labeling "holes" and "particles", see lower part of Fig. S2(d). For the SIAM, in contrast, left and right leads are combined in the sense of equation (S15a), so we separately tridiagonalize the "holes" ($\tilde{C}_{q,i=1}$) and the "particles" ($\tilde{C}_{q,i=2}$), see upper part of Fig. S2(d).

Due to energy scale separation, the first part of the chain corresponds to the energy scales of the log-sector, while the later part of the chain represents the lin-sector. Instead of counting the exact number of sites in the chain

geometry, we identify the log-sector by looking at the behavior of the hoppings which decay exponentially in the log-sector and are all of the same order in the lin-sector. Due to the smoothened transition from the linear to the logarithmic discretization also the hopping matrix elements show a smooth crossover from exponential decay to approaching a constant. We define the log-sector on the chain as the part for which (i) the hoppings decay strongly enough (the details of this condition slightly depend on the number of many-particle states kept in the NRG iterations) and (ii) the hoppings are larger than the energy scale D^* on which transport takes place. By construction the two conditions are roughly equivalent. Note that for the "holes" ("particles") in the log-sector of the star geometry only the positive (negative) energies contribute to the hybridization. This translates into a decay of the hoppings and on-site energies scaling as Λ^{-n} for the log-sector on the chain.

c. Re-combining "holes" and "particles" in the log-sector: For the NRG calculation it is disadvantageous to describe "holes" and "particles" in separate channels since particle-hole excitations are sharply separated in terms of the particle and the hole content along the chain geometry. Consequently, we apply a further tridiagonalization that remixes "holes" and "particles" of the log-sector into one channel, e.g. see upper part of Fig. S2(e). This then defines the renormalized impurity (RI). For the IRLM, this subsequent tridiagonalization is done for the left and right lead separately, see lower part of Fig. S2(e). After this recombination the hoppings in the channel(s) will decay as $\Lambda^{-n/2}$. The numerical complexity of the NRG calculation, therefore, is comparable to that of a standard equilibrium calculation in the sense that we obtain the same number of numerical channels (one spinful for the SIAM, two spinless for the IRLM) and the same exponential decay in the energy scales. Note that the tridiagonalization combining "holes" and "particles" for the log-sector comes with the caveat that it introduces a nonlocality in the Hamiltonian: after this further tridiagonalization, the first site in the lin-sector does not only couple to the last site of the log-sector but rather to the last few sites, see Fig. S2(e). The corresponding hopping term is therefore subject to truncation within the NRG iterations. However, energy-scale separation ensures that this nonlocality stretches only over a few sites, so the error introduced by the truncation of this hopping is considered minor.

d. Remaining lin-sector: For the DMRG calculation we order the channels such that the "holes" are on one side of the RI and the "particles" on the other side, see Fig. 1. The local dimension of each chain element is given by $2^2 = 4$: in the SIAM this is due to the spin degree of freedom σ, in the IRLM it represents the remaining degree of freedom in the physical leads α.

In case of the IRLM, where left and right lead are kept separate, there is one further point worth noting: at $T = 0$, also in the lin-sector either the "hole" or the "particle" decouples from the impurity for each lead level q. This implies that parts of the remaining chains representing "holes" and "particles" in the log-sector of the chain geometry decouple. This fact can be applied to further reduce the numerical cost, even though we have not done so here. It stems from the fact that no purification procedure is needed for $T = 0$, and therefore does not carry over to $T > 0$.

B. Renormalized Impurity

The log-sector traces out the high-energy degrees of freedom at energies $E \gg T, V$. Therefore the renormalized impurity represents the low-energy many body basis that still spans energies up to and beyond the transport window (TW) set by $\max(T, V)$. Typically we keep approximately 500 to 700 states to describe this basis. In the quench protocol, we can pick an arbitrary pure state $|\phi_{\text{ini}}\rangle$ in this effective low-energy space as the initial state for the RI. In order to avoid excess energy in the initial state, we choose the ground state of the log-sector.

If the ground state space is degenerate by symmetry, picking a single individual state may artificially break that symmetry. Therefore proper averaging over degenerate state spaces is required, either by actually running separate simulations for each degenerate ground state, or by simply exploiting the known effect of the symmetry on the numerical result. (This also applies to the case of quasi-degenerate ground states, e.g. when a symmetry present in the Hamiltonian is only weakly broken.) Overall, note that degeneracy within the log-sector is rather generic, since we choose to keep particle and hole channels symmetric. Therefore we combine the *same* number of "hole" and "particle" sites into the log-sector such that, including the impurity site, it always contains an odd number of sites [see Fig. S2].

For example, for the IRLM at particle-hole symmetry, the log-sector has a single zero-energy level, $\varepsilon_c = 0$, causing the ground state sector to be two-fold degenerate. Since our NRG code exploits abelian particle number conservation, we obtain two ground states for the log-sector that are particle-number eigenstates globally within the RI, say $|G_1\rangle$ and $|G_2\rangle$. We can initialize our quench calculations by taking $|\phi_{\text{ini}}\rangle$ equal to either $|G_1\rangle$ or $|G_2\rangle$.

Now, for a particle-hole-symmetric model involving a zero-energy level coupled to an *infinite* bath, the local (e.g. thermal) occupancy is $n_C = 1/2$. However, the initial local occupancies for the two number eigenstates above, say $n_{C,i} = \langle G_i|\hat{n}_C|G_i\rangle$ (for $i = 1, 2$), are not necessarily equal. In general, $n_{C,1} + n_{C,2} = 1$, yet $n_{C,1} \neq n_{C,2}$ due to finite-size effects (the log-sector involves only a *finite* number of bath levels). Correspondingly, during the post-quench time evolution, only the average of the local occupancies, $\langle n_C\rangle(t) \equiv \frac{1}{2}(n_{C,1} + n_{C,2})(t) = 1/2$, throughout, whereas the local occupancies for the two individual states, $n_{C,i}(t)$, reach the value $1/2$ only in the asymptotic limit $t \to \infty$ due to their hybridization with

the lin-sector. In practice, by knowing the underlying symmetry which enforces $n_{C,2}(t) = 1 - n_{C,1}(t)$, the inialization of the quench may only include e.g. $|G_1\rangle$, bearing in mind that the data must be symmetrized w.r.t. occupation.

Alternatively, one could construct linear combinations of $|G_{1,2}\rangle$, say $|G_\pm\rangle$, which are eigenstates of a particle-hole transformation with eigenvalues ± 1, and which yield local occupancies, $n_{C,\pm} = \langle G_\pm|\hat{n}_C|G_\pm\rangle$, that by construction satisfy $n_{c,\pm} = 1/2$. If we would initialize the quench by taking $|\phi_{\rm ini}\rangle$ equal to either $|G_+\rangle$ or $|G_-\rangle$, then we would find $n_{C,\pm}(t) = 1/2$ throughout the post-quench time evolution. However, since the post-quench time evolution conserves particle number within each particle-number eigensector, this strategy would be equivalent to averaging the result of two separate quenches, initialized with $|\phi_{\rm ini}\rangle$ equal to $|G_1\rangle$ or $|G_2\rangle$, respectively.

C. Trotter time evolution

The initial state is evolved in time, $|\Psi(t)\rangle = e^{-iHt}|\Psi(t=0)\rangle$, using tDMRG [27–29] with a standard second-order Trotter decomposition for a time step τ:

$$e^{-iH\tau} = e^{-iH_{\rm o}\tau/2}e^{-iH_{\rm e}\tau}e^{-iH_{\rm o}\tau/2} + \mathcal{O}(\tau^3)\,, \qquad \text{(S17)}$$

where $H_{\rm e}$ ($H_{\rm o}$) includes all "even" ("odd") bonds. The individual terms in Eq. (S17) w.r.t. $H_{\rm e}$ ($H_{\rm o}$) will be referred to as even (odd) Trotter steps or even (odd) iterations, respectively. The tensorial operations that are performed in practice within the MPS setup, are sketched in Fig. S3. The RI is described within a fixed effective low-energy basis. The main idea is to use this fixed basis as the local state space of an MPS site in the center when performing the Trotter time evolution. However, when constructing the time evolution operator that contains the coupling between the NRG sites and the first of the remaining sites, one has to be careful with the exponentiation of the coupling term. For this purpose, we need to consider two subsequent NRG iterations, e.g. at Wilson chain lengths N and $N+1$, where site $N+1$ will be referred to as flexible site. These will be treated differently in the even compared to the odd Trotter steps (depending on the exact chain length, the notion of "even" and "odd" may need to be interchanged). For the time steps which we call "even" in panel (a), we exponentiate the full Hamiltonian of N NRG sites plus the flexible site ($H^{\rm NRG}_{N+1}$), yet excluding the coupling to the rest of the chain. Therefore we *fully* associate the "local" Hamiltonian of the RI with even iterations which is allowed within the Trotter setup. Assuming that the Wilson chain length $N+1$ is still within the realm of energy scale separation, it can be dealt with in standard NRG manner. In particular, it can be exactly diagonalized in the expanded state space, including the state space of the flexible site, followed by simple exponentiation. The couplings between the flexible site and the subsequent sites, i.e. sites $N+1$ and $N+2$, both left and right, we reshape the tensors as depicted in Fig. S3(b). Note that this requires fermionic swap gates [41] to account for the correct treatment of fermionic signs. After this reshaping the performance of the "odd" time steps is standard, as sketched in Fig. S3(c).

At time $t = 0$, the RI is in its ground state, while the leads are thermal. Since we are interested in the nonequilibrium steady-state properties, we do not switch on the coupling between RI and thermal leads abruptly in our quench protocol, as this would introduce undesirable high-energy excitations into the system. Instead, with adiabaticity in mind, we turn on the coupling between RI and thermal leads smoothly over a short time interval. The detailed form of this procedure should not matter. In our calculation, we ramp up the coupling η between the RI and the thermal leads in a linear fashion: we use a time window of $t_{\rm ramp} = 2/D^*$ to $4/D^*$ and divide it into $N = 10$ to 20 equally spaced time intervals with stepwise constant couplings, $\eta(t_n) = \eta\frac{n}{N}$ where $n = 1, \ldots, N$.

The size of the actual Trotter time step τ in equation (S17) should scale with $E^{-1}_{\rm trunc}$, with $E_{\rm trunc}$ being the highest eigenenergy of the truncated NRG basis (or, if no NRG is required, the many-body energy bandwidth, i.e. since all energy scales are only moderately smaller as compared to the bandwidth of the leads). In practice, a prefactor of in the range 0.5 to 1 worked quite well. In our calculation this energy $E_{\rm trunc}$ typically is of the order $5D^*$ to $20D^*$.

When applying the Trotter gates, we keep all singular values larger than some threshold $\varepsilon_{\rm (SVD)}$. Within our calculation this threshold varies between $\varepsilon = 2\cdot 10^{-4}$ and $\varepsilon = 10^{-3}$. We time-evolve the system until a time $t_{\rm max}$ at which a maximal bond dimension $D_{\rm max}$ is reached in our MPS due to an increase in entanglement entropy following the quench. We used $D_{\rm max}$ up to 450 in our calculations. The above parameters implied typical accessible times in the post-ramp window up to $t_{\rm max} - t_{\rm ramp} > 8/D^*$. In case of $V \gg T$ this is equivalent to $t_{\rm max} > 16/V$. Compared to an oscillation period of $4\pi V^{-1}$ in the current (see below) this range might seem rather small. However, typically these oscillations are (a) strongly reduced in amplitude due to the quasi-adiabatic quench protocol as described above, and (b) in cases where the oscillations are nevertheless still strong, i.e. at large voltages, the accessible time window typically can be extended over many periods.

S-4. EXPECTATION VALUES AND CONVERGENCE

A. Current

For the IRLM, the current through the central site of the impurity can be defined by looking at the change of the corresponding occupation number, $\frac{d}{dt}\langle n_C\rangle$. In the steady state this derivative should be zero, of course, but we can identify the contribution, J_α, of the current flow-

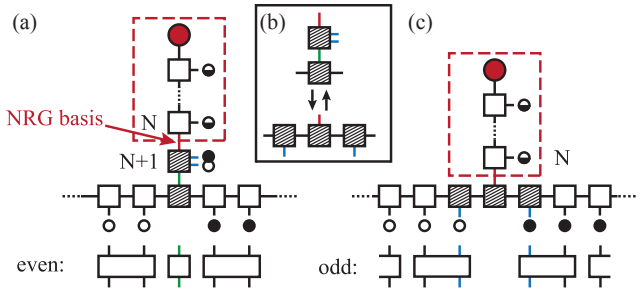

Figure S3. Sketch to illustrate how NRG and DMRG are combined in the Trotter time evolution. (a) For the performance of the "even" time steps we exponentiate the Hamiltonian of all NRG sites plus one additional site in the sense of standard NRG. For the "odd" time steps we rearrange the tensors as depicted in (b) including fermionic swap gates to bring the MPS into a form with local Trotter gates. (c) The time evolution on the "odd" bonds is then a standard tDMRG step. The boxes at the bottom in both, (a) and (c), indicate the Trotter gates to be applied.

ing from lead α into the dot from the formula

$$0 = \tfrac{d}{dt} e \langle \hat{n}_C \rangle = \sum_\alpha \underbrace{\tfrac{2e}{\hbar} \mathrm{Im}\big(t' \langle d_C^\dagger d_\alpha \rangle\big)}_{\equiv J_\alpha} . \tag{S18}$$

In the SIAM we combine the modes of the left and right channels as given in Eqs. (S15). Still, it is possible to deduce the current from the change of occupation $\frac{d}{dt}\langle \hat{n}_{d\sigma}\rangle$ at the central site:

$$\begin{aligned} J_{\alpha\sigma} &= \tfrac{2e}{\hbar} \sum_k \mathrm{Im}\big(v_q \langle d_\sigma^\dagger c_q \rangle\big) = \tfrac{2e}{\hbar} \sum_{ki} \mathrm{Im}\big(\tilde{v}_{qi} \langle d_\sigma^\dagger \tilde{c}_{qi} \rangle\big) \\ &= \tfrac{2e}{\hbar} \sum_{ki} \tfrac{|\tilde{v}_{qi}|^2}{\sqrt{\sum_{\alpha'} \tilde{v}^2_{\alpha' k\sigma i}}} \mathrm{Im}\big(\langle d_\sigma^\dagger \tilde{C}_{k\sigma i} \rangle\big) . \end{aligned} \tag{S19}$$

where we used Eq. (S16b), $\tilde{c}_{\alpha k\sigma i} = \frac{\tilde{v}^*_{\alpha k\sigma i}}{\mathcal{N}} \tilde{C}_{k\sigma i} + \ldots \tilde{C}^{(\perp)}_{k\sigma i}$, together with the fact that the mode $\tilde{C}^{(\perp)}_{k\sigma i}$ decouples from the impurity and therefore $\langle d_\sigma^\dagger \tilde{C}^{(\perp)}_{k\sigma i}\rangle = 0$. The chain operators underlying the MPS $f_{n\sigma(i)}$ are related to the modes $\tilde{C}_{k\sigma i}$ by a unitary transformation, which includes the mapping of "holes" and "particles" onto a chain and the re-combination of channels within the RI. The expectation values $\langle d_\sigma^\dagger \tilde{C}_{k\sigma i}\rangle$ can therefore be determined by calculating the expectation values $\langle d^\dagger f_{n\sigma(i)}\rangle$ for all chain sites n. For the SIAM, the current can further be divided into different spin contributions $J_{\alpha\sigma}$.

Interestingly, in most cases the *symmetrized* current

$$J_{(\sigma)} = \tfrac{1}{2}\left(J_{L(\sigma)} - J_{R(\sigma)}\right) . \tag{S20}$$

converges much faster than $J_{L(\sigma)}$ and $J_{R(\sigma)}$ separately [see discussion of Fig. S4(h) below for details]. For the SIAM, a similar statement holds when averaging over spin instead of averaging over channels. In practice, we take the mean over both by defining

$$J = (J_\uparrow + J_\downarrow) = \tfrac{1}{2}\left(J_{L\uparrow} - J_{R\uparrow} + J_{L\downarrow} - J_{R\downarrow}\right) \tag{S21}$$

We define the value of the steady-state current $J(V)$ by taking the mean over the last part of $J_V(t)$, where the current is converged to its steady-state value. If the oscillations are pronounced, we take the mean over a time window, which equals an integer number of periods, in many cases simply the last period. The conductance is obtained from

$$g(V^*) = \frac{J(V_1) - J(V_2)}{V_1 - V_2} \left(\frac{2e^2}{h}\right)^{-1} \tag{S22}$$

with $V^* = \frac{1}{2}(V_1 + V_2)$, and V_1 and V_2 close to each other, where we average $J_{V_1}(t)$ and $J_{V_2}(t)$ over similar time windows.

B. Dot Occupation

The occupation of the impurity in the SIAM, as well as the occupation of the central site of the impurity for the IRLM are of physical relevance. Their time evolution is related to that of the current via

$$\tfrac{d}{dt} e \langle n_{C/d}(t)\rangle = J_L(t) + J_R(t) \tag{S23}$$

In the present work, we focus on the particle-hole symmetric point. Because of this symmetry we expect the steady-state value of $n_{C/d}$ to be independent of voltage and given by $n_C = \frac{1}{2}$ in the IRLM and $n_d = n_{d\uparrow} + n_{d\downarrow} = 1$ in the SIAM. The magnetization $M = \frac{1}{2}(n_{d\uparrow} - n_{d\downarrow})$, however, is a nontrivial function of voltage and magnetic field.

C. Long-time convergence after the quench

By definition, in the nonequilibriuim steady state (NESS) all expectation values are converged in the sense that they do not change with time. However, we are limited to a finite time window and cannot fully reach this point. In this section, we discuss this aspect in more detail based on the behavior of the symmetrized current J, the currents from the left and right leads $J_{\alpha(\sigma)}$, and the (spin-resolved) dot occupation n_C or $n_{d(\sigma)}$.

As explained above, our initial state breaks certain symmetries. However, as we assume the steady state to be unambiguous, we expect it to obey the symmetries of the Hamiltonian.

For the IRLM we have done our calculations at the particle-hole symmetric point. We therefore expect $n_C = 1/2$ in the steady state. And, if the dot occupation is converged, one finds $J_L = -J_R$ because of Eq. (S23). This is, indeed, what we find for low voltages, see Fig. S4(b). For higher voltages, however, we do not see full convergence in n_C, see Fig. S4(d). Consequently, also the currents are not converged, so we do not find $J_L = -J_R$. However, the *symmetrized* current J is converged, except for oscillations around a well-defined mean value. These oscillations do have the expected period of $\frac{4\pi}{V}$ [42], and

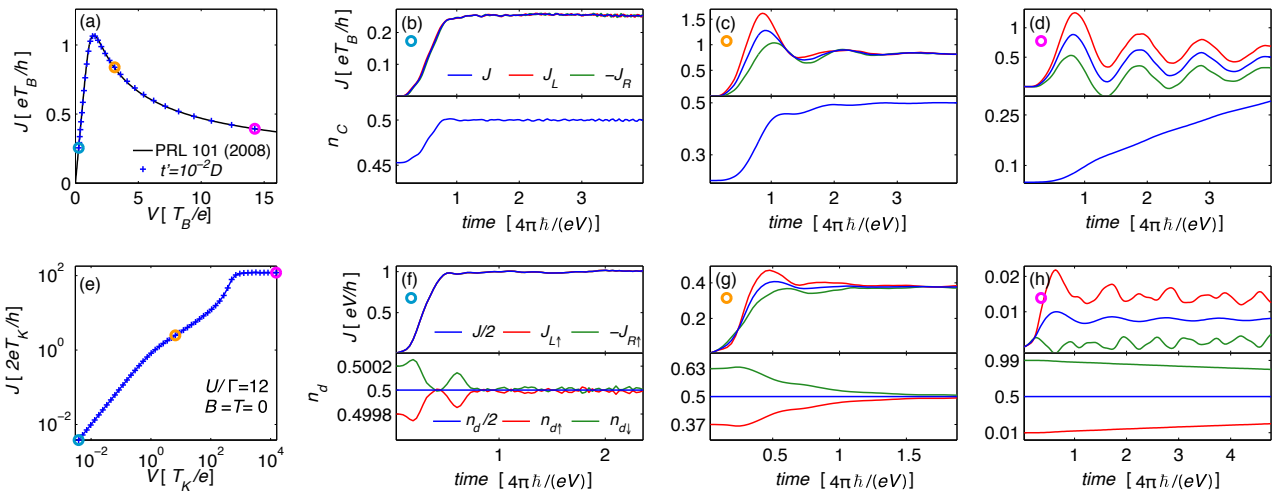

Figure S4. Upper panels: convergence in the IRLM — Panel (a) replots the data set for $t' = 10^{-2}D$ in Fig. 2 of the main text. Panels (b-d) show the time dependence of the currents J_L, $-J_R$ and $J = (J_L - J_R)/2$ and the dot occupation n_C, for the three different voltage values marked by circles in panel (a), respectively. For the lowest voltage which is still in the linear response regime, we find nice convergence in the dot occupation and the current (panel b). With increasing voltage, all three currents develop increasingly strong oscillations, with a period of $4\pi/V$, as expected (panels c,d). For the largest voltage we do not find convergence in n_C (panel d). This reflects in the fact that also J_L and J_R are not yet converged. However, the symmetrized current J (blue line) does oscillate around a well-defined mean value. Lower panels: convergence in the SIAM — Panel (e) replots the data for $U = 12\Gamma$ and $T = 0$ in Fig. 3 (a) of the main text. Panels (f-h) show the behavior of $J_{L\uparrow}$ and $J_{R\uparrow}$, J, and $n_{d\sigma}$ (at $T = B = 0$) for the voltage values marked in circles in panel (e), respectively. The current for the down-spin is not shown, since $J_{L\downarrow} \approx -J_{R\uparrow}$ and $J_{R\downarrow} \approx -J_{L\uparrow}$. The total dot occupation n_d is equal to 1 in the beginning and remains so throughout. However, for large voltages the numerically accessible time window is too short to find convergence for the spin-resolved occupations $n_{d\uparrow}$ and $n_{d\downarrow}$. In panel (h), the left and right components of the current (red and green lines) show seemingly irregular oscillations; these arising from a combination of large voltage and the finite level spacing in the lin-sector. The level-spacing effect cancels out, however, for the symmetrized current, $J = (J_L - J_R)/2$ (blue line), which shows regular oscillations with the expected period of $4\pi/V$.

the amplitudes decay rapidly. The initial state breaks particle-hole symmetry as explained above. This symmetry breaking is more pronounced for shorter NRG Wilson chains. This is the reason why for small voltages (for which the TW is small so that the NRG Wilson chain is long) we already start with $n_{d\sigma}(t = 0) \approx \frac{1}{2}$ while for high voltages (for which the TW is large and the NRG Wilson chain is short) the symmetry breaking in the beginning is very strong.

Analogous considerations apply for the SIAM. We numerically observe the behaviour

$$J_{L\sigma}(z) \approx -J_{R,-\sigma}(t) \tag{S24}$$

and $n_d(t) = n_{d\uparrow}(t) + n_{d\downarrow}(t) \approx 1$ for all times t, reflecting particle-hole and left-right symmetry (here $-\sigma$ stands for reverted spin σ). However, by choosing a specific initial pre-quench state out of a degenerate ground state multiplet, this breaks the spin symmetry, and hence we find $n_{d\uparrow}(t) \neq n_{d\downarrow}(t)$, even for $B = 0$. The effect of this symmetry breaking is largest for high voltages. Whereas for small voltages we do find convergence in the dot occupation [e.g. see Fig. S4(f)], for high voltages our numerically accessible time window is too small to see convergence [Fig. S4(h)]. Moreover, for large voltages the spin-resolved currents $J_{L\sigma}$ and $J_{R\sigma}$ show seemingly irregular oscillations, as seen in Fig. S4(h). A Fourier-transform analysis (not shown) reveals that the oscillations in $J_{\alpha\sigma}(t)$ have several characteristic frequencies, one being $\frac{V}{4\pi}$ (as expected from [43]), the others being the energies representing the intervals in the log-sector closest to D^*, which was chosen $D^* = V/2$ here. Thus, at large voltages the post-quench dynamics become sensitive to the rather crude discretization in the log-sector, causing the seemingly irregular oscillations in the spin-resolved currents at large voltages. This suggests that the strength of these discretization-related oscillations could be reduced, if desired, by using a slower ramp for the quench (i.e. a larger ramping time t_{ramp}), or by reducing the size of the log-sector (i.e. increasing D^*, while keeping the level spacing δ for the lin-sector fixed). In practice, though, we found this to be unnecessary, since the discretization-related oscillations cancel in the left-right symmetrized current: $J = (J_L - J_R)/2$ shows only regular oscillations around a well-defined mean value [Fig. S4(h)] with the expected time-period of $\frac{4\pi}{V}$ [43], similar to those found for the IRLM. We suspect that this cancellation of discretization-related oscillations occurs because our treatment of the leads respects left-

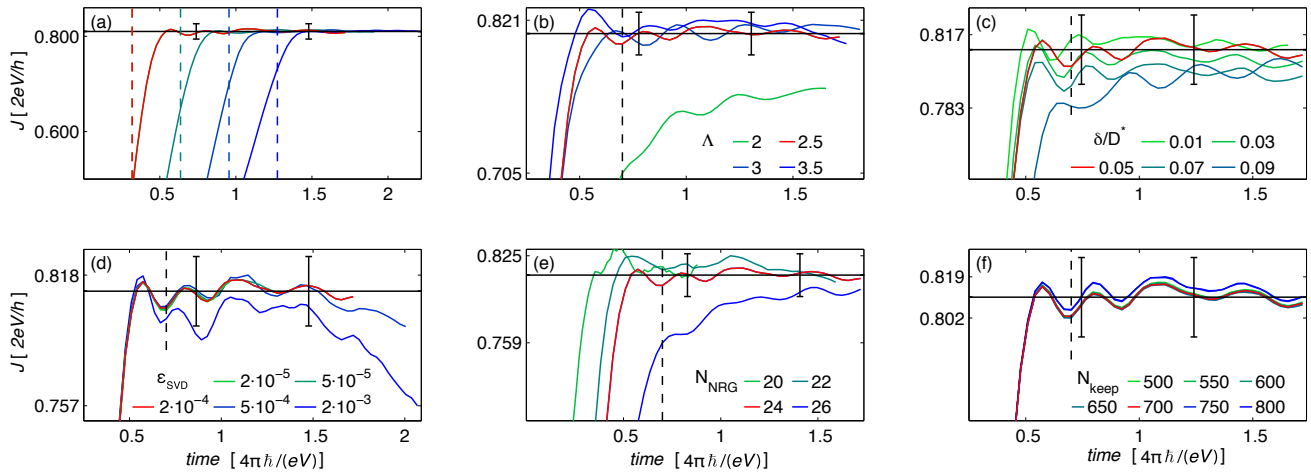

Figure S5. Illustration of the numerical accuracy using the example of $V = T_K$ with the parameters as in Fig. 3(a), with $U/\Gamma = 12$. In each of the panels the red curve corresponds to the parameters typically used for our calculations and the "error bars" indicate a relative range of $\pm 2\%$ around the mean. Panel (a) shows $J(t)$ where the coupling between RI and leads is turned on quasi-adiabatically over time windows of four different widths. All curves approach the same steady-state value. In (b) and (c) the discretization parameters Λ and δ are varied. In (d) different thresholds, $\varepsilon_{\rm SVD}$, are used for the SVD truncation in the tDMRG quench. In (e) the number of sites treated with NRG is changed (and therefore the number of sites treated with tDMRG is changed accordingly). And finally in (f) we use different numbers of kept states in the effective NRG basis for the renormalized impurity.

right symmetry, both regarding their discretization [see Fig. S2(d,e)] and when turning on the coupling between the log- and lin-sectors during the quench.

In the case of finite magnetic field in the SIAM, we do not have spin symmetry. In particular, we expect $n_{d\uparrow} \neq n_{d\downarrow}$, even in the steady state. The exact NESS values of $n_{d\sigma}$ are nontrivial and depend on voltage. However for large values of V, we are not able to see convergence in these occupations, analogously to Fig. S4(h). Still, it is in principle possible to predict the NESS occupation by extrapolating the data available within the accessible time window, e.g. using linear prediction [44].

S-5. NUMERICAL ACCURACY

Our approach treats the many-particle aspect of impurity models nonperturpatively. However, of course, the numerics contains approximations such as the discretization of the lead into a finite number of energy intervals, the truncation of states within the NRG, and the truncation of the MPS within the tDMRG time evolution. A further error arises from the fact that we have to take the mean over a curve $J(t)$ that often still oscillates over a well-converged mean value. Therefore it is difficult to give a precise value for our error. However, we can provide an estimate for the error bar. For the case of the current, it is approximately $\pm 3\%$, throughout, which at times may be considered conservative.

To illustrate this statement we go into more detail for the curve $J(t)$ for the parameters used in Fig. 3(a) with $U/\Gamma = 12$ at $V \approx T_K$: Fig. S5 shows the behavior of $J(t)$ when varying various different numerical parameters, such as discretization and truncation parameters. In each of the panels the red curve was obtained from the parameter choices typically used in our numerics. This curve is identical in each of the panels. The black horizontal line shows the mean value obtained for times after the vertical dashed black marker. The "error bars", for convenience, indicate a range of $\pm 2\%$ around the mean value. The essential message from all these plots is that even though our results do show slight dependence on the various numerical parameters that were varied here, this dependence is small, and within the stated error bars of $\lesssim 2$ to 3%. Depending on the precise parameters the curves in some cases wiggle more strongly, or for higher voltages show stronger oscillations. In this cases, the error is closer to the upper end of the estimated error range. Looking at the comparison of $U = 0$ with exact results and the comparison of $g(T, 0)$ with NRG values in Fig. 3(a), confirms this estimate for our error bar.

S-6. COMPARISON TO OTHER METHODS

In Ref. [6] previous tDMRG quench results on the high-voltage regime of the SIAM are compared to results obtained via the functional renormalization group (FRG) and real-time quantum Monte Carlo (rt-QMC), see Refs. [6, 7] for details on the different methods. Fig. S6 shows the data of Fig. 2 in Ref. [6] together with further rt-QMC results taken from Ref. [7]. For compar-

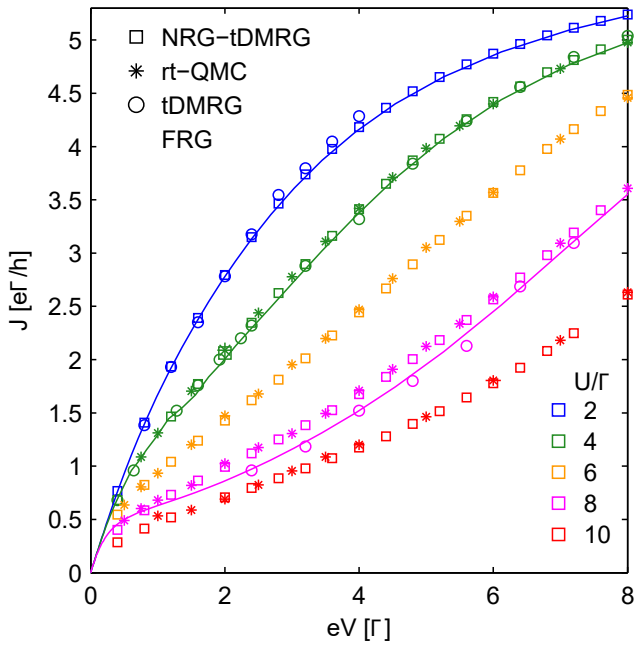

Figure S6. Current in the SIAM as a function of voltage in the high-voltage regime, $V \gtrsim \Gamma$, for different values of U/Γ: we compare results obtained with our method (NRG-tDMRG) to results from rt-QMC, previous tDMRG calculations, and FRG (see Refs. [6, 7] for details). For a range of U/Γ values our results nicely agree with previous results.

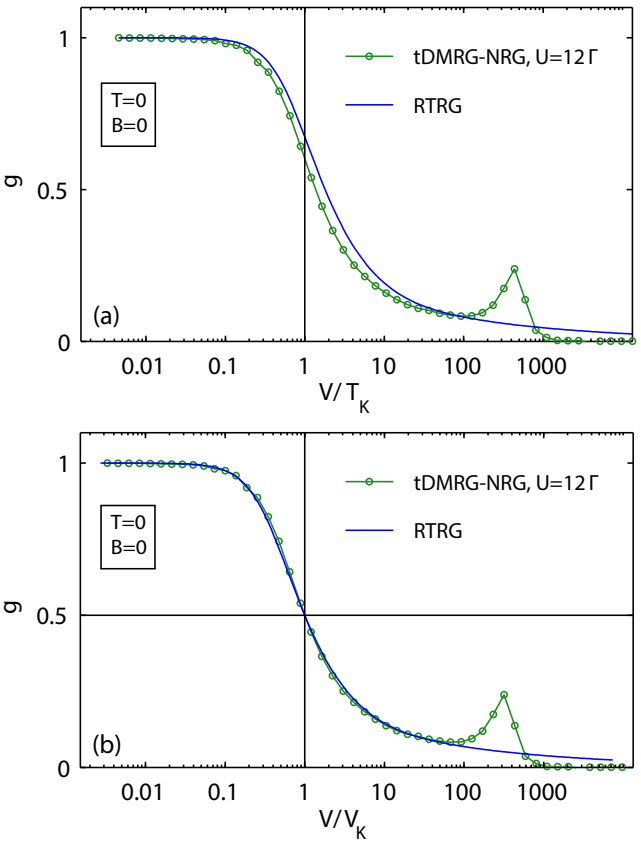

Figure S7. (a) Comparison of $g^{T=0}(V)$ vs. V/T_K on a logarithmic scale, computed at $B = 0$ in the Kondo limit. The data points (circles) show the NRG-tDMRG result for $U/\Gamma = 12$, replotting the corresponding curve from Fig. 3(a) of the main text. The solid curve shows the RTRG results of Pletyukhov and Schoeller [8] for the Kondo model, plotted using Eqs. (S26). The small high-energy peak of the tDMRG-NRG curve reflects charge fluctuations not captured by the Kondo model. (b) Same data, but now plotted vs. V/V_K.

ison, we here also include results obtained in our NRG-tDMRG quench setup. For all parameters our data nicely agree with the rt-QMC data. For $U/\Gamma = 8$, tDMRG and FRG slightly differ from the rt-QMC results (and thus also from our results). This has already been discussed in Ref. [6]. Note, however, that the parameter regimes of these reference systems stayed far away from low-energy Kondo scales since for the larger values of U/Γ the described regime corresponds to $V \gg T_K$, while the small values of U/Γ do not describe the Kondo limit.

We also compare our results for the nonlinear conductance to those obtained by Pletyukhov and Schoeller for the Kondo model using the real-time renormalization group (RTRG) in Ref. [8]. They found that the temperature and voltage scales at which the conductance reaches $\frac{1}{2}$, defined via

$$g^{V=0}(T = T_K) = \tfrac{1}{2}, \qquad g^{T=0}(V = V_K) = \tfrac{1}{2}, \qquad \text{(S25)}$$

differ, with $V_K/T_K \approx 1.8$. (They use the notation $T_K^* = T_K$ and $T_K^{**} = V_K$.) Their result for the nonlinear conductance can be fit well using the trial function

$$g^{T=0}_{\mathrm{RTRG}}(V) \approx \left\{1 + [V/T_K'(x)]^2\right\}^{-s}, \quad x = V/V_K,$$
$$T_K'(x) = T_K^{**}\left(\frac{1 - b + bx^{s'}}{2^{\frac{1}{s}} - 1}\right)^{\frac{1}{2}}, \qquad \text{(S26)}$$

using $s = 0.32$, $b = 0.05$ and $s' = 1.26$. Assuming that our data for $U/\Gamma = 12$ in Fig. 3 of the main text is deep in the Kondo limit, we compare our data for $g^{T=0}(V)$ vs. V/T_K to theirs in Fig. S7(a). Our curve for the nonlinear conductance has a shape similar to theirs, but differs quantitatively in that it bends downward somewhat more quickly. Another way to quantify the difference is to compare the predictions for the conductance at the voltage $V = T_K$. As mentioned in the main text, our calculations yield $g(V = T_K) \approx 0.6$, whereas RTRG predicts a value of approximately $2/3$.

Despite this discrepency, we note that if both our and the RTRG conductance curves are plotted versus V/V_K, thus making the comparison independent of the finite-temperature, equilibrium scale T_K, the two curves almost coincide over a wide range of V/V_K values, see Fig. S7(b). This suggests that the reason for the discrepancy in Fig. S7(a) is that the RTRG approach has an inaccuracy of a few percent in its determination of the ratio V_K/T_K.

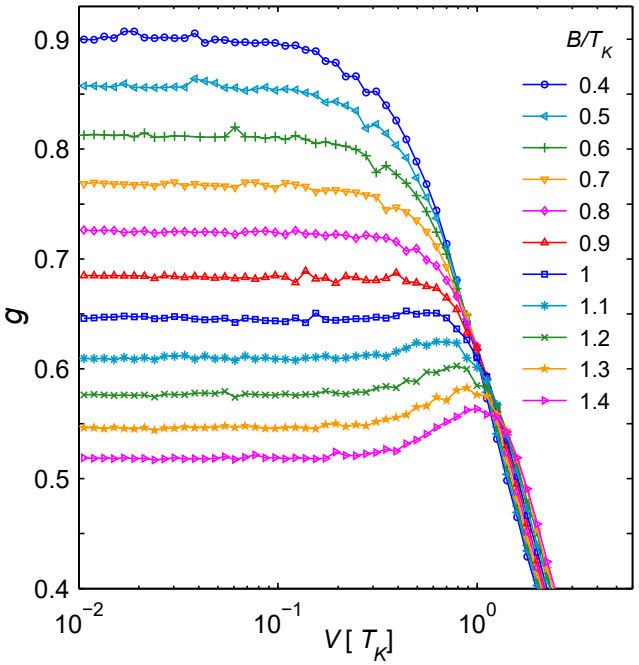

Figure S8. Conductance as a function of voltage at $T = 0$ for different magnetic fields B. We used the same physical parameters as in Fig. 3(c) of the main text, but for more values of the magnetic field B.

S-7. SPLITTING FIELD IN THE SIAM

With increasing magnetic field, the zero-bias peak in the conductance of the SIAM splits into two subpeaks, the position of which is approximately given by $V \approx \pm B$. It has long been of interest to have a quantitatively reliable value for the "splitting field" at which the peak splitting first becomes noticable. The splitting field can be defined in two ways: (i) as the field B_* at which the number of local maxima changes from one to larger than one; or (ii) as the field B_{**} at which the maximum at zero bias turns into a minimum. In principle, these two fields need not coincide: if two side peaks emerge in the flanks of the zero-bias peak before the central maximum has turned into a minimum, B_* would be smaller than B_{**}. However, we would like to argue this does not occur in the present case, for which the mechanism for the peak splitting is well understood. The zero-bias conductance peak is computed as the sum of two peaks, one for spin up and one for spin down. These are pushed apart with increasing field. Once their spacing becomes comparable to their widths, their sum changes from showing a single to a double maximum, with a local minimum in between. This implies $B_* = B_{**}$. Note, though, that for fields just above B_{**}, the local minimum between the two maxima will still be extremely weak and the curve will look essentially flat there. The two maxima will become discernable as unambiguous "peaks" only at fields somewhat larger than B_{**}. Therefore, if one attempts to estimate B_* from (noisy) numerical data, by determining the field, say $B_*^{\rm sp}$, at which side peaks (sp) first become clearly noticable, this will always yield values somewhat larger than $B_* = B_{**}$.

Fig. S8 shows our numerical results for the zero-temperature conductance as a function of voltage for different magnetic fields around $B \approx T_K$, for $U/\Gamma = 12$, as in Fig. 3(c-d) of the main text. While the curve for $B/T_K = 1$ exhibits a clear peak for non-zero voltage, this is not the case for $B/T_K = 0.8T_K$, and the curve for $B/T_K = 0.9$ is a bit too noisy to unambigously identify a side peak. We may therefore regard $B_*^{\rm sp} = T_K$ as a conservative upper bound for the actual splitting field. On the other hand, it is not possible to estimate B_{**} from our data. B_{**} is the field at which $-C_V = \left[\frac{\partial^2}{\partial V^2} g(V)\right]_{V=0}$, the curvature of the conductance at zero bias, changes from negative to positive. However, extracting this curvature reliably from our data would require a level of numerical noise on the order of 0.1%, all the more when tuning B such that C_V tends to zero.

Very recently, exact results for C_V and hence B_{**} have become available. Filippone, Moca, von Delft and Mora (FMDM) [52] have pointed out that C_V can be extracted from the magnetic field dependence of the local spin and charge susceptibilities of the SIAM, which can be computed using the Bethe Ansatz. However, the formula which FMDM obtained for C_V was incorrect due to a sign error in their calculations. A correct formula for C_V was first published by Oguri and Hewson [53], who showed that the Fermi-liquid relations discussed by FMDM could also be derived using Ward identities and the analytic and antisymmetry properties of the vertex function of the SIAM. Very recently FMDM reported (see version 2 of [52]) that upon eliminating their sign mistake, their corrected formula for C_V coincides with that of Oguri and Hewson. Moreover, NRG results by A. Weichselbaum, included in Appendix D of version 3 of [52], agree with the corrected FL predictions for C_V. Incidentally, Figs. 8(c,d) of that analysis illustrates why extracting C_V from $g^{T=0}(V)$ would require an accuracy of order 0.1% for the numerical determination of the conductance as function V.

In the Kondo limit $U/\Gamma \gg 1$, FMDM obtained a splitting field of $B_{**} = 0.75073T_K^{(\chi)}$, where $T_K^{(\chi)} = \frac{1}{4\chi_s}$ is the Kondo scale defined via the zero-field, zero-temperature spin susceptibility. As stated in the caption of Fig. 3 of the main text, $T_K^{(\chi)}$ is related to the Kondo temperature used in this work, defined via $g(T{=}T_K, V{=}0) = \frac{1}{2}$, by $T_K^{(\chi)} = T_K/1.04$ for the parameters used in Figs. 3 and S8. (For a detailed discussion of various different definitions of T_K, see Ref. [46].) Thus, the Fermi-liquid prediction for the splitting field translates to $B_{**} = 0.72T_K$. The fact that our upper bound estimate, $B_*^{\rm sp} = T_K$, is somewhat but not much larger than this value implies that our results are compatible with the slitting field predictions from Fermi liquid theory.

VIII Conclusion and Outlook

To our knowledge, the quench approach presented in chapters VI and VII is the first nonperturbative theoretical approach which was able to give quantitatively reliable results on the full zero-bias peak in the conductance of a quantum dot deep in the Kondo limit at zero temperature. Moreover, the method is also able to confirm the experimental findings in the behavior of this peak with increasing temperature and its splitting due to a finite magnetic field.

This itself is unquestionably the greatest achievement of this work and will hopefully be of much use to future experiments. Nevertheless, we emphasize that the methodological developments made regarding the description of nonequilibrium steady-state physics are not restricted to this single problem:

We employed the hybrid NRG-tDMRG approach to situations of steady-state nonequilibrium, showing explicitly that this combination makes it possible to describe nonequilibrium at exponentially small energy scales based on quenches. Using the thermofield approach and extending it to a form which preserves particle number conservation we have implemented a lead representation which is low in entanglement such that longer time scales can be reached. Furthermore, the purification included in the thermofield approach extends the quench approach to finite temperatures. Besides, although not exploited in this work, we have shown how one can choose a Lindblad driving for discretized leads such that these Lindblad-driven leads represent truly thermal leads. Closely connected to the thermofield approach we explained how this Lindblad equation can be recast into a form in which the Hamiltonian and the Lindblad driving is local on the MPS chain simultaneously.

This opens a wide range of possible applications: It will be straightforward to study further impurity models such as the Kondo model or double-dot structures. Also, the theoretical description of a recent experiment in the two-channel Kondo [97] might be possible with the methods presented in this work. Moreover, our approach is not restricted to the description of nonequilibrium due to a finite voltage difference: since it is able to capture a finite temperature in the leads, it can directly be employed to also study thermotransport, i.e., a current flowing through an impurity due to a finite temperature difference, as can be measured in experiment [98]. Furthermore, the hybrid NRG-tDMRG has many features that could be useful in the description of impurities coupled to superconducting leads.

From the methodological point of view, the quench approach and the Lindblad-driven discretized leads are strongly connected such that an extension of the quench approach to a truly open Lindblad system seems to be within reach. In particular, this possibly allows a direct determination of the steady state without the need for a time evolution. In addition

it would be favorable to extend our method to the calculations of spectral functions, e.g., similar to reference [94]. Ideas like the open Wilson chain construction could further improve the method, e.g., in terms of an even better discretization.

Concluding, the description of the zero-bias peak at zero temperature for a quantum dot in the Kondo regime is a milestone for the MPS-based evaluation of impurity models in nonequilibrium. At the same time it is hopefully just the beginning of a further exploration of many interesting nonequilibrium effects.

Bibliography

[P1] F. Schwarz, M. Goldstein, A. Dorda, E. Arrigoni, A. Weichselbaum and J. von Delft, *Lindblad-driven discretized leads for nonequilibrium steady-state transport in quantum impurity models: Recovering the continuum limit*, Phys. Rev. B **94** (2016), 155142.

[P2] F. Schwarz, I. Weymann, J. von Delft and A. Weichselbaum, *Nonequilibrium Steady-State Transport in Quantum Impurity Models: A Thermofield and Quantum Quench Approach Using Matrix Product States*, Phys. Rev. Lett. **121** (2018), 137702.

[P3] B. Bruognolo, N.-O. Linden, F. Schwarz, S.-S. B. Lee, K. Stadler, A. Weichselbaum, M. Vojta, F. B. Anders and J. von Delft, *Open Wilson chains for quantum impurity models: Keeping track of all bath modes*, Phys. Rev. B **95** (2017), 121115.

[P4] D. M. Fugger, A. Dorda, F. Schwarz, J. von Delft and E. Arrigoni, *Nonequilibrium Kondo effect in a magnetic field: auxiliary master equation approach*, New J. Phys. **20** (2018), 013030.

[5] W. de Haas, J. de Boer and G. van dën Berg, *The electrical resistance of gold, copper and lead at low temperatures*, Physica **1** (1934), 1115–1124.

[6] J. Kondo, *Resistance Minimum in Dilute Magnetic Alloys*, Progress of Theoretical Physics **32** (1964), 37.

[7] P. W. Anderson, *A poor man's derivation of scaling laws for the Kondo problem*, J. Phys. C: Solid State Phys. **3** (1970), 2436.

[8] K. G. Wilson, *The renormalization group: Critical phenomena and the Kondo problem*, Rev. Mod. Phys. **47** (1975), 773–840.

[9] H. R. Krishna-murthy, J. W. Wilkins and K. G. Wilson, *Renormalization-group approach to the Anderson model of dilute magnetic alloys. I. Static properties for the symmetric case*, Phys. Rev. B **21** (1980), 1003–1043.

[10] D. Goldhaber-Gordon, H. Shtrikman, D. Mahalu, D. Abusch-Magder, U. Meirav and M. A. Kastner, *Kondo effect in a single-electron transistor*, Nature **391** (1998), 156–159.

[11] S. M. Cronenwett, T. H. Oosterkamp and L. P. Kouwenhoven, *A Tunable Kondo Effect in Quantum Dots*, Science **281** (1998), 540–544.

[12] W. G. van der Wiel, S. D. Franceschi, T. Fujisawa, J. M. Elzerman, S. Tarucha and L. P. Kouwenhoven, *The Kondo Effect in the Unitary Limit*, Science **289** (2000), 2105–2108.

[13] P. W. Anderson, *Localized Magnetic States in Metals*, Phys. Rev. **124** (1961), 41–53.

[14] J. R. Schrieffer and P. A. Wolff, *Relation between the Anderson and Kondo Hamiltonians*, Phys. Rev. **149** (1966), 491–492.

[15] V. L. Campo and L. N. Oliveira, *Alternative discretization in the numerical renormalization-group method*, Phys. Rev. B **72** (2005), 104432.

[16] A. Kamenev, *Field Theory of Non-Equilibrium Systems*, Cambridge University Press, Cambridge, 2011.

[17] S. G. Jakobs, *Functional renormalization group studies of quantum transport through mesoscopic systems*, PhD thesis, Aachen, 2010.

[18] Y. Meir and N. S. Wingreen, *Landauer formula for the current through an interacting electron region*, Phys. Rev. Lett. **68** (1992), 2512–2515.

[19] J. E. Moore and X.-G. Wen, *Anomalous Magnetic Splitting of the Kondo Resonance*, Phys. Rev. Lett. **85** (2000), 1722–1725.

[20] T. A. Costi, *Kondo Effect in a Magnetic Field and the Magnetoresistivity of Kondo Alloys*, Phys. Rev. Lett. **85** (2000), 1504–1507.

[21] R. Bulla, T. A. Costi and T. Pruschke, *Numerical renormalization group method for quantum impurity systems*, Rev. Mod. Phys. **80** (2008), 395–450.

[22] P. B. Wiegmann and A. M. Tsvelick, *Exact solution of the Anderson model: I*, J. Phys. C: Solid State Phys. **16** (1983), 2281.

[23] A. M. Tsvelick and P. B. Wiegmann, *Exact solution of the Anderson model. II. Thermodynamic properties at finite temperatures*, J. Phys. C: Solid State Phys. **16** (1983), 2321.

[24] M. Hanl and A. Weichselbaum, *Local susceptibility and Kondo scaling in the presence of finite bandwidth*, Phys. Rev. B **89** (2014), 075130.

[25] D. C. Ralph and R. A. Buhrman, *Kondo-assisted and resonant tunneling via a single charge trap: A realization of the Anderson model out of equilibrium*, Phys. Rev. Lett. **72** (1994), 3401–3404.

[26] F. Simmel, R. H. Blick, J. P. Kotthaus, W. Wegscheider and M. Bichler, *Anomalous Kondo Effect in a Quantum Dot at Nonzero Bias*, Phys. Rev. Lett. **83** (1999), 804–807.

[27] A. V. Kretinin, H. Shtrikman, D. Goldhaber-Gordon, M. Hanl, A. Weichselbaum, J. von Delft, T. Costi and D. Mahalu, *Spin-$\frac{1}{2}$ Kondo effect in an InAs nanowire quantum dot: Unitary limit, conductance scaling, and Zeeman splitting*, Phys. Rev. B **84** (2011), 245316.

[28] A. V. Kretinin, H. Shtrikman and D. Mahalu, *Universal line shape of the Kondo zero-bias anomaly in a quantum dot*, Phys. Rev. B **85** (2012), 201301.

[29] A. Dorda, M. Ganahl, H. G. Evertz, W. von der Linden and E. Arrigoni, *Auxiliary master equation approach within matrix product states: Spectral properties of the nonequilibrium Anderson impurity model*, Phys. Rev. B **92** (2015), 125145.

[30] S. Kehrein, *Scaling and Decoherence in the Nonequilibrium Kondo Model*, Phys. Rev. Lett. **95** (2005), 056602.

[31] F. B. Anders, *Steady-State Currents through Nanodevices: A Scattering-States Numerical Renormalization-Group Approach to Open Quantum Systems*, Phys. Rev. Lett. **101** (2008), 066804.

[32] J. Eckel, F. Heidrich-Meisner, S. G. Jakobs, M. Thorwart, M. Pletyukhov and R. Egger, *Comparative study of theoretical methods for non-equilibrium quantum transport*, New J. Phys. **12** (2010), 043042.

[33] M. Pletyukhov and H. Schoeller, *Nonequilibrium Kondo model: Crossover from weak to strong coupling*, Phys. Rev. Lett. **108** (2012), 260601.

[34] S. Smirnov and M. Grifoni, *Keldysh effective action theory for universal physics in spin-$\frac{1}{2}$ Kondo dots*, Phys. Rev. B **87** (2013), 121302.

[35] G. Cohen, E. Gull, D. R. Reichman and A. J. Millis, *Green's Functions from Real-Time Bold-Line Monte Carlo Calculations: Spectral Properties of the Nonequilibrium Anderson Impurity Model*, Phys. Rev. Lett. **112** (2014), 146802.

[36] F. Reininghaus, M. Pletyukhov and H. Schoeller, *Kondo model in nonequilibrium: Interplay between voltage, temperature, and crossover from weak to strong coupling*, Phys. Rev. B **90** (2014), 085121.

[37] A. E. Antipov, Q. Dong and E. Gull, *Voltage Quench Dynamics of a Kondo System*, Phys. Rev. Lett. **116** (2016), 036801.

[38] F. Heidrich-Meisner, A. E. Feiguin and E. Dagotto, *Real-time simulations of nonequilibrium transport in the single-impurity Anderson model*, Phys. Rev. B **79** (2009), 235336.

[39] S. Kirino, T. Fujii, J. Zhao and K. Ueda, *Time-Dependent DMRG Study on Quantum Dot under a Finite Bias Voltage*, J. Phys. Soc. Jpn. **77** (2008), 084704.

[40] L. G. G. V. Dias da Silva, F. Heidrich-Meisner, A. E. Feiguin, C. A. Büsser, G. B. Martins, E. V. Anda and E. Dagotto, *Transport properties and Kondo correlations in nanostructures: Time-dependent DMRG method applied to quantum dots coupled to Wilson chains*, Phys. Rev. B **78** (2008), 195317.

[41] U. Schollwöck, *The density-matrix renormalization group in the age of matrix product states*, Ann. Phys. **326** (2011), 96–192.

[42] H. Saberi, A. Weichselbaum and J. von Delft, *Matrix-product-state comparison of the numerical renormalization group and the variational formulation of the density-matrix renormalization group*, Phys. Rev. B **78** (2008), 035124.

[43] A. Weichselbaum, F. Verstraete, U. Schollwöck, J. I. Cirac and J. von Delft, *Variational matrix-product-state approach to quantum impurity models*, Phys. Rev. B **80** (2009), 165117.

[44] J. Eisert, M. Cramer and M. B. Plenio, *Colloquium*, Rev. Mod. Phys. **82** (2010), 277–306.

[45] A. Weichselbaum, *Non-abelian symmetries in tensor networks: A quantum symmetry space approach*, Ann. Phys. **327** (2012), 2972–3047.

[46] G. Vidal, *Efficient Simulation of One-Dimensional Quantum Many-Body Systems*, Phys. Rev. Lett. **93** (2004), 040502.

[47] A. J. Daley, C. Kollath, U. Schollwöck and G. Vidal, *Time-dependent density-matrix renormalization-group using adaptive effective Hilbert spaces*, J. Stat. Mech. (2004), P04005.

[48] S. R. White and A. E. Feiguin, *Real-Time Evolution Using the Density Matrix Renormalization Group*, Phys. Rev. Lett. **93** (2004), 076401.

[49] *The Nobel Prize in Physics 1982*, Nobel Media AB 2014, URL: `http://www.nobelprize.org/nobel_prizes/physics/laureates/1982/` (visited on 27 Apr. 2017).

[50] H. O. Frota and L. N. Oliveira, *Photoemission spectroscopy for the spin-degenerate Anderson model*, Phys. Rev. B **33** (1986), 7871–7874.

[51] M. Yoshida, M. A. Whitaker and L. N. Oliveira, *Renormalization-group calculation of excitation properties for impurity models*, Phys. Rev. B **41** (1990), 9403–9414.

[52] W. C. Oliveira and L. N. Oliveira, *Generalized numerical renormalization-group method to calculate the thermodynamical properties of impurities in metals*, Phys. Rev. B **49** (1994), 11986–11994.

[53] R. Žitko, *Adaptive logarithmic discretization for numerical renormalization group methods*, Comput. Phys. Commun. **180** (2009), 1271–1276.

[54] A. Weichselbaum and J. von Delft, *Sum-Rule Conserving Spectral Functions from the Numerical Renormalization Group*, Phys. Rev. Lett. **99** (2007), 076402.

[55] A. Weichselbaum, *Tensor networks and the numerical renormalization group*, Phys. Rev. B **86** (2012), 245124.

[56] F. B. Anders and A. Schiller, *Real-Time Dynamics in Quantum-Impurity Systems: A Time-Dependent Numerical Renormalization-Group Approach*, Phys. Rev. Lett. **95** (2005), 196801.

[57] F. Verstraete, J. J. García-Ripoll and J. I. Cirac, *Matrix Product Density Operators: Simulation of Finite-Temperature and Dissipative Systems*, Phys. Rev. Lett. **93** (2004), 207204.

[58] A. E. Feiguin and S. R. White, *Finite-temperature density matrix renormalization using an enlarged Hilbert space*, Phys. Rev. B **72** (2005), 220401.

[59] C. Karrasch, J. H. Bardarson and J. E. Moore, *Finite-Temperature Dynamical Density Matrix Renormalization Group and the Drude Weight of Spin-1/2 Chains*, Phys. Rev. Lett. **108** (2012), 227206.

[60] C. W. Gardiner and P. Zoller, *Quantum Noise*, Springer, Berlin, 2000.

[61] G. Lindblad, *On the generators of quantum dynamical semigroups*, Commun. Math. Phys. **48** (1976), 119–130.

[62] G. Lindblad, *Non-Markovian quantum stochastic processes and their entropy*, Commun. Math. Phys. **65** (1979), 281–294.

[63] H.-P. Breuer and F. Petruccione, *The Theory Of Open Quantum Systems*, Oxford University Press, Oxford, 2002.

[64] M. Bauer, *Lindblad driving for nonequilibrium steady-state transport for noninteracting quantum impurity models*, Bachelor thesis, München, 2001.

[65] A. A. Dzhioev and D. S. Kosov, *Stability analysis of multiple nonequilibrium fixed points in self-consistent electron transport calculations*, J. Chem. Phys. **135** (2011), 174111.

[66] A. A. Dzhioev and D. S. Kosov, *Super-fermion representation of quantum kinetic equations for the electron transport problem*, J. Chem. Phys. **134** (2011), 044121.

[67] A. A. Dzhioev and D. S. Kosov, *Second-order post-Hartree–Fock perturbation theory for the electron current*, J. Chem. Phys. **134** (2011), 154107.

[68] A. A. Dzhioev and D. S. Kosov, *Nonequilibrium perturbation theory in Liouville-Fock space for inelastic electron transport*, J. Phys.: Condens. Matter **24** (2012), 225304.

[69] A. A. Dzhioev and D. S. Kosov, *Nonequilibrium configuration interaction method for transport in correlated quantum systems*, J. Phys. A **47** (2014), 095002.

[70] A. A. Dzhioev and D. S. Kosov, *Superoperator coupled cluster method for nonequilibrium density matrix*, J. Phys. A **48** (2015), 015004.

[71] E. Arrigoni, M. Knap and W. von der Linden, *Nonequilibrium Dynamical Mean-Field Theory: An Auxiliary Quantum Master Equation Approach*, Phys. Rev. Lett. **110** (2013), 086403.

[72] A. H. Werner, D. Jaschke, P. Silvi, M. Kliesch, T. Calarco, J. Eisert and S. Montangero, *Positive Tensor Network Approach for Simulating Open Quantum Many-Body Systems*, Phys. Rev. Lett. **116** (2016), 237201.

[73] K. Mølmer, Y. Castin and J. Dalibard, *Monte Carlo wave-function method in quantum optics*, J. Opt. Soc. Am. B **10** (1993), 524–538.

[74] H. Carmichael, *An open systems approach to quantum optics*, Springer, Berlin, 1993.

[75] A. J. Daley, *Quantum trajectories and open many-body quantum systems*, Adv. Phys. **63** (2014), 77–149.

[76] A. J. Daley, J. M. Taylor, S. Diehl, M. Baranov and P. Zoller, *Atomic Three-Body Loss as a Dynamical Three-Body Interaction*, Phys. Rev. Lett. **102** (2009), 040402.

[77] P. Barmettler and C. Kollath, *Controllable manipulation and detection of local densities and bipartite entanglement in a quantum gas by a dissipative defect*, Phys. Rev. A **84** (2011), 041606.

[78] M. B. Plenio and P. L. Knight, *The quantum-jump approach to dissipative dynamics in quantum optics*, Rev. Mod. Phys. **70** (1998), 101–144.

[79] G. J. M. Howard M. Wiseman, *Quantum measurement and control*, Cambridge University Press, 2010.

[80] J. Cui, J. I. Cirac and M. C. Bañuls, *Variational Matrix Product Operators for the Steady State of Dissipative Quantum Systems*, Phys. Rev. Lett. **114** (2015), 220601.

[81] E. Mascarenhas, H. Flayac and V. Savona, *Matrix-product-operator approach to the nonequilibrium steady state of driven-dissipative quantum arrays*, Phys. Rev. A **92** (2015), 022116.

[82] E. Boulat, H. Saleur and P. Schmitteckert, *Twofold Advance in the Theoretical Understanding of Far-From-Equilibrium Properties of Interacting Nanostructures*, Phys. Rev. Lett. **101** (2008), 140601.

[83] A. Branschädel, G. Schneider and P. Schmitteckert, *Conductance of inhomogeneous systems: Real-time dynamics*, Annalen der Physik **522** (2010), 657–678.

[84] K. Bidzhiev and G. Misguich, *Out-of-equilibrium dynamics in a quantum impurity model: Numerics for particle transport and entanglement entropy*, Phys. Rev. B **96** (2017), 195117.

[85] Y. Takahashi and H. Umezawa, *Thermo field dynamics*, Collective Phenomena **2** (1975), 55–80.

[86] A. Das, *Topics in Finite Temperature Field Theory*, (2000), arXiv: `hep-ph/0004125 [hep-ph]`.

[87] I. de Vega and M.-C. Bañuls, *Thermofield-based chain-mapping approach for open quantum systems*, Phys. Rev. A **92** (2015), 052116.

[88] E. Eidelstein, A. Schiller, F. Güttge and F. B. Anders, *Coherent control of correlated nanodevices: A hybrid time-dependent numerical renormalization-group approach to periodic switching*, Phys. Rev. B **85** (2012), 075118.

[89] F. Güttge, F. B. Anders, U. Schollwöck, E. Eidelstein and A. Schiller, *Hybrid NRG-DMRG approach to real-time dynamics of quantum impurity systems*, Phys. Rev. B **87** (2013), 115115.

[90] S. M. Barnett and B. J. Dalton, *Liouville space description of thermofields and their generalisations*, J. Phys. A: Math. Gen. **20** (1987), 411.

[91] C. Guo, I. de Vega, U. Schollwöck and D. Poletti, *Stable-unstable transition for a Bose-Hubbard chain coupled to an environment*, Phys. Rev. A **97** (2018), 053610.

[92] A. Weichselbaum, *Discarded weight and entanglement spectra in the numerical renormalization group*, Phys. Rev. B **84** (2011), 125130.

[93] P. Corboz, R. Orús, B. Bauer and G. Vidal, *Simulation of strongly correlated fermions in two spatial dimensions with fermionic projected entangled-pair states*, Phys. Rev. B **81** (2010), 165104.

[94] T. Barthel, U. Schollwöck and S. R. White, *Spectral functions in one-dimensional quantum systems at finite temperature using the density matrix renormalization group*, Phys. Rev. B **79** (2009), 245101.

[95] A. Dorda, M. Sorantin, W. von der Linden and E. Arrigoni, *Optimized auxiliary representation of non-Markovian impurity problems by a Lindblad equation*, New J. Phys. **19** (2017), 063005.

[96] A. Georges, G. Kotliar, W. Krauth and M. J. Rozenberg, *Dynamical mean-field theory of strongly correlated fermion systems and the limit of infinite dimensions*, Rev. Mod. Phys. **68** (1996), 13–125.

[97] Z. Iftikhar, S. Jezouin, A. Anthore, U. Gennser, F. D. Parmentier, A. Cavanna and F. Pierre, *Two-channel Kondo effect and renormalization flow with macroscopic quantum charge states*, Nature **526** (2015), 233–236.

[98] S. F. Svensson, E. A. Hoffmann, N. Nakpathomkun, P. M. Wu, H. Q. Xu, H. A. Nilsson, D. Sánchez, V. Kashcheyevs and H. Linke, *Nonlinear thermovoltage and thermocurrent in quantum dots*, New J. Phys. **15** (2013), 105011.

List of figures

Acknowledgements

First of all, I would like to thank Jan von Delft and Andreas Weichselbaum for offering me the possibility to join their group, for their guidance, and for the many helpful discussions. Without them this work would not have been possible. In particular, I would like to thank Andreas Weichselbaum for the permission to use his QSpace library.

I would also like to thank all my coworkers, Enrico Arrigoni, Jan von Delft, Antonius Dorda, Delia Fugger, Moshe Goldstein, Andreas Weichselbaum, and Ireneusz Weymann, for the fruitful collaboration and enlightening discussions.

I am grateful to Markus Hanl and Ireneusz Weymann, who guided me in my first steps, and to Benedikt Bruognolo for the many discussions on matrix product states.

Finally, I would like to thank all the people who are or have been part of the "Lehrstuhl für theoretische Festkörperphysik". I very much appreciated the pleasant atmosphere and the mutual support. A special word of thanks goes to Stephane Schoonover for all the help in the administrative work, as well as to Benedikt Bruognolo, Markus Hanl, and Katharina Stadler for sharing an office with me.

My research was supported by the Deutsche Forschungsgemeinschaft through SFB631, SFB-TR12, and NIM, and by the German-Israeli-Foundation through I-1259-303.10.